



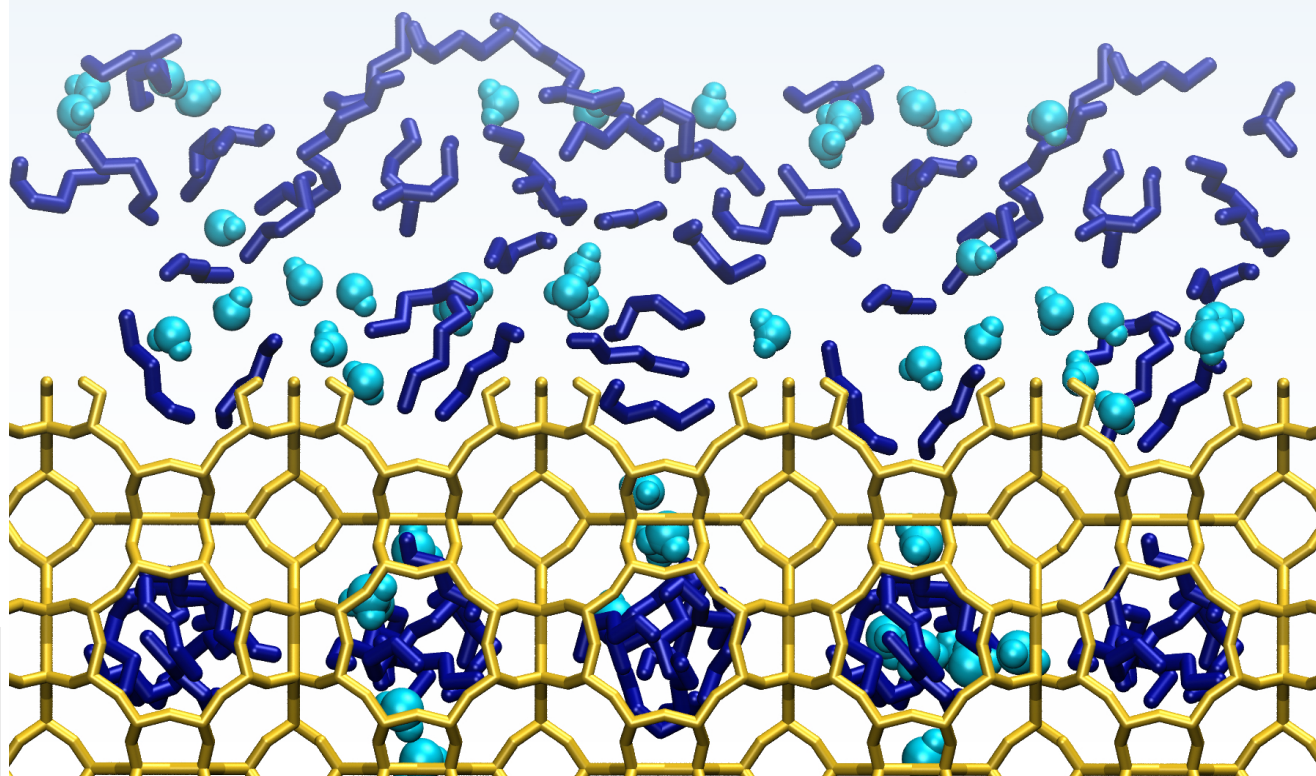
UNIVERSITAT  
POLITÈCNICA  
DE VALÈNCIA

# Mixture separations with zeolites: molecular view on adsorptive processes

Author: Alechania Misturini

Supervisors: Dr. Germán Ignacio Sastre Navarro  
Prof. Dr. Fernando Rey García

December 2022





---

# Mixture separations with zeolites: molecular view on adsorptive processes

December 2022

---

Author: Alechania Misturini

Supervisors: Dr. Germán Ignacio Sastre Navarro  
Prof. Dr. Fernando Rey García

EDITORIAL  
UNIVERSITAT POLITÈCNICA DE VALÈNCIA



UNIVERSITAT  
POLITÈCNICA  
DE VALÈNCIA



INSTITUTO DE  
TECNOLOGÍA  
QUÍMICA




**CSIC**  
CONSEJO SUPERIOR DE INVESTIGACIONES CIENTÍFICAS



Doctoral thesis developed from October 2019 to December 2022, in the  
Institute of Chemical Technology (ITQ – CSIC) at the Polytechnic  
University of Valencia (UPV), Spain.

**PhD candidate:**

MSc. Alechania Misturini

 0000-0002-5873-8679

**Dissertation Committee:**

Prof. Dr. Juan Carlos Castro Palacio (*President*)  
Departamento de Física Aplicada  
Universitat Politècnica de València

Dr. Salvador Rodríguez-Gómez Balestra (*Secretary*)  
Departamento de Sistemas Físicos, Químicos y Naturales  
Universidad Pablo de Olavide, Sevilla

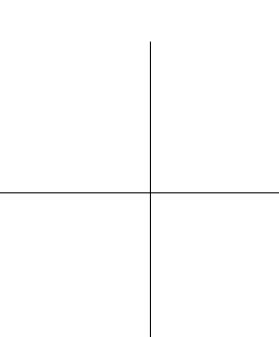
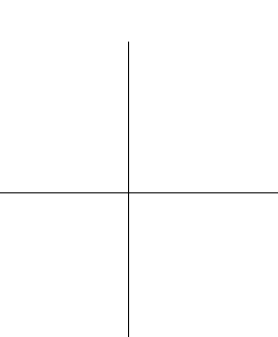
Prof. Dr. Manuel Martínez Piñeiro (*Tribunal member*)  
Facultad de Química  
Universidade de Vigo

Dr. Neyvis Almora Barrios (*Substitute*)  
Instituto de Ciencia Molecular  
Universitat de València

Dr. Luis Gómez-Hortigüela Sainz (*Substitute*)  
Instituto de Catálisis y Petroleoquímica, Madrid  
Consejo Superior de Investigaciones Científicas

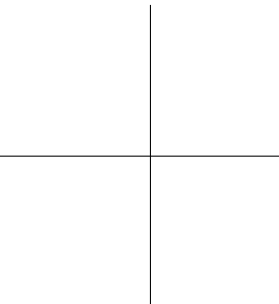
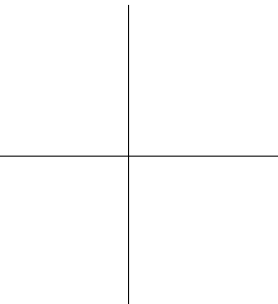
Prof. Dr. Benjamín Eduardo Solsona Espriu (*Substitute*)  
Departamento de Ingeniería Química  
Universitat de València





*“[...] talent means nothing, while experience,  
acquired in humility and with hard work,  
means everything.”  
— Patrick Süskind*

*“We are what we repeatedly do.  
Excellence, then, is not an act, but a habit.”  
— Will Durant*







# Abstract

Computational chemistry methods have been employed in the study of zeolite materials applied to separation processes. A classical approach was considered, where the force fields were selected during benchmark procedures among the models currently available. The obtained results have been validated considering experimental data, and models description was improved, when possible, by parameterization procedures. Thus, the best models described systems with different degrees of complexity, that were simulated through Molecular Dynamics and Monte Carlo methods. Diffusion and adsorption in zeolites' micropores (bulk) and external surface could be understood at a molecular level. The adsorption energy was calculated, and its magnitude also decomposed into the electrostatic and van der Waals contributions. Besides, a closer look into the host-guest and guest-guest interactions could be done during the trajectories simulated.

Considering the growing energetic demand worldwide, biofuels are considered a sustainable option obtained from biomass. The steps of the experimental process developed by Denayer et al. for biobutanol recovery from a fermented mixture have been successfully simulated. Both adsorption and desorption cycles in two zeolitic columns with complementary selectivity (LTA and CHA-type) were modeled as nanosheet systems, considering the main experimental features. Although the experimental time scales are unreachable for the current computational resources available, the systems simulated could capture the experimental phenomena, and were further evaluated through the microscopic behavior of the systems.

An experimental and computational study pointed pure silica STW (Si-STW) as a promising candidate for the separation of linear, monobranched and dibranched alkanes. C5 to C7 isomers were tested, and Si-STW material outperformed pure silica MFI adsorption capacity and selectivity, specially towards the dibranched isomers with quaternary carbon atoms. Adsorption isotherms, heat of adsorption and the diffusional behavior of the tested hydrocarbons have been calculated, and compared with the experimental results. Thus, Si-STW adsorptive properties can be further explored for its usage over the product obtained during the hydromeri-

---

sation process – that generates higher-octane components for gasoline mixture –, increasing its octane number.

The production of 6-kestose for industrial usage as prebiotic and low-glycemic sugar is dependent on its separation from sucrose molecules. The separation of an equimolar aqueous mixture, containing sucrose and 6-kestose, by zeolitic membranes have been investigated through Molecular Dynamics simulations. A screening considering the 253 zeolites structures reported, pointed out the three most promising candidates (AET, ETR and DON), by evaluating the size exclusion effect (adsorption of sucrose and exclusion of 6-kestose), the mobility of both sugars inside the frameworks (evaluated with bulk models), and simulating their future application as membrane systems. Among the best candidates, DON framework presented a significant selectivity for sucrose molecules, with the largest flux, and being feasible as a pure silica material, matching the chemical composition simulated.

## Resumen

Los métodos de química computacional se han empleado en el estudio de materiales de zeolita aplicados a procesos de separación. Se consideró un enfoque clásico, donde los campos de fuerza se seleccionaron durante los procedimientos de *benchmark* entre los modelos actualmente disponibles. Los resultados obtenidos han sido validados considerando datos experimentales y se mejoró la descripción de los modelos, cuando fue posible, mediante procedimientos de parametrización. Así, los mejores modelos describieron sistemas con diferentes grados de complejidad, que fueron simulados a través de los métodos de Dinámica Molecular y Monte Carlo. La difusión y la adsorción en los microporos (*bulk*) y en la superficie externa de las zeolitas se pueden entender a nivel molecular. Se calculó la energía de adsorción y también se descompuso su magnitud en las contribuciones electrostática y de van der Waals. Además, fue posible observar más de cerca las interacciones anfitrión–invitado e invitado–invitado durante las trayectorias simuladas.

Considerando la creciente demanda energética a nivel mundial, los biocombustibles se consideran una opción sostenible obtenida a partir de biomasa. Se han simulado con éxito los pasos del proceso experimental desarrollado por Denayer et al. para la recuperación de biobutanol a partir de una mezcla fermentada. Se modelaron los ciclos de adsorción y desorción en dos columnas zeolíticas con selectividad complementaria (tipo LTA y CHA), con sistemas de nanoláminas y considerando las principales características experimentales. Aunque las escalas de tiempo experimentales son inalcanzables para los recursos computacionales disponibles actualmente, los sistemas simulados pudieron capturar los fenómenos experimentales y fueron evaluados más a fondo a través del comportamiento microscópico de los sistemas.

Un estudio experimental y computacional señaló la STW sílice pura (Si-STW) como un candidato prometedor para la separación de alcanos lineales, monoramificados y diramificados. Se probaron los isómeros C5 a C7, y el material Si-STW superó la capacidad de adsorción y selectividad de MFI de sílice pura, especialmente hacia los isómeros diramificados con átomos de carbono cuaternarios. Se

---

calcularon las isothermas de adsorción, el calor de adsorción y el comportamiento de difusión de los hidrocarburos probados y se compararon con los resultados experimentales. Por lo tanto, las propiedades de adsorción de Si-STW pueden ser exploradas para su uso sobre el producto obtenido durante el proceso de hidromerización – que genera componentes de mayor octanaje para la mezcla de gasolina –, aumentando su número de octano.

La producción de 6-kestosa para uso industrial como prebiótico y azúcar de bajo índice glucémico depende de su separación de las moléculas de sacarosa. La separación de una mezcla acuosa equimolar, que contiene sacarosa y 6-kestosa, mediante membranas zeolíticas se ha investigado a través de simulaciones de Dinámica Molecular. Una selección considerando las 253 estructuras de zeolitas reportadas, señaló los tres candidatos más prometedores (AET, ETR y DON), al evaluar el efecto de exclusión por tamaño (adsorción de sacarosa y exclusión de 6-kestosa), la movilidad de ambos azúcares dentro de las estructuras (evaluados con modelos tipo *bulk*), y simulando su futura aplicación como sistemas de membranas. Entre los mejores candidatos, la zeolita DON presentó una selectividad significativa para las moléculas de sacarosa, con el mayor flujo y siendo factible como material de sílice pura, igualando la composición química simulada.

## Resum

Els mètodes de química computacional s'han emprat en l'estudi de materials de zeolita aplicats a processos de separació. Es va considerar un enfocament clàssic, on els camps de força es van seleccionar durant els procediments de *benchmark* entre els models actualment disponibles. Els resultats obtinguts han sigut validats considerant dades experimentals i es va millorar la descripció dels models, quan va ser possible, mitjançant procediments de parametrització. Així, els millors models van descriure sistemes amb diferents graus de complexitat, que van ser simulats a través dels mètodes de Dinàmica Molecular i Monte Carlo. La difusió i l'adsorció en els microporus (*bulk*) i en la superfície externa de les zeolites es poden entendre a nivell molecular. Es va calcular l'energia d'adsorció i també es va descompondre la seua magnitud en les contribucions electroestàtica i de van der Waals. A més, va ser possible observar més de prop les interaccions amfitrió-convidat i convidat-convidat durant les trajectòries simulades.

Considerant la creixent demanda energètica a nivell mundial, els biocombustibles es consideren una opció sostenible obtinguda a partir de biomassa. S'han simulat amb èxit els passos del procés experimental desenvolupat per Denayer et al. per a la recuperació de biobutanol a partir d'una mescla fermentada. Es van modelar els cicles d'adsorció i desorció en dues columnes de zeolites amb selectivitat complementària (tipus LTA i CHA), amb sistemes de nanolàminas i considerant les principals característiques experimentals. Encara que les escales de temps experimentals són inassolibles per als recursos computacionals disponibles actualment, els sistemes simulats van poder capturar els fenòmens experimentals i van ser avaluats més a fons a través del comportament microscòpic dels sistemes.

Un estudi experimental i computacional va assenyalar la STW sílice pura (Si-STW) com un candidat prometedor per a la separació d'alcans lineals, monoramificats i diramificats. Es van provar els isòmers C5 a C7, i el material Si-STW va superar la capacitat d'adsorció i selectivitat de MFI de sílice pura, especialment cap als isòmers diramificats amb àtoms de carboni quaternaris. Es van calcular les isotermes d'adsorció, la calor d'adsorció i el comportament de difusió dels hidrocarburs provats i es van comparar amb els resultats experimentals. Per tant,

---

les propietats d'adsorció de Si-STW poden ser explorades per al seu ús sobre el producte obtingut durant el procés de hidromerització – que genera components de major octanatge per a la mescla de gasolina –, augmentant el seu número d'octà.

La producció de 6-kestosa per a ús industrial com a prebiòtic i sucre de baix índex glucèmic depèn de la seua separació de les molècules de sacarosa. La separació d'una mescla aquosa equimolar que conté sacarosa i 6-kestosa mitjançant membranes de zeolites s'ha investigat amb simulacions de Dinàmica Molecular. Una selecció considerant les 253 estructures de zeolites reportades, va assenyalar els tres candidats més prometedors (AET, ETR i DON), en avaluar l'efecte d'exclusió per grandària (adsorció de sacarosa i exclusió de 6-kestosa), la mobilitat de tots dos sucres dins de les estructures (avaluats amb models tipus *bulk*), i simulant la seua futura aplicació com a sistemes de membranes. Entre els millors candidats, la zeolita DON va presentar una selectivitat significativa per a les molècules de sacarosa, amb el major flux i sent factible com a material de sílice pura, igualant la composició química simulada.

# Acronyms

- AA** All Atom model.
- AIPO** Aluminophosphate material.
- BAS** Brønsted acid sites.
- CBMC** Configurational-Bias Monte Carlo.
- FF** Force Field.
- HB** Hydrogen bond.
- IZA** International Zeolite Association.
- LJ** Lennard-Jones potential.
- MC** Monte Carlo simulation.
- MD** Molecular Dynamics simulation.
- PBC** Periodic boundary conditions.
- SAPO** Silicoaluminophosphate material.
- SM** Statistical Mechanics.
- UA** United Atom model.
- UFF** Universal Force Field.

**vdW** Van der Waals.



# Glossary

$A_{ij}$  General 12th power Lennard-Jones coefficient.

$B_{ij}$  General 6th power Lennard-Jones coefficient.

$C_{MC}$  Number of configurations generated by the MC method.

$D_e$  Well depth in the Morse potential.

$R$  Gas constant.

$V_n$  Torsional barrier for the dihedral angle between particles  $i$ ,  $j$ ,  $k$  and  $l$ .

$W$  Rosenbluth weight of the configuration.

$\Delta G$  Gibbs free energy.

$\Delta H$  Change in enthalpy.

$\Delta S$  Change in entropy.

$\Delta U$  Internal energy.

$\Lambda$  De Broglie wavelength.

$\Xi$  Partition function of the Grand Canonical ensemble.

$\alpha_{ij}$  Parameter of the Morse potential, equals to  $\sqrt{k_{min}/2D_e}$ .

$\alpha$  Underlying matrix of the Markov chain.

- $\beta$  Thermodynamic beta, equals to  $1/k_B T$ .
- $\ddot{\mathbf{r}}$  Second time derivative of the position, acceleration.
- $\dot{\mathbf{r}}$  First time derivative of the position, velocity.
- $\gamma$  Phase angle for the expression of the torsional angle between particles  $i$ ,  $j$ ,  $k$  and  $l$ .
- $\langle U_g \rangle$  Average ensemble energy of the guest, isolated.
- $\langle U_{hg} \rangle$  Average ensemble energy of the host-guest complex.
- $\langle U_h \rangle$  Average ensemble energy of the host, isolated.
- F** Force.
- p** Momentum of the particle.
- r** Particle coordinates, in the Cartesian space.
- $\mathcal{U}$  Potential energy.
- acc Acceptation rule.
- $u^{ext}$  External potential energy of the trial site.
- $u^{int}$  Internal potential energy of the trial site.
- $u^{trial}$  Potential energy of the trial site.
- $\mu_{IG}^0$  Chemical potential of the reference state (ideal gas).
- $\mu$  Chemical potential.
- $\phi_{ijkl}$  Torsional angle between particles  $i$ ,  $j$ ,  $k$  and  $l$ .
- $\phi$  Fugacity coefficient.
- $\pi$  Probability of moving the system from one state to another.
- $\rho$  Probability density of finding the system in a specific configuration.
- $\sigma_{ij}$  Distance between  $i$  and  $j$  particles, where the Lennard-Jones potential is zero.
- $\theta_0$  Equilibrium value for the bond angle.
- $\theta_{ijk}$  Bond angle between particles  $i$ ,  $j$  and  $k$ .

$\varepsilon_0$  Vacuum permittivity.

$\varepsilon_{ij}$  Well depth for the Lennard-Jones potential between particles  $i$  and  $j$ .

$\xi$  Space of the variables that defines system's microscopic state.

$b$  Trial orientations.

$f$  Fugacity.

$h$  Planck constant.

$k_B$  Boltzmann constant.

$k_\theta$  Spring constant for a bond angle.

$k_r$  Spring constant for a bond.

$k_{min}$  Force constant at the minimum of the well, in the Morse potential.

$m$  Mass.

$n$  Multiplicity in the expression of the torsional angle between particles  $i$ ,  $j$ ,  $k$  and  $l$ .

$q$  Point charge of the particle.

$r_0$  Equilibrium value for the bond length.

$r_{cut}$  Cutoff distance for the non-bonded interactions.

$r_{ij}^{min}$  Distance between  $i$  and  $j$  where the Lennard-Jones potential has its minimum value.

$r_{ij}$  Distance between particles  $i$  and  $j$ .

$s$  Fractional coordinates of the system.

$t$  Time.

$w$  Rosenbluth weight of the segment.

**E** Energy.

**N** Number of particles.

**P** Pressure.

**T** Temperature.

**V** Volume.

# Contents

<b>Dissertation Committee</b> . . . . .	<b>iii</b>
<b>Abstract</b> . . . . .	<b>vii</b>
<b>Resumen</b> . . . . .	<b>ix</b>
<b>Resum</b> . . . . .	<b>xi</b>
<b>Acronyms</b> . . . . .	<b>xiii</b>
<b>Glossary</b> . . . . .	<b>xv</b>
<b>Contents</b> . . . . .	<b>xix</b>
<b>1 Introduction</b> . . . . .	<b>1</b>
1.1 Zeolites . . . . .	2
1.2 Separation Mechanisms in Zeolites . . . . .	4
1.3 Zeolite ··· Adsorbate Interactions . . . . .	8
1.4 Computational Modeling of Separation Processes with Zeolites . . . . .	10
1.5 Outline of the Thesis . . . . .	11
References . . . . .	12
<b>2 Computational Methods</b> . . . . .	<b>25</b>
2.1 Statistical Mechanics Overview . . . . .	25
2.2 Modeling the System . . . . .	27
2.3 Simulating the System . . . . .	32
References . . . . .	40

<b>3</b>	<b>Molecular Simulation of Biobutanol Recovery Using LTA and CHA Zeolite Nanosheets with External Surface . . . . .</b>	<b>47</b>
3.1	Introduction . . . . .	48
3.2	Computational Methodology and Models . . . . .	51
3.3	Results and Discussion . . . . .	60
3.4	Conclusions . . . . .	66
	References . . . . .	67
<b>4</b>	<b>Insights into Adsorption of Linear, Monobranched, and Di-branched Alkanes on Pure Silica STW Zeolite as a Promising Material for Their Separation . . . . .</b>	<b>79</b>
4.1	Introduction . . . . .	80
4.2	Experimental and Theoretical Methods . . . . .	81
4.3	Results and Discussion . . . . .	84
4.4	Conclusions . . . . .	91
	References . . . . .	92
<b>5</b>	<b>Separation of an Aqueous Mixture of 6-kestose/sucrose with Zeolites: A Molecular Dynamics Simulation . . . . .</b>	<b>99</b>
5.1	Introduction . . . . .	100
5.2	Methodology and Models . . . . .	102
5.3	Results . . . . .	107
5.4	Conclusions . . . . .	116
	References . . . . .	117
<b>6</b>	<b>General Discussion of the Results . . . . .</b>	<b>125</b>
6.1	Simulation of Biobutanol Recovery Process by LTA and CHA Columns (Chapter 3) . . . . .	125
6.2	Linear and Branched Hydrocarbon Separation by Pure Silica STW Zeolite (Chapter 4) . . . . .	127
6.3	Separation of Sucrose/6-Kestose Aqueous Mixture by Zeolites (Chapter 5) . . . . .	133
	References . . . . .	134
<b>7</b>	<b>Conclusion . . . . .</b>	<b>137</b>

<b>List of Publications During the PhD . . . . .</b>	<b>139</b>
<b>Acknowledgments . . . . .</b>	<b>141</b>
<b>Appendices . . . . .</b>	<b>143</b>
A   Supplementary material for Chapter 3 . . . . .	143
B   Supplementary material for Chapter 4 . . . . .	167
C   Supplementary material for Chapter 5 . . . . .	197





# Chapter 1

## Introduction

Nowadays, one of our biggest challenges as a society is to ensure that all scientific, technological and economic advances are guided by sustainable premises. For instance, the chemical and petrochemical sector is highly dependent on non-renewable fossil resources, as 99% of the chemical feedstocks correspond to natural gas and petroleum, with smaller contributions of coal and biomass [1]. Also, this sector has the highest energetic consumption when compared with the remaining industrial sectors [2]. In this sense, chemistry research can contribute by establishing new environmentally friendly processes with high selectivity and performance, reducing their energetic and economic cost, using renewable feedstocks and energy sources [3], as well as following the Green Chemistry principles [4].

Starting from amazingly complex mixtures, such as crude oil (composed by thousands of chemical compounds [5]), its transformation into pure substances for industrial purposes rely on separation and purification processes. This initial mixture is usually fractionated by distillation, a widely used and well established method [6]. Employed since the antiquity, it takes advantage of the different vapor pressures of the liquids present in the mixture to separate them [7]. Nonetheless, for achieving the separation with the desired purity, the mixture should pass through several distillation cycles, where mixture components are repeatedly evaporated and condensed. As results, such separation method becomes significantly costly in terms of energy, and therefore, economically [8], which is magnified when mixture components present similar physicochemical properties.

## 1.1 Zeolites

Although the chemical separations are still dominated by the distillation method in an industrial level [8], adsorptive processes employing porous materials and membranes have proved to be effective alternatives that do not depend on such energy-intensive phase changes [8, 9]. Among the porous materials currently available, zeolites showed their potential as adsorbents early on, being reflected even in the origin of its name [10]. Discovered by the mineralogist Axel Fredrik Cronstedt in 1756, the analyzed sample was a natural mineral (a mixture of stellerite and stilbite) that released vapor when heated. Thus, by combining the Greek words for the verb *to boil* (“zein”) and *stone* (“lithos”), Cronstedt baptized a wide family of materials with remarkable adsorptive properties [11]. What was observed by the mineralogist was the desorption of water from zeolite micropores, that remain adsorbed at ambient conditions – solvating the extraframework cations of the material [10].

Composed by corner-sharing  $\text{TO}_4$  tetrahedral units ( $\text{T} = \text{Si}, \text{Al}, \text{P}, \text{etc.}$ ), these zeolite building blocks can be spatially arranged to form complex three-dimensional structures, as illustrated by Figure 1.1. Currently, 247 different frameworks (natural and synthetic) are described in the International Zeolite Association (IZA) Database of Zeolite Structures, and they grow to an estimated pace of 3-5 per

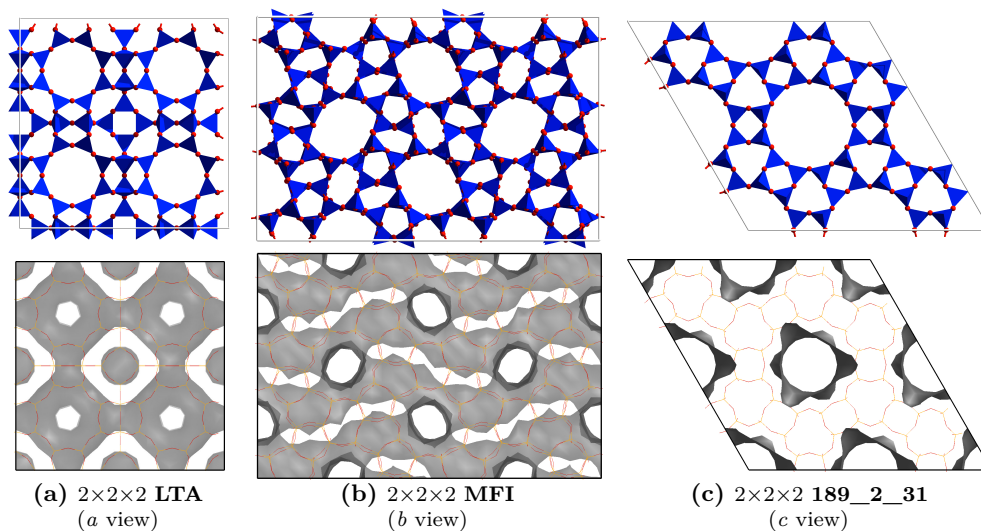


**Figure 1.1:** Examples of experimental (a,b) [12] and hypothetical (c) [13] zeolite frameworks ( $\text{TO}_4$  tetrahedral units in blue, oxygen atoms in red) and respective channel system (in gray).

year [12]. However, due to the large number of possible arrangements among those tetrahedral units, thousands of new structures have been predicted as thermodynamically accessible (as exemplified by Figure 1.1c) and compiled in databases of hypothetical zeolites [13–15]. As the feasibility of their synthesis is elucidated through experimental and computational studies, significant advances have been done in the last decade, and novel synthetic routes and conditions have been reported to obtain new framework types [16, 17].

In addition to the large number of different topologies, zeolites chemical composition can be tuned, maximizing its interaction with one component of the mixture, for example. As depicted by Figure 1.2, the same topology (CHA) can be obtained as pure silica (T = Si), aluminophosphate (AlPO, T = Al, P), aluminosilicate (T = Si, Al) and/or silicoaluminophosphate (SAPO, T = Si, Al, P) materials, the most frequent zeolite compositions as well as silicogermanates. Less conventional T atoms have also been reported, such as zinc, gallium and beryllium. Nonetheless, material's stability is related to T atoms nature and its spatial

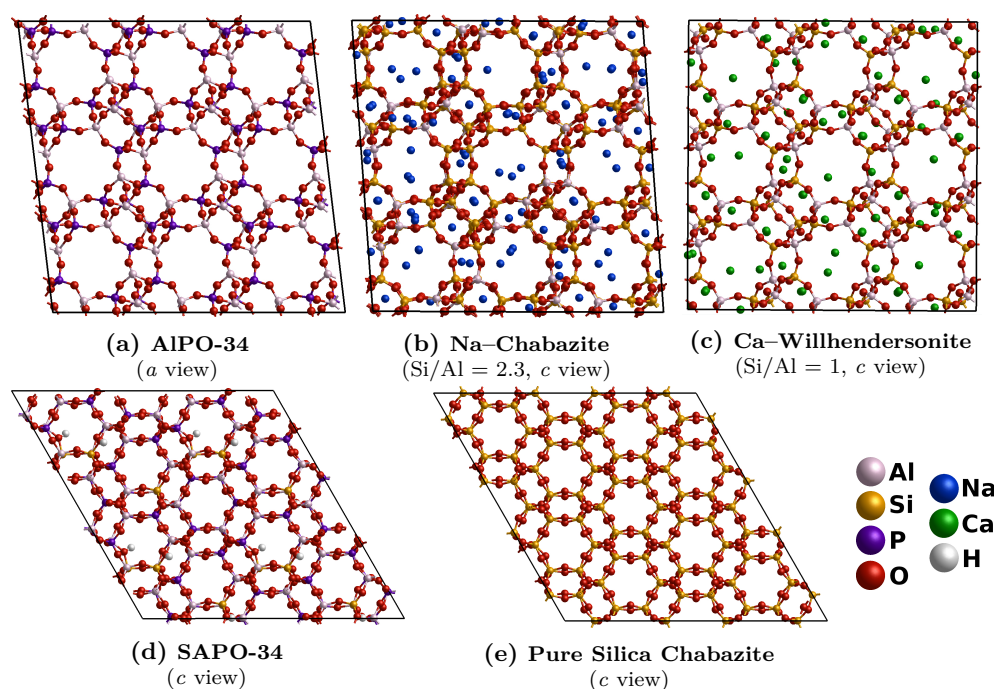


**Figure 1.2:** Geometries of CHA topology in different chemical compositions: aluminophosphate (a) [18], aluminosilicate with different Al content and extraframework cations (b) [19] and (c) [20], silicoaluminophosphate (d) [21–23] and pure silica (e) [24].

arrangement, consequently, not all chemical compositions are feasible, depending on the topology [25].

Despite neutral frameworks like silica and AlPO, the introduction of Al atoms in the former (Figure 1.2b,c) and Si in the latter (Figure 1.2d) incorporate negative charges to the framework, that are usually compensated by extraframework cations or Brønsted acid sites (BAS). Cations offer an additional interaction surface for adsorbate molecules, and the ion's nature can modulate adsorbates affinity for the material. Moreover, BAS strength, concentration, and accessibility to adsorbate molecules have been reported as crucial in many catalytic applications of zeolites [26, 27].

## 1.2 Separation Mechanisms in Zeolites

From the intricate arrangement of  $\text{TO}_4$  groups, cages, cavities, and channels with a large variety of sizes and shapes are formed (Figure 1.1). Naturally, when combined with the various chemical compositions available (Figure 1.2), a wide range of applications in catalytic and separation processes emerges. Considering a system composed by a zeolite in contact with a known mixture, different separation mechanisms can take place before and after the system reaches equilibrium (Figure 1.3). First, a selective separation can be performed by taking advantage of

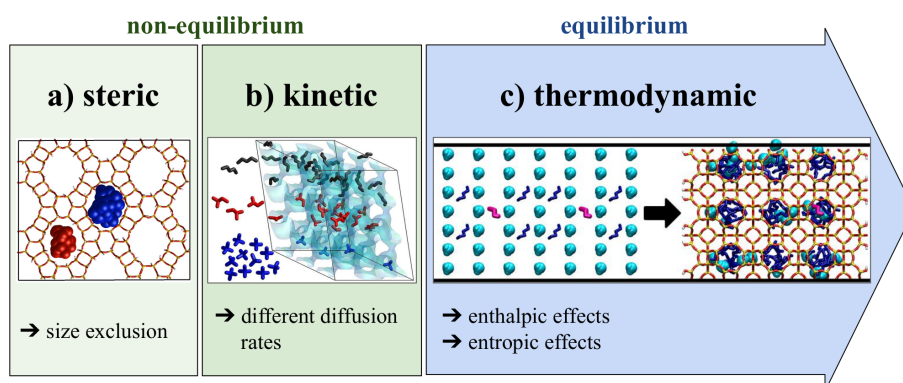


**Figure 1.3:** Examples of separation mechanisms in zeolites. (a) Adsorption of sucrose (red) and size-exclusion of 6-kestose (blue) by DON zeolite [28]. (b) Kinetic separation of linear (black) and monobranched (red) isomers of pentane from its dibranched isomer (blue) by STW framework (channel system in cyan) [29]. (c) Preferential adsorption of n-butanol (blue) from a fermented vapor phase also containing water (cyan) and ethanol (pink) by ITQ-29 zeolite, in equilibrium [23].

the molecular sieving effect, a well known feature of zeolites. Adsorbates access to the material's channel system occurs through the  $n$ -rings, where  $n$  is the number of consecutive T atoms in the ring. Topologies can be classified by the largest  $n$ -ring present, as possessing small ( $n = 8$ ), medium ( $n = 10$ ), large ( $n = 12$ ) and extra-large pores ( $n > 12$ ) [10], as depicted by Figure 1.4. Thus, by properly

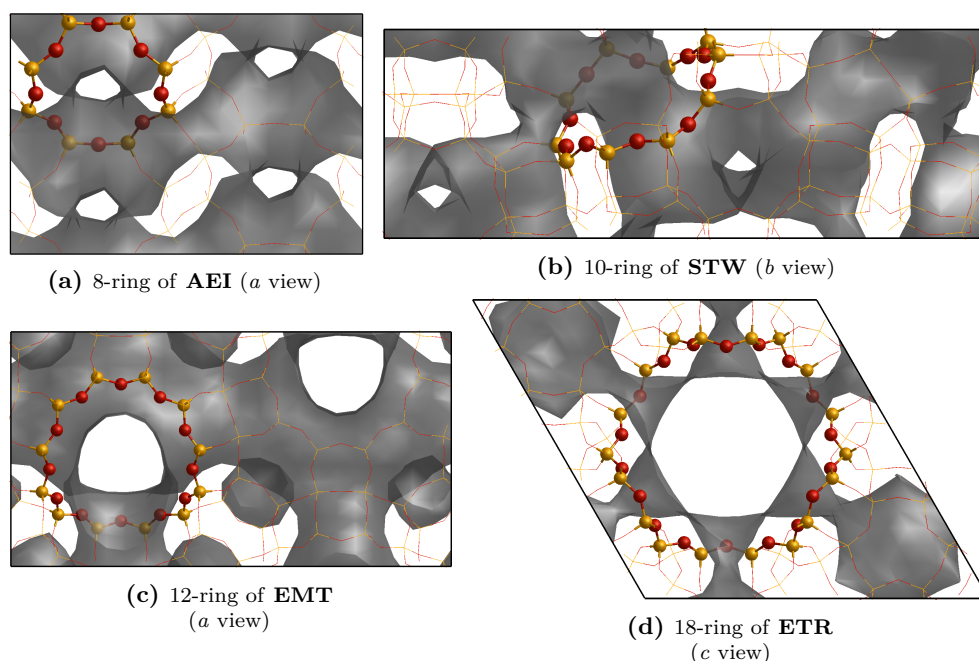


**Figure 1.4:** Examples of small (a), medium (b), large (c) and extra-large (d) pore zeolites. Unit cell channel system in gray and  $n$ -rings in ball sticks model.

selecting a framework with pore apertures that permit the diffusion of selected species, the remaining mixture components will be excluded by size (Figure 1.3a). Such effect can be achieved by both rigid and flexible materials, where the pore apertures of the latter can be selectively adjusted depending on the nature of the adsorbates [30]. For instance, the size-exclusion mechanism is used in the industry for removing water from various solvents with zeolite A (LTA topology) [31], and for the separation of linear from branched hydrocarbons by small-pore zeolites [10] – whose separation through 5A zeolite columns produces millions of tons of linear hydrocarbons per year [31]. In addition, the separation processes discussed in Chapters 3 and 5 further explore this mechanism.

Likewise, the selective adsorption of one or more mixture components can rely on both kinetic and thermodynamic aspects [32]. As illustrated by Figure 1.3b, a kinetic separation can take place by a fine-tuning of the zeolite pore openings, considering the kinetic diameter of the species in the mixture. Here, all molecules can be fitted in the adsorbent micropores and possess similar polarities [10], but separation is promoted by diffusion rate differences among adsorbates. Thus, guest molecules containing bulky groups, or in shapes that hinder its diffusion through the channels of the material, can be separated from components that easily flow across the micropores [30]. For instance, highly selective separations based in the kinetic method have been reported for n-hexane/2,2-dimethylbutane mixture with zeolite Y [33], ethane/ethylene separation with ITQ-55 [34], and propane/propylene mixture with ITQ-12 [35], ITQ-32 [36], and hierarchical ZSM-58 [37]. Membranes of SAPO-34 presented promising results in a wide variety of gas mixture separations, such as Kr/Xe, CO<sub>2</sub>/CH<sub>4</sub>, CO<sub>2</sub>/butane and CO<sub>2</sub>/N<sub>2</sub>, in which the diffusion of the smaller molecules are favored, but highly hindered for the larger ones [38]. The computational and experimental study discussed in Chapter 4 evaluates a separation of linear and branched hydrocarbon isomers, where the kinetic mechanism played an important role.

Nevertheless, if all mixture components possess adequate sizes to be adsorbed by the selected framework, a thermodynamic separation (Figure 1.3c) can also be explored. Before reaching equilibrium, mixture molecules can be adsorbed into the zeolite and also be replaced by other species from the mixture, depending on various factors, such as mixture pressure, temperature and host-guests affinity. The final uptake observed in a multi-component adsorption isotherm will depend on a complex interplay between enthalpic and entropic effects [39]. From an energy perspective, the adsorptive process happens spontaneously while the Gibbs free energy ( $\Delta G$ ) is negative. Thus, the process evolves until the equilibrium condition is established, and  $\Delta G$  goes to zero. As defined by Equation 1.1, the Gibbs free energy of adsorption is composed by  $\Delta H$  and  $\Delta S$  terms, that corresponds to the changes in the enthalpy and entropy of the system, respectively, and  $T$  is the temperature of the system [39].

$$\Delta G = \Delta H - T\Delta S \quad (1.1)$$

Adsorbates affinities for a specific framework are described by the  $\Delta H$  component (Equation 1.2), that will only depend on the internal energy ( $\Delta U$ ) when the system temperature is zero. In Equation 1.2,  $R$  is the gas constant.

$$\Delta H = \Delta U - RT \quad (1.2)$$

Therefore, the enthalpic component is related to the binding energy of the system, as  $\Delta U$  (Equation 1.3) is the difference between the average ensemble energy of the host-guest complex ( $\langle U_{hg} \rangle$ ) and the average ensemble energy values for both host and guest when isolated ( $\langle U_h \rangle$  and  $\langle U_g \rangle$ , respectively) [39].

$$\Delta U = \langle U_{hg} \rangle - ( \langle U_h \rangle + \langle U_g \rangle ) \quad (1.3)$$

When mixture components possess different polarities, the equilibrium separations can be performed based on enthalpic effects. Consequently, not only the choice of topology, but the chemical composition of the material is crucial, aiming to maximize zeolite...adsorbate interactions [30]. In this sense, silica materials are usually applied for their affinity to non-polar molecules, and its considerable hydrophobicity [40]. Oppositely, a significant hydrophilicity is observed for SAPO materials [41]. Adsorbent interaction with polar molecules can be controlled by tuning the Al content of aluminosilicate materials, for example [10]. The presence, distribution, and nature of the extraframework cations in these materials were also reported to be important factors in the separation of olefins from paraffins, where some materials presenting LTA and FAU topologies are among the best performing found to date [9]. For example, AgA (LTA type) presented a high performance over ethane/ethylene separation, by combining the steric exclusion of the hydrocarbon and the enhanced adsorption of the olefin due to the  $\pi$ -complexes present between  $\text{Ag}^+$  cations and ethylene [42]. By using two frameworks with complementary selectivities, computational insights are given for an experimental process discussed in Chapter 3, where the thermodynamic separation plays an important role. Besides, the separation or purification of hydrocarbons with water,  $\text{CH}_4/\text{CO}_2$  and  $\text{O}_2/\text{N}_2$  mixtures in the equilibrium by zeolites have already been reported in the literature [10].

On the other hand, the importance of the entropic component in a series of equilibrium separations by porous materials have been reported in the literature [39, 43, 44], such as linear/branched alkanes [43, 45–47] and aromatics [48, 49] mixture separations. Here, the adsorbed content in the equilibrium will highly depend on the packing of molecules in the micropores [32, 44]. At low loading, uptake is controlled by enthalpic factors, and molecules with superior affinities to the zeolite will usually present preferential loading. By increasing the mixture's pressure, smaller molecules can fit in regions of the channel system that become inaccessible for the larger, leading to an increased uptake. Due to this larger amount of molecules per unit cell, a higher entropic contribution appears, and such adsorption close to saturation pressures is favored by the so-called *size entropy effect* [39]. This is illustrated by the separation of C2/C4/C6 linear alkanes in TON ze-

olite, where the entropic effect drives a C2 preferential adsorption at both higher pressures and temperatures [39] – a logic consequence in the latter condition, as the entropic term of  $\Delta G$  is multiplied by T (Equation 1.1). Depending on the material’s microporosity, one component of the mixture can be better packed than others, presenting a favored adsorption due to the *configurational entropy effect* [43]. For instance, considering a mixture of linear and dibranched hydrocarbons, as the pressure increases, the latter isomer is replaced by the linear alkane in the pure silica MFI zeolite, due to their superior packing efficiency, specially in the intersections of sinusoidal and straight channels (depicted, respectively, by Figure 1.1b and perpendicular the figure plane) [39]. Likewise, in cylindrical channels, the *length entropy effect* can play an important role. Considering that all alkane isomers with the same amount of carbon atoms can be fitted in a straight channel and are aligned to it, more molecules with shorter length can be packed, and an entropic contribution will favor their adsorption, as previously mentioned for the *size entropy effect* [43]. This is the case of hydrocarbon linear and branched isomers in AFI and MOR zeolites, where the dibranched molecules are preferentially adsorbed close to saturation conditions [39]. Additionally, other entropic effects have been reported for aromatic systems, such as the *orientational entropy* and *commensurate stacking* [39].

### 1.3 Zeolite ··· Adsorbate Interactions

As discussed in the previous section, the diffusion, packing efficiency and affinity of adsorbates for zeolite frameworks are key factors to design new separation processes with high selectivity. Both chemisorption and physisorption are observed in zeolites, being suitable for different processes. When zeolite ··· adsorbate interactions involves sharing, transfer or exchange of electrons, these strong interactions characterize a chemisorption. This type of sorption can promote separations with high selectivity and adsorption capacity [50]. As long as the established interactions still permit a reversible adsorption, it can be used in purifications with the temperature-swing adsorption process [30]. However, in a physisorption, only intermolecular interactions occur, and this weaker affinity is appropriate for bulk separations within the pressure-swing adsorption process [30]. It is important to notice other advantages of zeolitic materials: their hydrothermal stability and possibility of reusing the material through sorption-desorption cycles. A complete understanding of the interactions arising among zeolite and adsorbates allows the design of the target separation for working at mild conditions (on both adsorption and desorption steps, if possible).



The physisorption is composed by electrostatic and van der Waals contributions. The magnitude of the first will depend on the chemical nature of adsorbates (charge distribution, presence of ionic species and multipolar moments) and electric fields intensity inside the micropores. A negatively charged framework, as well as the presence of extraframework cations, can produce considerably large electric fields [51]. Thus, the presence of these local electric fields can produce regions highly polarized along the channel system, favoring the adsorption of guests with significant dipoles and higher multipolar moments [30, 40]. Van der Waals (vdW) interactions comprise both repulsive and attractive intermolecular forces, that can include dispersion (also known as London forces), orientation and induction forces [52]. Dispersive interactions are always present, even among non-polar molecules, and usually are the most important contributor for the vdW interactions [40]. At short distances, repulsive interactions arise due to the interaction between atoms/molecules' electronic clouds. The long-range dispersive interaction is driven by the coupling of instantaneous induced dipoles, as well as (to a lesser extent), from induced dipole–induced quadrupole and between induced quadrupole moments [51]. The polarizability of a non-spherical molecule is anisotropic, possessing different values across its geometry, which depends on the electronic polarizability of the bonds present. Thus, the vdW interaction depends on the distance and relative orientation of both interacting particles [52].

In accordance with the aforementioned interactions, the adsorption of non-polar species in pure/high-silica materials is mainly driven by dispersive forces [40]. The presence of BAS enables the Hydrogen bond (HB) formation inside the micropores, which can also be present in the external surface of the material (terminal –OH groups). Depending on the adsorbate nature, weak to strong HBs can be established (BAS ··· guest and surface OH ··· guest), enhancing the adsorption in the micropores and external surface. Finally, the high affinity of unsaturated molecules by extraframework cations is a good example of a reversible chemisorption phenomena, widely used for the separation of olefins from paraffins (C2-C4 fractions) and CO capture [9, 30]. In these  $\pi$ -complexations, vacant s-orbitals from a metallic cation (e.g.  $\text{Cu}^+$  or  $\text{Ag}^+$ ) interact with adsorbate  $\pi$  bond/system, while its d-orbitals can be involved in a back donation to adsorbate  $\pi^*$  orbitals [30]. In the case of the CO molecule,  $\sigma$ -bonds with those cations can also be present. Besides, the nature of the interaction between extraframework cations and  $\pi$ -systems will depend on the cation's nature and loading [53, 54], where the importance of the electrostatic and dispersive contributions to the interaction have also been reported in the literature [55].

## 1.4 Computational Modeling of Separation Processes with Zeolites

When a guest molecule goes from the gas phase to be adsorbed in the zeolite, the cohesive energy acquired by the adsorbate is a result of the forces previously described. From experiments, the isosteric heat of adsorption can be measured, providing insights about the magnitude of this cohesive energy for a given system [40]. Such value can also be estimated by simulations, and depending on the modeling employed, be decomposed into its electrostatic and vdW contributions. In fact, computational chemistry provides robust tools for a deeper understanding of the nature and magnitude of adsorptive interactions. Well established computational methodologies have been widely employed during the last decades, and due to the expanding computational power, significant advances have been done. There is an extensive literature devoted to the computational approach of separation processes employing zeolites [56–63].

With the Molecular Dynamics method, diffusion coefficients can be calculated from the simulations, and guests diffusional behavior can be evaluated during the time evolution of the system [64–69]. In these simulations, it is possible to keep track of the contacts present, and the intermolecular interactions that occur, such as the HBs [28, 70]. The equilibrium properties, pure component and mixture adsorption isotherms, selectivity and performance estimations, and sorption capacities can be simulated through the Monte Carlo method and validated/compared with experiments [71, 72]. By ensuring that the simulation reproduces the system behavior and measured properties, insights on zeolite · · · adsorbates affinities, their packing and preferential location in the micropores can be obtained. The adsorption of various guest molecules were already investigated by computational methodologies, such as linear and branched hydrocarbon isomers [29, 73, 74], benzene and other aromatic molecules [75–78], alcohols [79, 80], paraffin/olefin mixtures [9, 50, 81], and other small molecules ( $\text{H}_2\text{O}$ ,  $\text{CO}$ ,  $\text{CO}_2$ ,  $\text{N}_2$ ,  $\text{O}_2$  and  $\text{CH}_4$ ) [70, 82–86].

As slight differences in the size of the pores can impact significantly the diffusion of adsorbate molecules [10], and considering the large amount of available topologies at different chemical compositions (which continues to grow every year), there are countless possibilities for discovering new selective and efficient materials applied to separation processes. With accurate models, systematic investigation of a target separation process can be done. In this sense, several force fields have been reported for a proper reproduction of adsorption uptakes [87, 88], structures and energetics of zeolites [22, 89–91] and guest molecules [92–98] with various

chemical compositions, framework features such as flexibility [22, 23, 89, 91], extraframework cations [50], BAS [22] and external surface  $-OH$  [23, 94].

These molecular simulations are appealing not only by providing an insightful connection between particles dynamics and its macroscopic behavior and properties, but also by allowing to study expensive, dangerous or difficult processes computationally. For instance, only the promising frameworks, first selected by the simulations, can be further tested experimentally. In this sense, computational chemistry arises as an ally towards a sustainable development of the research. In summary, the present work seeks to investigate new solutions for separation processes, from a sustainable perspective, by exploring zeolites promising properties with computational chemistry tools.

## 1.5 Outline of the Thesis

After this introduction, a brief overview of the computational methods employed is summarized in Chapter 2. Then, the chapters of results will illustrate the capabilities of the computational approach to study applications of zeolites in the separation and/or purification of different mixtures.

In Chapter 3, the experimental process of biobutanol recovery from a vapor-phase fermented mixture is simulated. The 1-butanol produced from biomass fermentation by anaerobic bacteria can be experimentally separated and purified by a concerted adsorption in LTA and CHA columns. Besides the parameterization and methods validation (considering experimental data), this work highlights how computational methods are capable of reproducing experimental processes, bringing insights at the molecular level, as well as enabling the design and improvement of other separation processes by simulations.

Next, Chapter 4 illustrates how computational and experimental studies can be complementary, connecting the molecular behavior with the macroscopic phenomena. The study investigates the application of STW zeolite in hydrocarbon separation. Linear and branched isomers of pentane, hexane and heptane present different diffusion rates and adsorption affinities for this pure silica framework, allowing their separation. Hydrocarbons adsorptive and diffusional behavior in STW and MFI zeolites is further understood by the molecular simulations, being also confirmed by experiments.

In Chapter 5, a computational screening is performed to select suitable zeolites for the separation of sugars from an aqueous mixture. The proposed candidates for this process of industrial interest should selectively adsorb the sucrose molecules in

an equimolar solution of 6-kestose and sucrose. Frameworks are selected by their performance in simulations with different complexity levels – from bulk simulations to more elaborate membrane systems. Therefore, this purely computational study aims to provide a ‘shortcut’ for the future experimental work, pointing out the most promising candidates to be tested. This is another powerful utilization of simulations from a sustainable perspective, that contributes to decrease the use of reagents and the generation of waste in research work.

Lastly, a general discussion of obtained results and concluding remarks are summarized in Chapters 6 and 7, respectively. The Appendices A to C collect the supplementary material of Chapters 3 to 5.

## References

- [1] Tickner, J.; Geiser, K.; Baima, S. Transitioning the Chemical Industry: The Case for Addressing the Climate, Toxics, and Plastics Crises. *Environ.: Sci. Policy Sustain. Dev.* **2021**, *63* (6), 4–15. DOI: 10.1080/00139157.2021.1979857.
- [2] Levi, P. G.; Cullen, J. M. Mapping Global Flows of Chemicals: From Fossil Fuel Feedstocks to Chemical Products. *Environ. Sci. Technol.* **2018**, *52* (4), 1725–1734. DOI: 10.1021/acs.est.7b04573.
- [3] Li, Y.; Li, L.; Yu, J. Applications of Zeolites in Sustainable Chemistry. *Chem* **2017**, *3* (6), 928–949. DOI: 10.1016/j.chempr.2017.10.009.
- [4] Horváth, I. T.; Anastas, P. T. Innovations and Green Chemistry. *Chem. Rev.* **2007**, *107* (6), 2169–2173. DOI: 10.1021/cr078380v.
- [5] Fraser, S. Distillation in Refining. In *Distillation*; Academic Press, 2014, 155–190. DOI: 10.1016/B978-0-12-386876-3.00004-1.
- [6] Kockmann, N. History of Distillation. In *Distillation*; Academic Press, 2014, 1–43. DOI: 10.1016/B978-0-12-386547-2.00001-6.
- [7] Geankoplis, C. J.; Lepek, D. H. *Transport Processes and Separation Process Principles*, 5th ed.; Prentice Hall, 2017.

- [8] Brennecke, J. F.; Freeman, B. Reimagining Petroleum Refining. *Science* **2020**, *369* (6501), 254–255. DOI: 10.1126/science.abd1307.
- [9] Mahdi, H. I.; Muraza, O. An Exciting Opportunity for Zeolite Adsorbent Design in Separation of C4 Olefins Through Adsorptive Separation. *Sep. Purif. Technol.* **2019**, *221*, 126–151. DOI: 10.1016/j.seppur.2018.12.004.
- [10] Pérez-Botella, E.; Palomino, M.; Valencia, S.; Rey, F. Zeolites and Other Adsorbents. In *Nanoporous Materials for Gas Storage*; Springer, 2019, 173–208. DOI: 10.1007/978-981-13-3504-4\_7.
- [11] Masters, A. F.; Maschmeyer, T. Zeolites – From Curiosity to Cornerstone. *Microporous Mesoporous Mater.* **2011**, *142* (2), 423–438. DOI: 10.1016/j.micromeso.2010.12.026.
- [12] Baerlocher Ch.; McCusker, L. B. Database of Zeolite Structures, <http://www.iza-structure.org/databases/> (accessed 2021-10-15).
- [13] Atlas of Prospective Zeolite Structures, <http://www.hypotheticalzeolites.net> (accessed 2021-11-01).
- [14] Bai, P.; Jeon, M. Y.; Ren, L.; Knight, C.; Deem, M. W.; Tsapatsis, M.; Siepmann, J. I. Discovery of Optimal Zeolites for Challenging Separations and Chemical Transformations Using Predictive Materials Modeling. *Nat. Commun.* **2015**, *6* (5912), 1–9. DOI: 10.1038/ncomms6912.
- [15] Earl, D. J.; Deem, M. W. Toward a Database of Hypothetical Zeolite Structures. *Ind. Eng. Chem. Res.* **2006**, *45* (16), 5449–5454. DOI: 10.1021/ie0510728.
- [16] Li, Y.; Cao, H.; Yu, J. Toward a New Era of Designed Synthesis of Nanoporous Zeolitic Materials. *ACS Nano* **2018**, *12* (5), 4096–4104. DOI: 10.1021/acsnano.8b02625.
- [17] Li, J.; Corma, A.; Yu, J. Synthesis of New Zeolite Structures. *Chem. Soc. Rev.* **2015**, *44* (20), 7112–7127. DOI: 10.1039/C5CS00023H.
- [18] Varlec, J.; Krajnc, A.; Mazaj, M.; Ristić, A.; Vanatalu, K.; Oss, A.; Samoson, A.; Kaučič, V.; Mali, G. Dehydration of AlPO<sub>4</sub>-34 Studied by Variable-

- temperature NMR, XRD and First-principles Calculations. *New J. Chem.* **2016**, *40* (5), 4178–4186. DOI: 10.1039/C5NJ02838H.
- [19] Mortier, W. J.; Pluth, J. J.; Smith, J. V. Positions of Cations and Molecules in Zeolites with the Chabazite Framework III. Dehydrated Na-exchanged Chabazite. *Mater. Res. Bull.* **1977**, *12* (3), 241–249. DOI: 10.1016/0025-5408(77)90141-6.
- [20] Fischer, R. X.; Kahlenberg, V.; Lengauer, C. L.; Tillmanns, E. Thermal Behavior and Structural Transformation in the Chabazite-type Zeolite Willhendersonite,  $\text{KCaAl}_3\text{Si}_3\text{O}_{12}\cdot 5\text{H}_2\text{O}$ . *Am. Mineral.* **2008**, *93* (8–9), 1317–1325. DOI: 10.2138/am.2008.2745.
- [21] Sastre, G.; Lewis, D. W.; Catlow, C. R. A. Modeling of Silicon Substitution in SAPO-5 and SAPO-34 Molecular Sieves. *J. Phys. Chem. B* **1997**, *101* (27), 5249–5262. DOI: 10.1021/jp963736k.
- [22] Ghysels, A.; Moors, S. L. C.; Hemelsoet, K.; De Wispelaere, K.; Waroquier, M.; Sastre, G.; Van Speybroeck, V. Shape-Selective Diffusion of Olefins in 8-Ring Solid Acid Microporous Zeolites. *J. Phys. Chem. C* **2015**, *119* (41), 23721–23734. DOI: 10.1021/acs.jpcc.5b06010.
- [23] Misturini, A.; Rey, F.; Sastre, G. Molecular Simulation of Biobutanol Recovery Using LTA and CHA Zeolite Nanosheets with an External Surface. *J. Phys. Chem. C* **2022**, *126* (41), 17680–17691. DOI: 10.1021/acs.jpcc.2c04331.
- [24] Díaz-Cabañas, M.-J.; Barrett, P. A.; Cambor, M. A. Synthesis and Structure of Pure  $\text{SiO}_2$  Chabazite: the  $\text{SiO}_2$  Polymorph with the Lowest Framework Density. *Chem. Commun.* **1998**, (17), 1881–1882. DOI: 10.1039/A804800B.
- [25] Li, Y.; Yu, J. New Stories of Zeolite Structures: Their Descriptions, Determinations, Predictions, and Evaluations. *Chem. Rev.* **2014**, *114* (14), 7268–7316. DOI: 10.1021/cr500010r.
- [26] Li, G.; Pidko, E. A. The Nature and Catalytic Function of Cation Sites in Zeolites: a Computational Perspective. *ChemCatChem* **2019**, *11* (1), 134–156. DOI: 10.1002/cctc.201801493.

- [27] Xu, B.; Sievers, C.; Hong, S. B.; Prins, R.; van Bokhoven, J. A. Catalytic Activity of Brønsted Acid Sites in Zeolites: Intrinsic Activity, Rate-limiting Step, and Influence of the Local Structure of the Acid Sites. *J. Catal.* **2006**, *244* (2), 163–168. DOI: 10.1016/j.jcat.2006.08.022.
- [28] Losada, I. B.; Grobas-Illobre, P.; Misturini, A.; Polaina, J.; Seminovski, Y.; Sastre, G. Separation of an Aqueous Mixture of 6-Kestose/Sucrose with Zeolites: A Molecular Dynamics Simulation. *Microporous Mesoporous Mater.* **2021**, *319*, 111031. DOI: 10.1016/j.micromeso.2021.111031.
- [29] Pérez-Botella, E.; Misturini, A.; Sala, A.; Palomino, M.; Corma, A.; Sastre, G.; Valencia, S.; Rey, F. Insights into Adsorption of Linear, Monobranched, and Dibranching Alkanes on Pure Silica STW Zeolite as a Promising Material for Their Separation. *J. Phys. Chem. C* **2020**, *124* (49), 26821–26829. DOI: 10.1021/acs.jpcc.0c08517.
- [30] Yue, B.; Liu, S.; Chai, Y.; Wu, G.; Guan, N.; Li, L. Zeolites for Separation: Fundamental and Application. *J. Energy Chem.* **2022**, *71*, 288–303. DOI: 10.1016/j.jechem.2022.03.035.
- [31] Rhodes, C. J. Properties and Applications of Zeolites. *Sci. Prog.* **2010**, *93* (3), 223–284. DOI: 10.3184/003685010X12800828155007.
- [32] Van Tassel, P. R.; Davis, H. T.; McCormick, A. V. Adsorption of Binary Mixtures in a Zeolite Micropore. *Mol. Simul.* **1996**, *17* (4–6), 239–254. DOI: 10.1080/08927029608024111.
- [33] Nag, S.; Yashonath, S. Kinetic Separation of n-Hexane from 2,2-Dimethyl Butane in Zeolite Y Using the Novel Levi–Blow Method. *Adv. Theor. Simul.* **2022**, *5* (2), 2100204. DOI: 10.1002/adts.202100204.
- [34] Bereciartua, P. J.; Cantín, A.; Corma, A.; Jordá, J. L.; Palomino, M.; Rey, F.; Valencia, S.; Corcoran, E. W.; Kortunov, P.; Ravikovitch, P. I.; Burton, A.; Yoon, C.; Wang, Y.; Paur, C.; Guzman, J.; Bishop, A. R.; Casty, G. L. Control of Zeolite Framework Flexibility and Pore Topology for Separation of Ethane and Ethylene. *Science* **2017**, *358* (6366), 1068–1071. DOI: 10.1126/science.aao0092.
- [35] Barrett, P. A.; Boix, T.; Puche, M.; Olson, D. H.; Jordan, E.; Koller, H.; Cambor, M. A. ITQ-12: a New Microporous Silica Polymorph Potentially

- Useful for Light Hydrocarbon Separations. *Chem. Commun.* **2003**, (17), 2114–2115. DOI: 10.1039/B306440A.
- [36] Palomino, M.; Cantín, A.; Corma, A.; Leiva, S.; Rey, F.; Valencia, S. Pure Silica ITQ-32 Zeolite Allows Separation of Linear Olefins from Paraffins. *Chem. Commun.* **2007**, (12), 1233–1235. DOI: 10.1039/B700358G.
- [37] Selzer, C.; Werner, A.; Kaskel, S. Selective Adsorption of Propene Over Propane on Hierarchical Zeolite ZSM-58. *Ind. Eng. Chem. Res.* **2018**, *57* (19), 6609–6617. DOI: 10.1021/acs.iecr.8b00377.
- [38] Carreon, M. A. Molecular Sieve Membranes for N<sub>2</sub>/CH<sub>4</sub> Separation. *J. Mater. Res.* **2018**, *33* (1), 32–43. DOI: 10.1557/jmr.2017.297.
- [39] Torres-Knoop, A.; Dubbeldam, D. Exploiting Large-Pore Metal–Organic Frameworks for Separations through Entropic Molecular Mechanisms. *ChemPhysChem* **2015**, *16* (10), 2046–2067. DOI: 10.1002/cphc.201500195.
- [40] Lobo, R. F. Intermolecular Forces in Zeolite Adsorption and Catalysis. In *Ordered Porous Solids*; Elsevier, 2009, 239–261. DOI: 10.1016/B978-0-444-53189-6.00009-3.
- [41] Van der Perre, S.; Gelin, P.; Claessens, B.; Martin-Calvo, A.; Remi, J. C. S.; Duerinck, T.; Baron, G. V.; Palomino, M.; Sánchez, L. Y.; Valencia, S.; Shang, J.; Singh, R.; Webley, P. A.; Rey, F.; Denayer, J. F. M. Intensified Biobutanol Recovery by Using Zeolites with Complementary Selectivity. *ChemSusChem* **2017**, *10* (14), 2968–2977. DOI: 10.1002/cssc.201700667.
- [42] Aguado, S.; Bergeret, G.; Daniel, C.; Farrusseng, D. Absolute Molecular Sieve Separation of Ethylene/Ethane Mixtures with Silver Zeolite A. *J. Am. Chem. Soc.* **2012**, *134* (36), 14635–14637. DOI: 10.1021/ja305663k.
- [43] Krishna, R.; Smit, B.; Calero, S. Entropy Effects During Sorption of Alkanes in Zeolites. *Chem. Soc. Rev.* **2002**, *31* (3), 185–194. DOI: 10.1039/B101267N.
- [44] Krishna, R. Separating Mixtures by Exploiting Molecular Packing Effects in Microporous Materials. *Phys. Chem. Chem. Phys.* **2014**, *17* (1), 39–59. DOI: 10.1039/C4CP03939D.



- [45] Krishna, R.; Smit, B.; Vlucht, T. J. H. Sorption-Induced Diffusion-Selective Separation of Hydrocarbon Isomers Using Silicalite. *J. Phys. Chem. A* **1998**, *102* (40), 7727–7730. DOI: 10.1021/jp982438f.
- [46] Vlucht, T. J. H.; Krishna, R.; Smit, B. Molecular Simulations of Adsorption Isotherms for Linear and Branched Alkanes and Their Mixtures in Silicalite. *J. Phys. Chem. B* **1999**, *103* (7), 1102–1118. DOI: 10.1021/jp982736c.
- [47] Vlucht, T. J. H.; Zhu, W.; Kapteijn, F.; Moulijn, J. A.; Smit, B.; Krishna, R. Adsorption of Linear and Branched Alkanes in the Zeolite Silicalite-1. *J. Am. Chem. Soc.* **1998**, *120* (22), 5599–5600. DOI: 10.1021/ja974336t.
- [48] Torres-Knoop, A.; Heinen, J.; Krishna, R.; Dubbeldam, D. Entropic Separation of Styrene/Ethylbenzene Mixtures by Exploitation of Subtle Differences in Molecular Configurations in Ordered Crystalline Nanoporous Adsorbents. *Langmuir* **2015**, *31* (12), 3771–3778. DOI: 10.1021/acs.langmuir.5b00363.
- [49] Torres-Knoop, A.; Balestra, S. R. G.; Krishna, R.; Calero, S.; Dubbeldam, D. Entropic Separations of Mixtures of Aromatics by Selective Face-to-Face Molecular Stacking in One-Dimensional Channels of Metal–Organic Frameworks and Zeolites. *ChemPhysChem* **2015**, *16* (3), 532–535. DOI: 10.1002/cphc.201402819.
- [50] Luna-Triguero, A.; Sławek, A.; de Armas, R. S.; Gutiérrez-Sevillano, J.; Ania, C.; Parra, J.; Vicent-Luna, J.; Calero, S.  $\pi$ -Complexation for Olefin/paraffin Separation Using Aluminosilicates. *Chem. Eng. J.* **2020**, *380*, 122482. DOI: 10.1016/j.cej.2019.122482.
- [51] Rees, L. V. C.; Shen, D. Adsorption of Gases in Zeolite Molecular Sieves. In *Studies in Surface Science and Catalysis*; Elsevier, 2001; Vol. 137; Chapter 13, 579–631. DOI: 10.1016/S0167-2991(01)80255-X.
- [52] Israelachvili, J. N. *Intermolecular and Surface Forces*, 3rd revised; Academic Press, 2011.
- [53] Bulanek, R.; Frolich, K.; Cicmanec, P.; Nachtigallova, D.; Pulido, A.; Nachtigall, P. Combined Experimental and Theoretical Investigations of Heterogeneous Dual Cation Sites in Cu,M-FER Zeolites. *J. Phys. Chem. C* **2011**, *115* (27), 13312–13321. DOI: 10.1021/jp200293y.

- [54] Hadjiivanov, K.; Knözinger, H. Characterization of vacant coordination sites of cations on the surfaces of oxides and zeolites using infrared spectroscopy of adsorbed probe molecules. *Surf. Sci.* **2009**, *603* (10), 1629–1636. DOI: 10.1016/j.susc.2008.09.052.
- [55] Fischer, M.; Delgado, M. R.; Areán, C. O.; Duran, C. O. CO adsorption complexes in zeolites: How does the inclusion of dispersion interactions affect predictions made from DFT calculations? The case of Na-CHA. *Theor. Chem. Acc.* **2015**, *134* (7), 1–18. DOI: 10.1007/s00214-015-1692-9.
- [56] Gutiérrez-Sevillano, J. J.; Calero, S. Computational Approaches to Zeolite-Based Adsorption Processes. In *New Developments in Adsorption/Separation of Small Molecules by Zeolites*; Springer, 2020, 57–83. DOI: 10.1007/430\_2020\_66.
- [57] Yang, G. Computational Insights of Adsorption and Catalysis Within Nanoporous Zeolites. In *Nanoscience and Computational Chemistry: Research Progress*; Apple Academic Press, 2013, 249–269. DOI: 10.1201/b16368.
- [58] Pidko, E. A.; van Santen, R. A. Computational Approach in Zeolite Science. In *Zeolite Characterization and Catalysis*; Springer, 2009, 223–250. DOI: 10.1007/978-1-4020-9678-5\_6.
- [59] Keil, F. J. Molecular Simulation of Adsorption in Zeolites and Carbon Nanotubes. In *Adsorption and Phase Behaviour in Nanochannels and Nanotubes*; Springer, 2010, 9–40. DOI: 10.1007/978-90-481-2481-7\_2.
- [60] Evans, J. D.; Fraux, G.; Gaillac, R.; Kohen, D.; Trouselet, F.; Vanson, J.-M.; Coudert, F.-X. Computational Chemistry Methods for Nanoporous Materials. *Chem. Mater.* **2017**, *29* (1), 199–212. DOI: 10.1021/acs.chemmater.6b02994.
- [61] Smit, B.; Maesen, T. L. M. Towards a Molecular Understanding of Shape Selectivity. *Nature* **2008**, *451*, 671–678. DOI: 10.1038/nature06552.
- [62] Abdelrasoul, A.; Zhang, H.; Cheng, C.-H.; Doan, H. Applications of Molecular Simulations for Separation and Adsorption in Zeolites. *Microporous Mesoporous Mater.* **2017**, *242*, 294–348. DOI: 10.1016/j.micromeso.2017.01.038.

- [63] Fuchs, A. H.; Cheetham, A. K. Adsorption of Guest Molecules in Zeolitic Materials: Computational Aspects. *J. Phys. Chem. B* **2001**, *105* (31), 7375–7383. DOI: 10.1021/jp010702q.
- [64] Bukowski, B. C.; Keil, F. J.; Ravikovitch, P. I.; Sastre, G.; Snurr, R. Q.; Coppens, M.-O. Connecting Theory and Simulation with Experiment for the Study of Diffusion in Nanoporous Solids. *Adsorption* **2021**, *27* (5), 683–760. DOI: 10.1007/s10450-021-00314-y.
- [65] Sastre, G. Molecular Dynamics of Hydrocarbons in Zeolites: Historical Perspective and Current Developments. In *Modelling and Simulation in the Science of Micro- and Meso-Porous Materials*; Elsevier, 2018, 27–62. DOI: 10.1016/B978-0-12-805057-6.00002-8.
- [66] Krishna, R.; van Baten, J. M. Using Molecular Dynamics Simulations for Elucidation of Molecular Traffic in Ordered Crystalline Microporous Materials. *Microporous Mesoporous Mater.* **2018**, *258*, 151–169. DOI: 10.1016/j.micromeso.2017.09.014.
- [67] Smit, B.; Maesen, T. L. M. Molecular Simulations of Zeolites: Adsorption, Diffusion, and Shape Selectivity. *Chem. Rev.* **2008**, *108* (10), 4125–4184. DOI: 10.1021/cr8002642.
- [68] Keil, F. J.; Krishna, R.; Coppens, M.-O. Modeling of Diffusion in Zeolites. *Rev. Chem. Eng.* **2000**, *16* (2), 71–197. DOI: 10.1515/REVCE.2000.16.2.71.
- [69] Smit, B. Molecular Simulations of the Adsorption and Diffusion of Hydrocarbons in Molecular Sieves. In *Studies in Surface Science and Catalysis*; Elsevier, 2007; Vol. 170, 121–129. DOI: 10.1016/S0167-2991(07)80830-5.
- [70] Rassoulinejad-Mousavi, S. M.; Azamat, J.; Khataee, A.; Zhang, Y. Molecular Dynamics Simulation of Water Purification Using Zeolite MFI Nanosheets. *Sep. Purif. Technol.* **2020**, *234*, 116080. DOI: 10.1016/j.seppur.2019.11.6080.
- [71] Pacheco, K. A.; Guirardello, R. Isotherm Parameters for Gas-solid Adsorption Using Monte Carlo Simulation. *AIP Conf. Proc.* **2018**, *1978* (1), 470038. DOI: 10.1063/1.5044108.

- [72] Smit, B.; Krishna, R. Monte Carlo Simulations in Zeolites. *Curr. Opin. Solid State Mater. Sci.* **2001**, *5* (5), 455–461. DOI: 10.1016/S1359-0286(01)00027-4.
- [73] Luna-Triguero, A.; Gómez-Álvarez, P.; Calero, S. Adsorptive Process Design for the Separation of Hexane Isomers Using Zeolites. *Phys. Chem. Chem. Phys.* **2017**, *19* (7), 5037–5042. DOI: 10.1039/C6CP08025A.
- [74] Chung, Y. G.; Bai, P.; Haranczyk, M.; Leperi, K. T.; Li, P.; Zhang, H.; Wang, T. C.; Duerinck, T.; You, F.; Hupp, J. T.; Farha, O. K.; Siepmann, J. I.; Snurr, R. Q. Computational Screening of Nanoporous Materials for Hexane and Heptane Isomer Separation. *Chem. Mater.* **2017**, *29* (15), 6315–6328. DOI: 10.1021/acs.chemmater.7b01565.
- [75] González-Galán, C.; Luna-Triguero, A.; Vicent-Luna, J.; Zaderenko, A.; Sławek, A.; de Armas, R. S.; Calero, S. Exploiting the  $\pi$ -bonding for the Separation of Benzene and Cyclohexane in Zeolites. *Chem. Eng. J.* **2020**, *398*, 125678. DOI: 10.1016/j.cej.2020.125678.
- [76] Toda, J.; Corma, A.; Sastre, G. Diffusion of Trimethylbenzenes and Xylenes in Zeolites with 12- and 10-Ring Channels as Catalyst for Toluene-Trimethylbenzene Transalkylation. *J. Phys. Chem. C* **2016**, *120* (30), 16668–16680. DOI: 10.1021/acs.jpcc.6b03806.
- [77] Toda, J.; Corma, A.; Abudawoud, R. H.; Elanany, M. S.; Al-Zahrani, I. M.; Sastre, G. Influence of Force Fields on the Selective Diffusion of Para-xylene over Ortho-xylene in 10-ring Zeolites. *Mol. Simul.* **2015**, *41* (16–17), 1438–1448. DOI: 10.1080/08927022.2015.1047370.
- [78] Rungsisirakun, R.; Nanok, T.; Probst, M.; Limtrakul, J. Adsorption and Diffusion of Benzene in the Nanoporous Catalysts FAU, ZSM-5 and MCM-22: A Molecular Dynamics Study. *J. Mol. Graphics Model.* **2006**, *24* (5), 373–382. DOI: 10.1016/j.jmgn.2005.10.003.
- [79] Keyvanloo, Z.; Nakhaei Pour, A.; Moosavi, F.; Kamali Shahri, S. M. Molecular Dynamic Simulation Studies of Adsorption and Diffusion Behaviors of Methanol and Ethanol Through ZSM-5 Zeolite. *J. Mol. Graphics Model.* **2022**, *110*, 108048. DOI: 10.1016/j.jmgn.2021.108048.

- [80] Gómez-Álvarez, P.; Noya, E. G.; Lomba, E.; Valencia, S.; Pires, J. Study of Short-Chain Alcohol and Alcohol–Water Adsorption in MEL and MFI Zeolites. *Langmuir* **2018**, *34* (43), 12739–12750. DOI: 10.1021/acs.langmuir.8b02326.
- [81] Kim, J.; Lin, L.-C.; Martin, R. L.; Swisher, J. A.; Haranczyk, M.; Smit, B. Large-Scale Computational Screening of Zeolites for Ethane/Ethene Separation. *Langmuir* **2012**, *28* (32), 11914–11919. DOI: 10.1021/1a302230z.
- [82] García-Pérez, E.; Parra, J. B.; Ania, C. O.; García-Sánchez, A.; van Baten, J. M.; Krishna, R.; Dubbeldam, D.; Calero, S. A Computational Study of CO<sub>2</sub>, N<sub>2</sub>, and CH<sub>4</sub> Adsorption in Zeolites. *Adsorption* **2007**, *13* (5), 469–476. DOI: 10.1007/s10450-007-9039-z.
- [83] Martin-Calvo, A.; Van der Perre, S.; Claessens, B.; Calero, S.; Denayer, J. F. M. Unravelling the Influence of Carbon Dioxide on the Adsorptive Recovery of Butanol from Fermentation Broth Using ITQ-29 and ZIF-8. *Phys. Chem. Chem. Phys.* **2018**, *20* (15), 9957–9964. DOI: 10.1039/C8CP01034J.
- [84] Perez-Carbajo, J.; Matito-Martos, I.; Balestra, S. R. G.; Tsampas, M. N.; van de Sanden, M. C. M.; Delgado, J. A.; Águeda, V. I.; Merklings, P. J.; Calero, S. Zeolites for CO<sub>2</sub>–CO–O<sub>2</sub> Separation to Obtain CO<sub>2</sub>-Neutral Fuels. *ACS Appl. Mater. Interfaces* **2018**, *10* (24), 20512–20520. DOI: 10.1021/acsami.8b04507.
- [85] Han, K. N.; Bernardi, S.; Wang, L.; Searles, D. J. Water Diffusion in Zeolite Membranes: Molecular Dynamics Studies on Effects of Water Loading and Thermostat. *J. Membr. Sci.* **2015**, *495*, 322–333. DOI: 10.1016/j.memsci.2015.08.033.
- [86] Porter, A. J.; O’Malley, A. J. A Classical Molecular Dynamics Study on the Effect of Si/Al Ratio and Silanol Nest Defects on Water Diffusion in Zeolite HY. *J. Phys. Chem. C* **2021**, *125* (21), 11567–11579. DOI: 10.1021/acs.jpcc.1c01094.
- [87] Dubbeldam, D.; Walton, K. S.; Vlugt, T. J. H.; Calero, S. Design, Parameterization, and Implementation of Atomic Force Fields for Adsorption in Nanoporous Materials. *Adv. Theory Simul.* **2019**, *2* (11), 1900135. DOI: 10.1002/adts.201900135.

- [88] Dubbeldam, D.; Calero, S.; Vlugt, T. J. H.; Krishna, R.; Maesen, T. L. M.; Smit, B. United Atom Force Field for Alkanes in Nanoporous Materials. *J. Phys. Chem. B* **2004**, *108* (33), 12301–12313. DOI: 10.1021/jp0376727.
- [89] Sastre, G.; Gale, J. D. Derivation of an Interatomic Potential for Fluoride-Containing Microporous Silicates and Germanates. *Chem. Mater.* **2005**, *17* (4), 730–740. DOI: 10.1021/cm048406o.
- [90] Bai, P.; Tsapatsis, M.; Siepmann, J. I. TraPPE-zeo: Transferable Potentials for Phase Equilibria Force Field for All-Silica Zeolites. *J. Phys. Chem. C* **2013**, *117* (46), 24375–24387. DOI: 10.1021/jp4074224.
- [91] Combariza, A. F.; Gomez, D. A.; Sastre, G. Simulating the Properties of Small Pore Silica Zeolites Using Interatomic Potentials. *Chem. Soc. Rev.* **2012**, *42* (1), 114–127. DOI: 10.1039/C2CS35243E.
- [92] Castillo, J. M.; Dubbeldam, D.; Vlugt, T. J. H.; Smit, B.; Calero, S. Evaluation of Various Water Models for Simulation of Adsorption in Hydrophobic Zeolites. *Mol. Simul.* **2009**, *35* (12–13), 1067–1076. DOI: 10.1080/08927020902865923.
- [93] Bushuev, Y. G.; Sastre, G. Atomistic Simulation of Water Intrusion–Extrusion in ITQ-4 (IFR) and ZSM-22 (TON): The Role of Silanol Defects. *J. Phys. Chem. C* **2011**, *115* (44), 21942–21953. DOI: 10.1021/jp207020w.
- [94] Bushuev, Y. G.; Sastre, G. Atomistic Simulations of Structural Defects and Water Occluded in SSZ-74 Zeolite. *J. Phys. Chem. C* **2009**, *113* (25), 10877–10886. DOI: 10.1021/jp9013306.
- [95] Shah, M. S.; Siepmann, J. I.; Tsapatsis, M. Transferable Potentials for Phase Equilibria. Improved United-atom Description of Ethane and Ethylene. *AIChE J.* **2017**, *63* (11), 5098–5110. DOI: 10.1002/aic.15816.
- [96] Liu, B.; Smit, B.; Rey, F.; Valencia, S.; Calero, S. A New United Atom Force Field for Adsorption of Alkenes in Zeolites. *J. Phys. Chem. C* **2008**, *112* (7), 2492–2498. DOI: 10.1021/jp075809d.
- [97] Wick, C. D.; Martin, M. G.; Siepmann, J. I. Transferable Potentials for Phase Equilibria. 4. United-Atom Description of Linear and Branched Alke-

nes and Alkylbenzenes. *J. Phys. Chem. B* **2000**, *104* (33), 8008–8016. DOI: 10.1021/jp001044x.

- [98] Jorgensen, W. L. Optimized Intermolecular Potential Functions for Liquid Alcohols. *J. Phys. Chem.* **1986**, *90* (7), 1276–1284. DOI: 10.1021/j100398a015.





## Chapter 2

# Computational Methods

Computational chemistry offers powerful tools for researchers who aim to calculate, predict and interpret the properties of the studied system from a molecular perspective. In order to interpret such results, Statistical Mechanics (SM) provide a rigorous theoretical background that connects the macroscopic phenomena and the microscopic behavior of the particles composing the system. Key SM concepts will be briefly mentioned here, but can be found in detail elsewhere [1, 2].

### 2.1 Statistical Mechanics Overview

Considering a system in thermodynamic equilibrium, where the interacting particles are atoms and/or molecules, its macroscopic state can be specified by a set of measurable thermodynamic parameters, such as pressure ( $P$ ), volume ( $V$ ), temperature ( $T$ ) and number of particles ( $N$ ). The macrostate of an isolated system, for example, can be defined in terms of its internal energy ( $E$ ),  $N$  and  $V$ , since it does not exchange energy or mass with the surroundings. However, at a microscopic level, a very large number of states are consistent to the set of macroscopic properties defined [2]. Thus, a microstate of the system is obtained by specifying the states of all particles in the system, which, in the case of a classical treatment, occurs when defining the position ( $\mathbf{r}$ ) and the associated moment ( $\mathbf{p}$ ) of every particle [3]. The representation of all possible microstates of a system, that is, all possible values of position ( $3N$  spatial coordinates) and moment ( $3N$  momentum components) of the  $N$  particles, corresponds to the  $6N$ -dimensional phase space. Therefore, one microstate corresponds to a point in this phase space [2].

An ensemble collects an enormous number of microstates that are in a given macrostate. For instance, a system defined by certain values of  $N$ ,  $V$  and  $T$  (which characterize their macroscopic state), microscopically presents a large number of

accessible states – translational, vibrational, rotational and electronic, if the latter is considered by the model. Also, different spatial configurations among system particles generate different instantaneous interactions among them, and consequently, different energy stabilizations. Therefore, all the possible configurations (microstates) of the same macrostate (characterized by  $N$ ,  $V$  and  $T$ ) comprise the  $NVT$  ensemble, also called *Canonical Ensemble*. Other commonly simulated ensembles are the *Grand Canonical* (where the chemical potential  $\mu$ ,  $V$ ,  $T$  are constant), *Microcanonical* ( $N$ ,  $V$  and  $E$  are constant) and *Isothermal-Isobaric* ( $N$ ,  $P$  and  $T$  are constant) [4].

The following postulates are important considerations to the Statistical Mechanics formalism: *i*) for a specific macrostate, at a given time  $t$ , the system is equally likely to be in any of the possible microstates of the ensemble, and this is the so-called *equal probability a priori* postulate [2]. *ii*) Considering *i*, the system can move from one microstate to another, and with enough time, all possible microstates will be addressed. In SM, a system is in equilibrium when all the different microstates are sampled with the *equal a priori probability* [3]. It is possible to obtain the value of any thermodynamic property  $\mathbf{A}$ , in equilibrium, through the statistical average (ensemble average,  $\langle \mathbf{A} \rangle$ ), while the experimental measurement of this physical observable corresponds to a time average ( $\overline{\mathbf{A}}$ ). Simulating the system long enough to achieve the equilibrium, the *ergodicity principle* ensures that  $\langle \mathbf{A} \rangle \equiv \overline{\mathbf{A}}$ , i.e., the calculated statistical average is equivalent to the average value of the macroscopic measurement [3].

Based on the above postulates, thermodynamic properties can be calculated in terms of molecular properties [2]. Consequently, computer simulations of a specific ensemble can establish a bridge between the measurable properties and the microscopic behavior of the system. Nevertheless, depending on the phase space of the studied system, a complete sampling over all possible states requires very long simulations, in timescales not yet reached by the computational resources currently available. In these cases, the *ergodicity principle* is not satisfied, and therefore, the measurement of macroscopic properties through simulation will be approximated to the experimentally measured. In the following sections, two main methods for sampling the system configurations will be discussed, and for performing these simulations, the description of the system should be first addressed.

## 2.2 Modeling the System

Once the system and its properties of interest are defined, a crucial task is the definition of a model that can mimic the real system and reproduce its behavior under the selected conditions [5]. Each atom composing the system can be defined as a spherical particle of mass  $m$  (All Atom model (AA), Figure 2.1a), or groups of atoms can be incorporated in a single bead (United Atom model (UA), Figure 2.1b), simplifying the model. In the latter approach,  $m$  corresponds to the sum of the masses of all atoms included in the bead.



**Figure 2.1:** Ethane molecule modeled by (a) all atom and (b) united atom approaches.

As mentioned before, the macroscopic behavior of a system is closely related to the interactions among its atoms and/or molecules. Such interactions can be modeled in a classic way by a Force Field (FF), which describes the relation of the potential energy ( $\mathcal{U}$ ) with particles coordinates ( $\mathbf{r}$ ). A FF consists in a set of equations and parameters that recall fundamental concepts such as chemical bonds, angles and torsions, as well as intra and intermolecular interactions [6], as exemplified by Equation 2.1.

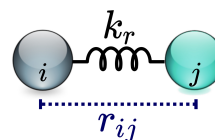
$$\mathcal{U}(\mathbf{r}) = \mathcal{U}_{\text{bonds}} + \mathcal{U}_{\text{bends}} + \mathcal{U}_{\text{torsions}} + \mathcal{U}_{\text{electrostatic}} + \mathcal{U}_{\text{vdW}} + \dots \quad (2.1)$$

Equivalent atoms or beads of the system are usually labeled under the same code, the so-called Atom Type, and are described by the same set of parameters needed in the FF equations. Force field parameters are obtained considering experimental data and/or *ab initio* calculations of the target molecules during a parameterization procedure. Although general force fields are available (such as the Universal Force Field (UFF) [7]), there are an extensive list of models developed to accurately describe specific properties of selected systems, such as geometry and energy, reproducing structural properties of zeolites [8–11], inflections of gas adsorption isotherms from porous materials [12], specific conformations and interactions among amino acids [13], dipolar moment and other water properties [14–18], among others.

In the literature, there are numerous functional forms to describe each term of Equation 2.1, and specific terms can be added depending on the specificities of the system. For example, explicit terms dealing with hydrogen bonds can be considered, or improper torsional expressions to ensure planarity on unsaturated regions of a molecule can be necessary. For a classical FF, the terms responsible to maintain the molecule's topology during the simulation are called *bonded terms*. The description of a bond stretching can be provided by the Harmonic Oscillator approximation, or by a Morse Potential, Equations 2.2 and 2.3, respectively. The harmonic potential contains 2 parameters: spring constant  $k_r$  and bond length equilibrium value  $r_0$ . Besides  $r_0$ , Morse expression possess other 2 parameters: well depth  $D_e$  and  $\alpha_{ij} = \sqrt{k_{min}/2D_e}$ , where  $k_{min}$  is the force constant at the minimum of the well.

$$U^{harm}(r_{ij}) = \sum_{\text{bonds}} \frac{k_r}{2} (r_{ij} - r_0)^2 \quad (2.2)$$

$$U^{morse}(r_{ij}) = \sum_{\text{bonds}} D_e \{ [1 - e^{-\alpha_{ij}(r_{ij}-r_0)}]^2 - 1 \} \quad (2.3)$$



Both  $U_{bonds}$  functional forms are exemplified by Figure 2.2a. While the harmonic approach has a simpler expression, that is valid when the bond length oscillations are small (close to  $r_0$ ), Morse potential provide a more accurate description, also taking into account anharmonic effects, but increasing the computational cost.

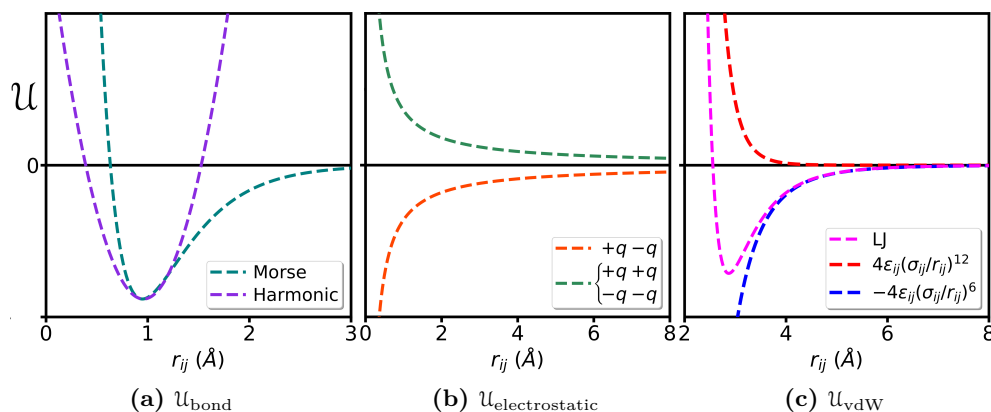
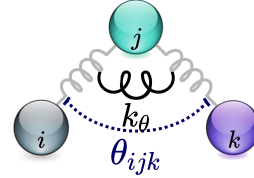


**Figure 2.2:** Plots of potential energy ( $U$ ) versus particles distance ( $r_{ij}$ ) for a (a) bond described by Morse and Harmonic potentials, (b) electrostatic interaction using Coulomb potential for particles with same charge magnitude ( $q$ ) and of opposite (orange) or equal (green) signs, and (c) van der Waals interaction described by the Lennard-Jones potential (magenta) and its repulsive (red) and attractive (blue) components.

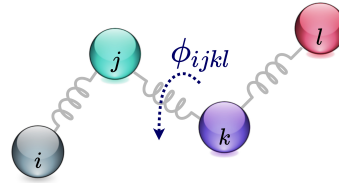
Similarly, the angle bending can be modeled by a harmonic expression, Equation 2.4, where  $k_\theta$  is the spring constant and  $\theta_0$  the bond angle equilibrium value.

$$\mathcal{U}^{harm}(\theta_{ijk}) = \sum_{\text{bends}} \frac{k_\theta}{2} (\theta_{ijk} - \theta_0)^2 \quad (2.4)$$



The reproduction of the dihedral angle rotation can be done with a truncated Fourier series like Equation 2.5, in which  $V_n$  is the torsional barrier,  $n$  is the periodicity of the rotational barrier, and  $\gamma$  is the phase angle.

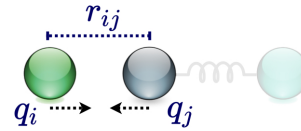
$$\mathcal{U}(\phi_{ijkl}) = \sum_{\text{torsions}} V_n [1 + \cos(n\phi_{ijkl} - \gamma)] \quad (2.5)$$



Among the *non-bonded terms*, there are two main contributions for the intermolecular interactions: electrostatic and van der Waals forces. In a system of charged particles, the interaction between point charges  $q_i$  and  $q_j$  can be expressed in terms of the Coulomb potential, Equation 2.6. As depicted by Figure 2.2b, for two atoms with the same magnitude of charge, an attractive interaction is established between charges of opposite sign (orange curve). Contrarily, repulsion arises when the interacting charges have the same sign (green curve).

$$\mathcal{U}^{Coulomb}(r_{ij}) = \sum_{i < j} \frac{1}{4\pi\epsilon_0} \frac{q_i q_j}{r_{ij}} \quad (2.6)$$

$$\mathcal{U}^{LJ}(r_{ij}) = \sum_{i < j} 4\epsilon_{ij} \left[ \left( \frac{\sigma_{ij}}{r_{ij}} \right)^{12} - \left( \frac{\sigma_{ij}}{r_{ij}} \right)^6 \right] \quad (2.7)$$



Considering a pair of atoms infinitely separated, as the distance between each other,  $r_{ij}$ , is reduced, attractive forces arise from the interactions between the induced dipoles, until a maximum stabilization is reached. By bringing the two particles even closer, repulsive forces arise from the forced overlap of both electronic clouds. These vdW interactions between pairs of atoms can be described by the Lennard-Jones potential (LJ), Equation 2.7, in which  $\epsilon_{ij}$  is the depth of the potential well for the interaction, and  $\sigma_{ij}$  is the distance where the potential is zero. As can be seen in the Figure 2.2c, the LJ potential (magenta curve) is composed by a sum of an attractive (red curve) and repulsive term (blue curve) in the

sixth and twelfth power, respectively. In addition to the functional form shown in Equation 2.7, LJ potential can be expressed as a function of  $r_{ij}^{min}$  (Equation 2.8), which is the distance between  $i$  and  $j$  where the potential has its minimum value; or in the AB form (Equation 2.9).

$$\mathcal{U}^{LJ}(r_{ij}) = \sum_{i < j} \varepsilon_{ij} \left[ \left( \frac{r_{ij}^{min}}{r_{ij}} \right)^{12} - 2 \left( \frac{r_{ij}^{min}}{r_{ij}} \right)^6 \right] \quad (2.8)$$

$$= \sum_{i < j} \left[ \left( \frac{A_{ij}}{r_{ij}^{12}} \right) - \left( \frac{B_{ij}}{r_{ij}^6} \right) \right] \quad (2.9)$$

These three LJ expressions are employed by different simulation packages and force field definitions, and their parameters can be converted to be used in other functional forms using the following conversion factors:

<p>• <math>\sigma \rightarrow</math> <b>AB form</b></p> $\begin{cases} A_{ij} = 4\varepsilon_{ij}(\sigma_{ij})^{12} \\ B_{ij} = 4\varepsilon_{ij}(\sigma_{ij})^6 \end{cases}$	<p>• <b>AB</b> <math>\rightarrow</math> <b><math>r^{min}</math> form</b></p> $\begin{cases} r_{ij}^{min} = (2A_{ij}/B_{ij})^{1/6} \\ \varepsilon_{ij} = (B_{ij})^2/4A_{ij} \end{cases}$	<p>• <b>AB</b> <math>\rightarrow</math> <b><math>\sigma</math> form</b></p> $\begin{cases} \sigma_{ij} = (A_{ij}/B_{ij})^{1/6} \\ \varepsilon_{ij} = (B_{ij})^2/4A_{ij} \end{cases}$
<p>• <b><math>r^{min}</math></b> <math>\rightarrow</math> <b>AB form</b></p> $\begin{cases} A_{ij} = \varepsilon_{ij}(r_{ij}^{min})^{12} \\ B_{ij} = 2\varepsilon_{ij}(r_{ij}^{min})^6 \end{cases}$	<p>• <math>\sigma \rightarrow</math> <b><math>r^{min}</math> form</b></p> $\begin{cases} r_{ij}^{min} = 2^{1/6}\sigma_{ij} \\ \varepsilon_{ij} \text{ is the same} \end{cases}$	<p>• <b><math>r^{min}</math></b> <math>\rightarrow</math> <b><math>\sigma</math> form</b></p> $\begin{cases} \sigma_{ij} = 2^{-1/6}r_{ij}^{min} \\ \varepsilon_{ij} \text{ is the same} \end{cases}$

A convenient way to store Lennard-Jones parameters is through their values for a pair of equivalent atoms (particles with the same atom type). Thus, the interaction between different particles,  $i$  and  $j$ , can be derived through combination rules. An example is the Lorentz-Berthelot mixing rule, where  $\sigma_{ij}$  is obtained by an arithmetic mean value (Equation 2.10), and  $\varepsilon_{ij}$  by the geometric mean value (Equation 2.11).

$$\sigma_{ij} = \frac{\sigma_{ii} + \sigma_{jj}}{2} \quad (2.10)$$

$$\varepsilon_{ij} = \sqrt{\varepsilon_{ii}\varepsilon_{jj}} \quad (2.11)$$

However, there are force fields that derive the LJ parameters for each pair of interacting atoms individually, in order to reproduce more accurately certain proper-

ties and experimental values. Such approach is adopted by United Atom models applied in Monte Carlo simulations to compute adsorption isotherms, for example [19, 20]. Furthermore, the *non-bonded terms* are usually pairwise additive, e.g. accounted between every pair of atoms in the system, unless specified otherwise. For instance, the electrostatic interaction between atoms directly bonded (and within two or three bonds of distance) may be not considered in force fields for small molecules. A careful examination of the force field definition, as well as the validation of the generated simulations, is an important procedure to ensure the quality and reliability of obtained results.

As a logical consequence of evaluating the non-bonded interactions for, in principle, every pair of atoms composing the system, such calculation is the most time-consuming procedure during the simulations [21]. For practical purposes, the truncation of the short-range vdW potentials needs to be done, and functions can be shifted to zero at the cutoff distance ( $r_{cut}$ ). Although  $r_{cut}$  should be sufficiently large to account for the main interactions [22], the neglected ones (beyond the selected cutoff) can be estimated, and tail corrections be applied. Oppositely, the Coulombic interactions can still be significant at long-range, which prevents applying cutoffs in the same way [22]. Instead,  $r_{cut}$  can be used to switch the treatment given to short-range and long-range interactions [23]. Besides, for an accurate computation of the latter set of interactions, the Ewald summation [24] is applicable for neutral and periodic systems [6].

It should also be mentioned that, by selecting this classical modeling, molecules' topology is kept during the simulations (by the *bonded terms*), and therefore, the breaking and formation of bonds will not occur. For the study of chemical reactions, a proper modeling must be provided, where the description of the electronic structure (by DFT, Density Functional Theory, or *ab initio* methods) is mandatory. On the other hand, the classical approach is suitable to study systems where mainly intermolecular interactions take place, as the physisorption in zeolites. By this simpler approach, longer simulations can be performed for bigger systems, allowing to further analyze their microscopic behavior.

## 2.3 Simulating the System

With a model and initial conditions clearly stated for the system, a key point is the sampling technique selected to perform the simulations. Different methods can be used to generate system trajectories and/or equilibrium configurations, from which the average properties can be calculated. In the present work, simulations were performed with the classical Molecular Dynamics (MD) and Monte Carlo (MC) methods.

### 2.3.1 Molecular Dynamics simulations

In the MD, the temporal evolution of a system is computed through the numerical integration of the equations of motion. From the classical mechanics, Newton's second law of motion defines the force on a particle  $i$  ( $\mathbf{F}_i$ ) as

$$\mathbf{F}_i = m\ddot{\mathbf{r}}_i = m_i \frac{d\dot{\mathbf{r}}_i}{dt}, \quad (2.12)$$

where  $m_i$  is the mass, and  $\ddot{\mathbf{r}}$  the acceleration of the particle, which is the first derivative of velocity ( $\dot{\mathbf{r}}$ ) with respect to time ( $t$ ), or the second derivative of position ( $\mathbf{r}_i$ ) with respect to time. In a system of  $N$  particles, the force  $\mathbf{F}_i$  acting on a particle  $i$  due to its interaction with the  $N-1$  remaining particles of the system is related to the potential energy by

$$\mathbf{F}_i = -\frac{\partial U(\mathbf{r})}{\partial \mathbf{r}_i}. \quad (2.13)$$

Thus, momentum and position of the particles over time can be accessed by the iterative integration of Equations 2.12 and 2.13, and this temporal evolution can be saved as a trajectory [5]. Various algorithms for the numerical integration of the equations of motion are available. For instance, with Velocity Verlet scheme [25], particle's  $i$  position and force on the next time instant ( $t + \Delta t$ , where  $\Delta t$  is the time step) can be obtained by knowing their values in the actual instant  $t$ . First, the velocity half step ahead ( $\dot{\mathbf{r}}_i(t + \frac{1}{2}\Delta t)$ ) is computed, using the force and velocity in the present step ( $\mathbf{F}_i(t)$  and  $\dot{\mathbf{r}}_i(t)$ , respectively):

$$\dot{\mathbf{r}}_i(t + \frac{1}{2}\Delta t) = \dot{\mathbf{r}}_i(t) + \frac{1}{2}\Delta t \frac{\mathbf{F}_i(t)}{m_i}. \quad (2.14)$$



Then, particle position in the next step ( $\mathbf{r}_i(t + \Delta t)$ ) can be calculated (Equation 2.15), the force is derived for the next step ( $\mathbf{F}_i(t + \Delta t)$ , considering the updated position) and applied to the Equation 2.16 to obtain the velocity in the next instant ( $\dot{\mathbf{r}}_i(t + \Delta t)$ ).

$$\mathbf{r}_i(t + \Delta t) = \mathbf{r}_i(t) + \Delta t \dot{\mathbf{r}}_i(t + \frac{1}{2}\Delta t) \quad (2.15)$$

$$\dot{\mathbf{r}}_i(t + \Delta t) = \dot{\mathbf{r}}_i(t + \frac{1}{2}\Delta t) + \frac{1}{2}\Delta t \frac{\mathbf{F}_i(t + \Delta t)}{m_i} \quad (2.16)$$

The selected time step should be sufficiently small to capture the fastest vibrational modes, associated with the lighter atoms present in the system. When hydrogen atoms are present, time steps around 0.5–1.0 fs need to be employed, for example [22]. On the other hand, larger time steps allow longer simulation times with the same amount of computational resources. Depending on the studied system, the phenomenon of interest can only be observed in really long simulations, feasible if using bigger time step values. This can be done by using the SHAKE algorithm [26] to constrain the bonds involving such smaller atoms, for example.

As previously mentioned, time-average properties can be estimated from the computed trajectories. However, for a direct comparison with the experimental data, a proper ensemble needs to be simulated. Usually, temperature and/or pressure are controlled during experiments, leading to an NVT or NPT ensemble in the case of a closed system. Thus, for reproducing the experimental conditions, thermostats [27] and barostats [23] need to be coupled to the simulation boxes, in order to keep the average T and P of the system close to its target value. Various approaches for controlling the temperature and pressure have been reported in the literature, in the works of Berendsen [28], Andersen [29], Nosé and Hoover [30–32], Langevin [33, 34], among others. While pressure control can be done by controlling the system’s volume, its temperature is directly related to the average kinetic energy of the constituent particles. Thus, the thermal control during the simulation involve the modification of particles’ velocities [22]. This can be done from a simple scaling of the velocities every  $n$  steps, to a more rigorous scheme that correctly samples the canonical ensemble, like for the Nosé-Hoover thermostat [22].

Still concerning the simulation of experimental properties, its dependency upon system size also needs to be evaluated. An ensemble average property, when measured in small systems, can mainly reflect the surface phenomena. If we are interested in bulk properties and in avoiding finite size effects, besides increasing

the size of the simulation box, Periodic boundary conditions (PBC) can be employed. Virtual replicas of the real system (central boxes in Figure 2.3, with black edges) are generated in every direction, mimicking an infinite system. Therefore,

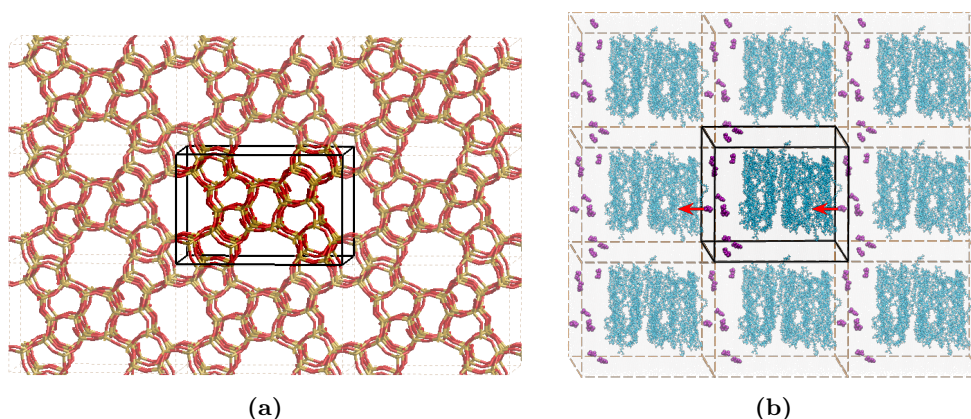


**Figure 2.3:** Simulation box (center) and its virtual images of (a) MFI framework and (b) polymeric matrix (cyan) with sorbate molecules (magenta) in water (transparent). The red arrows in (b) indicates the concerted exit of a sorbate molecule from the simulation box and the entrance of its virtual image on the opposite side.

as illustrated by the red arrows in Figure 2.3b, when a particle from the real system moves out of box boundaries, its virtual image from the opposite side enters the simulation box [3]. This approach introduces periodicity to the studied system, a feature already needed for periodic materials such as zeolites (Figure 2.3a), but artificially introduced in other types of systems (liquids, gases, or phase mixtures, as exemplified by Figure 2.3b) [5]. Finally, to avoid accounting the interaction of a particle with the virtual images multiples times, the length of the simulation box in every direction should be at least twice the cutoff value for the non-bonded interactions [23], which is usually defined by the force field scheme.

### 2.3.2 Monte Carlo simulations

In contrast to the previous method – that employed a purely deterministic way of sampling every point of the configuration space –, Monte Carlo simulations consider stochastic methods for the generation of every new configuration of the system. The MC simulations do not depend upon the integration of the equations of the motion, and consequently, there is no connection with time [5]. Therefore, only static properties can be studied by MC, whereas the dynamical ones can be

assessed by the MD or the Kinetic Monte Carlo methodologies (outside the scope of this thesis), for example.

Considering  $N$  particles arranged in a specific configuration, defined by their set of Cartesian coordinates  $\mathbf{r}^N$ , such arrangement can be randomly constructed from scratch, or consider the actual configuration to derive the following one. In each cycle of MC, system particles are randomly selected, and attempts are made to move them. Those MC moves, also randomly chosen, are accepted or not, depending on the acceptance rules stated for them by the specified ensemble [35]. Thereby, the next configuration generated can be a new one (derived from the previous conformation of the system), or exactly the same if no MC move is accepted. For every new configuration, a property  $A$  is calculated, and after a considerable amount of MC cycles, an accurate ensemble average  $\langle A \rangle$  can be obtained from this chain of states, also called a Markov chain [36]. In Equation 2.17,  $\langle A \rangle$  is related to the property  $A$  and the probability density function ( $\rho$ ) of the ensemble, in the space of variables  $\xi$  [37]. For instance, in the canonical ensemble, Equation 2.18 states the dependency of  $\langle A \rangle$  on the potential energy of the system ( $\mathcal{U}(\mathbf{r}^N)$ , defined by the selected force field) and of the thermodynamic  $\beta$ , equal to  $1/k_B T$ , where  $k_B$  is the Boltzmann constant [36].

$$\langle A \rangle = \int A(\xi) \rho(\xi) \, d\xi \quad (2.17)$$

$$= \frac{\int A(\mathbf{r}^N) \exp[-\beta \mathcal{U}(\mathbf{r}^N)] \, d^N \mathbf{r}}{\int \exp[-\beta \mathcal{U}(\mathbf{r}^N)] \, d^N \mathbf{r}} \quad (2.18)$$

For a given configuration  $\mathbf{r}^N$ , the probability density ( $\rho(\mathbf{r}^N)$ ) of finding the system in such state is defined by Equation 2.19.

$$\rho(\mathbf{r}^N) = \frac{\exp[-\beta \mathcal{U}(\mathbf{r}^N)]}{\int \exp[-\beta \mathcal{U}(\mathbf{r}^N)] \, d^N \mathbf{r}} \quad (2.19)$$

By randomly generating configurations in a MC simulation, following the probability densities stated by Equation 2.19, the average ensemble property can be approximated to Equation 2.20, where  $C_{MC}$  is the number of points from the configuration space that were sampled by the MC method [36].

$$\langle A \rangle \approx \frac{1}{C_{MC}} \sum_{x=1}^{C_{MC}} A(\mathbf{r}_x^N) \quad (2.20)$$

Furthermore, to compare the simulated results of the property with its experimentally measured value, the *ergodicity principle* should be ensured during the MC simulation. This implies that, in a finite number of MC moves, all possible states in the configuration space should be sampled, starting from a state previously reached [35].

There is a wide variety of MC moves implemented in the software packages available [38–40]. In fact, here lies the potentialities of this method, since ingenious MC moves can be designed to improve the sampling of complex systems, for the study of the molecular adsorption on materials with diffusional bottlenecks [35], and macromolecules conformations in solution [36], for example. As long as the MC move ensures the correct ensemble sampling and that the configurations are accessed in the appropriate frequency, there are no additional constraints [35]. Basic MC moves focus on molecules translation at random directions, as well as rotation at their center of mass. Depending on the ensemble simulated, attempts to change the volume of the simulation box need to be employed. When the number of particles is not constant during the simulation (e.g.  $\mu$ VT ensemble), random insertion and deletion of molecules should be attempted. Also, for the adsorption of mixtures in a porous material, identity changes among adsorbate species can be performed. Advanced strategies concerning the MC moves will be briefly discussed later in this section.

As previously mentioned, during a MC simulation, the current (*old*) state of the system is used to derive the next (*new*) one. The probability of finding the system in one of these configurations is  $\rho_o$  and  $\rho_n$ , respectively, while the transition probability of going from the *old* to the *new* state is  $\pi_{o \rightarrow n}$  [41]. As we are interested in the equilibrium properties, a logical condition needs to be fulfilled: once the equilibrium is established in the system, it is not destroyed by the matrix elements  $\pi_{o \rightarrow n}$  [41]. In such condition, the average state transitions  $old \rightarrow new = new \rightarrow old$ . Thus, by applying the so-called *detailed balance* condition, Equation 2.21 is obtained.

$$\rho_o \pi_{o \rightarrow n} = \rho_n \pi_{n \rightarrow o} \quad (2.21)$$

The transition matrix can be defined as expressed by Equation 2.22, where  $\alpha_{o \rightarrow n}$  is the underlying matrix of the Markov chain [42], and  $\text{acc}_{o \rightarrow n}$  as the probability of accepting such trial move.

$$\pi_{o \rightarrow n} = \alpha_{o \rightarrow n} \times \text{acc}_{o \rightarrow n} \quad (2.22)$$

By specifying  $\alpha$  as a symmetric matrix, the acceptance rules  $\text{acc}_{o \rightarrow n}$  and  $\text{acc}_{n \rightarrow o}$  become equal [41], allowing to rewrite the Equation 2.21 as

$$\frac{\text{acc}_{o \rightarrow n}}{\text{acc}_{n \rightarrow o}} = \frac{\rho_n}{\rho_o}. \quad (2.23)$$

Among the different forms of acceptance rules, the selected by Metropolis et al. in its original work [43, 44] (Equation 2.24) leads to an efficient sampling of the accessible states of a system [41]. Therefore, the transition from the *old* to a *new* state will possess the maximum probability ( $\text{acc}_{o \rightarrow n} = 1$ ) when the probability of finding the state in the *new* configuration ( $\rho_n$ ) is higher or equal to  $\rho_o$ , being the value of the ratio  $\rho_n/\rho_o$  otherwise (Equation 2.24).

$$\text{acc}_{o \rightarrow n} = \min\left(1, \frac{\rho_n}{\rho_o}\right) \quad (2.24)$$

As, in the canonical ensemble, the probability of finding the system in a specific state  $x$  is proportional to the Boltzmann factor ( $\exp[-\beta\mathcal{U}_x(\mathbf{r}^N)]$ ), the acceptance rule for translating or performing a rigid rotation of some particle in the simulation box is defined by Equation 2.25.

$$\text{acc}_{o \rightarrow n} = \min\left(1, \exp\{-\beta[\mathcal{U}_n(\mathbf{r}^N) - \mathcal{U}_o(\mathbf{r}^N)]\}\right) \quad (2.25)$$

For the study of porous materials adsorptive properties, adsorption isotherms can be simulated by the MC method. If considering the *grand canonical* ensemble, its partition function is given by Equation 2.26. In such definition, the potential energy is expressed as a function of  $s^N$ , the fractional coordinates of N particles system. Besides, the de Broglie wavelength,  $\Lambda$ , is defined by Equation 2.27, where  $h$  is the Planck constant [35].

$$\Xi(\mu, V, T) = \sum_{N=0}^{\infty} \frac{V^N \exp[\beta\mu N]}{\Lambda^{3N} N!} \int \exp[-\beta\mathcal{U}(s^N)] d^N s \quad (2.26)$$

$$\Lambda \equiv \left(\frac{h^2\beta}{2\pi m}\right)^{1/2} \quad (2.27)$$

Thus, adsorbates' uptake in the studied material can be simulated by the  $\mu VT$  ensemble, for a specific pressure and temperature. The pressure is directly con-

nected to the fugacity ( $f$ , Equation 2.28, where  $\phi$  is the fugacity coefficient), and consequently, to the chemical potential (Equation 2.29). In the latter expression,  $\mu$  depends on  $\mu_{IG}^0$ , which corresponds to the chemical potential using the ideal gas as a reference state and can be obtained by Equation 2.30.

$$f = \phi \mathbf{p} \quad (2.28)$$

$$\beta\mu = \beta\mu_{IG}^0 + \ln(\beta f) \quad (2.29)$$

$$\beta\mu_{IG}^0 \equiv \frac{\ln(\Lambda^3)}{\beta} \quad (2.30)$$

For the  $\mu$ VT ensemble, the acceptance rules for translation and rotation are the same stated to the canonical ensemble (Equation 2.25), as the form of the probability  $\rho_x$  (Equation 2.31) leads to the same  $\rho_n/\rho_o$  result (Equation 2.32).

$$\rho_x(s^N, V) \propto \frac{V^N \exp(\beta\mu N)}{\Lambda^{3N} N!} \exp[-\beta\mathcal{U}_x(s^N)] \quad (2.31)$$

$$\frac{\rho_n}{\rho_o} = \frac{\frac{V^N \exp(\beta\mu N)}{\Lambda^{3N} N!} \exp[-\beta\mathcal{U}_n(s^N)]}{\frac{V^N \exp(\beta\mu N)}{\Lambda^{3N} N!} \exp[-\beta\mathcal{U}_o(s^N)]} \quad (2.32)$$

$$= \exp\{-\beta[\mathcal{U}_n(s^N) - \mathcal{U}_o(s^N)]\}$$

Whereas the number of particles is not constant, trial moves to add or remove guest molecules should be performed during the simulation. The acceptance rules for the insertion or deletion of one particle in a  $N$  particle system are given by Equations 2.33 and 2.34, respectively [35].

$$\text{acc}_{N \rightarrow N+1} = \min\left(1, \frac{\beta V \phi P}{N+1} \exp\{-\beta[\mathcal{U}_n(s^{N+1}) - \mathcal{U}_o(s^N)]\}\right) \quad (2.33)$$

$$\text{acc}_{N \rightarrow N-1} = \min\left(1, \frac{N}{\beta V \phi P} \exp\{-\beta[\mathcal{U}_n(s^{N-1}) - \mathcal{U}_o(s^N)]\}\right) \quad (2.34)$$

Still focusing on the equilibrium properties, the nature of the MC moves will dictate how quickly the equilibrium is established in the simulated system [45]. Aiming to reach a conformational equilibrium, molecular conformations need to be sampled by specific MC moves, as they are not changed during translational or rotational moves. Depending on molecules size and system density, the attempts towards such conformational sampling are often not accepted, since they frequently lead to unstable system configurations. To overcome such problem, advanced sampling techniques have been developed, such as the Configurational-Bias Monte Carlo (CBMC) [45–48]. In this biased move, a randomly selected molecule is partially or completely regrown, segment by segment. The generation and selection of trial positions for each segment depend on the potential energy  $u^{trial}$ , which is conveniently split into its internal ( $u^{int}$ ) and external ( $u^{ext}$ ) contributions (Equation 2.35).

$$u^{trial} = u^{int} + u^{ext} \quad (2.35)$$

Considering a segment  $l$ , a set of  $k$  possible orientations  $b_i$  are generated according to Equation 2.36, based in the force field bonded terms accounted by  $u^{int}$  [48].

$$\rho_{li}^{generating}(b_i) db = \frac{\exp(-\beta u_{li}^{int}) db}{\int \exp(-\beta u_i^{int}) db} \quad (2.36)$$

Among the  $k$  trial orientations, one is selected to be regrown following the probability

$$\rho_{li}^{selecting}(b_i) = \frac{\exp(-\beta u_i^{ext})}{\sum_{j=1}^k \exp(-\beta u_j^{ext})} = \frac{\exp(-\beta u_i^{ext})}{w_l}, \quad (2.37)$$

which is dependent on the external potential. In Equation 2.37,  $w_l$  is the Rosenbluth weight of the segment  $l$ . The remaining segments are regrown by the above-mentioned procedure, and the new configuration is accepted or not by the modified acceptance rule:

$$\text{acc}_{o \rightarrow n} = \min\left(1, \frac{W_n}{W_o}\right). \quad (2.38)$$

$W_n$  and  $W_o$  from Equation 2.38 are the Rosenbluth weight of the *new* and *old* configurations, respectively, being obtained as exemplified by Equation 2.39, considering the Rosenbluth weight of the regrown segments.

$$W_n = \prod_l w_l \quad (2.39)$$

Further discussion about CBMC, as well as other biased moves can be found in the literature [35, 49, 50]. Both simulation methods (MC and MD) have been employed for the studies presented in the following chapters, mainly focusing on the adsorptive and separation properties of zeolites.

## References

- [1] McQuarrie, D. *Molecular Thermodynamics*; University Science Books, 1999.
- [2] McQuarrie, D. *Statistical Mechanics*; University Science Books, 2000.
- [3] *Computational Statistical Physics: Lecture Notes, Guwahati SERC School*; Sitangshu Bikas Santra, P. R., Ed.; Hindustan Book Agency, 2011.
- [4] Adcock, S. A.; McCammon, J. A. Molecular Dynamics: Survey of Methods for Simulating the Activity of Proteins. *Chem. Rev.* **2006**, *106* (5), 1589–1615. DOI: 10.1021/cr040426m.
- [5] Haile, J. M. *Molecular Dynamics Simulation: Elementary Methods*; Wiley, 1997.
- [6] Dubbeldam, D.; Walton, K. S.; Vlugt, T. J. H.; Calero, S. Design, Parameterization, and Implementation of Atomic Force Fields for Adsorption in Nanoporous Materials. *Adv. Theory Simul.* **2019**, *2* (11), 1900135. DOI: 10.1002/adts.201900135.
- [7] Rappe, A. K.; Casewit, C. J.; Colwell, K. S.; Goddard, W. A.; Skiff, W. M. UFF, a Full Periodic Table Force Field for Molecular Mechanics and Molecular Dynamics Simulations. *J. Am. Chem. Soc.* **1992**, *114* (25), 10024–10035. DOI: 10.1021/ja00051a040.
- [8] Combariza, A. F.; Gomez, D. A.; Sastre, G. Simulating the Properties of Small Pore Silica Zeolites Using Interatomic Potentials. *Chem. Soc. Rev.* **2012**, *42* (1), 114–127. DOI: 10.1039/C2CS35243E.
- [9] Gale, J. D. Analytical Free Energy Minimization of Silica Polymorphs. *J. Phys. Chem. B* **1998**, *102* (28), 5423–5431. DOI: 10.1021/jp980396p.



- [10] Sanders, M. J.; Leslie, M.; Catlow, C. R. A. Interatomic Potentials for SiO<sub>2</sub>. *J. Chem. Soc., Chem. Commun.* **1984**, (19), 1271–1273. DOI: 10.1039/C39840001271.
- [11] Ghysels, A.; Moors, S. L. C.; Hemelsoet, K.; De Wispelaere, K.; Waroquier, M.; Sastre, G.; Van Speybroeck, V. Shape-Selective Diffusion of Olefins in 8-Ring Solid Acid Microporous Zeolites. *J. Phys. Chem. C* **2015**, *119* (41), 23721–23734. DOI: 10.1021/acs.jpcc.5b06010.
- [12] Dubbeldam, D.; Calero, S.; Vlugt, T. J. H.; Krishna, R.; Maesen, T. L. M.; Beerdsen, E.; Smit, B. Force Field Parametrization Through Fitting on Inflection Points in Isotherms. *Phys. Rev. Lett.* **2004**, *93* (8), 088302. DOI: 10.1103/PhysRevLett.93.088302.
- [13] Lindorff-Larsen, K.; Piana, S.; Palmo, K.; Maragakis, P.; Klepeis, J. L.; Dror, R. O.; Shaw, D. E. Improved Side-chain Torsion Potentials for the Amber ff99SB Protein Force Field. *Proteins Struct. Funct. Bioinf.* **2010**, *78* (8), 1950–1958. DOI: 10.1002/prot.22711.
- [14] Jorgensen, W. L.; Chandrasekhar, J.; Madura, J. D.; Impey, R. W.; Klein, M. L. Comparison of Simple Potential Functions for Simulating Liquid Water. *J. Chem. Phys.* **1983**, *79* (2), 926–935. DOI: 10.1063/1.445869.
- [15] Abascal, J. L. F.; Vega, C. A General Purpose Model for the Condensed Phases of Water: TIP4P/2005. *J. Chem. Phys.* **2005**, *123* (23), 234505. DOI: 10.1063/1.2121687.
- [16] Berendsen, H. J. C.; Grigera, J. R.; Straatsma, T. P. The Missing Term in Effective Pair Potentials. *J. Phys. Chem.* **1987**, *91* (24), 6269–6271. DOI: 10.1021/j100308a038.
- [17] Rick, S. W. A Reoptimization of the Five-site Water Potential (TIP5P) for Use with Ewald Sums. *J. Chem. Phys.* **2004**, *120* (13), 6085–6093. DOI: 10.1063/1.1652434.
- [18] Horn, H. W.; Swope, W. C.; Pitner, J. W.; Madura, J. D.; Dick, T. J.; Hura, G. L.; Head-Gordon, T. Development of an Improved Four-site Water Model for Biomolecular Simulations: TIP4P-Ew. *J. Chem. Phys.* **2004**, *120* (20), 9665–9678. DOI: 10.1063/1.1683075.

- [19] Dubbeldam, D.; Calero, S.; Vlugt, T. J. H.; Krishna, R.; Maesen, T. L. M.; Smit, B. United Atom Force Field for Alkanes in Nanoporous Materials. *J. Phys. Chem. B* **2004**, *108* (33), 12301–12313. DOI: 10.1021/jp0376727.
- [20] Sławek, A.; Vicent-Luna, J. M.; Ogorzały, K.; Valencia, S.; Rey, F.; Makowski, W.; Calero, S. Adsorption of Alkanes in Zeolites LTA and FAU: Quasi-Equilibrated Thermodesorption Supported by Molecular Simulations. *J. Phys. Chem. C* **2019**, *123* (49), 29665–29678. DOI: 10.1021/acs.jpcc.9b07907.
- [21] Eastman, P.; Pande, V. S. Efficient Nonbonded Interactions for Molecular Dynamics on a Graphics Processing Unit. *J. Comput. Chem.* **2010**, *31* (6), 1268. DOI: 10.1002/jcc.21413.
- [22] González, M. A. Force Fields and Molecular Dynamics Simulations. *Collection SFN* **2011**, *12*, 169–200. DOI: 10.1051/sfn/201112009.
- [23] Braun, E.; Gilmer, J.; Mayes, H. B.; Mobley, D. L.; Monroe, J. I.; Prasad, S.; Zuckerman, D. M. Best Practices for Foundations in Molecular Simulations [Article v1.0]. *Living J. Comp. Mol. Sci.* **2019**, *1* (1), 5957. DOI: 10.33011/livecoms.1.1.5957.
- [24] Ewald, P. P. Die Berechnung Optischer und Elektrostatischer Gitterpotentiale. *Ann. Phys.* **1921**, *369* (3), 253–287. DOI: 10.1002/andp.19213690304.
- [25] Verlet, L. Computer “Experiments” on Classical Fluids. I. Thermodynamical Properties of Lennard-Jones Molecules. *Phys. Rev.* **1967**, *159* (1), 98–103. DOI: 10.1103/physrev.159.98.
- [26] Miyamoto, S.; Kollman, P. A. Settle: An Analytical Version of the SHAKE and RATTLE Algorithm for Rigid Water Models. *J. Comput. Chem.* **1992**, *13* (8), 952–962. DOI: 10.1002/jcc.540130805.
- [27] Hünenberger, P. H. Thermostat Algorithms for Molecular Dynamics Simulations. In *Advanced Computer Simulation*; Springer, 2005, 105–149. DOI: 10.1007/b99427.
- [28] Berendsen, H. J. C.; Postma, J. P. M.; van Gunsteren, W. F.; DiNola, A.; Haak, J. R. Molecular Dynamics with Coupling to an External Bath. *J. Chem. Phys.* **1984**, *81* (8), 3684–3690. DOI: 10.1063/1.448118.

- [29] Andersen, H. C. Molecular Dynamics Simulations at Constant Pressure and/or Temperature. *J. Chem. Phys.* **1980**, *72* (4), 2384–2393. DOI: 10.1063/1.439486.
- [30] Nosé, S. A Molecular Dynamics Method for Simulations in the Canonical Ensemble. *Mol. Phys.* **1984**, *52* (2), 255–268. DOI: 10.1080/00268978400101201.
- [31] Hoover, W. G. Canonical Dynamics: Equilibrium Phase-space Distributions. *Phys. Rev. A* **1985**, *31* (3), 1695–1697. DOI: 10.1103/PhysRevA.31.1695.
- [32] Martyna, G. J.; Tobias, D. J.; Klein, M. L. Constant Pressure Molecular Dynamics Algorithms. *J. Chem. Phys.* **1994**, *101* (5), 4177–4189. DOI: 10.1063/1.467468.
- [33] Loncharich, R. J.; Brooks, B. R.; Pastor, R. W. Langevin Dynamics of Peptides: The Frictional Dependence of Isomerization Rates of N-acetylalanyl-N'-methylamide. *Biopolymers* **1992**, *32* (5), 523–535. DOI: 10.1002/bip.360320508.
- [34] Feller, S. E.; Zhang, Y.; Pastor, R. W.; Brooks, B. R. Constant Pressure Molecular Dynamics Simulation: The Langevin Piston Method. *J. Chem. Phys.* **1995**, *103* (11), 4613–4621. DOI: 10.1063/1.470648.
- [35] Dubbeldam, D.; Torres-Knoop, A.; Walton, K. S. On the Inner Workings of Monte Carlo Codes. *Mol. Simul.* **2013**, *39* (14–15), 1253–1292. DOI: 10.1080/08927022.2013.819102.
- [36] Earl, D. J.; Deem, M. W. Monte Carlo Simulations. In *Molecular Modeling of Proteins*; Humana Press, 2008, 25–36. DOI: 10.1007/978-1-59745-177-2\_2.
- [37] Valleau, J. P.; Whittington, S. G. A Guide to Monte Carlo for Statistical Mechanics: 1. Highways. In *Statistical Mechanics*; Springer, 1977, 137–168. DOI: 10.1007/978-1-4684-2553-6\_4.
- [38] Dubbeldam, D.; Calero, S.; Ellis, D. E.; Snurr, R. Q. RASPA: Molecular Simulation Software for Adsorption and Diffusion in Flexible Nanoporous Materials. *Mol. Simul.* **2016**, *42* (2), 81–101. DOI: 10.1080/08927022.2015.1010082.

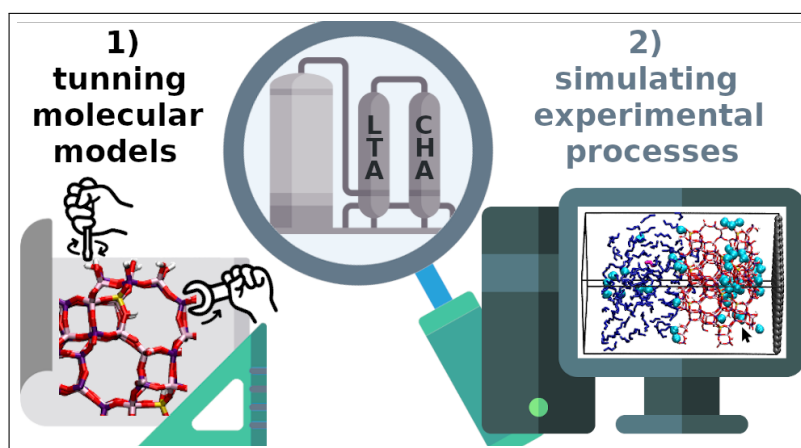
- [39] Martin, M. G. MCCCSTowhee: a Tool for Monte Carlo Molecular Simulation. *Mol. Simul.* **2013**, *39* (14–15), 1212–1222. DOI: 10.1080/08927022.2013.828208.
- [40] Gupta, A.; Chempath, S.; Sanborn, M. J.; Clark, L. A.; Snurr, R. Q. Object-oriented Programming Paradigms for Molecular Modeling. *Mol. Simul.* **2003**, *29* (1), 29–46. DOI: 10.1080/0892702031000065719.
- [41] *Computational Soft Matter: From Synthetic Polymers to Proteins*, 1st ed.; Attig, N., Binder, K., Grubmüller, H., Kremer, K., Eds.; Forschungszentrum Jülich, 2004.
- [42] Van Kampen, N. G. *Stochastic Processes in Physics and Chemistry*; North Holland, 1981.
- [43] Metropolis, N.; Rosenbluth, A. W.; Rosenbluth, M. N.; Teller, A. H.; Teller, E. Equation of State Calculations by Fast Computing Machines. *J. Chem. Phys.* **1953**, *21* (6), 1087–1092. DOI: 10.1063/1.1699114.
- [44] Metropolis, N. The Beginning of the Monte Carlo Method. *Los Alamos Sci.* **1987**, *12*, 125130.
- [45] Siepmann, J. I.; Frenkel, D. Configurational Bias Monte Carlo: a New Sampling Scheme for Flexible Chains. *Mol. Phys.* **1992**, *75* (1), 59–70. DOI: 10.1080/00268979200100061.
- [46] Frenkel, D.; Mooij, G. C. A. M.; Smit, B. Novel Scheme to Study Structural and Thermal Properties of Continuously Deformable Molecules. *J. Phys.: Condens. Matter* **1992**, *4* (12), 3053–3076. DOI: 10.1088/0953-8984/4/12/006.
- [47] De Pablo, J. J.; Laso, M.; Suter, U. W. Estimation of the Chemical Potential of Chain Molecules by Simulation. *J. Chem. Phys.* **1992**, *96* (8), 6157–6162. DOI: 10.1063/1.462658.
- [48] Vlugt, T. J. H.; Martin, M. G.; Smit, B.; Siepmann, J. I.; Krishna, R. Improving the Efficiency of the Configurational-bias Monte Carlo Algorithm. *Mol. Phys.* **1998**, *94* (4), 727–733. DOI: 10.1080/002689798167881.

- [49] Frenkel, D. *Understanding Molecular Simulation: From Algorithms to Applications*; Academic Press, 2002.
- [50] Martin, M. *MCCCS Towhee: Configurational-bias Monte Carlo*, <http://towhee.sourceforge.net/algorithm/cbmc.html> (accessed 2022-08-02).



## Chapter 3

# Molecular Simulation of Biobutanol Recovery Using LTA and CHA Zeolite Nanosheets with an External Surface



The Journal of Physical Chemistry C, 2022, 126, 41, 17680–17691.  
DOI: 10.1021/acs.jpcc.2c04331

Alechania Misturini<sup>1</sup>, Fernando Rey<sup>1</sup>, German Sastre<sup>1\*</sup>

<sup>1</sup> Instituto de Tecnología Química, Universitat Politècnica de València, Avda. de los Naranjos s/n, 46022 Valencia, Spain. \*E-mail: gsastre@itq.upv.es

## **Abstract**

LTA and CHA zeolites with silica and silico-alumino-phosphate (SAPO) composition have been recently proposed by Van der Perre et al. [1] to recover butanol from a mixture of butanol, ethanol, acetone and water. Such a mixture is obtained from biomass fermentation, which is a sustainable alternative for butanol production. Here, we establish a computational methodology to simulate the three-step process, consisting of: selective adsorption of butanol, with some ethanol and water, from the initial mixture, using a silica LTA nanosheet; desorption of the adsorbed mixture by increasing the temperature; and adsorption of the desorbed products in a CHA (silica or SAPO) nanosheet. A combination of Monte Carlo simulations, allowing to reproduce or predict single- or multiple-component gas adsorption isotherms, and molecular dynamics, giving the time evolution of the selective adsorption and desorption processes, have been used to model the experimental setup. A recently parameterized force field of general use for zeolites, APOs, and SAPOs has been tuned up in order to describe all interactions arising from this model, allowing to capture the thermodynamics of the system, the flexibility of the frameworks, and the effects of surface and bulk in the permeability of the nanosheets.

**Keywords:** Biobutanol, Water, Zeolite, force field, SAPO, Adsorption, External surface, Molecular Dynamics.

## **3.1 Introduction**

The use of biofuels can be a sustainable option for the world's growing energy demand. For instance, biobutanol (1-butanol, also known as biogasoline) can be used by the actual engines without modifications and possess approximately 85% of the energy content in gasoline, besides other advantages [2]. Through the ABE (Acetone, Butanol and Ethanol) fermentation process, biobutanol can be obtained from biomass [1]. This fermentation of renewable feedstocks by anaerobic bacteria produces a mixture with a ratio 3 acetone/6 butanol/1 ethanol, diluted in water [3]. The following separation and purification of the produced biobutanol can be done by adsorptive methods, requiring significantly less energy than distillations [4]. In this sense, zeolites present a wide variety of structures, where the microporosity and chemical composition can be tuned for highly selective adsorptions and separations. Experimental and computational studies employing zeolitic materials for the separation of ABE fermented mixture have been reported, analyzing the performance of pure silica and aluminosilicate zeolites with MFI [5–12], BEA [5, 6, 13], FAU [6], MEL [11], and CHA [14] topologies, as well as the ZIF-8 [15, 16] metal-organic framework. Material hydrophobicity has been highlighted as an important aspect for the selective adsorption of butanol from the fermented aqueous mixture [1, 6, 10]. Besides, various experimental setups have been designed, such as the adsorption-drying-desorption process for recovering butanol



from water with silicalite pellets [8]; as well as membranes of silicalite-1 (MFI) supported on Al-free-yttria stabilized zirconia substrates, that presented high selectivity to ethanol in aqueous media [7] and high performance for separation of ABE fermented solution at low temperature [12]; and also the combination of frameworks with complementary selectivity, such as ZIF-8 and SAPO-34 [15], or LTA and SAPO-34 [1]. The effect of  $\text{CO}_2$  in the recovery of biobutanol from the fermented broth by silica LTA and ZIF-8 hydrophobic adsorbents was also investigated experimentally and computationally [16].

In the selective adsorption process proposed by Denayer and co-workers [1], the hydrophobicity and affinity of LTA for butanol are combined with the high affinity of SAPO-34 for water and ethanol, allowing butanol recovery with high purity. This experimental procedure involves butanol separation from the fermented mixture vapor phase, followed by its purification. It is performed in three steps, as illustrated by Figure 3.1, and three main processes occurs in the columns: (A)

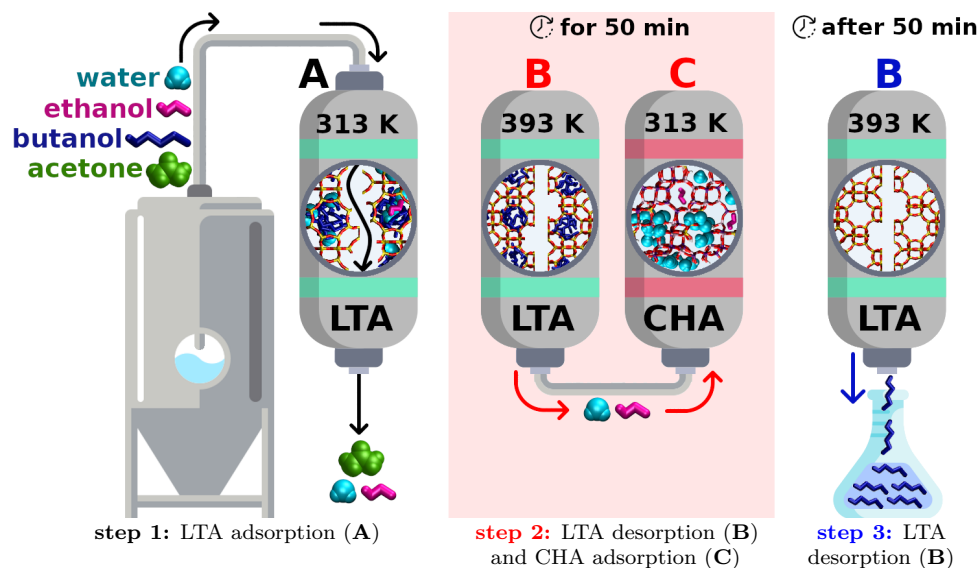


**Figure 3.1:** Scheme of the experimental setup for biobutanol recovery designed by Van der Perre et al. [1], illustrating the processes (A-C) that occur in each step.

first, the fermented vapor phase (mixture containing acetone, butanol, ethanol, and water) passes through an ITQ-29 (pure silica LTA) column at 313 K (during step 1, Figure 3.1). Butanol and small amounts of ethanol and water are adsorbed by ITQ-29, while acetone and remaining ethanol and water molecules flow through the column, being discarded. The acetone fraction present in the

vapor mixture is excluded by size from both employed zeolites, as their 8-ring dimensions ( $4.2 \times 4.2$  Å for LTA and  $3.8 \times 4.2$  Å for CHA) are smaller than the acetone kinetic diameter (4.7 Å) [1]; **(B)** second, the temperature of the ITQ-29 column is increased (393 K) to promote the desorption of its adsorbed content. During the first 50 minutes (step 2, Figure 3.1), ITQ-29 mainly desorbs ethanol and water. **(C)** The above desorbed gases are redirected by a stripping gas towards a CHA column (either silicate or silico-alumino-phosphate, SAPO, called, respectively SSZ-13 and SAPO-34), which operates at 313 K (also during step 2, Figure 3.1). Although SSZ-13 is not pure silica, albeit of a high Si/Al ratio [17], its name is usually employed, by extension and in the absence of a specific name, as a synonym of pure silica CHA. As confirmed by breakthrough experiments [1], ethanol and water are first desorbed from ITQ-29 and become adsorbed by the CHA material, while butanol remains adsorbed in ITQ-29. After 50 minutes of CHA column operation, this second column is disconnected from the system, and the desorbed content from ITQ-29 is butanol of high purity (step 3, Figure 3.1).

A computational simulation of this process is very convenient in order to try to improve this and other similar processes by, for instance, testing the effect of using a large variety of other zeolite topologies as well as chemical compositions, Si/Al ratios in aluminosilicate zeolites, or Si/(Si+Al+P) content in SAPOs. In the future, other effects such as the morphology and thickness of the crystals can be introduced as important variables to fine tune the process. By having performed a detailed experimental study [1], it is possible to benchmark our computational methodology and models. This methodology could be employed in order to design and simulate other related chemical engineering processes with separation purposes. Previous studies have assessed the suitability of materials for separation by only taking into account bulk models [18–23], although an increasing number of studies also include the effect of the external surface [24–26] and crystal morphology [27, 28], as well as crystal thickness [29, 30].

In this study we try to move along with recent studies, introducing sophisticated models resembling the experimental columns or nanosheets and also taking into account the engineering aspects such as the presence of three differentiated steps in the separation process, involving adsorption/desorption cycles, with different temperatures and materials. This requires not only an updated force field but also a unified approach for the Monte Carlo and Molecular Dynamics (MD) calculations, which are usually made in the literature using different force fields. For instance, adsorption isotherms will be calculated in the present study in order to find the equilibrium mixture of adsorbed butane, ethane and water in pure silica LTA. Various models will be compared with the experimental pure component adsorption isotherms [1], and the best model will be employed for the calcula-

tion of the mixture adsorption isotherms, considering the experimental ratio of butanol, ethanol and water in the fermented vapor-phase. The corresponding system at equilibrium (process A) should then be calculated using MD in order to find whether the kinetics corresponding to the second process (B, desorption of the adsorbed mixture at equilibrium) leads to a selective desorption of ethanol and water while butanol remains adsorbed. Also, the diffusion and preferential adsorption of desorbed ethanol and water molecules in the CHA material (process C) can be simulated with MD, where adsorbate affinity and dynamics in the zeolite or SAPO material can be further analyzed. MC and MD calculations employ different zeolite-adsorbate force fields because diffusivity of adsorbates cannot be accurately reproduced with MC potentials. Further, a significant flexibility can be observed in SAPO-34, enhancing the diffusion of large molecules through its channel system, a behavior that is less pronounced in its siliceous counterpart [31]. We have checked that force fields used in MC and MD lead to similar results (section A2, Appendix A). In summary, the aim of this study is to improve models and methods so that they can describe as accurately as possible the industrially relevant process of biobutanol recovery, from the ABE fermentation, based on the combined use of several zeolite materials.

## 3.2 Computational Methodology and Models

### 3.2.1 MC calculation of adsorption isotherms

The adsorption of butanol, ethanol and water in ITQ-29 was investigated through adsorption isotherms. Using the ITQ-29 crystallographic structure reported by Corma et al. in 2004 [32], a  $3 \times 3 \times 3$  cell was simulated ( $a = b = c = 35.6013 \text{ \AA}$ ,  $\alpha = \beta = \gamma = 90.0^\circ$ ). Pure component and mixture adsorption isotherms were computed by the Monte Carlo method, using RASPA package (version 2.0.38) [33]. Simulations sampling the grand-canonical ensemble were performed during  $8 \times 10^4$  initiation cycles and  $5 \times 10^5$  production cycles. During the simulations, four MC moves were considered, with the same probability: adsorbates could be randomly rotated, translated, fully reinserted in the simulation box, and inserted or deleted (so-called swap move). Of these moves, ‘swap’ starts with multiple first beads, and grows the remainder of the molecule using biasing, although the explicit Configurational-bias Monte Carlo move has not been used. Ewald summation method was used to handle long-range electrostatic interactions, as implemented in RASPA software. The nonbonded interactions were cut at  $12.0 \text{ \AA}$  and shifted, without tail corrections. Zeolite unit cells were replicated to ensure

that the simulation box size was larger than twice the cutoff distance in each direction.

The employed force field was successfully tested in similar systems previously [11, 16] and has also been validated in the present study using the experimental pure component adsorption isotherms of water, ethanol, and butanol in ITQ-29 [1] (further details in section A1, Appendix A). Butanol and ethanol were described by TRAPPE-UA (united atom) force field [34] and water molecules by TIP4P/2005 [35]. Zeolite-alcohol nonbonded interactions were taken from Martin-Calvo and co-workers [16], while zeolite-water were derived by Lorentz-Bethelot combination rules. The calculation of adsorption isotherms using Monte Carlo simulations in the Grand Canonical ensemble is usually performed considering a rigid framework [36]. Such an approach significantly reduces the computational cost, enabling a larger amount of MC cycles to ensure that the equilibrium is reached and the ensemble average properties of the system are computed correctly. More importantly, we only performed the MC simulations for a pure silica material (ITQ-29), which does not present significant flexibility, hence with little impact on the adsorption properties [36, 37]. Thus, the zeolite framework was kept rigid during the MC simulations, and its interaction with adsorbate molecules was considered only through zeolite oxygen atoms. Furthermore, the sodalite cages in LTA are not connected to the main zeolite channel system, and were blocked during the MC simulations to prevent an overestimation of the calculated uptake.

### ***3.2.2 Molecular Dynamics simulations***

The diffusional or adsorptive behavior of water, ethanol and butanol in ITQ-29, SSZ-13 and SAPO-34 has been assessed through MD simulations, performed with DL\_POLY Classic (version 2.20) [38]. All MD simulations employed the velocity Verlet integration scheme [39]. The NVT ensemble was sampled, with thermal control being carried out by a Nosé-Hoover thermostat [40]. A time step of 1.0 fs was used for unit cells containing silica frameworks, and a time step of 0.5 fs was used for SAPO-34 structure. SAPO materials are more flexible than, in general, silica zeolites, and the resulting larger bond elongations need to be evaluated over shorter periods of time, hence the shorter time step. The simulations were computed until the processes of interest could be captured, also taking into account the computational resources available. The initial configurations were equilibrated during 20 ps, before computing the production run. During the simulations, Ewald sums were employed for the long-range Coulombic interactions, and a cutoff of 9.0 Å was applied for the van der Waals interactions. The adsorbates were modeled by the same force fields previously employed in the MC simulations (TIP4P/2005 [35] for water and TRAPPE-UA for alcohol [34] molecules),

whereas flexible zeolite and SAPO frameworks were described through the force field described in Ghysels et al. [41] force field, with modifications to improve the stability of AIPO and SAPO-34 structures containing surface (terminal) OH groups, discussed in detail in Section 3.2.5.

As illustrated by Figure 3.2a, all MD simulation unit cells contain two unconnected reservoirs across the crystallographic  $c$  direction (R1 and R2, divided by an attractive or repulsive wall, depending on the simulation), and zeolite/SAPO materials were simulated by converting the bulk MC model into a nanosheet with surface OH groups at both sides facing the reservoirs. In the remaining directions (crystallographically  $a, b$ ), zeolite periodicity was maintained. As the crystal lat-

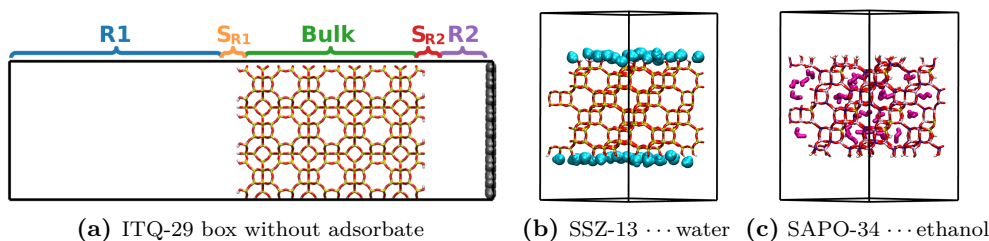


**Figure 3.2:** Example of an MD simulation unit cell without adsorbate molecules (a), where R1 and R2 are the reservoirs,  $S_{R1}$  and  $S_{R2}$  are the OH external surfaces in contact with the respective reservoirs, and the bulk region corresponds to the zeolite framework. The repulsive (or attractive) wall is depicted in gray. Example of optimized structures considered for the adsorption energy ( $\Delta E^{ads}$ ) calculation of molecules adsorbed in the external surface (b) or in the bulk (c).

tice is flexible during the MD simulations, the SSZ-13 trigonal structure came from the IZA database ( $a = b = 13.675 \text{ \AA}$ ,  $c = 14.767 \text{ \AA}$ ,  $\alpha = \beta = 90.0^\circ$ ,  $\gamma = 120.0^\circ$ ) [42]. Based on a  $2 \times 2 \times 2$  cell, the SSZ-13 external surface was generated in the  $c$  crystallographic direction, leading to a nanosheet approximately  $28.0 \text{ \AA}$  thick. The SAPO-34 structure was obtained from previous works [41, 43]. Isolated Brønsted acid sites were included in the structure, respecting the experimental Si/Al/P molar composition reported by Dai and co-workers [44], in which no significant numbers of Si islands are formed. A  $2 \times 2 \times 2$  unit cell was generated with the chemical composition of  $\text{Si}_{24}\text{Al}_{144}\text{P}_{120}\text{O}_{576}\text{H}_{24}$  and with cell parameters of  $a = 27.4095 \text{ \AA}$ ,  $b = 27.5039 \text{ \AA}$ ,  $c = 29.5008 \text{ \AA}$ ,  $\alpha = 89.9749^\circ$ ,  $\beta = 90.0198^\circ$ , and  $\gamma = 119.8945^\circ$  (CIF available in section A6, Appendix A). After the generation of the external surface, a  $\sim 28.0 \text{ \AA}$  thick SAPO-34 nanosheet was also generated. Finally, the same crystallographic structure of ITQ-29 employed for MC calculations [32] was used in the MD simulations. Starting with the  $3 \times 3 \times 3$  cell, an ITQ-29 nanosheet was constructed with a thickness of approximately  $50.0 \text{ \AA}$ .

### 3.2.3 Systems to be simulated using MD resembling biobutanol recovery

As indicated above, process A was not simulated through MD. The dynamical behavior of ITQ-29 desorption, process B, was analyzed by the MD method. Both reservoirs were initially empty, and zeolite bulk contains the uptake obtained at the end of the Monte Carlo simulation corresponding to the adsorption of the fermented vapor mixture in ITQ-29 at 313 K. As the system evolves, ethanol and water become desorbed from ITQ-29 and occupy reservoirs R1 and R2. The simulation was performed at 393 K during 165 ns. During the experiment, the molecules that migrate from ITQ-29 bulk to the surface are removed by the stripping gas toward the second column. In order to simulate this experimental procedure, the wall that delimits R1 and R2 reservoirs was modeled with an attractive potential for the adsorbates. Therefore, when a molecule desorbs from the zeolite towards the center of the reservoirs (moves away at least 5.0 Å far from the zeolite surface), it becomes attracted by the wall, remaining in contact with it (within 2.5 Å) until the end of the simulation. This ensures that reservoirs (R1 and R2) remain almost empty, resembling the experiments using the stripping gas.

In continuation of process B, the adsorptive process C was simulated by systems containing the fully desorbed phase from ITQ-29, initially located at R1 reservoir, and exposed to either SSZ-13 or SAPO-34 (CHA) nanosheets in order to compare their relative adsorption efficiency. The aim is to observe a selective adsorption of water and ethanol in CHA, while butanol remains in the gas phase (reservoir) and can be recovered with high purity. The MD simulations run at 313 K for 250 and 200 ns, respectively.

In process C, water adsorption by CHA nanosheets is a particularly important issue. Over the computed trajectories, the water content in each region of the simulation box was calculated (based on geometrical criteria) so that the water uptake at the CHA material can be quantified. This is also done for ethanol and butanol molecules, although the first is a minor component, and only a small fraction of the latter is adsorbed. A molecule was classified as being at the zeolite surface ( $S_{R1}$  or  $S_{R2}$ ) if at least a weak hydrogen bond (HB) with a silanol group was detected, whose strength could be estimated through well-established geometric criteria [45]. The selected criteria were distance between HB donor (D) and acceptor (A) closer than 4.0 Å, distance  $A \cdots H \leq 3.2 \text{ \AA}$ , and angle  $D-H \cdots A$  at least  $90^\circ$  (being stronger at  $180^\circ$ ). Consequently, the remaining molecules located inside and outside the framework composed *bulk* and *reservoir* ( $R_1$  or  $R_2$ ) loadings, respectively.

### 3.2.4 Summary of calculations performed

Along this study, it is important not only to employ an accurate force field and to design realistic models of the nanosheets resembling the experimental columns, but also to integrate the different process steps so that they all describe the experimental procedure. This way, we summarize below (Table 3.1) all details of each calculation in order to facilitate an overall comparison to the real process.

**Table 3.1:** Summary of calculations, the respective experimental process simulated, and employed conditions.

calculation	MC1 (Figure 3.3)	MD1 (Figure 3.4)	MD2 (Figure 3.5a-c)	MD3 (Figure 3.5d-f)
step (Figure 3.1)	1	2	2	2
process (Figure 3.1)	A	B	C	C
material	ITQ-29	ITQ-29	SSZ-13	SAPO-34
T (K)	313	393	313	313
initial	zeo is initially empty, and R1 contains the fermented vapor mixture ( <b>mix1</b> ): 0.07 butanol : 0.01 ethanol : 0.92 water	zeo = <b>mix2</b> R1 = R2 = empty	R1 = <b>mix2</b> R2 = empty zeo = empty	R1 = <b>mix2</b> R2 = empty zeo = empty
final	zeo contains <b>mix2</b> : 0.71 butanol : 0.01 ethanol : 0.28 water	R1+R2 containing ethanol and water; zeo containing butanol	zeo adsorbs 2.5% of butanol and 39% of the water initially contained in R1	zeo adsorbs 2.5% of butanol and 78% of the water initially contained in R1
MD time (ns)	not MD calculation	165	250	200
aim	check selective adsorption of butanol by ITQ-29	check preferential desorption of water and ethanol from ITQ-29	check preferential adsorption of water and ethanol by SSZ-13	check preferential adsorption of water and ethanol by SAPO-34

### 3.2.5 General force field for zeolite/SAPO materials with surface OH groups

The general force field presented here is an extension from previous work [41, 46, 47] to describe flexible zeolite, AlPO, and SAPO bulk structures, as well the respective nanosheets with surface OH groups. Electrostatic and van der Waals interactions were defined by the Coulomb (eq. 3.1) and Lennard-Jones (LJ, eq. 3.2) potential, respectively. Such parameters (Tables 3.2 and 3.3) were taken from the original works of Ghysels et al. [41] (pure silica and SAPO frameworks with Brønsted sites), and Bushuev and Sastre (surface OH charges [46] and their three-body potentials [47]). Remaining LJ parameters between surface OH and zeolite atoms were derived by Lorentz-Berthelot mixing rules. Furthermore, O–H bonds (Brønsted sites and surface groups) were described by a Morse potential (eq. 3.3), with  $E_0 = 7.0525$  eV,  $k = 2.1986$  Å<sup>-1</sup>, and  $r_0 = 0.94760$  Å [41].

$$U^{Coulomb}(r_{ij}) = \frac{q_i q_j}{4\pi\epsilon_0 r_{ij}} \quad (3.1)$$

$$U^{LJ}(r_{ij}) = \left( \frac{A}{r_{ij}^{12}} \right) - \left( \frac{B}{r_{ij}^6} \right) \quad (3.2)$$

**Table 3.2:** Species described by the force field, with respective Atom Type (AT) and charges (eq. 3.1). <sup>a</sup> taken from ref. [41], and <sup>b</sup> taken from ref. [46].

species	AT	charge (e <sup>-</sup> )
Zeolite silicon <sup>a</sup>	Si	2.100
Zeolite aluminum <sup>a</sup>	Al	1.575
Zeolite phosphorus <sup>a</sup>	P	2.625
Zeolite oxygen <sup>a</sup>	O2	-1.050
	O1	-0.725
Zeolite Brønsted site <sup>a</sup>	H1	0.200
	O3	-0.950
Zeolite surface hydroxyl <sup>b</sup>	H3	0.425

$$U^{morse}(r_{ij}) = E_0[\{1 - \exp[-k(r_{ij} - r_0)]\}^2 - 1] \quad (3.3)$$

When using the original parameters for SAPO frameworks with OH surface groups in the MD simulations, the flexible structure of the zeolite presented certain distortions that were absent when a completely periodic system was optimized or simulated through MD, mainly due to the removed constraints along the crystallographic *c* direction, where the surface was generated. These distortions were related to a significant flexibility of tetrahedral units near the surface containing Al or P centers. In the original parameterization, three-body potentials (eq. 3.4) did not take into account the O–Al–O or O–P–O terms. However, in the less rigid nanosheet considered here, the need for those terms became evident. Therefore, in this general version of the force field, both O–Al–O and O–P–O three body interactions were added, while the force constants ( $k_\theta$ ) for Si–O–Si and P–O–Al terms were properly adjusted to be consistent with the new terms (Table 3.4).

$$U^{three-body}(\theta_{ijk}) = k_\theta(\theta_{ijk} - \theta_0)^2 \quad (3.4)$$



**Table 3.3:** Lennard-Jones parameters (eq. 3.2) for intermolecular interactions. <sup>a</sup> taken from ref. [41], <sup>b</sup> derived by Lorentz-Berthelot combination rules of parameters from refs. [41] and [46], and <sup>c</sup> taken from ref. [46].

pair	A (eV/Å <sup>12</sup> )	B (eV/Å <sup>6</sup> )
Si ... Si <sup>a</sup>	0.5601	0.0004
Si ... O2 <sup>a</sup>	172.6992	0.1086
Si ... O1 <sup>a</sup>	218.1689	0.9583
Si ... O3 <sup>b</sup>	124.1989	0.1044
Si ... Al <sup>a</sup>	1.0153	0.0005
Si ... P <sup>a</sup>	0.5403	0.0003
O2 ... O2 <sup>a</sup>	26 877.9664	29.8306
O2 ... O1 <sup>a</sup>	26 877.9664	29.8306
O2 ... O3 <sup>b</sup>	27 097.4251	28.4516
O2 ... Al <sup>a</sup>	342.4165	0.0786
O2 ... P <sup>a</sup>	118.3529	0.093
O1 ... O1 <sup>a</sup>	26 877.9664	29.8306
O1 ... O3 <sup>b</sup>	27 097.4251	28.4516
O1 ... Al <sup>a</sup>	259.9127	0.0786
O1 ... P <sup>a</sup>	118.3529	0.093
O3 ... O3 <sup>c</sup>	27 290.9346	27.1226
O3 ... Al <sup>b</sup>	236.009	0.1309
O3 ... P <sup>b</sup>	120.743	0.0908
Al ... Al <sup>a</sup>	1.8405	0.0006
Al ... P <sup>a</sup>	0.9794	0.0004
P ... P <sup>a</sup>	0.5211	0.0003

**Table 3.4:** Three-body potential (eq. 3.4) parameters: force constant ( $k_\theta$ ) and equilibrium angle ( $\theta_0$ ). <sup>a</sup> taken from ref. [41], <sup>b</sup> this work, <sup>c</sup> taken from ref. [47]. Generic atom types Ox ( $x=1,2,3$ ), Oy ( $y=2,3$ ), Oz ( $z=1,2$ ) and T=Si,Al,P.

three-body	new ff		old ff	
	$k_\theta$ (eV/rad <sup>2</sup> )	$\theta_0$ (°)	$k_\theta$ (eV/rad <sup>2</sup> )	$\theta_0$ (°)
Ox-Si-Ox <sup>a</sup>	1.4944	109.470	1.4944	109.470
Ox-Al-Ox <sup>b</sup>	0.4747	109.470	-	-
Oy-P-Oy <sup>b</sup>	0.6998	109.470	-	-
Si-O2-Si <sup>b</sup>	3.1731	142.712	1.5509	142.712
Si-Oz-Al <sup>a</sup>	1.7875	140.831	1.7875	140.831
P-O2-Al <sup>b</sup>	3.8604	139.689	2.0468	139.689
H3-O3-T <sup>c</sup>	1.3000	100.000	1.3000	100.000

For the new parameters obtained, Al and P tetrahedra are more flexible (smaller  $k_\theta$  values) than the Si ones, a logic result that corresponds to the tetrahedral stability of each element [48]. It is well known that high silica zeolites are widely employed as well due to their high hydrothermal stability [49] and that there is less thermal stability in AIPOs than in SAPO materials [50].

In order to evaluate the capability of the new parameters to reproduce crystallographic structures, the old and new force field definitions were employed, using lattice energy minimization calculations, to obtain structural parameters of zeolites whose experimental results are available in the literature (Table 3.5). A

**Table 3.5:** Percent of deviation ( $\% \Delta$ ) from experimental unit cell volume (V) and parameters ( $a$ ,  $b$ ,  $c$ ,  $\alpha$ ,  $\beta$  and  $\gamma$ ) in the optimized structures with the new and old [41] force field (ff). \* Structure determination corresponds to  $\text{Al}_4\text{SiP}_3\text{HO}_{16} \cdot n\text{H}_2\text{O}$ .

ff	exp. structure	$\% \Delta V$	$\% \Delta a$	$\% \Delta b$	$\% \Delta c$	$\% \Delta \alpha$	$\% \Delta \beta$	$\% \Delta \gamma$
new	AIPO-18 (1991) [51]	3.6	1.6	0.8	1.1	0.0	0.0	0.0
	AIPO-34 (1985) [52]*	3.1	1.0	1.0	1.1	0.0	0.0	0.0
	SSZ-13 (1998) [53]	2.6	1.2	1.2	0.2	0.0	0.0	0.0
	ITQ-29 (2004) [32]	1.7	0.6	0.6	0.6	0.0	0.0	0.0
	ITQ-29 (2012) [54]	2.1	0.7	0.7	0.7	0.0	0.0	0.0
old	AIPO-18 (1991) [51]	5.0	2.1	1.3	1.6	0.0	0.0	0.0
	AIPO-34 (1985) [52]*	4.5	1.4	1.4	1.6	0.0	0.0	0.0
	SSZ-13 (1998) [53]	3.2	1.3	1.3	0.5	0.0	0.0	0.0
	ITQ-29 (2004) [32]	2.6	0.9	0.9	0.9	0.0	0.0	0.0
	ITQ-29 (2012) [54]	3.0	1.0	1.0	1.0	0.0	0.0	0.0

fully periodic unit cell was considered, and geometry optimizations at constant pressure were performed with GULP software (version 4.3.2) [55]. As summarized in Table 3.5, for both silica and AIPO materials, geometries optimized with the new version of the force field presented smaller deviations from the experimental unit cell parameters and volumes, when compared with the old force field. Thus, suggested modifications not only improved the accuracy of the silica and AIPO structures but also, more importantly, added generality to the force field, allowing to simulate flexibility and dynamics of silica, AIPO, and SAPO materials containing surface OH groups. This effort adds to previous studies in which the role of surface silanol groups on diffusivity and catalytic properties has been put forward [56–61], while the role of other terminal OH groups has been suggested [62, 63].

Surface effects that can hopefully be better described by the updated force field have been long described to have a large effect on the dynamics of occluded molecules [30, 64–67]. In spite of recent combined computational and experimen-

tal efforts trying to shed light on the existence of surface barriers for diffusing molecules, this is still an open question that needs further studies [68–77].

Finally, during long MD simulations, a few occurrences of surface O–H bond breaking could be observed, caused by a strong electrostatic interaction with neighboring OH groups. The probably excessive ionic character of this H–O bond ( $q(\text{O}) = -0.950 e^-$  and  $q(\text{H}) = 0.425 e^-$ , Table 3.2) was then balanced by the addition of a repulsive Buckingham potential (eq. 3.5), applied between O $\cdots$ H atoms not directly bonded to each other: O $x\cdots$ H $z$  (where  $x=1,2,3$  and  $z=1,3$ ), with  $A = 311.97 \text{ eV}$ ,  $\rho = 0.25 \text{ \AA}$  and  $C = 0.0 \text{ eV \AA}^6$ . These parameters were taken from Schröder and co-workers [78], indicating that this strategy has already been employed successfully.

$$U^{buck}(r_{ij}) = A \exp\left(-\frac{r_{ij}}{\rho}\right) - \left(\frac{C}{r_{ij}^6}\right) \quad (3.5)$$

### 3.2.6 Calculation of adsorption energies

The bulk and surface adsorption interactions between mixture components (guests) and zeolite/SAPO frameworks were numerically estimated in terms of the average adsorption energy ( $\overline{\Delta E^{ads}}$ ), as defined by Equation 3.6, where  $E_{zeo\cdots guests}$  is the single-point energy of zeolite $\cdots$ guests complex,  $E_{zeo}$  corresponds to the single-point energy of the zeolite isolated, and  $n_{guests}$  is the amount of adsorbate molecules. The single-point energy of the guests isolated ( $E_{guests}$ ) is composed of their intramolecular ( $E_{guests}^{intra}$ ) and intermolecular ( $E_{guest\cdots guest}$ ) energy components. Thus, by subtracting only the intramolecular guests contribution in Equation 3.6,  $\overline{\Delta E^{ads}}$  will take into account both zeo $\cdots$ guests and guest $\cdots$ guest intermolecular interactions. The effect of intermolecular guest–guest interactions increases at large loading, being a large part in the adsorption energy [19].

$$\overline{\Delta E^{ads}} = \frac{E_{zeo\cdots guests} - (E_{zeo} + E_{guests}^{intra})}{n_{guests}} \quad (3.6)$$

Thus, for each adsorbate (butanol, ethanol, or water) and framework (ITQ-29, SSZ-13 or SAPO-34) interacting complex, a box containing water or alcohol molecules adsorbed either in the bulk or surface was simulated by the MD methodology during 10 ns. The final configuration was split into two configurations, containing the zeolite and adsorbate over the surface or bulk (as illustrated by Figure 3.2b,c, respectively). For each configuration, an energy minimization was

performed at constant volume, using GULP software and the optimized structures (Figure A9, Appendix A) were considered in order to calculate  $\overline{\Delta E^{ads}}$ .

### 3.3 Results and Discussion

#### 3.3.1 Process A) adsorption of ‘fermented vapor mixture’ in ITQ-29, 313 K

Adsorption isotherms were calculated in order to obtain information about the gas mixture compositions that can be adsorbed as a function of pressure at equilibrium. According to the previous study [1], the adsorbate pressures in the fermented vapor phase are 299 Pa of butanol, 50 Pa of ethanol, and 4220 Pa of water, giving a total pressure of 4569 Pa. By considering the mixture with molar fractions of 0.07 butanol/0.01 ethanol/0.92 water, the partial pressures simulated for each component when considering a total pressure of 4569 Pa are similar to the experimental ones: 4203.5 Pa (water), 45.7 Pa (ethanol), and 319.8 Pa (butanol). Mixtures with this composition ratio are what we call ‘fermented vapor mixture’ (mix1, Table 3.1) since this is the resulting gas phase mixture from the ABE process, as described in the Introduction.

Calculated pure component isotherms of butanol and ethanol were in close agreement with experimental results (Figure 3.3a), which is a good validation of the

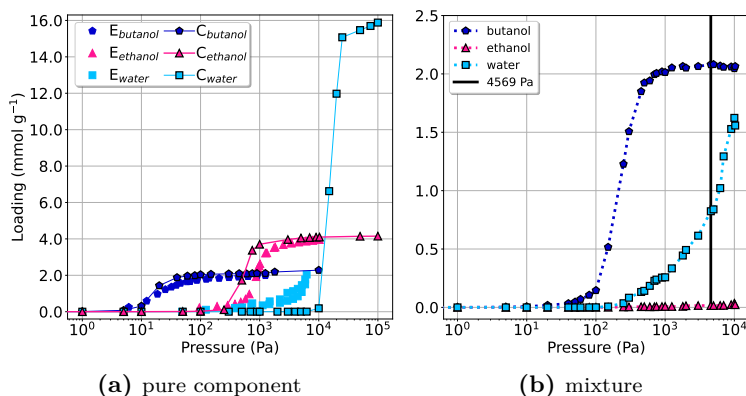


**Figure 3.3:** MC1 calculation (see Table 3.1). (a) Experimental (E) and calculated (C) pure component (butanol, ethanol, water) adsorption isotherms in ITQ-29 at 313 K. (b) Calculated adsorption isotherms of ‘fermented vapor mixture’ in ITQ-29 at 313 K, with the experimental pressure highlighted as a vertical black bar.

models and method employed. Regarding water, the results were also in reasonable agreement, although the step at pressure above  $10^3$  Pa shows some disagreement with experimental results. Several force fields were tested for water, with the best results obtained with TIP4P/2005. For the selected water model, the simulation predicts more pressure than the experiment for the zeolite to start adsorbing. However, very similar effects appear with a whole series of tested potentials (sections A1 and A2 of Appendix A). Various factors involving water behavior in zeolite micropores make it difficult to provide a simple and accurate modeling. For instance, the presence of defects in hydrophobic frameworks, and the changes in water dipole moment when confined in the pores, requires a more complex description [79] (with polarization and functional forms that are usually not available in the software packages), beyond our study.

Considering the fermented vapor mixture (0.07 butanol/0.01 ethanol/0.92 water and a total pressure of 4569 Pa, black line of Figure 3.3b), ethanol uptake is considerably low ( $0.015 \text{ mmol}\cdot\text{g}^{-1}$ ) as it corresponds to its relative low pressure in the initial mixture (50 Pa). The concentration of the adsorbed mixture at equilibrium is 0.71 butanol/0.01 ethanol/0.28 water, showing a butanol concentration 10 times larger than the initial mixture and a water content reduced by 70%, demonstrating that ITQ-29 structure is well suited for the butanol separation step. The higher affinity of ITQ-29 for butanol molecules is also highlighted by its  $\overline{\Delta E^{ads}}$  value. The adsorption energy of butanol in the bulk is approximately 20 and 13 kJ/mol more stabilizing than those of water and ethanol, respectively (Table 3.6).

**Table 3.6:** Adsorption energy ( $\overline{\Delta E^{ads}}$ ) of adsorbates in the bulk or external surface of studied frameworks, in kJ/mol. More details in section A5, Appendix A.

zeolite	guest	$\overline{\Delta E^{ads}}$ (bulk)	$\overline{\Delta E^{ads}}$ (surface)
ITQ-29	butanol	-84.3	-72.0
	ethanol	-71.1	-66.7
	water	-64.6	-42.7
SSZ-13	butanol	-83.7	-77.7
	ethanol	-57.6	-66.8
	water	-45.4	-57.0
SAPO-34	butanol	-79.2	-74.7
	ethanol	-68.1	-72.2
	water	-62.6	-66.2

### 3.3.2 Process B) selective desorption of water and ethanol in ITQ-29, 393 K

Once ITQ-29 zeolite has selectively adsorbed butanol, plus water and ethanol (end of process A), the temperature is increased (from 313 to 393 K) and the desorption cycle starts (process B). The preferential desorption of water and ethanol from ITQ-29 bulk is expected from their weaker adsorption energies (Table 3.6). The MD simulation of ITQ-29 desorption was done using as initial geometry the final configuration from the previous (process A) MC calculation, corresponding to the adsorption of the fermented vapor mixture (Figure 3.4a, 81 butanol, 1 ethanol, and 32 water molecules, referred to as mix2 in Table 3.1).

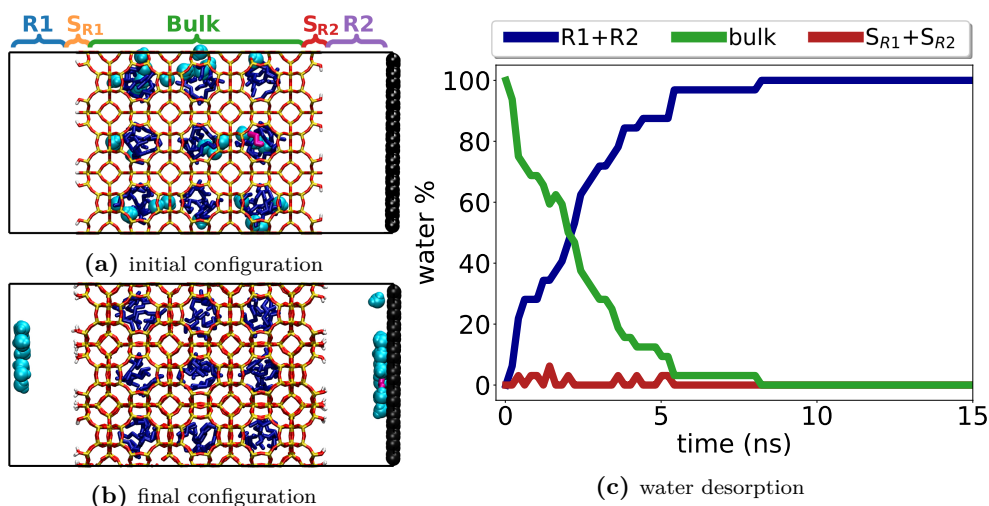


**Figure 3.4:** MD1 calculation (see Table 3.1). Snapshots from MD simulation of vapor mixture desorption in ITQ-29 nanosheet with (a,b) attractive wall (right end of cell, in black) at 393 K. Initial configuration contains 81 butanol, 1 ethanol, and 32 water molecules adsorbed. (c) %water desorption during the simulation.

As experimentally, due to the continuous flux of a stripping gas redirecting the desorbed molecules to the next column (CHA material), the equilibrium is shifted and desorption is favored. This is confirmed by the MD simulation (Figure 3.4b) containing an attractive wall that removes adsorbate molecules from R1 and R2 central regions. All water molecules were desorbed from ITQ-29 at 8.7 ns, and the only ethanol molecule also desorbed at 5.2 ns, while butanol molecules remained in the bulk until the end of the simulation (165 ns). This fast desorption of water and ethanol is in agreement with the experimental breakthrough curves [1]. The

experimental timescale of water and ethanol desorption from ITQ-29 (50 minutes) is impossible to reach by the current simulation methods. However, our nanosheet is only a few nm thick, while the experimental particles are usually on the order of  $\mu\text{m}$  thick ( $\times 1000$  factor). As a logical consequence, the desorption process could be seen in a few ns of simulation, corresponding to several minutes in the experiments. On the other hand, any butanol molecule was desorbed during the time simulated, indicating that our model is able to successfully simulate the preferential desorption of water and ethanol and that butanol desorption is a totally independent process. Furthermore, the complete desorption of butanol is a slower process due to its slow diffusion and stronger adsorption energy in ITQ-29 bulk ( $\overline{\Delta E^{ads}} = -84.3$  kJ/mol, Table 3.6).

### 3.3.3 Process C) selective adsorption of water and ethanol in CHA materials, 313 K

Simultaneously with process B, the desorbed vapor from ITQ-29 goes to the CHA material, and a second adsorption process (C) takes place. Here, the chemical composition of the second column and its affinity for ethanol and water play an important role.

In the initial configuration of the simulation boxes (Figure 3.5a,d), R1 contains what we call ‘mix2’ vapor mixture (Table 3.1), which corresponds to the total amount of molecules adsorbed by ITQ-29, which we multiply 2 times in order to have a larger ensemble (162 butanol, 2 ethanol, and 64 water molecules). Strictly, not all butanol will be in contact with the CHA nanosheet since process (C) lasts only 50 minutes, and butanol molecules are released after approximately 150 minutes of the ITQ-29 desorption process (B) [1]. However, by considering here all butanol, it will be possible to estimate, by having a larger sampling, if CHA nanosheets do really have the capacity to exclude butanol (as aimed) from the adsorbed molecules. In other words, this will be a stringent test to check how good are CHA nanosheets (SSZ-13 and SAPO-34) to selectively capture water and ethanol (Figure 3.5b,e).

The higher hydrophilicity of SAPO-34 material was clearly evidenced by the simulations, which reached a bulk+surface adsorption of 78% of the water molecules present after 200 ns, without still reaching equilibrium, hence suggesting that more water can be captured if the simulation is extended longer (green line of Figure 3.5f). Contrarily, the equilibrium could be reached after 40 ns of the simulation with SSZ-13 (green line of Figure 3.5c), showing a much lower performance (bulk+surface water adsorption of 39%) than SAPO-34. For both zeolites, the surface adsorption accounted for approximately 20% of the water content, being

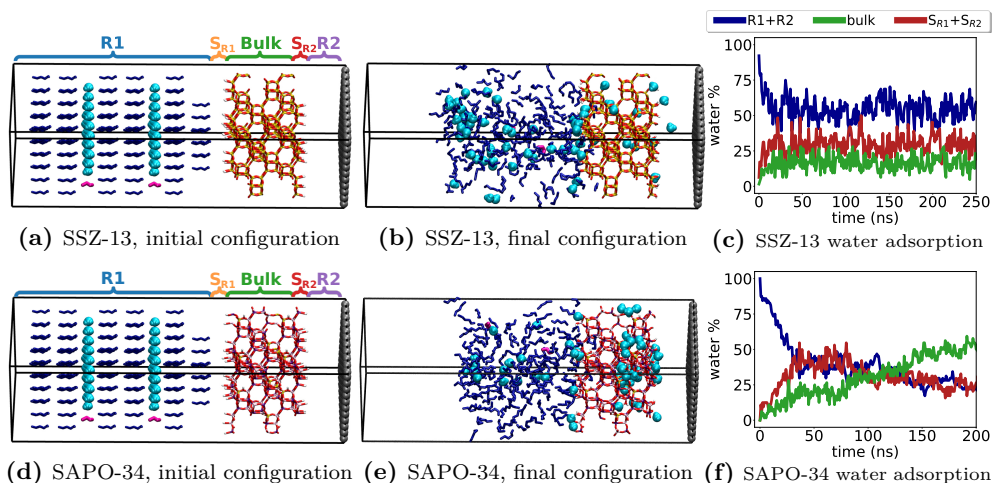


**Figure 3.5:** MD2 (top) and MD3 (bottom) calculations (see Table 3.1). Snapshots from MD simulations of selective adsorption of water and ethanol in SSZ-13 (a,b) and SAPO-34 (d,e) nanosheets, at 313 K. In the simulations, R1 contains initially 162 butanol, 2 ethanol and 64 water molecules. A repulsive wall (right end of the cell, in gray) separates R1 from R2. %Water adsorption over time for simulations with SSZ-13 (c) or SAPO-34 (f).

limited by the amount of terminal OH available for HB interactions. Concerning only the bulk adsorption, SAPO-34 superior adsorption of water is directly related with the larger charge separation in SAPO-34 than in silica zeolite, as well as the acid sites present in the SAPO-34 structure [80].

All ethanol and most butanol molecules were located in R1 or interacting with the surface ( $S_{R1}$ ). At the end of both simulations, only 2.5% of the butanol became adsorbed in the bulk. This illustrates the slower diffusion (uptake) of butanol when compared with water molecules (Figure 3.5b,e), in agreement with previous experimental observations showing that butanol molecules are almost fully excluded from SAPO-34 pores [15]. On the other hand, the absence of ethanol uptake in both CHA materials is a consequence of its small fraction in the ‘mix2’ mixture (see Table 3.1), and hence, no reliable data can be given for ethanol, although a behavior similar to water can be expected.

The magnitude of  $\overline{\Delta E^{ads}}$  increases with the size of the molecule adsorbed on SSZ-13, SAPO-34, or ITQ-29 (butanol > ethanol > water, Table 3.6), according to the amount of atoms taking part in short- and long-range interactions. This trend is observed for both surface and bulk adsorption. For the smaller and more polar guests (water and ethanol), the surface adsorption at SSZ-13 and SAPO-



34 leads to a greater stabilization when compared with the bulk, due to the greater availability of OH groups in the surface to establish HBs, but this effect is only observed at low loading. This can be seen from the results of Table A4 if the guest-guest contribution is subtracted from the total adsorption energy, leading to values (for water in ITQ-29) of -24.4 kJ/mol (surface) and -12.0 kJ/mol (bulk). The same effect is observed for ethanol in ITQ-29. The above-mentioned preferential affinity of polar molecules, such as water, to the external surface of zeolite nanosheets has already been reported by Farzaneh and collaborators for silica materials [10]. Their study highlighted that the presence of OH groups in the structure, as well as the external surface of the nanosheets, indicates regions of low selectivity for butanol as a significant content of water can be found in both regions, in particular the surface [10]. For water and ethanol in SSZ-13 and SAPO-34, this trend is also observed even at large water loadings, with values in Table 3.6 indicating a larger adsorption energy for water and ethanol in the surface than in the bulk. Some values in Table 3.6 may seem surprising, such as similar water adsorption energy in bulk ITQ-29 and SAPO-34, but this is due to the different weight of guest-guest interactions. If we only take the zeo-guest contributions (Table A4), the larger hydrophilicity of SAPO-34 leads to a stronger adsorption (-27.4 kJ/mol) than for ITQ-29 (-12.1 kJ/mol). The different loadings and contributions to the adsorption energies are more detailed in section A5, Appendix A.

Owing to the difficulty to fine-tune water force fields to reproduce adsorption energies, it is convenient to compare our calculated values with experimental values as well as with other calculated values. Various experimental and simulated values for the heat of adsorption of water in SAPO-34 can be found in the literature, such as -61.8 [81, 82], -60.3 [83], -65.8 [84], and -64.8 [85] kJ/mol, obtained at similar loading than our calculations. Taking into account that the values of heat of adsorption differ from adsorption energies by  $RT$  ( $\Delta H^{ads} = \Delta E^{ads} - RT$ ), which is 2.6 kJ/mol at 313 K, it can be considered that our results ( $\Delta E^{ads} = -62.6$  kJ/mol, bulk, and -66.2 kJ/mol, surface, Table 3.6) are in reasonable agreement with the experimentally reported.

### **3.4 Conclusions**

The combination of a general force field plus computational models including zeolite frameworks with the external surface and reservoirs, mimicking nanosheets, seems to be capable of reproducing the essential behavior of the experimental process of biobutanol recovery. Since the simulations allow quantifying the results in terms of each component selectivity, this opens the way to compare computationally the performance of analogous systems by modifying not only the chemical composition of each nanosheet, but also the effect of the zeolite structure by testing other frameworks. Although this can not be done in a fast way, since the simulations are time-consuming, possible ways to speed up the calculations are underway and may allow a more systematic treatment of similar separation processes based on using multiple zeolite nanosheets and different adsorption/desorption process steps. Recent works have been reported associating machine learning models with molecular simulations as an alternative to reduce the computational cost and allow a broader exploration of the studied systems (involving different materials and types of mixtures) [86–90]. For instance, Sun and co-workers combined deep neural networks and canonical Gibbs ensemble Monte Carlo simulations to study the drying process of mixtures containing 1,4-butanediol or 1,5-pentanediol in water, as well as 1,5-pentanediol and ethanol by silica MFI and LTA zeolites [90].

From our computational study, some relations between zeolite features and process performance can be highlighted. For instance, specific silica materials with an appropriate pore size allow the selective adsorption of butanol, with impurities of ethanol and water, as well as the exclusion by size of acetone. Likewise, specific SAPO materials, highly hydrophilic, allow the selective adsorption of ethanol and water desorbed from silica material upon heating. This allows butanol of high purity to remain adsorbed in the silica material. Further heating of this material allows recovering butanol of high purity.

For the studied separation process, ITQ-29 allowed the entrance of butanol, ethanol and water, but the larger adsorption energy of the largest molecule (butanol) allows its selective adsorption in the first step. A combination of two subsequent steps follow with an influence of the ITQ-29 desorption kinetics, leading to the faster desorption of water and ethanol, which become selectively adsorbed in the hydrophilic SAPO-34 material. Once the fast process of water and ethanol desorption from ITQ-29 and simultaneous adsorption in SAPO-34 is completed, butanol of high purity remains in ITQ-29 and can be recovered.

### **Acknowledgements**

This work was supported by Generalitat Valenciana (GVA) predoctoral fellowship GRISOLIAP/2019/084. We also thank GVA for PROMETEO/2021/077 project and ASIC-UPV and SGAI-CSIC for the use of computational facilities.

### Supporting Information

The Supporting Information is available at Appendix A. Validation of the force fields employed on Monte Carlo and Molecular Dynamics simulations. Further details on mixture adsorption isotherms. Size and composition of Molecular Dynamics simulation boxes. Optimized Geometries of adsorbates ··· framework complexes and further discussion about adsorption energy calculation. CIF structure of SAPO-34 used in the calculations.

### References

- [1] Van der Perre, S.; Gelin, P.; Claessens, B.; Martin-Calvo, A.; Remi, J. C. S.; Duerinck, T.; Baron, G. V.; Palomino, M.; Sánchez, L. Y.; Valencia, S.; Shang, J.; Singh, R.; Webley, P. A.; Rey, F.; Denayer, J. F. M. Intensified Biobutanol Recovery by Using Zeolites with Complementary Selectivity. *ChemSusChem* **2017**, *10* (14), 2968–2977. DOI: 10.1002/cssc.201700667.
- [2] Luque, R.; Herrero-Davila, L.; Campelo, J. M.; Clark, J. H.; Hidalgo, J. M.; Luna, D.; Marinas, J. M.; Romero, A. A. Biofuels: a Technological Perspective. *Energy Environ. Sci.* **2008**, *1* (5), 542–564. DOI: 10.1039/B807094F.
- [3] Huang, H.-J.; Ramaswamy, S.; Liu, Y. Separation and Purification of Biobutanol During Bioconversion of Biomass. *Sep. Purif. Technol.* **2014**, *132*, 513–540. DOI: 10.1016/j.seppur.2014.06.013.
- [4] Abdehagh, N.; Tezel, F. H.; Thibault, J. Adsorbent Screening for Biobutanol Separation by Adsorption: Kinetics, Isotherms and Competitive Effect of Other Compounds. *Adsorption* **2013**, *19* (6), 1263–1272. DOI: 10.1007/s10450-013-9566-8.
- [5] Bowen, T. C.; Vane, L. M. Ethanol, Acetic Acid, and Water Adsorption from Binary and Ternary Liquid Mixtures on High-Silica Zeolites. *Langmuir* **2006**, *22* (8), 3721–3727. DOI: 10.1021/la052538u.

- [6] Oudshoorn, A.; van der Wielen, L. A. M.; Straathof, A. J. J. Adsorption Equilibria of Bio-based Butanol Solutions Using Zeolite. *Biochem. Eng. J.* **2009**, *48* (1), 99–103. DOI: 10.1016/j.bej.2009.08.014.
- [7] Shu, X.; Wang, X.; Kong, Q.; Gu, X.; Xu, N. High-Flux MFI Zeolite Membrane Supported on YSZ Hollow Fiber for Separation of Ethanol/Water. *Ind. Eng. Chem. Res.* **2012**, *51* (37), 12073–12080. DOI: 10.1021/ie301087u.
- [8] Águeda, V. I.; Delgado, J. A.; Uguina, M. A.; Sotelo, J. L.; García, . Column Dynamics of an Adsorption–Drying–Desorption Process for Butanol Recovery From Aqueous Solutions With Silicalite Pellets. *Sep. Purif. Technol.* **2013**, *104*, 307–321. DOI: 10.1016/j.seppur.2012.11.036.
- [9] Faisal, A.; Zhou, M.; Hedlund, J.; Grahn, M. Recovery of Butanol From Model ABE Fermentation Broths Using MFI Adsorbent: A Comparison Between Traditional Beads and a Structured Adsorbent in the Form of a Film. *Adsorption* **2016**, *22* (2), 205–214. DOI: 10.1007/s10450-016-9759-z.
- [10] Farzaneh, A.; DeJaco, R. F.; Ohlin, L.; Holmgren, A.; Siepmann, J. I.; Grahn, M. Comparative Study of the Effect of Defects on Selective Adsorption of Butanol from Butanol/Water Binary Vapor Mixtures in Silicalite-1 Films. *Langmuir* **2017**, *33* (34), 8420–8427. DOI: 10.1021/acs.langmuir.7b02097.
- [11] Gómez-Álvarez, P.; Noya, E. G.; Lomba, E.; Valencia, S.; Pires, J. Study of Short-Chain Alcohol and Alcohol–Water Adsorption in MEL and MFI Zeolites. *Langmuir* **2018**, *34* (43), 12739–12750. DOI: 10.1021/acs.langmuir.8b02326.
- [12] Wu, Z.; Peng, L.; Zhang, C.; Wang, X.; Liu, H.; Wang, J.; Yan, W.; Gu, X. Extraction of Butanol From ABE Solution by MFI Zeolite Membranes. *Sep. Purif. Technol.* **2020**, *242*, 116771. DOI: 10.1016/j.seppur.2020.116771.
- [13] Claessens, B.; Wittevrongel, G. R.; Rey, F.; Valencia, S.; Cousin-Saint-Remi, J.; Baron, G. V.; Denayer, J. F. M. Capturing Renewable Isobutanol From Model Vapor Mixtures Using an All-Silica Beta Zeolite. *Chem. Eng. J.* **2021**, *412*, 128658. DOI: 10.1016/j.cej.2021.128658.

- [14] Miyamoto, M.; Iwatsuka, H.; Oumi, Y.; Uemiya, S.; Van den Perre, S.; Baron, G. V.; Denayer, J. F. M. Effect of Core-Shell Structuring of Chabazite Zeolite With a Siliceous Zeolite Thin Layer on the Separation of Acetone-Butanol-Ethanol Vapor in Humid Vapor Conditions. *Chem. Eng. J.* **2019**, *363*, 292–299. DOI: 10.1016/j.cej.2019.01.106.
- [15] Cousin Saint Remi, J.; Baron, G.; Denayer, J. Adsorptive Separations for the Recovery and Purification of Biobutanol. *Adsorption* **2012**, *18* (5), 367–373. DOI: 10.1007/s10450-012-9415-1.
- [16] Martin-Calvo, A.; Van der Perre, S.; Claessens, B.; Calero, S.; Denayer, J. F. M. Unravelling the Influence of Carbon Dioxide on the Adsorptive Recovery of Butanol from Fermentation Broth Using ITQ-29 and ZIF-8. *Phys. Chem. Chem. Phys.* **2018**, *20* (15), 9957–9964. DOI: 10.1039/C8CP01034J.
- [17] Zones, S. I. Zeolite SSZ-13 and Its Method of Preparation. Patent US454453 8A pat., August, 1983.
- [18] Keyvanloo, Z.; Nakhaei Pour, A.; Moosavi, F.; Kamali Shahri, S. M. Molecular Dynamic Simulation Studies of Adsorption and Diffusion Behaviors of Methanol and Ethanol Through ZSM-5 Zeolite. *J. Mol. Graphics Model.* **2022**, *110*, 108048. DOI: 10.1016/j.jmgm.2021.108048.
- [19] Pérez-Botella, E.; Misturini, A.; Sala, A.; Palomino, M.; Corma, A.; Sastre, G.; Valencia, S.; Rey, F. Insights into Adsorption of Linear, Monobranched, and Dibranched Alkanes on Pure Silica STW Zeolite as a Promising Material for Their Separation. *J. Phys. Chem. C* **2020**, *124* (49), 26821–26829. DOI: 10.1021/acs.jpcc.0c08517.
- [20] Al-Bahri, O. H. S.; Borah, B.; Elzain, M.; Varanasi, S. R. Thermodynamics of Translational and Rotational Dynamics of C9 Hydrocarbons in the Pores of Zeolite-beta. *J. Mol. Graphics Model.* **2022**, *114*, 108188. DOI: 10.1016/j.jmgm.2022.108188.
- [21] Xiong, P.; He, P.; Qu, Y.; Wang, L.; Cao, Y.; Xu, S.; Chen, J.; Ammar, M.; Li, H. The Adsorption Properties of NaY Zeolite for Separation of Ethylene Glycol and 1,2-Butanediol: Experiment and Molecular Modelling. *Green Energy Environ.* **2021**, *6* (1), 102–113. DOI: 10.1016/j.gee.2019.12.006.

- [22] Guliants, V. V.; Huth, A. J. Force Fields for Classical Atomistic Simulations of Small Gas Molecules in Silicalite-1 for Energy-related Gas Separations at High Temperatures. *J. Porous Mater.* **2013**, *20* (4), 741–751. DOI: 10.1007/s10934-012-9649-z.
- [23] Krishna, R.; van Baten, J. M. Highlighting the Anti-Synergy Between Adsorption and Diffusion in Cation-Exchanged Faujasite Zeolites. *ACS Omega* **2022**, *7* (15), 13050–13056. DOI: 10.1021/acsomega.2c00427.
- [24] Madero-Castro, R. M.; Calero, S.; Yazaydin, A. O. The Role of Hydrogen Bonding in the Dehydration of Bioalcohols in Hydrophobic Pervaporation Membranes. *J. Mol. Liq.* **2021**, *340*, 117297. DOI: 10.1016/j.molliq.2021.117297.
- [25] Losada, I. B.; Grobas-Illobre, P.; Misturini, A.; Polaina, J.; Seminovski, Y.; Sastre, G. Separation of an Aqueous Mixture of 6-Kestose/Sucrose with Zeolites: A Molecular Dynamics Simulation. *Microporous Mesoporous Mater.* **2021**, *319*, 111031. DOI: 10.1016/j.micromeso.2021.111031.
- [26] Azizi, B.; Vessally, E.; Ahmadi, S.; Ebadi, A. G.; Azamat, J. Separation of CH<sub>4</sub>/N<sub>2</sub> Gas Mixture Using MFI Zeolite Nanosheet: Insights From Molecular Dynamics Simulation. *Colloids Surf., A* **2022**, *641*, 128527. DOI: 10.1016/j.colsurfa.2022.128527.
- [27] Pérez-Mendoza, M.; González, J.; Ferreiro-Rangel, C. A.; Lozinska, M. M.; Fairén-Jiménez, D.; Düren, T.; Wright, P. A.; Seaton, N. A. Pore-Network Connectivity and Molecular Sieving of Normal and Isoalkanes in the Mesoporous Silica SBA-2. *J. Phys. Chem. C* **2014**, *118* (19), 10183–10190. DOI: 10.1021/jp502390p.
- [28] Rezlerová, E.; Zukal, A.; Čejka, J.; Siperstein, F. R.; Brennan, J. K.; Lísal, M. Adsorption and Diffusion of C1 to C4 Alkanes in Dual-Porosity Zeolites by Molecular Simulations. *Langmuir* **2017**, *33* (42), 11126–11137. DOI: 10.1021/acs.langmuir.7b01772.
- [29] Knio, O.; Fang, H.; Boulfelfel, S. E.; Nair, S.; Sholl, D. S. Molecular Dynamics Investigation of Surface Resistances in Zeolite Nanosheets. *J. Phys. Chem. C* **2020**, *124* (28), 15241–15252. DOI: 10.1021/acs.jpcc.0c03572.

- [30] Zimmermann, N. E. R.; Zabel, T. J.; Keil, F. J. Transport into Nanosheets: Diffusion Equations Put to Test. *J. Phys. Chem. C* **2013**, *117* (14), 7384–7390. DOI: 10.1021/jp400152q.
- [31] Ferri, P.; Li, C.; Millán, R.; Martínez-Triguero, J.; Moliner, M.; Boronat, M.; Corma, A. Impact of Zeolite Framework Composition and Flexibility on Methanol-To-Olefins Selectivity: Confinement or Diffusion? *Angew. Chem. Int. Ed.* **2020**, *59* (44), 19708–19715. DOI: 10.1002/anie.202007609.
- [32] Corma, A.; Rey, F.; Rius, J.; Sabater, M. J.; Valencia, S. Supramolecular Self-assembled Molecules as Organic Directing Agent for Synthesis of Zeolites. *Nature* **2004**, *431*, 287–290. DOI: 10.1038/nature02909.
- [33] Dubbeldam, D.; Calero, S.; Ellis, D. E.; Snurr, R. Q. RASPA: Molecular Simulation Software for Adsorption and Diffusion in Flexible Nanoporous Materials. *Mol. Simul.* **2016**, *42* (2), 81–101. DOI: 10.1080/08927022.2015.1010082.
- [34] Chen, B.; Potoff, J. J.; Siepmann, J. I. Monte Carlo Calculations for Alcohols and Their Mixtures with Alkanes. Transferable Potentials for Phase Equilibria. 5. United-Atom Description of Primary, Secondary, and Tertiary Alcohols. *J. Phys. Chem. B* **2001**, *105* (15), 3093–3104. DOI: 10.1021/jp003882x.
- [35] Abascal, J. L. F.; Vega, C. A General Purpose Model for the Condensed Phases of Water: TIP4P/2005. *J. Chem. Phys.* **2005**, *123* (23), 234505. DOI: 10.1063/1.2121687.
- [36] Dubbeldam, D.; Walton, K. S.; Vlugt, T. J. H.; Calero, S. Design, Parameterization, and Implementation of Atomic Force Fields for Adsorption in Nanoporous Materials. *Adv. Theory Simul.* **2019**, *2* (11), 1900135. DOI: 10.1002/adts.201900135.
- [37] Vlugt, T. J. H.; Schenk, M. Influence of Framework Flexibility on the Adsorption Properties of Hydrocarbons in the Zeolite Silicalite. *J. Phys. Chem. B* **2002**, *106* (49), 12757–12763. DOI: 10.1021/jp0263931.
- [38] Smith, W.; Forester, T. R. DL\_POLY\_2.0: A General-purpose Parallel Molecular Dynamics Simulation Package. *J. Mol. Graphics* **1996**, *14* (3), 136–141. DOI: 10.1016/S0263-7855(96)00043-4.

- [39] Allen, M. P.; Allen, M. P.; Tildesley, D. J.; Tildesley, D. J.; Allen, T. *Computer Simulation of Liquids*; Clarendon Press, 1989.
- [40] Hoover, W. G. Canonical Dynamics: Equilibrium Phase-space Distributions. *Phys. Rev. A* **1985**, *31* (3), 1695–1697. DOI: 10.1103/PhysRevA.31.1695.
- [41] Ghysels, A.; Moors, S. L. C.; Hemelsoet, K.; De Wispelaere, K.; Waroquier, M.; Sastre, G.; Van Speybroeck, V. Shape-Selective Diffusion of Olefins in 8-Ring Solid Acid Microporous Zeolites. *J. Phys. Chem. C* **2015**, *119* (41), 23721–23734. DOI: 10.1021/acs.jpcc.5b06010.
- [42] CHA: Framework Type, <https://europe.iza-structure.org/IZA-SC/framework.php?STC=CHA> (accessed 2021-09-17).
- [43] Sastre, G.; Lewis, D. W.; Catlow, C. R. A. Modeling of Silicon Substitution in SAPO-5 and SAPO-34 Molecular Sieves. *J. Phys. Chem. B* **1997**, *101* (27), 5249–5262. DOI: 10.1021/jp963736k.
- [44] Dai, W.; Scheibe, M.; Li, L.; Guan, N.; Hunger, M. Effect of the Methanol-to-Olefin Conversion on the PFG NMR Self-Diffusivities of Ethane and Ethene in Large-Crystalline SAPO-34. *J. Phys. Chem. C* **2012**, *116* (3), 2469–2476. DOI: 10.1021/jp208815g.
- [45] Gilli, G. *The Nature of the Hydrogen Bond : Outline of a Comprehensive Hydrogen Bond Theory*; Oxford University Press, 2009.
- [46] Bushuev, Y. G.; Sastre, G. Atomistic Simulations of Structural Defects and Water Occluded in SSZ-74 Zeolite. *J. Phys. Chem. C* **2009**, *113* (25), 10877–10886. DOI: 10.1021/jp9013306.
- [47] Bushuev, Y. G.; Sastre, G. Atomistic Simulation of Water Intrusion–Extrusion in ITQ-4 (IFR) and ZSM-22 (TON): The Role of Silanol Defects. *J. Phys. Chem. C* **2011**, *115* (44), 21942–21953. DOI: 10.1021/jp207020w.
- [48] Sinha, A. K.; Sainkar, S.; Sivasanker, S. An Improved Method for the Synthesis of the Silicoaluminophosphate Molecular Sieves, SAPO-5, SAPO-11 and SAPO-31. *Microporous Mesoporous Mater.* **1999**, *31* (3), 321–331. DOI: 10.1016/S1387-1811(99)00081-5.



- [49] Simancas, R.; Chokkalingam, A.; Elangovan, S. P.; Liu, Z.; Sano, T.; Iyoki, K.; Wakihara, T.; Okubo, T. Recent Progress in the Improvement of Hydrothermal Stability of Zeolites. *Chem. Sci.* **2021**, *12* (22), 7677–7695. DOI: 10.1039/d1sc01179k.
- [50] Zanjanchi, M. A.; Ghanadzadeh, A.; Khadem-Nahvi, F. Incorporation of Silicon into AlPO-5 Framework Sites: Higher Thermal Stability and Lower Extra-Framework Aluminum Concentration. *J. Inclusion Phenom. Macrocyclic Chem.* **2002**, *42* (3), 295–299. DOI: 10.1023/A:1016015210310.
- [51] Simmen, A.; McCusker, L. B.; Baerlocher, Ch.; Meier, W. M. The Structure Determination and Rietveld Refinement of the Aluminophosphate AlPO<sub>4</sub>-18. *Zeolites* **1991**, *11* (7), 654–661. DOI: 10.1016/S0144-2449(05)80167-8.
- [52] Ito, M.; Shimoyama, Y.; Saito, Y.; Tsurita, Y.; Otake, M. Structure of an Aluminosilicophosphate. *Acta Crystallogr., Sect. C: Cryst. Struct. Commun.* **1985**, *41* (12), 1698–1700. DOI: 10.1107/S010827018500912X.
- [53] Díaz-Cabañas, M.-J.; Barrett, P. A.; Cambor, M. A. Synthesis and Structure of Pure SiO<sub>2</sub> Chabazite: the SiO<sub>2</sub> Polymorph with the Lowest Framework Density. *Chem. Commun.* **1998**, (17), 1881–1882. DOI: 10.1039/A804800B.
- [54] Carey, T.; Corma, A.; Rey, F.; Tang, C. C.; Hriljac, J. A.; Anderson, P. A. The Effect of Extra Framework Species on the Intrinsic Negative Thermal Expansion Property of Zeolites with the LTA Topology. *Chem. Commun.* **2012**, *48* (47), 5829–5831. DOI: 10.1039/C2CC30582H.
- [55] Gale, J. D.; Rohl, A. L. The General Utility Lattice Program (GULP). *Mol. Simul.* **2003**, *29* (5), 291–341. DOI: 10.1080/0892702031000104887.
- [56] Abril, D. M.; Slater, B.; Blanco, C. Modeling Dynamics of the External Surface of Zeolite LTA. *Microporous Mesoporous Mater.* **2009**, *123* (1), 268–273. DOI: 10.1016/j.micromeso.2009.04.010.
- [57] Slater, B.; Titiloye, J. O.; Higgins, F. M.; Parker, S. C. Atomistic Simulation of Zeolite Surfaces. *Curr. Opin. Solid State Mater. Sci.* **2001**, *5* (5), 417–424. DOI: 10.1016/S1359-0286(01)00039-0.

- [58] Boscoboinik, J. A.; Yu, X.; Emmez, E.; Yang, B.; Shaikhutdinov, S.; Fischer, F. D.; Sauer, J.; Freund, H. Interaction of Probe Molecules with Bridging Hydroxyls of Two-Dimensional Zeolites: A Surface Science Approach. *J. Phys. Chem. C* **2013**, *117* (26), 13547–13556. DOI: 10.1021/jp405533s.
- [59] Dib, E.; Costa, I. M.; Vayssilov, G. N.; Aleksandrov, H. A.; Mintova, S. Complex H-bonded Silanol Network in Zeolites Revealed by IR and NMR Spectroscopy Combined with DFT Calculations. *J. Mater. Chem. A* **2021**, *9* (48), 27347–27352. DOI: 10.1039/D1TA06908J.
- [60] Dědeček, J.; Sklenak, S.; Li, C.; Gao, F.; Brus, J.; Zhu, Q.; Tatsumi, T. Effect of Al/Si Substitutions and Silanol Nests on the Local Geometry of Si and Al Framework Sites in Silicone-Rich Zeolites: A Combined High Resolution  $^{27}\text{Al}$  and  $^{29}\text{Si}$  NMR and Density Functional Theory/Molecular Mechanics Study. *J. Phys. Chem. C* **2009**, *113* (32), 14454–14466. DOI: 10.1021/jp9042232.
- [61] Medeiros-Costa, I. C.; Dib, E.; Nesterenko, N.; Dath, J.-P.; Gilson, J.-P.; Mintova, S. Silanol Defect Engineering and Healing in Zeolites: Opportunities to Fine-tune Their Properties and Performances. *Chem. Soc. Rev.* **2021**, *50* (19), 11156–11179. DOI: 10.1039/D1CS00395J.
- [62] Chizallet, C.; Raybaud, P. Pseudo-Bridging Silanols as Versatile Brønsted Acid Sites of Amorphous Aluminosilicate Surfaces. *Angew. Chem. Int. Ed.* **2009**, *48* (16), 2891–2893. DOI: 10.1002/anie.200804580.
- [63] Rey, J.; Raybaud, P.; Chizallet, C. Ab Initio Simulation of the Acid Sites at the External Surface of Zeolite Beta. *ChemCatChem* **2017**, *9* (12), 2176–2185. DOI: 10.1002/cctc.201700080.
- [64] Arya, G.; Maginn, E. J.; Chang, H.-C. Effect of the Surface Energy Barrier on Sorbate Diffusion in  $\text{AlPO}_4\text{-5}$ . *J. Phys. Chem. B* **2001**, *105* (14), 2725–2735. DOI: 10.1021/jp003350g.
- [65] Zimmermann, N. E. R.; Smit, B.; Keil, F. J. On the Effects of the External Surface on the Equilibrium Transport in Zeolite Crystals. *J. Phys. Chem. C* **2010**, *114* (1), 300–310. DOI: 10.1021/jp904267a.

- [66] Kärger, J.; Heink, W.; Pfeifer, H.; Rauscher, M.; Hoffmann, J. N.m.r. Evidence of the Existence of Surface Barriers on Zeolite Crystallites. *Zeolites* **1982**, *2* (4), 275–278. DOI: 10.1016/S0144-2449(82)80070-5.
- [67] Whitmore, L.; Slater, B.; Catlow, C. R. A. Adsorption of Benzene at the Hydroxylated (111) External Surface of Faujasite. *Phys. Chem. Chem. Phys.* **2000**, *2* (23), 5354–5356. DOI: 10.1039/B008080M.
- [68] Glavatskiy, K. S.; Bhatia, S. K. Thermodynamic Resistance to Matter Flow at The Interface of a Porous Membrane. *Langmuir* **2016**, *32* (14), 3400–3411. DOI: 10.1021/acs.langmuir.6b00375.
- [69] Rao, S. M.; Saraçi, E.; Gläser, R.; Coppens, M.-O. Surface Barriers as Dominant Mechanism to Transport Limitations in Hierarchically Structured Catalysts – Application to the Zeolite-catalyzed Alkylation of Benzene with Ethylene. *Chem. Eng. J.* **2017**, *329*, 45–55. DOI: 10.1016/j.cej.2017.04.015.
- [70] Thompho, S.; Chanajaree, R.; Remsungnen, T.; Hannongbua, S.; Bopp, P. A.; Fritzsche, S. The Permeation of Methane Molecules through Silicalite-1 Surfaces. *J. Phys. Chem. A* **2009**, *113* (10), 2004–2014. DOI: 10.1021/jp808588n.
- [71] Jentys, A.; Tanaka, H.; Lercher, J. A. Surface Processes During Sorption of Aromatic Molecules on Medium Pore Zeolites. *J. Phys. Chem. B* **2005**, *109* (6), 2254–2261. DOI: 10.1021/jp0488362.
- [72] Schnell, S. K.; Vlugt, T. J. H.; Simon, J.-M.; Bedeaux, D.; Kjelstrup, S. Thermodynamics of Small Systems Embedded in a Reservoir: a Detailed Analysis of Finite Size Effects. *Mol. Phys.* **2012**, *110* (11-12), 1069–1079. DOI: 10.1080/00268976.2011.637524.
- [73] Sastre, G.; Kärger, J.; Ruthven, D. M. Diffusion Path Reversibility Confirms Symmetry of Surface Barriers. *J. Phys. Chem. C* **2019**, *123* (32), 19596–19601. DOI: 10.1021/acs.jpcc.9b04528.
- [74] García-Pérez, E.; Schnell, S. K.; Castillo, J. M.; Calero, S.; Kjelstrup, S.; Dubbeldam, D.; Vlugt, T. J. H. External Surface Adsorption on Silicalite-1 Zeolite Studied by Molecular Simulation. *J. Phys. Chem. C* **2011**, *115* (31), 15355–15360. DOI: 10.1021/jp201570z.

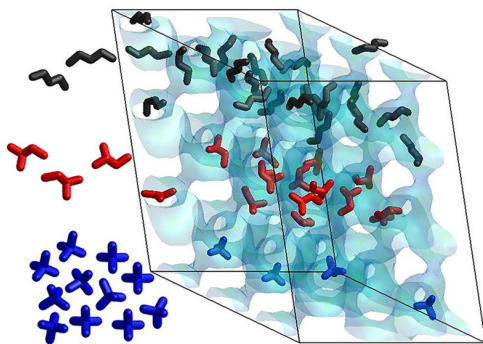
- [75] Van de Graaf, J. M.; Kapteijn, F.; Moulijn, J. A. Diffusivities of Light Alkanes in a Silicalite-1 Membrane Layer. *Microporous Mesoporous Mater.* **2000**, *35-36*, 267–281. DOI: 10.1016/S1387-1811(99)00227-9.
- [76] Remi, J. C. S.; Lauerer, A.; Chmelik, C.; Vandendael, I.; Terryn, H.; Baron, G. V.; Denayer, J. F. M.; Kärger, J. The Role of Crystal Diversity in Understanding Mass Transfer in Nanoporous Materials. *Nat. Mater.* **2016**, *15* (4), 401–406. DOI: 10.1038/nmat4510.
- [77] Sholl, D. S. A Porous Maze. *Nat. Chem.* **2011**, *3* (6), 429–430. DOI: 10.1038/nchem.1054.
- [78] Schröder, K.-P.; Sauer, J.; Leslie, M.; Richard, C.; Catlow, A.; Thomas, J. M. Bridging Hydroxyl Groups in Zeolitic Catalysts: a Computer Simulation of Their Structure, Vibrational Properties and Acidity in Protonated Faujasites (H-Y Zeolites). *Chem. Phys. Lett.* **1992**, *188* (3), 320–325. DOI: 10.1016/0009-2614(92)90030-Q.
- [79] Claessens, B.; Cousin-Saint-Remi, J.; Denayer, J. F. M. Efficient Downstream Processing of Renewable Alcohols Using Zeolite Adsorbents. In *New Developments in Adsorption/Separation of Small Molecules by Zeolites*, Valencia, S., Rey, F., Eds.; Springer International Publishing, 2020, 85–119. DOI: 10.1007/430\_2020\_68, [https://doi.org/10.1007/430\\_2020\\_68](https://doi.org/10.1007/430_2020_68).
- [80] Bauer, J.; Selvam, T.; Ofili, J.; Che, E.; Herrmann, R.; Schwieger, W. Stability of AlPO and SAPO Molecular Sieves During Adsorption-desorption Cycles of Water Vapor Investigated by In-situ XRD Measurements. In *Studies in Surface Science and Catalysis*; Elsevier, 2007; Vol. 170, 837–844. DOI: 10.1016/S0167-2991(07)80930-X.
- [81] Jänchen, J.; Stach, H.; Hellwig, U. Water Sorption in Faujasite- and Chabazite Type Zeolites of Varying Lattice Composition for Heat Storage Applications. In *Zeolites and Related Materials: Trends, Targets and Challenges*, Gédéon, A., Massiani, P., Babonneau, F., Eds.; Studies in Surface Science and Catalysis, Vol. 174; Elsevier, 2008, 599–602. DOI: [https://doi.org/10.1016/S0167-2991\(08\)80271-6](https://doi.org/10.1016/S0167-2991(08)80271-6), <https://www.sciencedirect.com/science/article/pii/S0167299108802716>.
- [82] Fasano, M.; Falciani, G.; Brancato, V.; Palomba, V.; Asinari, P.; Chiavazzo, E.; Frazzica, A. Atomistic Modelling of Water Transport and Adsorption

- Mechanisms in Silicoaluminophosphate for Thermal Energy Storage. *Appl. Therm. Eng.* **2019**, *160*, 114075. DOI: 10.1016/j.applthermaleng.2019.114075.
- [83] Kayal, S.; Baichuan, S.; Saha, B. B. Adsorption Characteristics of AQSOA Zeolites and Water for Adsorption Chillers. *Int. J. Heat Mass Transfer* **2016**, *92*, 1120–1127. DOI: 10.1016/j.ijheatmasstransfer.2015.09.060.
- [84] Jänchen, J.; Stach, H. Shaping Adsorption Properties of Nano-porous Molecular Sieves for Solar Thermal Energy Storage and Heat Pump Applications. *Sol. Energy* **2014**, *104*, 16–18. DOI: 10.1016/j.solener.2013.07.018.
- [85] Sun, B.; Chakraborty, A. Thermodynamic Formalism of Water Uptakes on Solid Porous Adsorbents for Adsorption Cooling Applications. *Appl. Phys. Lett.* **2014**, *104* (20), 201901. DOI: 10.1063/1.4876922.
- [86] Deng, X.; Yang, W.; Li, S.; Liang, H.; Shi, Z.; Qiao, Z. Large-Scale Screening and Machine Learning to Predict the Computation-Ready, Experimental Metal-Organic Frameworks for CO<sub>2</sub> Capture from Air. *Appl. Sci.* **2020**, *10* (2), 569. DOI: 10.3390/app10020569.
- [87] Dureckova, H.; Krykunov, M.; Aghaji, M. Z.; Woo, T. K. Robust Machine Learning Models for Predicting High CO<sub>2</sub> Working Capacity and CO<sub>2</sub>/H<sub>2</sub> Selectivity of Gas Adsorption in Metal Organic Frameworks for Precombustion Carbon Capture. *J. Phys. Chem. C* **2019**, *123* (7), 4133–4139. DOI: 10.1021/acs.jpcc.8b10644.
- [88] Arora, A.; Iyer, S. S.; Hasan, M. M. F. Computational Material Screening Using Artificial Neural Networks for Adsorption Gas Separation. *J. Phys. Chem. C* **2020**, *124* (39), 21446–21460. DOI: 10.1021/acs.jpcc.0c05900.
- [89] Braun, E.; Zurhelle, A. F.; Thijssen, W.; Schnell, S. K.; Lin, L.-C.; Kim, J.; Thompson, J. A.; Smit, B. High-throughput Computational Screening of Nanoporous Adsorbents for CO<sub>2</sub> Capture from Natural Gas. *Mol. Syst. Des. Eng.* **2016**, *1* (2), 175–188. DOI: 10.1039/C6ME00043F.
- [90] Sun, Y.; DeJaco, R. F.; Siepmann, J. I. Deep Neural Network Learning of Complex Binary Sorption Equilibria From Molecular Simulation Data. *Chem. Sci.* **2019**, *10* (16), 4377–4388. DOI: 10.1039/C8SC05340E.



## Chapter 4

# Insights into Adsorption of Linear, Monobranched, and Dibranched Alkanes on Pure Silica STW Zeolite as a Promising Material for Their Separation



The Journal of Physical Chemistry C 2020, 124, 49, 26821-26829  
DOI: 10.1021/acs.jpcc.0c08517 (adapted)<sup>†</sup>

Eduardo Pérez-Botella<sup>1</sup>, Alechania Misturini<sup>1</sup>, Andrés Sala<sup>1</sup>, Miguel Palomino<sup>1</sup>,  
Avelino Corma<sup>1</sup>, German Sastre<sup>1</sup>, Susana Valencia<sup>1</sup>, and Fernando Rey<sup>1\*</sup>

<sup>1</sup> Instituto de Tecnología Química, Universitat Politècnica de València, Avda. de los Naranjos s/n, 46022 Valencia, Spain. \*E-mail: frey@itq.upv.es

<sup>†</sup>The work presented here was adapted to mainly reflect the computational results. For the full text, please refer to the reference above.

## **Abstract**

The adsorption of linear, monobranched and dibranched saturated hydrocarbons in the gasoline range has been studied on pure silica STW zeolite (Si-STW) by using pentane, hexane, and heptane isomers as model adsorbates. Experimental single-component adsorption isotherms and kinetic measurements together with configurational bias Monte Carlo (CBMC) and molecular dynamics (MD) simulations were carried out. Significant differences in both the equilibrium adsorption and especially the adsorption kinetics were found, which suggests that the separation of the quaternary-carbon dibranched isomer is feasible. The adsorption capacities and selectivities surpass those of pure silica MFI (Si-MFI), considered as reference. Altogether, Si-STW is presented as a promising adsorbent for increasing the octane number (ON) of the hydroisomerization product by selectively excluding quaternary-carbon dibranched hydrocarbons.

**Keywords:** hydrocarbon separation, zeolite, STW, molecular dynamics, Monte Carlo simulations.

## **4.1 Introduction**

Gasoline is a liquid mixture mainly consisting of hydrocarbons in the C4–C12 fractions and is one of the most used fuels worldwide. Its performance is evaluated in terms of the octane number (ON). High octane numbers (ca. 100) are desired, and official institutions establish minimum values. The ON of gasoline depends on its composition. Some of its components, such as branched paraffins, aromatics, or olefins, contribute to a higher ON of the mixture [1]. However, some of these, that is, benzene, aromatics, olefins, or oxygenates, are subject to restrictions due to their effects on health or the environment [2].

Hydroisomerization of linear short chain paraffins is an effective method of obtaining higher-octane components for the gasoline blend. The feed of this process is straight run naphta, which mainly consists of linear C4–C10 normal paraffins. Highly active supported metal hydrogenation catalysts and hydrogen are required for the desired reactions to take place. The reaction is equilibrium limited and low temperatures are needed to minimize hydrocracking of the more reactive branched products [2-4]. Separation of the dibranched products from the effluent and recycling of the monobranched and nonreacted linear paraffins are another desirable way of maximizing the yield and productivity of the unit [5,6].

The separation of linear from branched paraffins has been known and used for years in the industry [7]. Zeolite 5A has found widespread use for this application, although other commercial zeolites, such as pure or high silica MFI, X, or Y, have been utilized as well [8]. However, the separation of monobranched from dibranched (or multibranched) paraffins is the ideal target, as it would



make the whole process much more efficient, obtaining a multibranched product enriched raffinate with a high ON, while recycling both low-octane linear and monobranched paraffins to the hydroisomerization unit. On the other hand, this separation is also more complicated technically. Silicalite-1 (Si-MFI) and other MFI-structured materials and membranes have been the most frequently studied and patented materials for this separation [9-18]. Other materials with MWW, EUO, NES [16,19-21], AFI [22], BEA, FER, FAU, ATO, AEL [9,23], MEL, MTT, MRE [17], ATS, and CFI structures [24,25] can as well be found in the patent literature for this purpose, but none of them are clearly superior to Si-MFI [21].

In this work, we present pure silica zeolite STW (Si-STW) as an adsorbent that could act as a molecular sieve toward multibranched hydrocarbons, especially those presenting quaternary carbons, by selectively adsorbing linear and monobranched molecules. We have used pentane, hexane, and heptane isomers as model molecules (see Scheme B1, Appendix B) and studied their single-component adsorption. Differences are observed under both thermodynamic and kinetic control, as some of the multibranched species present lower maximum loadings and rates of adsorption in comparison to the monobranched and linear isomers. A comparison with Si-MFI has been established. Si-STW outperforms Si-MFI in both selectivity and maximum loading. In the case of dibranched hexane and heptane isomers, the relative position of the ramifications impacts their adsorptive behavior greatly. These tendencies have been studied computationally through configurational bias Monte Carlo (CBMC), using a united atom force field, and molecular dynamics (MD) simulations, using an all-atom force field, to gain insight into the processes at a molecular level. The computational results agree with the experimental results qualitatively and quantitatively in the cases where dibranched isomers are not involved.

## 4.2 Experimental and Theoretical Methods

### 4.2.1 Zeolitic materials

Si-STW is a chiral medium pore zeolite containing a helicoidal 10-ring channel across [001] with openings of  $5.2 \times 5.7 \text{ \AA}^2$ , intersected perpendicularly by 8-ring windows of  $3.0 \times 4.4 \text{ \AA}^2$  [26]. Only the 10-ring channels will take part in the adsorption of the molecules of interest of this study, as even linear hydrocarbons, which have the smallest size of the studied adsorbates, present minimum diameters in perpendicular directions of 4.0 and 4.5  $\text{\AA}$ , respectively [27,28].

### 4.2.2 Adsorption experiments

The adsorption on Si-STW of the model molecules was performed in a Hiden Intelligent Gravimetric Analyzer (IGA-3). The chosen model hydrocarbons with different ON (Scheme B1, Appendix B) were n-pentane (nC5), n-hexane (nC6), and n-heptane (nC7) as linear, 2-methylbutane (2MB), 2-methylpentane (2MPe), and 3-methylhexane (3MH) as monobranched paraffins and 2,2-dimethylpropane (22DMPPr), 2,2-dimethyl-butane (22DMB), 2,3-dimethylbutane (23DMB), 2,3-dimethylpentane (23DMPe), and 2,4-dimethylpentane (24DMPe) as dibranched paraffins. Isotherms up to 300 mbar and temperatures ranging from 10 to 60 °C and kinetic experiments at 1, 50, 150, and 300 mbar and 25 °C were recorded. The choice of pressures was made to ensure that no bulk condensation took place in the system. The analogous experiments with the C5-fraction were performed on Si-MFI materials for comparison.

The experimental isosteric heat of adsorption ( $q_{st}$ ) was calculated for each pure component from the isotherms measured at different temperatures by using the Clausius-Clapeyron equation

$$q_{st} = -R \left[ \frac{\delta \ln P}{\delta \frac{1}{T}} \right]_Q,$$

where R is the ideal gas constant, P is the pressure, T is the temperature, and the subindex Q is the loading. As will be seen below, because of the very steep isotherms, in some cases, we could not obtain  $q_{st}$  at zero coverage.

The diffusional time constants were calculated from the kinetic data by fitting to the solution of the transient diffusion equation assuming micropore diffusion control and a spherical particle shape [29].

### 4.2.3 Monte Carlo simulations

Calculated adsorption isotherms were determined through configurational bias Monte Carlo simulations (CBMC) as implemented in the RASPA [30] software package (version 2.0.25), using the grand canonical ensemble, with constant volume, temperature (300 K), and chemical potential. The latter is converted by the software into pressures by using the Peng-Robinson equation of state. Hydrocarbon pressures ranged from 0.001 to 1000.0 mbar.

The force field description of Calero et al. [31], successfully applied for hexane isomer separations in MFI and MEL zeolite types, was employed. Simulated systems were modeled by considering the zeolite framework fixed, and flexible hydrocar-

bon molecules with a united atom force field, taking into account CH<sub>x</sub> (x = 0, 1, 2, 3) groups as unique beads of neutral charge. Bonds and bends between adsorbate pseudoatoms were described by harmonic potentials and torsions by TraPPE cosine series. Lennard-Jones potentials modeled zeolite–hydrocarbon and adsorbate intramolecular interactions (for beads more than three bonds distant), being cut and shifted with the cutoff distance of 12 Å. Host-guest Lennard-Jones interactions are considered only through zeolite O atoms, computed as an effective interaction in which the smaller effect of Si (which is a cation of small size) was included in the O parameters. Zeolite frameworks were obtained from crystallographic data available for all silica MFI (ZSM-5) [32] and STW (HPM-1) [33] and were simulated with unit cells  $2 \times 2 \times 2$  (a = 40.0 Å, b = 39.8 Å, c = 26.8 Å,  $\alpha = \beta = \gamma = 90.0^\circ$ ) and  $3 \times 3 \times 1$  (a = b = 35.7 Å, c = 29.9 Å,  $\alpha = \beta = 90.0^\circ$ ,  $\gamma = 120.0^\circ$ ), respectively.

Simulations were performed during  $10^4$  initiation cycles (sufficient for the equilibration of our systems energy) and  $10^6$  production cycles. Even for the adsorption isotherms performed only with pure components, the use of Rosenbluth factor was crucial for the direct comparison with experiments. It represents the reference state of the ideal gas, and it is used by RASPA package for correcting the gas pressure. Such a factor was previously calculated, as the helium void fraction.

#### 4.2.4 Molecular Dynamics simulations

To facilitate a visual understanding of the diffusivity of pentane, hexane, and heptane isomers in the zeolites studied, the trajectories from molecular dynamics (MD) simulations, performed with DL\_POLY (version 2.20) [34], were analyzed. Simulation boxes contained six alkane molecules inside each zeolite (low loading), defining a fully flexible system. The unit cells considered for each zeolite are MFI  $2 \times 1 \times 2$  (a = 40.2 Å, b = 19.7 Å, c = 26.3 Å,  $\alpha = \beta = \gamma = 90.0^\circ$ ) and STW  $2 \times 2 \times 2$  (a = b = 23.8 Å, c = 59.8 Å,  $\alpha = \beta = 90.0^\circ$ ,  $\gamma = 120.0^\circ$ ), with both crystallographic data taken from IZA database [33]. After equilibration, time evolution of the system was computed on the NVT ensemble for 10 ns, using the Leapfrog integrator and with a 1.0 fs time step. Temperature was maintained at 298.0 K with an Evans thermostat, periodic boundary conditions were considered, and a cutoff of 9.0 Å was selected for the nonbonding forces.

For zeolite modeling, the force field of Sastre et al. was employed [35]. The Coulombic interaction is accounted for and point charges of 2.1 and -1.05 e<sup>-</sup> are assigned for silicon and oxygen atoms, respectively. Three body potentials for O–Si–O and Si–O–Si interactions are treated by a screened harmonic function and van der Waals terms by Lennard-Jones potentials.

Alkane topologies are ensured by means of bonds and bends defined as harmonic potentials, and truncated Fourier series describing rotational barriers of dihedral angles, as developed by Oie et al. [36] Adsorbate molecules were modeled by using an all-atom force field, in which the atomic charges were calculated by using the HF/6-31G\* level of theory with Gaussian 09 (Revision A.02) [37] and subsequently adjusted to ensure CHx as neutral groups. Host-guest interactions are described by Lennard-Jones terms using parameters reported by Catlow and co-workers [38]. Force field parameters employed on MD simulations are summarized in Tables B6 to B8 (Appendix B).

### 4.3 Results and Discussion

The experimental and computational adsorption isotherms of the different vapors at 25 °C and up to 50/150/300 mbar on STW are shown in Figure 4.1.

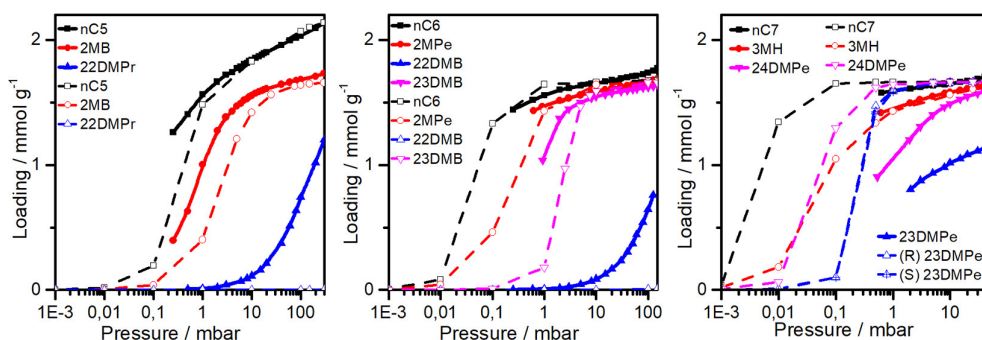


**Figure 4.1:** Experimental (solid) and computational (dashed) isotherms of C5 (left), C6 (center), and C7 (right) isomers on Si-STW. The 22DMB and 23DMPe experimental isotherms are not fully equilibrated.

It can be seen that the linear and monobranched pentane isomers present type I(a) isotherms [39], while the more weakly adsorbed dibranched isomer presents a type I(b) isotherm. The simulated isotherms match fairly well the experimental data of the linear and monobranched isomers, especially in the high-pressure regime. The isotherm for the dibranched isomer could not be calculated accurately due to a configurational shortcoming in the MC algorithm, which does not find suitable conformations inside STW, probably related to their high entropy. As a consequence, we obtained zero adsorption, which is clearly not the case, as confirmed by independent lattice energy minimization calculations showing that up to seven molecules (1.94 mmol/g) of the dibranched isomer can fit in the STW unit cell. In

the case of hexane isomers, the relative position of the methyl groups influences their behavior. 22DMB behaves similarly to 22DMP<sub>r</sub> while 23DMB behaves similarly to the monobranched compounds. This could be due to faster rates of chain rotation compared to diffusion. The simulated isotherms match the experimental data quite well again, for nC<sub>6</sub>, 2MPe, and 23DMB. Unfortunately, we lack experimental data in the low-pressure regime. As for 22DMB, the dibranched isomer, the same result as in the equivalent C<sub>5</sub> dibranched (22DMP<sub>r</sub>) is observed. The MC simulation predicts no adsorption while lattice energy minimizations show it is perfectly possible to adsorb 22DMB in STW (Figure B11, Appendix B). The experimental data show that adsorption takes place more weakly and at a slower rate than for the other isomers. Note that the isotherm of 22DMB is not fully equilibrated. In the case of the heptane isomers, we see that the linear and the monobranched isomers again behave similarly, and in these cases, the simulated isotherms match the experimental quite well in the measured range. However, the isotherms of the two chosen dibranched isomers, 23DMPe and 24DMPe, behave in a significantly different way than predicted. The predicted isotherms reach a much higher maximum loading in both cases, even surpassing the monobranched isotherm. Still, the conclusion drawn from both experimental and computational data is that 24DMPe behaves similarly to linear and monobranched isomers. In the case of 23DMPe, even though the mentioned difference is larger, the experimental isotherm does not reach equilibrium in a reasonable time (see Figure B2, Appendix B), and we cannot establish a quantitative comparison.

The experimental and computational adsorption isotherms of the pentane isomers at 25 °C and up to 300 mbar on the MFI samples are presented in Figure 4.2. In comparison to STW, all experimental maximum loadings are lower. The linear and monobranched isomers present extremely similar simulated and experimental isotherms on both samples, with Si-MFI<sub>small</sub> being slightly above Si-MFI<sub>large</sub>. The experimental isotherm of 22DMP<sub>r</sub> on Si-MFI<sub>small</sub> is well above that on Si-MFI<sub>large</sub> at pressures below 150 mbar. The simulated isotherm has a closer resemblance to the isotherm on Si-MFI<sub>small</sub>. This is due to nonequilibrated points in Si-MFI<sub>large</sub> isotherm below 200 mbar. The theoretical model successfully reproduces MFI adsorption isotherms, in agreement with previous literature for pentane [40-44], hexane, and heptane [31,40-43,45-49] isomers (Table B9, Appendix B). To the best of our knowledge, this is the first adsorption isotherm reported for 22DMP<sub>r</sub> on silica MFI (from both experiments and simulations).

The spatial arrangement of the pentane isomers in the zeolite frameworks with MFI and STW structures at the end of the CMBC simulations at pressures above saturation is presented in Figure 4.3.

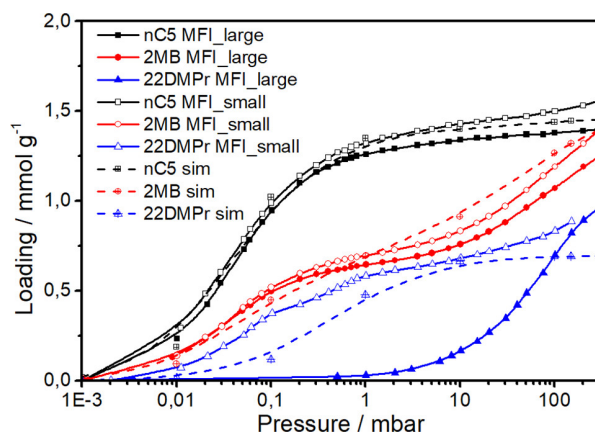


**Figure 4.2:** Experimental (solid lines) and computational (dashed lines and crossed symbols) isotherms of the studied hydrocarbons on Si-MFI\_large (solid symbols) and Si-MFI\_small (open symbols).

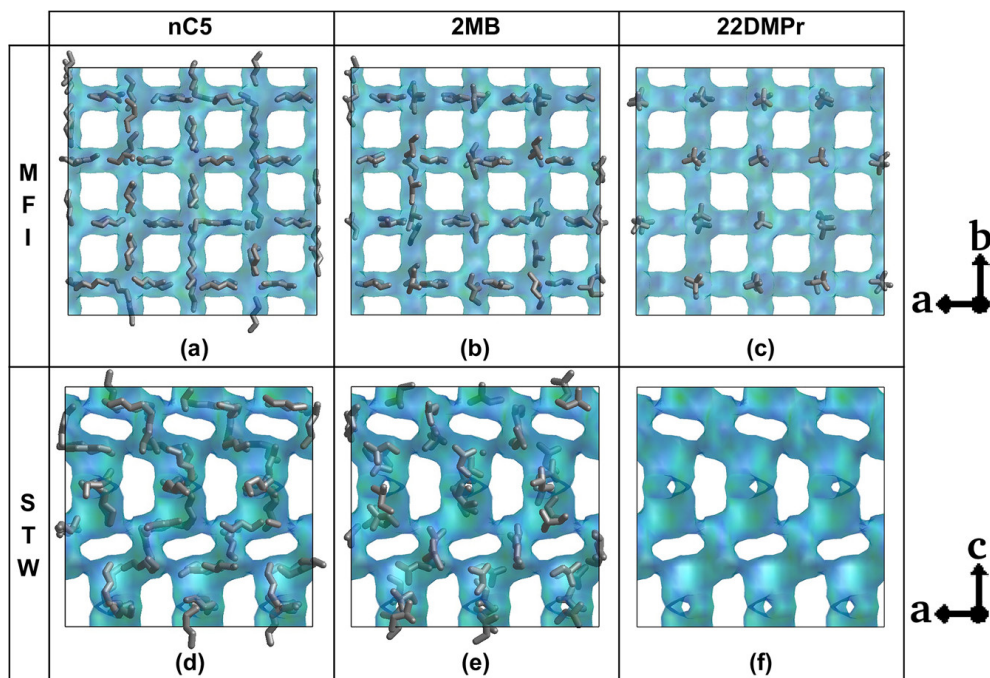


**Figure 4.3:** Final configurations from CBMC simulations of MFI and STW with n-pentane (a, d), 2-methylbutane (b, e), and 2,2-dimethylpropane (c, f) at 1000.0 mbar. Further details are given in the Supporting Information (Appendix B).

While 22DMP<sub>r</sub> molecules are uniquely located in the intersections of MFI channel system (Figure 4.3c), monobranched and linear isomers of pentane can also fit inside the channels, increasing their concentration until they are completely loaded (Figures 4.3b and 4.3a, respectively). Such preferential adsorption sites in Si-MFI have already been reported in the literature [43,50,51].

With an increase in alkane chain, different preferential orientations are observed in the STW channel system. n-Hexane and n-heptane are arranged horizontally (along a, Figure 4.4a,b).

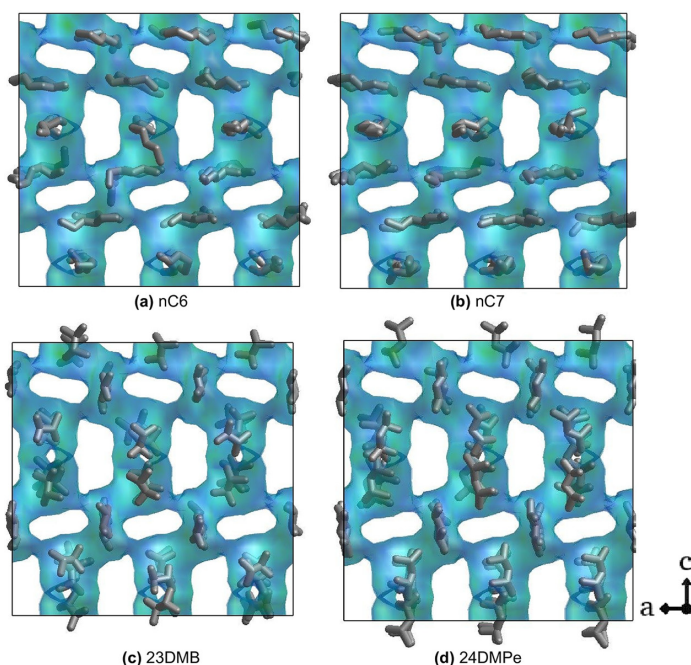


**Figure 4.4:** Final configurations from CBMC simulations of STW with n-hexane (a), n-heptane (b), 2,3-dimethylbutane (c), and 2,4-dimethylpentane (d) at 1000.0 mbar.

Contrarily, all the branched isomers fill the channels aligned to the c-axis (Figure 4.4c,d). These arrangements are related to channel width, allowing the adsorption of molecules with the most efficient packing. More information about the spatial arrangement of the studied hydrocarbons in Si-MFI and Si-STW materials can be found in Figures B4 to B9, Appendix B.

The analysis of the isosteric heats of adsorption (Table 4.1) is closely related to the analysis of the isotherm shape. As can be seen, linear and monobranched

**Table 4.1:** Experimental Isosteric Heats of Adsorption, Diffusional Time Constants at 1, 50 (C7), 150 (C6), or 300 mar (C5), and Maximum Loadings at the Said Maximum Pressures on Si-STW.

compd	$q_{st}$ (kJ mol <sup>-1</sup> ) <sup>a</sup>	$D_1 r^{-2}$ (s <sup>-1</sup> ) <sup>b</sup>	$D_{high} r^{-2}$ (s <sup>-1</sup> ) <sup>b</sup>	$Q_{high}$ (mmol g <sup>-1</sup> ) <sup>b</sup>
nC5	61.5 (1.5)	$1.3 \times 10^{-3}$	$3.0 \times 10^{-3}$	2.17
2MB	55.3 (0.9)	$9.1 \times 10^{-4}$	$1.9 \times 10^{-3}$	1.70
22DMP <sub>r</sub>	33.3	$3.4 \times 10^{-5}$	$2.2 \times 10^{-5}$	1.22
nC6	81.0 (1.6)	$1.9 \times 10^{-3}$	$1.7 \times 10^{-3}$	1.77
2MP	72.2 (1.4)	$1.2 \times 10^{-3}$	$2.2 \times 10^{-3}$	1.66
22DMB		$3.5 \times 10^{-6}$	$2.9 \times 10^{-6}$	1.00
23DMB	46.0 (1.4)	$3.0 \times 10^{-4}$	$9.5 \times 10^{-4}$	1.64
nC7	85.8 (1.6)	$1.2 \times 10^{-3}$	$1.7 \times 10^{-3}$	1.70
3MH	76.3 (1.4)	$1.0 \times 10^{-3}$	$1.8 \times 10^{-3}$	1.64
23DMP <sub>e</sub>		$<5 \times 10^{-6}$	$<5 \times 10^{-6}$	>1
24DMP <sub>e</sub>	58.9 (0.9)	$0.9 \times 10^{-3}$	$1.8 \times 10^{-3}$	1.60

<sup>a</sup> The isosteric heat of adsorption could not be calculated at low coverage in many cases due to the very steep isotherms. The values at the lowest loading possible (in parentheses) are shown for these.  
<sup>b</sup> All values at 25 °C.

isomers in the C5-C7 fractions present large heats of adsorption at low loading (55–86 kJ/mol), while dibranched isomers present a notably lower value. A general trend is that for the same type of alkane (linear, monobranched, or dibranched),  $q_{st}$  increases with chain length. The results of theoretical heat of adsorption ( $\overline{\Delta H_{ads}}$ ) estimated with optimized geometries achieved during MD simulations agree closely with the experimental data of the linear and monobranched isomers ( $\pm 4$  and  $\pm 9$  kJ/mol, respectively; see Figure 4.5), although for dibranched isomers the errors become very large ( $\pm 25$  kJ/mol). Nevertheless, the reported results were those showing the best agreement with experiments from a benchmark between five force fields (not reproduced in full for the sake of brevity). We have not found a straightforward explanation for these discrepancies between experiments and simulations. However, it is possible that the apparently equilibrated isotherms of 22DMP<sub>r</sub> (Figure B1, Appendix B), from which the experimental  $q_{st}$  is calculated, may be at a pseudoequilibrium state. This could be related to the presence of two very different diffusional regimes depending on the coverage of 22DMP<sub>r</sub>. This behavior has been previously observed in other pure silica zeolites upon hydrocarbon adsorption. Indeed, Si-ITW shows two different diffusional regimes upon propane adsorption, a phenomenon which has been attributed to the flexibility of the framework [52,53]. Structural flexibility in uncharged frame-



works has been observed in cases where the kinetic diameter ( $\sigma$ ) of the adsorbate is slightly larger than the pore opening, in which pore expansion takes place upon adsorption [54]. This could be the case for adsorption of 22DMPr ( $\sigma = 6.2 \text{ \AA}$ ) on Si-STW (pore opening  $5.2 \times 5.7 \text{ \AA}^2$ ). Tables with all the experimental and simulated heats of adsorption can be found in the Supporting Information (Appendix B).

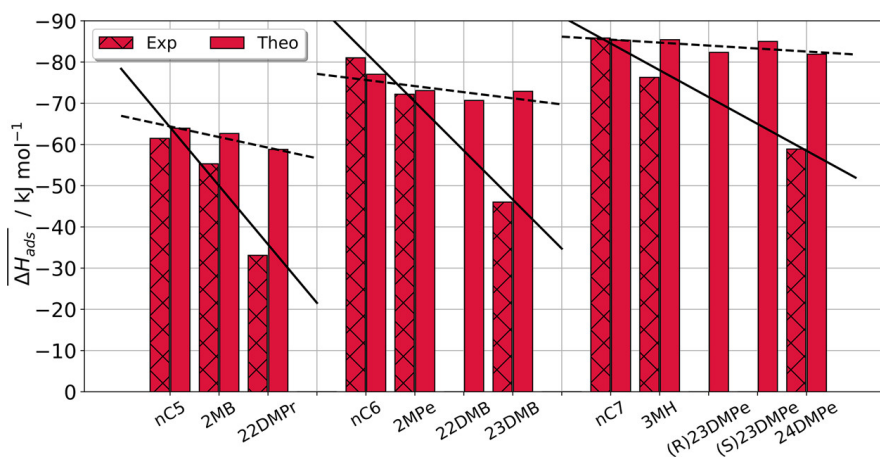


**Figure 4.5:** Experimental and simulated heats of adsorption of the different adsorbates on Si-STW. Lines illustrate the discrepancies between the experimental and calculated values of the dibranched hydrocarbons.

The calculated values for adsorption of dibranched, monobranched, and linear alkanes in MFI are in agreement with experimental results in this study as well as in previous studies [47,55], with errors ranging from  $\pm 0.6$  to  $\pm 4.5$  kJ/mol, which are reasonable. Also, our computational results (Figures B21 and B22, Appendix B) are in close agreement with those obtained by Dubbeldam et al. [43], at 300 K, with a different methodology ( $\pm 4.4$  kJ/mol, values collected in Table B9, Appendix B).

Considering the good performance of the computational models applied to adsorption of alkanes in silica MFI, as well as the linear and monobranched isomers in STW framework, the systematic failure of dibranched adsorption in STW can be considered as a special case. An improved computational model as well as new experiments are in progress in order to obtain more accurate results.

The diffusivities of the hydrocarbons on Si-STW were studied, as well, to see whether, apart from a thermodynamic separation, a kinetic separation could also

possible. A joint analysis of the experimental and computational results (diffusional time constants in Table 4.1 and Table B1, Appendix B, and trajectories from MD simulations in Figure 4.6 and Figures B14 to B18 and B20, Appendix B) is highly illustrative.

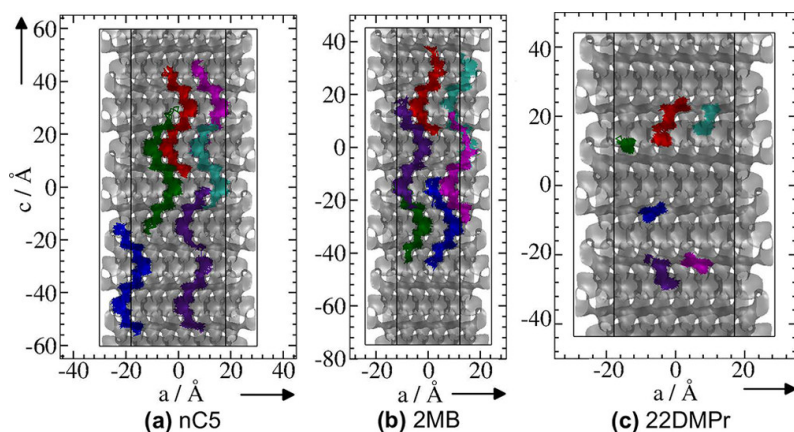


**Figure 4.6:** Trajectories of pentane isomers on STW  $2 \times 2 \times 2$  zeolite during MD simulation (same as Figure B20, Appendix B).

The linear and monobranched pentane isomers are adsorbed at similar rates, while the dibranched isomer diffuses much more slowly into the pores of both Si-MFI and Si-STW. This is observed, too, for Si-STW in Figure 4.6, where it can be seen that both linear and monobranched isomers present trajectories that cover a 40 Å in the  $c$ -axis direction, while the dibranched isomer does not exceed 12 Å. However, the MD simulations predict that in Si-MFI the monobranched isomer will be hindered in its diffusion, similarly to the dibranched one, which does not exactly match the experimental observation. For the C6 fraction on Si-STW, 22DMB is the isomer with the slowest diffusion, while nC6, 2MPe, and 23DMB diffuse much faster, 23DMB being slightly slower than the other two. This is accordingly reproduced by the MD simulation results presented in Figure B18, Appendix B. This is most probably due to the relative position of the two methyl groups. When they are positioned on different C atoms, the rotation of the chain can result in atomic configurations which allow for the molecule to diffuse through the minimum pore openings of the zeolite. If rotation happens faster than diffusion between these minimum openings, the branching will not hinder diffusion notably. However, if two methyl groups are bound to the same C atom, rotation of the chain will not have this effect. In the case of Si-MFI, and similarly to the C5 fraction, no remarkable differences in diffusion are observed between the monobranched and

any of the dibranched isomers in their trajectories and MSD charts (Figures B13b and B15, Appendix B). In the C7 fraction, we went further and studied a third relative position of the methyl substituents. We determined that, the further away from each other the branchings, the less hindered is the diffusion of the molecule in Si-STW. This means nC7, 3MH, and 24DMPe present similar diffusion time constants, while 23DMPe is more hindered. The trajectories presented in B19, Appendix B, reproduce the same trend. The rotation of the chain is a possible explanation in this case as well. The comparison between dibranched hydrocarbons in contiguous C atoms in the C6 and C7 fractions (23DMB and 23DMPe) indicates that the steric volume of the alkyl chain reduces the diffusion as it becomes larger. This could have very positive consequences if Si-STW were implemented at the end of an hydroisomerization process, as quaternary-carbon-dibranched isomers tend to be more prone to undergo cracking, while ternary-carbon-multibranched isomers may still undergo further isomerization, thus increasing their RON and MON numbers. Oppositely, on Si-MFI it seems that going from C6 to C7 hydrocarbons decreases largely the overall diffusion of the molecules. Out of these, only the linear isomer diffuses notably, while the other studied molecules do not present significant diffusion (Figures B13c and B16, Appendix B).

#### 4.4 Conclusions

We have demonstrated that a zeolite with 10-ring channels connected by 8-ring windows (Si-STW) presents molecular sieving properties and could be used as an adsorbent to separate linear and monobranched from multibranched alkanes in the gasoline range. Further separation selectivity can be achieved among the multibranched products, by preferentially adsorbing those in which the ramifications are further away and practically excluding those with quaternary C atoms. This zeolite could then be coupled with an alkane hydroisomerization process to maximize the final yield of multibranched products, with the corresponding increase of the octane number of the gasoline. Furthermore, our experimental and computational results point at Si-STW being superior to Si-MFI in the achievable thermodynamic and kinetic selectivities. Also importantly, Si-STW presents a larger maximum loading (in a factor of ca. 1.5) at almost all pressures. This means that a separation process using Si-STW instead of Si-MFI could use a smaller adsorbent bed while maintaining or even increasing the gasoline yield.

#### Author Contributions

A.S. performed the synthesis and characterization of zeolite STW. E.P.B. performed the adsorption experiments and its analysis, wrote the main part of the

work, and coordinated the work of the team. A.M. did the computational calculations and wrote the corresponding part. M.P. performed part of the adsorption experiments and analysis. G.S. conceived and supervised all the computational work. The original concept of this work was conceived by A.C., F.R., and S.V. All the authors revised and discussed the results in every step of the study. All authors have given approval to the final version of the manuscript.

## Acknowledgments

We acknowledge the Spanish Ministry of Sciences, Innovation and Universities (MCIU), State Research Agency (AEI), and the European Fund for Regional Development (FEDER) for their funding via project RTI2018-101784-B-I00 and Program Severo Ochoa SEV-2016-0683. A.S. thanks the MCIU for his grant BES-2016-078684. E.P.B. thanks the MCIU for his grant(FPU15/01602). A.M. thanks to the Generalitat Valenciana for a predoctoral fellowship GRISOLIAP/2019/084. A.M. and G.S. thank ASIC-UPV for the computational facilities. The Electron Microscopy Service of the UPV is acknowledged for their help in sample characterization.

## References

- [1] Demirbas, A.; Balubaid, M. A.; Basahel, A. M.; Ahmad, W.; Sheikh, M. H. Octane Rating of Gasoline and Octane Booster Additives. *Pet. Sci. Technol.* **2015**, *33* (11), 1190–1197. DOI: 10.1080/10916466.2015.1050506.
- [2] Valavarasu, G.; Sairam, B. Light Naphtha Isomerization Process: A Review. *Pet. Sci. Technol.* **2013**, *31* (6), 580–595. DOI: 10.1080/10916466.2010.504931.
- [3] Aitani, A.; Akhtar, M. N.; Al-Khattaf, S.; Jin, Y.; Koseoglo, O.; Klein, M. T. Catalytic Upgrading of Light Naphtha to Gasoline Blending Components: A Mini Review. *Energy Fuels* **2019**, *33* (5), 3828–3843. DOI: 10.1021/acs.energyfuels.9b00704.
- [4] Martínez, C.; Corma, A. Inorganic Molecular Sieves: Preparation, Modification and Industrial Application in Catalytic Processes. *Coord. Chem. Rev.* **2011**, *255* (13–14), 1558–1580. DOI: 10.1016/j.ccr.2011.03.014.
- [5] Graeme, S.; Ross, J. *Advanced Solutions for Paraffins Isomerization*; Washington, DC, 2004.

- [6] Denayer, J. F. M.; Ocakoglu, R. A.; Arik, I. C.; Kirschhock, C. E. A.; Martens, J. A.; Baron, G. V. Rotational Entropy Driven Separation of Alkane/Isoalkane Mixtures in Zeolite Cages. *Angew. Chem., Int. Ed.* **2005**, *44* (6), 400–403. DOI: 10.1002/anie.200454058.
- [7] Asher, W. J.; Epperly, W. R. Hydrocarbon Separation Process. US Patent 3070542, 1962.
- [8] Pérez-Botella, E.; Palomino, M.; Valencia, S.; Rey, F. Zeolites and Other Adsorbents. In *Nanoporous Materials for Gas Storage*; Springer, 2019; pp 173–208. DOI: 10.1007/978-981-13-3504-4\_7.
- [9] Dandekar, H. W.; Funk, G. A.; Zinnen, H. A. Process for Separating and Recovering Multimethyl-Branched Alkanes. US Patent 6069289 A, 2000.
- [10] Calero, S.; Smit, B.; Krishna, R. Separation of Linear, Mono-Methyl and Di-Methyl Alkanes in the 5–7 Carbon Atom Range by Exploiting Configurational Entropy Effects during Sorption on Silicalite-1. *Phys. Chem. Chem. Phys.* **2001**, *3* (19), 4390–4398. DOI: 10.1039/b103118j.
- [11] Dubbeldam, D.; Krishna, R.; Calero, S.; Yazaydin, A. Ö. Computer-Assisted Screening of Ordered Crystalline Nanoporous Adsorbents for Separation of Alkane Isomers. *Angew. Chem., Int. Ed.* **2012**, *51* (47), 11867–11871. DOI: 10.1002/anie.201205040.
- [12] Bayati, B.; Belbasi, Z.; Ejtemaei, M.; Charchi Aghdam, N.; Babaluo, A. A.; Haghighi, M.; Drioli, E. Separation of Pentane Isomers Using MFI Zeolite Membrane. *Sep. Purif. Technol.* **2013**, *106*, 56–62. DOI: 10.1016/j.seppur.2012.12.017.
- [13] Funke, H. H.; Argo, A. M.; Falconer, J. L.; Noble, R. D. Separations of Cyclic, Branched, and Linear Hydrocarbon Mixtures through Silicalite Membranes. *Ind. Eng. Chem. Res.* **1997**, *36* (1), 137–143. DOI: 10.1021/ie960472f.
- [14] Ragil, K.; Prevost, I.; Clause, O.; Larue, J.; Millot, B. Process for Separating a C5-C8 Feed or an Intermediate Feed into Three Effluents, Respectively Rich in Straight Chain, Non-Branched and Multi-Branched Paraffins. US Patent 6156950, 2000.
- [15] Baudot, A.; Bournay, L. Integration of MFI Zeolite Membranes in the Light Gasoline Isomerisation Process. *Oil Gas Sci. Technol.* **2009**, *64* (6), 759–771. DOI: 10.2516/ogst/2009073.

- [16] Ducreux, O.; Jolimaitre, E. Process Combining Hydroisomerization and Separation Using a Zeolitic Adsorbent with a Mixed Structure for the Production of High Octane Number Gasolines. US Patent 6809228 B2, 2004.
- [17] Ragil, K.; Jullian, S.; Durand, J.-P.; Hotier, G.; Clause, O. High Octane Number Gasolines and Their Production Using a Process Associating Hydroisomerization and Separation. US Patent 6338791 B1, 2002.
- [18] Jolimaitre, E.; Ragil, K.; Tayakout-Fayolle, M.; Jallut, C. Separation of Mono- and Dibranched Hydrocarbons on Silicalite. *AIChE J.* **2002**, *48* (9), 1927–1937. DOI: 10.1002/aic.690480910.
- [19] Jolimaitre, E.; Ducreux, O. Process for Separating Multibranched Paraffins Using a Zeolitic Adsorbent with a Mixed Structure. US Patent 6784334 B2, 2004.
- [20] Denayer, J.; Ocakoglu, R.; Baron, G. Method for Separating Hydrocarbons and Use of a Zeolite Therefor. US Patent 7435865 B2, 2008.
- [21] Laredo, G. C.; Trejo-Zarraga, F.; Jimenez-Cruz, F.; Garcia-Gutierrez, J. L. Separation of Linear and Branched Paraffins by Adsorption Processes for Gasoline Octane Number Improvement. *Recent Patents Chem. Eng.* **2013**, *5* (3), 153–173. DOI: 10.2174/2211334711205030001.
- [22] McCulloch, B.; Lansbarkis, J. R.; Raghuram, S.; Haizmann, R. S. Extraction of Dimethyl Paraffins from Isomerates. US Patent 5107052, 1992.
- [23] Neuzil, R. W. Selectively Adsorbing Multibranched Paraffins. US Patent 3706813, 1972.
- [24] Maesen, T.; Harris, T. Process for Producing High RON Gasoline Using ATS Zeolite. US Patent 7029572 B2, 2006.
- [25] Maesen, T.; Harris, T. Process for Producing High RON Gasoline Using CFI Zeolite. US Patent 7037422 B2, 2006.
- [26] Rojas, A.; Arteaga, O.; Kahr, B.; Cambolor, M. A. Synthesis, Structure, and Optical Activity of HPM-1, a Pure Silica Chiral Zeolite. *J. Am. Chem. Soc.* **2013**, *135* (32), 11975–11984. DOI: 10.1021/ja405088c.
- [27] Webster, C. E.; Drago, R. S.; Zerner, M. C. A Method for Characterizing Effective Pore Sizes of Catalysts. *J. Phys. Chem. B* **1999**, *103* (8), 1242–1249. DOI: 10.1021/jp984055n.

- [28] Sing, K. S. W.; Williams, R. T. The Use of Molecular Probes for the Characterization of Nanoporous Adsorbents. *Part. Part. Syst. Charact.* **2004**, *21* (2), 71–79. DOI: 10.1002/ppsc.200400923.
- [29] Kärger, J.; Ruthven, D. M.; Theodorou, D. N. *Diffusion in Nanoporous Materials*; Wiley-VCH Verlag & Co. KGaA, 2012.
- [30] Dubbeldam, D.; Calero, S.; Ellis, D. E.; Snurr, R. Q. RASPA: Molecular Simulation Software for Adsorption and Diffusion in Flexible Nanoporous Materials. *Mol. Simul.* **2016**, *42* (2), 81–101. DOI: 10.1080/08927022.2015.1010082.
- [31] Sławek, A.; Vicent-Luna, J. M.; Marszałek, B.; Makowski, W.; Calero, S. Quasi-Equilibrated Thermodesorption Combined with Molecular Simulation for Adsorption and Separation of Hexane Isomers in Zeolites MFI and MEL. *J. Phys. Chem. C* **2017**, *121* (35), 19226–19238. DOI: 10.1021/acs.jpcc.7b05347.
- [32] Van Koningsveld, H.; Van Bekkum, H.; Jansen, J. C. On the Location and Disorder of the Tetrapropylammonium (TPA) Ion in Zeolite ZSM-5 with Improved Framework Accuracy. *Acta Crystallogr., Sect. B: Struct. Sci.* **1987**, *43* (2), 127–132. DOI: 10.1107/S0108768187098173.
- [33] Baerlocher, Ch.; McCusker, L. B. Database of Zeolite Structures; <http://www.iza-structure.org/databases/> (accessed 2021-10-15).
- [34] Smith, W.; Forester, T. R. DL\_POLY 2.20: A General-Purpose Parallel Molecular Dynamics Simulation Package. *J. Mol. Graphics* **1996**, *14* (3), 136–141. DOI: 10.1016/S0263-7855(96)00043-4.
- [35] Ghysels, A.; Moors, S. L. C.; Hemelsoet, K.; De Wispelaere, K.; Waroquier, M.; Sastre, G.; Van Speybroeck, V. Shape-Selective Diffusion of Olefins in 8-Ring Solid Acid Microporous Zeolites. *J. Phys. Chem. C* **2015**, *119* (41), 23721–23734. DOI: 10.1021/acs.jpcc.5b06010.
- [36] Oie, T.; Maggiora, G. M.; Christoffersen, R. E.; Duchamp, D. J. Development of a Flexible Intra- and Intermolecular Empirical Potential Function for Large Molecular Systems. *Int. J. Quantum Chem.* **1981**, *20* (S8), 1–47. DOI: 10.1002/qua.560200703.
- [37] Frisch, M. J.; Trucks, G. W.; Schlegel, H. B.; Scuseria, G. E.; Robb, M. A.; Cheeseman, J. R.; Scalmani, G.; Barone, V.; Mennucci, B.; Petersson, G. A.; et al. *Gaussian 09*; Gaussian, Inc.: Wallingford, CT, 2009.

- [38] Catlow, C. R. A.; Freeman, C. M.; Vessal, B.; Tomlinson, S. M.; Leslie, M. Molecular Dynamics Studies of Hydrocarbon Diffusion in Zeolites. *J. Chem. Soc., Faraday Trans.* **1991**, *87* (13), 1947–1950. DOI: 10.1039/ft9918701947.
- [39] Thommes, M.; Kaneko, K.; Neimark, A. V.; Olivier, J. P.; Rodriguez-Reinoso, F.; Rouquerol, J.; Sing, K. S. W. Physisorption of Gases, with Special Reference to the Evaluation of Surface Area and Pore Size Distribution (IUPAC Technical Report). *Pure Appl. Chem.* **2015**, *87* (9–10), 1051–1069. DOI: 10.1515/pac-2014-1117.
- [40] Krishna, R.; Smit, B.; Calero, S. Entropy Effects during Sorption of Alkanes in Zeolites. *Chem. Soc. Rev.* **2002**, *31* (3), 185–194. DOI: 10.1039/b101267n.
- [41] Ocakoglu, R. A.; Denayer, J. F. M.; Marin, G. B.; Martens, J. A.; Baron, G. V. Tracer Chromatographic Study of Pore and Pore Mouth Adsorption of Linear and Monobranched Alkanes on ZSM-22 Zeolite. *J. Phys. Chem. B* **2003**, *107* (1), 398–406. DOI: 10.1021/jp0264533.
- [42] Pascual, P.; Ungerer, P.; Tavitian, B.; Pernot, P.; Boutin, A. Development of a Transferable Guest-Host Force Field for Adsorption of Hydrocarbons in Zeolites: I. Reinvestigation of Alkane Adsorption in Silicalite by Grand Canonical Monte Carlo Simulation. *Phys. Chem. Chem. Phys.* **2003**, *5* (17), 3684–3693. DOI: 10.1039/B304209J.
- [43] Dubbeldam, D.; Calero, S.; Vlugt, T. J. H.; Krishna, R.; Maesen, T. L. M.; Smit, B. United Atom Force Field for Alkanes in Nanoporous Materials. *J. Phys. Chem. B* **2004**, *108* (33), 12301–12313. DOI: 10.1021/jp0376727.
- [44] Lu, L.; Wang, Q.; Liu, Y. The Adsorption and Localization of Mixtures of C4- C7 Alkane Isomers in Zeolites by Computer Simulation. *J. Phys. Chem. B* **2005**, *109* (18), 8845–8851. DOI: 10.1021/jp0447439.
- [45] Smit, B.; Krishna, R. Molecular Simulations in Zeolitic Process Design. *Chem. Eng. Sci.* **2003**, *58* (3–6), 557–568. DOI: 10.1016/S0009-2509(02)00580-8.
- [46] Krishna, R.; van Baten, J. M. Diffusion of Hydrocarbon Mixtures in MFI Zeolite: Influence of Intersection Blocking. *Chem. Eng. J.* **2008**, *140* (1–3), 614–620. DOI: 10.1016/j.cej.2007.11.026.

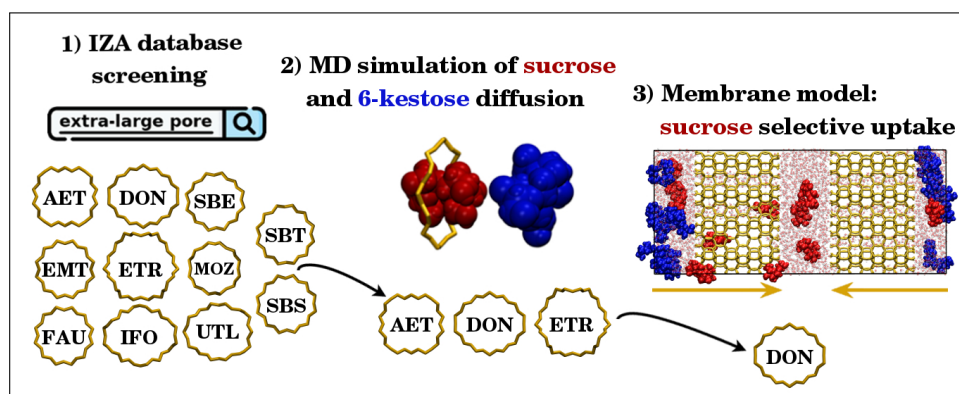


- [47] Denayer, J. F.; Souverijns, W.; Jacobs, P. A.; Martens, J. A.; Baron, G. V. High-Temperature Low-Pressure Adsorption of Branched C5-C8 Alkanes on Zeolite Beta, ZSM-5, ZSM-22, Zeolite Y, and Mordenite. *J. Phys. Chem. B* **1998**, *102* (23), 4588–4597. DOI: 10.1021/jp980674k.
- [48] Zhu, W.; Kapteijn, F.; Van der Linden, B.; Moulijn, J. A. Equilibrium Adsorption of Linear and Branched C6 Alkanes on Silicalite-1 Studied by the Tapered Element Oscillating Microbalance. *Phys. Chem. Chem. Phys.* **2001**, *3* (9), 1755–1761. DOI: 10.1039/b100941i.
- [49] Leflaive, P.; Pirngruber, G. D.; Faraj, A.; Martin, P.; Baron, G. V.; Denayer, J. F. M. Statistical Analysis and Partial Least Square Regression as New Tools for Modelling and Understanding the Adsorption Properties of Zeolites. *Microporous Mesoporous Mater.* **2010**, *132* (1–2), 246–257. DOI: 10.1016/j.micromeso.2010.03.004.
- [50] Vlught, T. J. H.; Zhu, W.; Kapteijn, F.; Moulijn, J. A.; Smit, B.; Krishna, R. Adsorption of Linear and Branched Alkanes in the Zeolite Silicalite-1. *J. Am. Chem. Soc.* **1998**, *120* (22), 5599–5600. DOI: 10.1021/ja974336t.
- [51] Vlught, T. J. H.; Krishna, R.; Smit, B. Molecular Simulations of Adsorption Isotherms for Linear and Branched Alkanes and Their Mixtures in Silicalite. *J. Phys. Chem. B* **1999**, *103* (7), 1102–1118. DOI: 10.1021/jp982736c.
- [52] Min, J. G.; Luna-Triguero, A.; Byun, Y.; Balestra, S. R. G.; Vicent-Luna, J. M.; Calero, S.; Hong, S. B.; Cambor, M. A. Stepped Propane Adsorption in Pure-Silica ITW Zeolite. *Langmuir* **2018**, *34* (16), 4774–4779. DOI: 10.1021/acs.langmuir.8b00628.
- [53] Olson, D. H.; Yang, X.; Cambor, M. A. ITQ-12: A Zeolite Having Temperature Dependent Adsorption Selectivity and Potential for Propene Separation. *J. Phys. Chem. B* **2004**, *108* (30), 11044–11048. DOI: 10.1021/jp040216d.
- [54] Bereciartua, P. J.; Cantín, A.; Corma, A.; Jordá, J. L.; Palomino, M.; Rey, F.; Valencia, S.; Corcoran, E. W.; Kortunov, P.; Ravikovitch, P. I.; Burton, A.; Yoon, C.; Wang, Y.; Paur, C.; Guzman, J.; Bishop, A. R.; Casty, G. L. Control of Zeolite Framework Flexibility and Pore Topology for Separation of Ethane and Ethylene. *Science* **2017**, *358* (6366), 1068–1071. DOI: 10.1126/science.aao0092.

- [55] Ferreira, A. F. P.; Mittelmeijer-Hazeleger, M. C.; Blik, A. Can Alkane Isomers Be Separated? Adsorption Equilibrium and Kinetic Data for Hexane Isomers and Their Binary Mixtures on MFI. *Adsorption* **2007**, *13* (2), 105–114. DOI: 10.1007/s10450-007-9010-z.

## Chapter 5

# Separation of an Aqueous Mixture of 6-kestose/sucrose with Zeolites: A Molecular Dynamics Simulation



Microporous and Mesoporous Materials, 2021, 319, 111031.

DOI: 10.1016/j.micromeso.2021.111031

Iria Bolaño Losada<sup>1</sup>, Pablo Grobas-Illobre<sup>1</sup>, Alechania Misturini<sup>1</sup>, Julio Polaina<sup>2</sup>, Yohanna Seminovski<sup>1</sup>, German Sastre<sup>1\*</sup>

<sup>1</sup> Instituto de Tecnología Química, Universitat Politècnica de València, Avda. de los Naranjos s/n, 46022 Valencia, Spain. \*E-mail: gsastre@itq.upv.es

<sup>2</sup> Instituto de Agroquímica y Tecnología de Alimentos, CSIC, Av. Agustín Escardino 7, Paterna, 46980 Valencia, Spain

## **Abstract**

Extra-large pore zeolites are a small subset (21) among the whole list of 253 zeolites available. The discovery of new low-glycemic sugars is very attractive as new healthy additives in the food field. This is the case of the 6-kestose. In the present case, it appears in a mixture in aqueous solution together with sucrose, the separation of the mixture being necessary. For this, we have focused on using certain zeolites with adequate pore sizes that allow the separation of this mixture, considering that since the molecular size of 6-kestose is greater than sucrose, it is necessary to promote the sorption of the latter, so that the first can be purified. After a computational screening of micropores of the 253 IZA zeolites, 11 zeolites were selected. Of these, 3 extra-large pore zeolites (AET, DON, ETR) have been proposed, which were analyzed in-depth through a molecular dynamics study considering the external surface. The results show that DON presents the most promising theoretical results for a selective sucrose/6-kestose separation.

**Keywords:** Zeolites, Sucrose, 6-kestose, Molecular Dynamics, Computational screening.

## **5.1 Introduction**

Zeolites constitute a substantial family of crystalline materials, whose application covers different fields, such as catalysis, separations, ion exchangers, and adsorbents [1]. Their structure is shaped by a three-dimensional tetrahedral periodic framework, from which a high porosity arises due to the nanometer-sized channels that they host. This feature, combined with their wide surface area, explains their adsorption properties. Thus, they are used as molecular sieves for the separation of molecules and ions, being the microporous size of the structures that defines their size-separation capacity [2, 3]. At the present time, 253 different zeolite framework types have been described, and can be found at the International Zeolite Association (IZA) website [4].

The presence of hydrophilic silanol surface groups and aluminum atoms locally compensate for the rest of the silica framework, which is hydrophobic. The presence of hydrophilic centres creates the possibility to selectively adsorb polar molecules. In particular, water molecules interact with the oxygens of the zeolite framework through H-bonding and also with Brønsted sites in the zeolite, if present, through the water oxygens. Additional effects may be achieved regarding selectivity, which can be due not to the chemical nature of the framework but rather due to the topology of the micropores in what is usually called ‘shape selectivity’. This phenomenon favours the adsorption of molecules, through van der Waals interactions, when their shape is similar to that of the micropore [5].

Computer simulations approaches based in a combination of classical force fields and molecular dynamics (MD), are considered an outstanding tool to tackle the

theoretical evaluations concerning diffusion [6–9]. The use of MD allows to study the evolution of a molecule of interest with time, under specific selected conditions while analyzing a wide area of the potential energy surface involved, conditions which might be chosen so its direct comparison or application to an experimental problem [10]. Regarding the use of a flexible zeolite framework, it has been cautioned in several publications that the calculation of the diffusion coefficients from these studies are really sensitive to the force field used [11, 12].

Using separation technology, zeolites can be suggested as key materials in glucose-fructose separation. The adsorption of carbohydrates in the liquid phase has been successfully investigated in hydrophobic Y zeolites where the pores of the zeolite are enriched with the saccharide molecules and there is therefore a high specific adsorption of carbohydrates [13]. Beta zeolites have also been shown to have similar effects [14, 15]. The use of zeolites in the chromatographic separation of carbohydrates has been investigated for the separation of the mixture glucose-fructose [16–18], glucose-sucrose-sorbitol [19] and oligosaccharides of fructose [20]. In addition, the adaptation of FAU zeolite to replace organic polymeric resins as inorganic ion exchangers was investigated in the separation of isomaltose-oligosaccharide saccharide mixture in a liquid chromatography [21].

6-Kestose is an oligosaccharide of industrial interest because of its prebiotic and other functional properties. Consequently, efficient procedures for the production of this sugar have been devised [22]. A significant technical problem of the production procedure is the need to purify 6-kestose from sucrose. The separation of sucrose and 6-kestose in zeolites modeled in this study is just a representative example whose results could be applied to the separation of other oligosaccharides obtained by enzymatic synthesis, a procedure which is gaining industrial relevance [23]. In the present work, the capability of different zeolites for the separation of a sucrose/6-kestose mixture in aqueous solution has been evaluated.

In the separation of 6-kestose and sucrose, as well as other oligosaccharides, sugar concentration and temperature are crucial parameters. For practical reasons (productivity), sugar concentration, limited by solubility (an intrinsic property of each sugar, which is a function of temperature), should be as high as possible. An optimum temperature should be selected that maximizes sugar solubility, stability and energy saving. Approaching boiling point temperature risks sugar denaturalization either by Maillard reaction or caramelization [24]. The presence of amino acids, causing Maillard reaction, in oligosaccharide preparations obtained by enzymatic synthesis should be taken into account. Zeolites can be an alternative to nanofiltration, currently used industrially for oligosaccharide separation [25].

Taking advantage of the large variety of pore sizes in zeolites, we explore whether there are suitable candidates for the separation of sugars. We employ the IZA (International Zeolite Association) database and a definition of ad hoc parameters that may maximize the separation in order to select candidates [4]. After a short list was generated, MD simulations of sugars in a selection of candidate zeolites allowed us to estimate if there are large differences in the mobility of the sugars selected.

## 5.2 Methodology and Models

### 5.2.1 Sucrose and 6-kestose geometries for diffusion.

Sucrose and 6-kestose are two relatively large molecules whose conformations, in molecular dynamics simulations, are expected to give rise to a variability in their corresponding molecular size, which in turn will influence whether or not the sugar molecules can fit in different zeolite micropores. As a first estimation, their molecular size was roughly estimated, using a recently developed algorithm, from the ground state geometries obtained through first-principles calculations using the Gaussian16 package [26].

Density functional theory (DFT) geometry optimizations were performed with the B3LYP [27] exchange-correlation hybrid functional and the Pople-type 6-311G basis set [28]. Grimme's D3 empirical dispersion correction [29, 30] were also included to account for van der Waals interactions. Geometry optimizations were performed without including the effect of solvent (water).

Once ground state geometries (Figure 5.1) have been obtained, molecular size has been calculated with the 'shoebox' algorithm [31]. The algorithm finds the two atoms of maximum intramolecular distance and makes a rotation to define a new x axis along those two atoms, and calculates maximum intramolecular distances along two axes (y,z) perpendicular to x. In the new coordinate system, the maximum and minimum coordinates over the three axes define a box (xmax-xmin, ymax-ymin, zmax-zmin) of nearly minimum size (similarly to shoe boxes), and whose values, ordered from largest to shortest are our definition of molecular size ( $\Phi$ ). The results obtained (in Å) are  $\Phi_S$  : 9.4, 7.5, 6.3 for sucrose and  $\Phi_K$  : 11.4, 9.1, 6.7 for 6-kestose molecules. A configuration search study [32] was carried out to find how molecular size (and hence fitting in zeolite pores) can be affected by sugar conformations. Details are given in Section C1 of Appendix C. The molecular size of the selected configuration (Figure 5.1) is representative of the

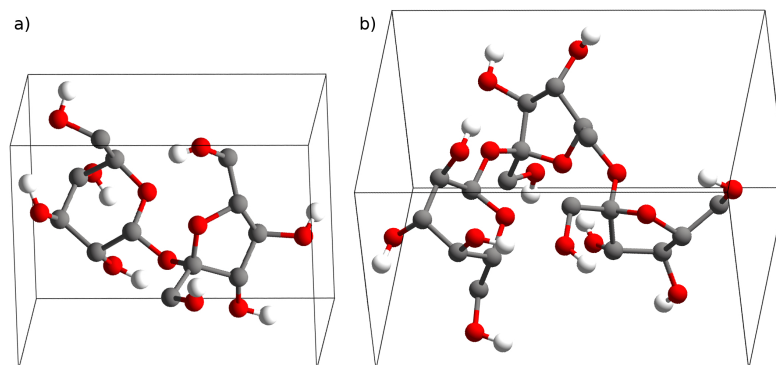


**Figure 5.1:** Structures of the sugar molecules framed by shoebox algorithm. a) sucrose ( $C_{12}H_{22}O_{11}$ ) disaccharide showing cyclohexane (glucose) and cyclopentane (fructose) rings; and b) 6-kestose ( $C_{18}H_{32}O_{16}$ ) trisaccharide, showing cyclohexane (glucose) and 2 cyclopentane (fructose) rings. The dimensions  $\Phi(x,y,z)$ , in Å, are  $\Phi_S : (9.4, 7.5, 6.3)$  for sucrose and  $\Phi_K : (11.4, 9.1, 6.7)$  for 6-kestose. Atoms colors are O: red, C: gray, H: white. For the sake of clear visualization, aliphatic hydrogens were omitted.

configurations found during the search and can be considered a valid estimation to assess candidate zeolites for separation of the sugars.

### 5.2.2 Selection of potential zeolites for sucrose/6-kestose separation.

The main objective of this work is to find an appropriate zeolite to separate 6-kestose and sucrose. Target zeolites should allow the diffusion of sucrose and preclude 6-kestose. A first selection of zeolites has been made by comparing micropore size with sugar dimensions. Micropore size has been tabulated according to the maximum diameter of a sphere that can diffuse (along a,b,c crystallographic directions), defined according to Foster et al. [33], available from the IZA Atlas [4]. Molecular size has been calculated according to the ‘shoebox’ algorithm, as explained in the above section (Figure 5.1). Molecular diffusion proceeds with the molecule aligned with the diffusion channel, hence only ‘y’ and ‘z’ dimensions need to be compared with the micropore size. For diffusion to be allowed, y and z should be smaller than one (or more) zeolite channel dimension (either a, b, or c). For diffusion to be precluded, y or z should be larger than all zeolite micropore dimensions (a, b and c). Applying these criteria to all 253 zeolites in the IZA database, a selection of 11 (Table 5.1) was made that, in principle, may allow the diffusion of sucrose and preclude the diffusion of 6-kestose. The zeolites are: AET, DON, EMT, ETR, FAU, IFO, MOZ, SBE, SBS, SBT, and UTL (Figure 5.2).

**Table 5.1:** Preliminary analysis of 11 zeolites for sucrose and 6-kestose separation. Micropore data for zeolites includes: maximum diameter of sphere that can be included (d), maximum diameter of sphere that can diffuse in directions a, b, c (relevant values in bold), channel size (Å), and ring size. Sucrose diffusion will be allowed if  $\Phi_S(y,z)$  (Figure 5.1) is equal or smaller than zeolite diffusion channel. 6-kestose diffusion will be precluded if  $\Phi_K(y$  and/or  $z)$  (Figure 5.1) is larger than zeolite diffusion channel.

Zeolite	Micropore Size (Å)						Molecular size and comparison with micropore size	
	d	a	b	c	channel size	ring size	$\Phi_S$ : 9.4, 7.5, 6.3	$\Phi_K$ : 11.4, 9.1, 6.7
AET	8.4	1.8	1.8	<b>7.6</b>	7.9×8.7	14	$\Phi_S(y,z) \cong \text{AET}(c)$	$\Phi_K(y) > \text{AET}(c)$
DON	8.8	2.2	1.8	<b>8.1</b>	8.1×8.2	14	$\Phi_S(y,z) > \text{DON}(c)$	$\Phi_K(y) > \text{DON}(c)$
EMT	11.6	<b>6.5</b>	<b>6.5</b>	<b>7.4</b>	7.3×7.3	12	$\Phi_S(y,z) \cong \text{EMT}(a,b,c)$	$\Phi_K(y) > \text{EMT}(a,b,c)$
ETR	10.1	2.9	2.9	<b>9.3</b>	10.1×10.1	18	$\Phi_S(y,z) > \text{ETR}(c)$	$\Phi_K(y,z) > \text{ETR}(c)$
FAU	11.2	<b>7.4</b>	<b>7.4</b>	<b>7.4</b>	7.4×7.4	12	$\Phi_S(y,z) \cong \text{FAU}(a,b,c)$	$\Phi_K(y) > \text{FAU}(a,b,c)$
IFO	7.8	<b>7.2</b>	2.0	1.1	9.3×10.6	16	$\Phi_S(y,z) \cong \text{IFO}(a)$	$\Phi_K(y) > \text{IFO}(a)$
MOZ	10.0	3.4	3.4	<b>7.5</b>	6.8×7.0	12	$\Phi_S(y,z) \cong \text{MOZ}(c)$	$\Phi_K(y) > \text{MOZ}(c)$
SBE	12.5	<b>7.3</b>	<b>7.3</b>	3.9	7.2×7.4	12	$\Phi_S(y,z) \cong \text{SBE}(a,b)$	$\Phi_K(y) > \text{SBE}(a,b)$
SBS	11.5	<b>7.3</b>	<b>7.3</b>	5.7	6.9×7.0	12	$\Phi_S(y,z) \cong \text{SBS}(a,b)$	$\Phi_K(y) > \text{SBS}(a,b)$
SBT	11.2	<b>7.3</b>	<b>7.3</b>	5.7	7.3×7.8	12	$\Phi_S(y,z) \cong \text{SBT}(a,b)$	$\Phi_K(y) > \text{SBT}(a,b)$
UTL	9.3	1.4	5.8	<b>7.6</b>	7.1×9.5	14	$\Phi_S(y,z) \cong \text{UTL}(c)$	$\Phi_K(y) > \text{UTL}(c)$

### 5.2.3 Molecular Dynamic Simulation.

Molecular dynamics was performed using the DL\_POLY program (version 2.20) [34]. The force field of Bushuev and Sastre [5] was employed for zeolite frameworks, consisting of a harmonic expression for three body interactions, along with Coulomb and Lennard-Jones potentials for the nonbonded interactions. When the zeolite surface was modeled, H–O bonds of silanol groups were defined by a Morse potential [10]. A flexible version of the SPC model [35] was employed for the water molecules, proposed for zeolite systems in aqueous media [5]. Sucrose and 6-kestose bonded terms described bond stretching and bending with harmonic expressions, and torsional barriers by a truncated Fourier series, as defined by Oie et al. force field [36]. The point charges assigned to sugar atoms were computed by the Gasteiger-Marsili method [37] as implemented in Open Babel [38]. Van der Waals interactions between sugar atoms came from the UFF force field [39], while its interaction with zeolite were considered as reported by Kiselev and co-workers [40, 41]. The remaining Lennard-Jones parameters needed were obtained by applying Lorentz-Berthelot combination rules. A complete force field description can be found in the Appendix C (Section C2).

Systems were simulated in the NVT ensemble, where the constant temperature of 338 K was ensured by Evans thermostat [42]. Periodic boundary conditions were applied to avoid finite box-size effects. For the nonbonded forces, a cutoff of 9.0 Å was considered, and the Ewald summation was applied to deal with



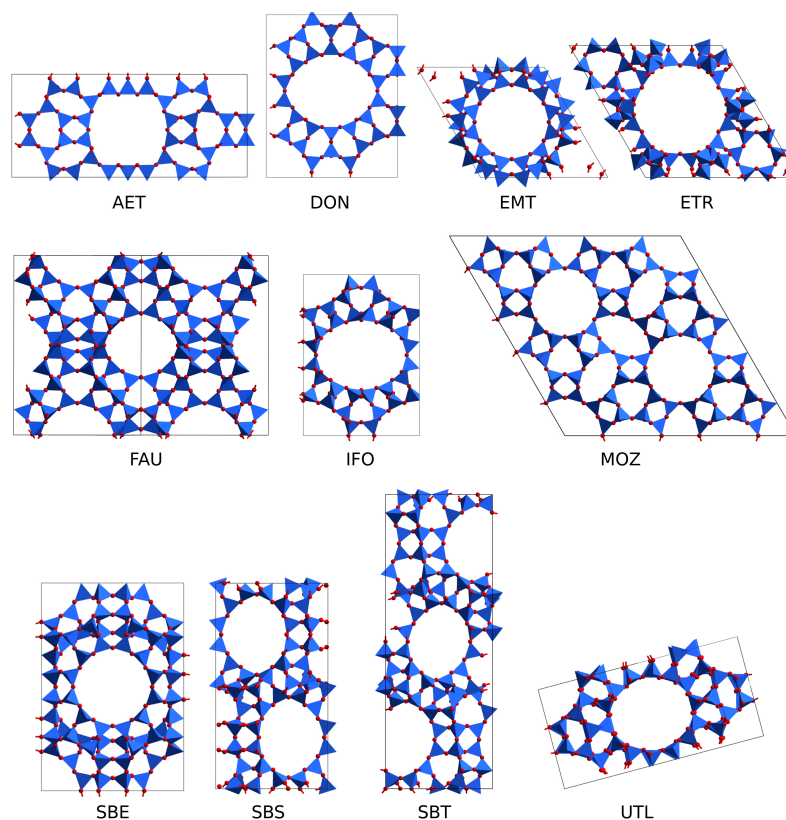


**Figure 5.2:** Zeolite structures selected to study sucrose and 6-kestose diffusion. Views show the channel for diffusion in AET, DON, EMT, ETR, FAU, IFO, MOZ, SBE, SBS, SBT and UTL. The same scale is used for all figures.

long-range interactions. Considering a time step of 1.0 fs, simulation boxes were equilibrated for 20 ps, thereafter the trajectories were calculated for either 10 (bulk) or 20 (membrane) ns, with time evolution being computed by the Velocity Verlet algorithm. Diffusion coefficients were calculated (Appendix C, Section C3) for the bulk systems using the data from the first 5 ns of the mean square displacement plots.

Two types of systems (Table 5.2) were simulated, called bulk and membrane, corresponding to increasing accuracy. ‘Bulk’ models contain the usual 3-D zeolite periodic model without external surface and one sugar molecule is located inside the micropore, with all atoms of the system (between 729 and 2277) allowed to relax and their trajectories being recorded for 10 ns. ‘Membrane’ models

contain two zeolite layers separated by 20 Å, producing two reservoirs, with sugar molecules initially located in one of these reservoirs, outside the zeolite, and were run for 20 ns. Some zeolite atoms were fixed in order to keep the zeolite layer separation since, otherwise, both tend to approximate each other.

**Table 5.2:** Models employed for the molecular dynamics simulations, specifying the number of silanol groups ( $\text{SiO}_{3/2}\text{H}$ ) and silica units ( $\text{SiO}_2$ ) of the zeolite, as well as the number of sucrose, 6-kestose, and water molecules. Bulk models (without silanols) contain only 1 sugar molecule, run for 10 ns, and were used for low accuracy calculations. Membrane models (those with silanols) run for 20 ns, and contain much larger unit cells, with number of sugar molecules being: 8 (AET, DON, ETR) at low loading (Section 5.3.2.1); and 18 (ETR) or 24 (AET, DON) at high loading (Section 5.3.2.2).

Zeolite	$\text{SiO}_2$	$\text{SiO}_{3/2}\text{H}$	Suc	Kes	Water	Zeolite	$\text{SiO}_2$	$\text{SiO}_{3/2}\text{H}$	Suc	Kes	Water
AET	575	0	1	0	54	SBE	256	0	1	0	57
AET	575	0	0	1	56	SBE	256	0	0	1	55
DON	256	0	1	0	31	SBS	384	0	1	0	94
DON	256	0	0	1	30	SBS	384	0	1	0	92
EMT	384	0	1	0	99	SBT	576	0	1	0	140
EMT	384	0	0	1	97	SBT	576	0	0	1	133
ETR	192	0	1	0	36	UTL	304	0	1	0	54
ETR	192	0	0	1	37	UTL	304	0	0	1	48
FAU	192	0	1	0	52	AET	1728	288	4	4	3347
FAU	192	0	0	1	51	DON	1536	256	4	4	3150
IFO	384	0	1	0	113	ETR	1344	192	4	4	2400
IFO	384	0	0	1	111	AET	1728	288	12	12	3054
MOZ	648	0	1	0	89	DON	1536	256	12	12	2868
MOZ	648	0	0	1	89	ETR	1344	192	9	9	2190

Zeolite layers were terminated by silanol groups, which were allowed to relax. To obtain more realistic results, water molecules were added to all systems, using Packmol software [43], to simulate the aqueous solution in which the sugar separation process should be performed. The water content could not be calculated according to the expected uptake, since no water isotherms on these systems are available. Instead, a water content was selected so that full solvation of sugar molecules was achieved, and the water density was 0.98 g/cm<sup>3</sup>. Selected membrane systems were simulated during 20 ns for simulation boxes with low (four sucrose and four 6-kestose) and high sugar loading (nine sucrose and nine 6-kestose for ETR; twelve sucrose and twelve 6-kestose for AET and DON).

## 5.3 Results

### 5.3.1 Mobility of sucrose and 6-kestose in AET, DON, EMT, ETR, FAU, IFO, MOZ, SBE, SBS, SBT, UTL zeolites.

As a first insight into the mobility of sugars in the 11 candidate zeolites (AET, DON, EMT, ETR, FAU, IFO, MOZ, SBE, SBS, SBT, UTL), 10 ns molecular dynamics in bulk systems with only one sugar molecule were performed (Table 5.2). Although 10 ns is a moderately large simulation time, having only one sugar molecule in the unit cell will preclude obtaining valuable statistics, and these calculations will be taken only to qualitatively guess the most promising zeolites for sucrose/6-kestose separation.

Figures 5.3 and 5.4 show the mobility of sucrose and 6-kestose in the different zeolites. Mobility itself will not be used as the main criteria, but rather diffusion coefficients, obtained from mobility-related parameters (mean square displacements versus time), will be used. Although displacements are small, only a qualitatively different mobility for sucrose, larger than that for 6-kestose is needed in order to select the corresponding system for a more in-depth study that will assess more accurately the possible separation of sucrose/6-kestose mixtures. Figures 5.3 and 5.4 show a similar mobility for sucrose and 6-kestose except in the cases of DON, AET, ETR and IFO.

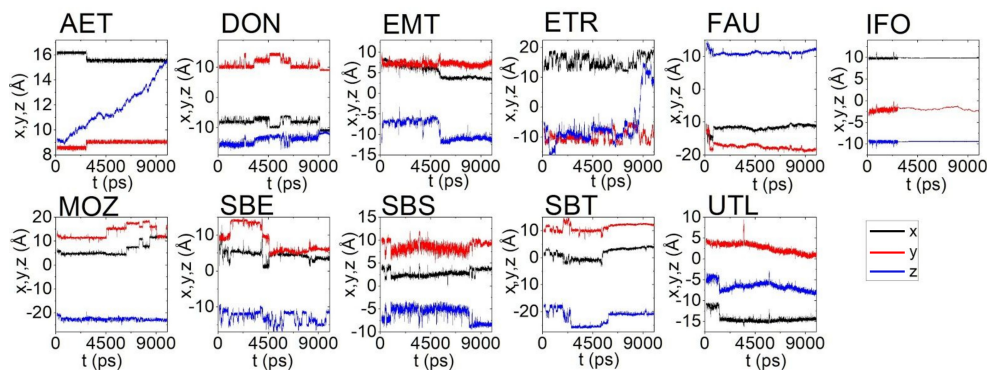


**Figure 5.3:** Mobility of sucrose in: AET, DON, EMT, ETR, FAU, IFO, MOZ, SBE, SBS, SBT, UTL, at 338 K. All systems contain water molecules. Black, red and blue colors represent sucrose position in the x, y and z axis respectively.

In AET and ETR a clearly larger mobility for sucrose than 6-kestose can be observed. In DON, although the mobility of sucrose is small, the mobility of 6-kestose is extremely small. IFO is a representative case of zeolites in which,

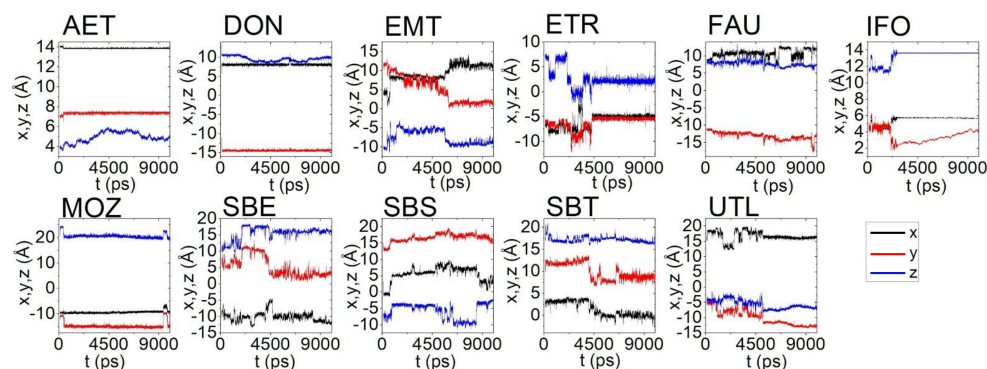


**Figure 5.4:** Mobility of 6-kestose in: AET, DON, EMT, ETR, FAU, IFO, MOZ, SBE, SBS, SBT, UTL, at 338 K. All systems contain water molecules. Black, red and blue colors represent 6-kestose position in the x, y and z axis respectively.

surprisingly, the mobility of 6-kestose is larger than that of sucrose. The small mobility of sucrose might be due to a nearly perfect match of  $O \cdots H$  bonding between zeolite oxygens and alcohol hydrogens. With the larger 6-kestose, the fit would be less pronounced, leading to a larger mobility. Other zeolites in which this ‘anomalous’ behaviour of lower mobility for the smaller sugar is observed are FAU, MOZ, SBE, SBS, UTL.

Diffusion coefficients show low diffusivity, but the values obtained allow to confirm the conclusions above regarding the relative mobility of sugars. Mean square displacement plots are included in the Appendix C (Section C3), from which diffusion coefficients have been obtained. For the purpose here, the ratio of diffusion coefficient sucrose/6-kestose in each zeolite is meaningful (Table 5.3). The values indicate a larger preliminary separation value for ETR, AET, DON, in agreement with the conclusion above. We have disregarded the subset of zeolites showing ‘anomalous’ behaviour (IFO, FAU, MOZ, SBE, SBS, UTL), with larger diffusivity for the bulkier sugar. In particular, IFO is not a good candidate since although having a large pore dimension,  $9.3 \times 10.6 \text{ \AA}$ , sufficient for diffusion of sucrose and 6-kestose, the largest sphere that can diffuse through IFO channels is much smaller (due to channel ellipticity),  $7.2 \text{ \AA}$  along [100]. Hence, the zeolites selected for a more in-depth study of their capability for sucrose/6-kestose separation are: AET, DON, ETR.

The temperature selected for our molecular dynamics runs was 338 K, since it is the best temperature fulfilling the conditions of: i) being not too high, which would pose an economic penalty in any further possible application, and ii) being

**Table 5.3:** Ratio of diffusion coefficients for sucrose/6-kestose in zeolites at 338 K.

Zeolite	$D_S/D_K$
AET	7.5
DON	4.8
EMT	0.9
ETR	8.5
FAU	0.8
IFO	0.01
MOZ	0.6
SBE	0.2
SBS	0.2
SBT	2.2
UTL	0.3

able to give sufficiently different mobility for sucrose and 6-kestose. Results at 298 K give too similar mobilities for sucrose and 6-kestose, whilst temperatures of 378 K and higher do not give significant differences from the results shown here at 338 K. Results at 378 K are shown in the Appendix C (Section C3). Operating conditions at 338 K (chosen for this study) represent a convenient upper limit that maximizes sugar solubility and stability. Although degradation of sucrose and 6-kestose in an environment free of enzymes and acids is not expected to happen at the considered temperatures, it is safer to avoid large temperatures such as 378 K to avoid the risk of sugar denaturalization either by Maillard reaction or caramelization.

### 5.3.2 Uptake of sucrose/6-kestose mixture in AET, DON and ETR membranes.

#### 5.3.2.1 Dilute sugar loading

The mobilities of sucrose and 6-kestose in the AET, DON and ETR membranes (Figure 5.5) are shown in the Appendix C (Section C4). Membranes have been created with the general strategy of allowing uptake of sucrose and 6-kestose in a realistic system in which a mixture of both sugars is present. In a first approach, 4 molecules of each sugar have been introduced near the external surface of the zeolite to improve statistics, instead of only one as in previous zeolite-bulk calculations. A sufficient number of water molecules has been introduced in each of the AET, DON and ETR systems (3347, 3150 and 2400, respectively, see Table 5.2), which have been distributed along all parts of the system (both reservoirs and channels of zeolite layers).

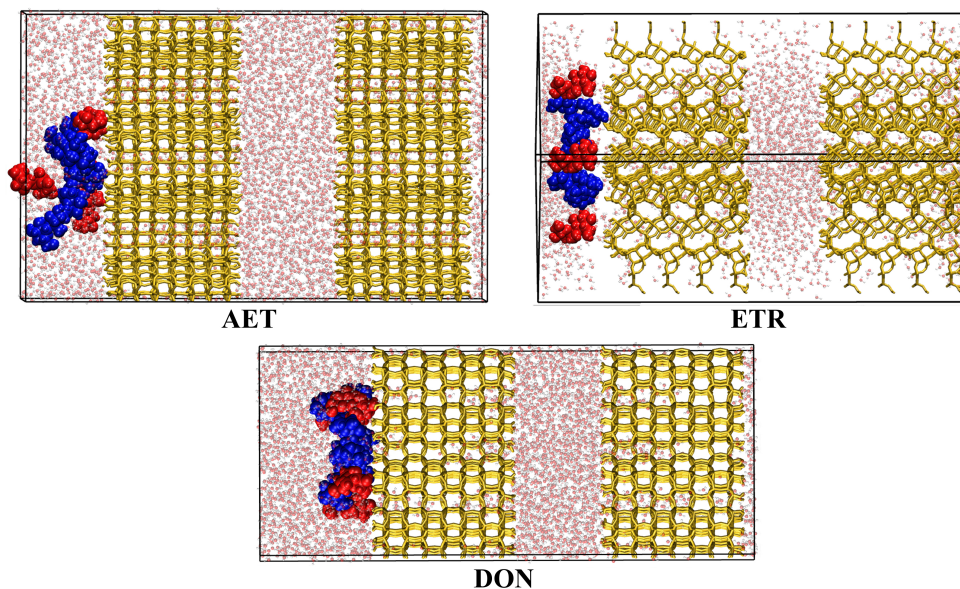


**Figure 5.5:** Initial configurations of AET, DON and ETR membrane systems (yellow) containing two parallel layers (terminated by silanol groups) of ca. 31-36 Å thickness, separated by two reservoirs. Reservoir-1 (left) is initially filled with water (transparent), 4 sucrose (red) and 4 6-kestose (blue) molecules, whilst reservoir-2 (middle) is initially filled only with water molecules. Water molecules do also locate inside zeolite micropores.

At low loading (4 sucrose and 4 6-kestose molecules) none of the membranes show significant uptake after 20 ns (Figures 5.6 and 5.7). The reason is that sugar molecules interact strongly with the zeolite external surface and remain attached, with little probability to jump into the channel (Figures C7 to C10), in agreement with the so called ‘surface barrier’ effect [44].

Sugar adsorption over the zeolite surface is more energetically accessible, rather than the sugar flow through the zeolite cavity. At dilute solutions, the significant sugar-zeolite interaction in the surface hinders the sugar displacement through the zeolite. At increased loadings the external surface will become quickly saturated with a monolayer of sugar molecules, after which the incoming molecules will interact less strongly with the zeolite external surface and hence diffusion into the channel will become more probable. In our models this can be simulated by increasing the sugar loading, which is compatible with its high solubility (2100 g/L for sucrose at 298 K [45]). Among the membranes investigated, ETR presents the thickest external surface (Figure C11), that together with the number of silanol sites to anchor the sugar molecule, contributes to increase the barrier to enter the

zeolite channel. More details of surface effects are analysed in the Appendix C (Section C5).

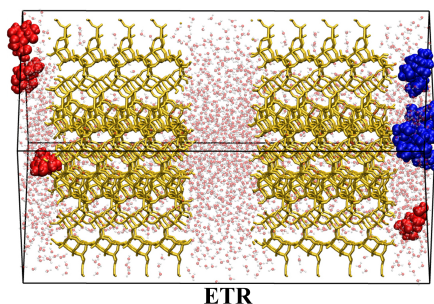


**Figure 5.6:** Uptake of a low loading sucrose (red, 4 molecules)/6-kestose (blue, 4 molecules) mixture in water (transparent) in ETR membrane (yellow) at 338 K after 20 ns. The figure shows no uptake at this low sugar loading after 20 ns.

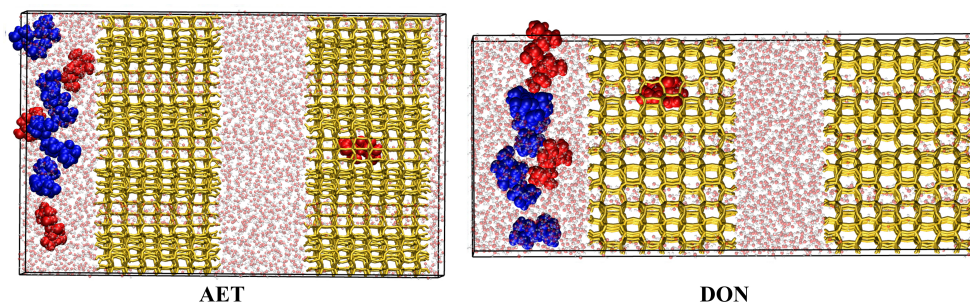


**Figure 5.7:** Configuration showing the largest uptake of sucrose into AET (left) and DON (right) membranes (yellow) at 338 K after 20 ns with low sugar concentration (4 sucrose molecules in red, and 4 6-kestose molecules, in blue) in water (transparent). The figure shows a maximum uptake of 1 sucrose molecule at this low sugar loading.

### 5.3.2.2 Large sugar loading

In order to remove the effect of the surface barrier, two large loadings, 9+9 (ETR) and 12+12 (AET and DON) molecules of sucrose and 6-kestose were considered (Figures 5.8 and 5.9).

An analysis was carried out of the sugar location throughout the 20 ns simulation, with detailed trajectories shown in Figures C12 to C14. A representative configuration is shown in Figure 5.10 for each zeolite. It can be seen that sugar uptake is, in all three cases (AET, DON, ETR), preferentially observed for sucrose

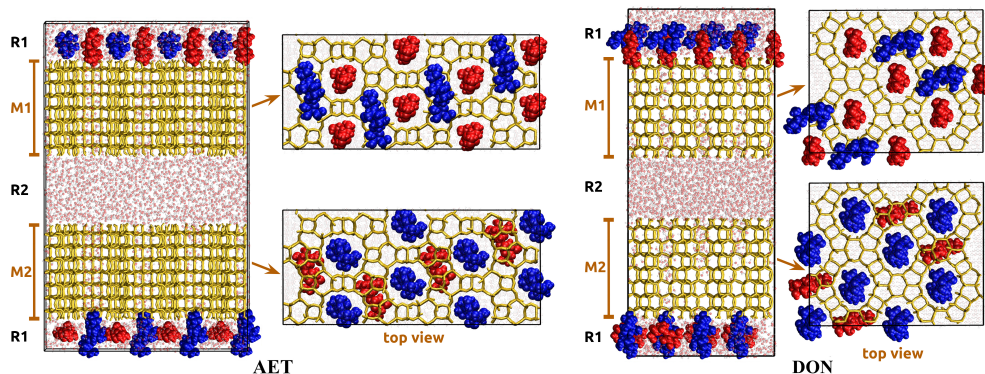


**Figure 5.8:** Initial configuration of AET (left) and DON (right) membranes with the largest sugar loading, 12 sucrose (red) and 12 6-kestose (blue) molecules, in water (transparent). The MD simulations are carried out for 20 ns at 338 K. All sugar molecules are initially located at reservoir-1 (top and bottom part of the unit cell) whilst reservoir-2 (middle part of the unit cell) is initially empty of sugar molecules.

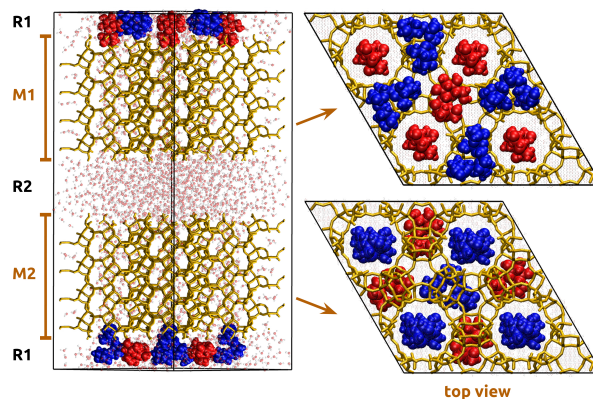


**Figure 5.9:** Initial configuration of ETR membrane with large sugar loading, 9 sucrose (red) and 9 6-kestose (blue) molecules, in water (transparent). The MD simulations are carried out for 20 ns at 338 K. All sugar molecules are initially located at reservoir-1 (top and bottom part of the unit cell) whilst reservoir-2 (middle part of the unit cell) is initially empty of sugar molecules.

(red) whilst 6-kestose (blue) remains outside the zeolite, in reservoir-1. Although AET and ETR are selective for sucrose uptake, the flux of molecules does not seem particularly large. Nevertheless, DON shows not only a selective uptake of sucrose but also a very high molecular flux (Figure 5.11), as can be seen from some molecules reaching, or being very close to, reservoir-2. The increase in sugar



concentration substantially promoted the uptake and diffusion of sucrose into the three systems.

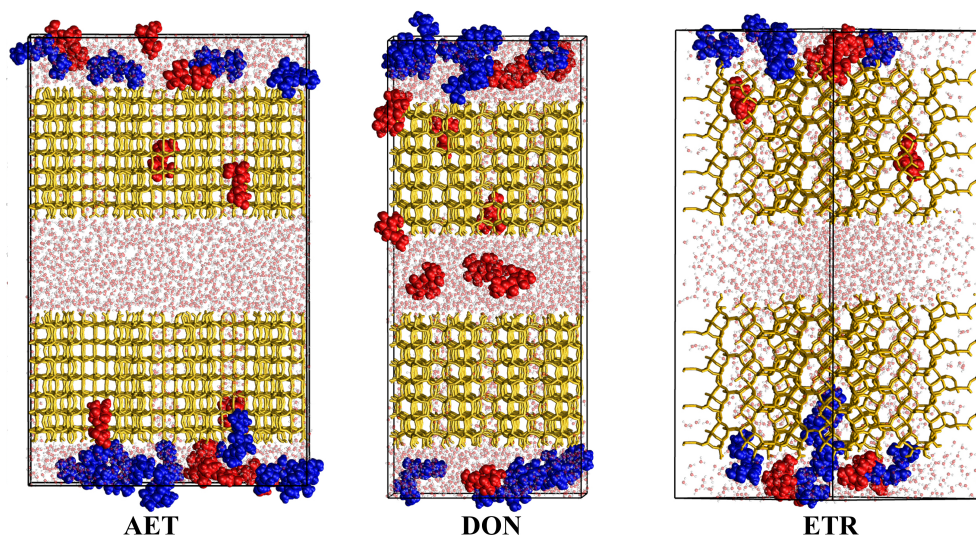


**Figure 5.10:** Representative configurations showing sugar uptake into AET, DON and ETR membranes (yellow) with large loading of: 9+9 (ETR) and 12+12 (AET, DON) sucrose (red) and 6-kestose (blue) molecules. Water molecules shown with transparency.

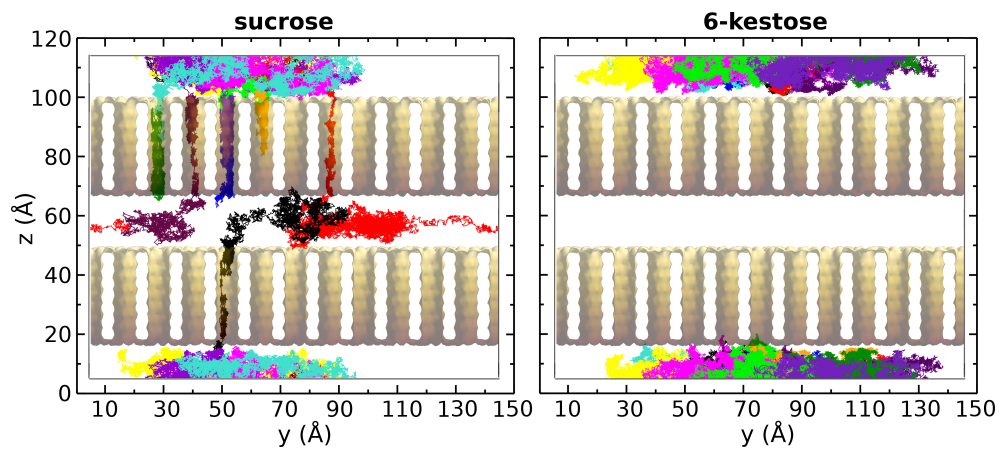


**Figure 5.11:** Sucrose (left) and 6-kestose (right) trajectories during MD simulation (at 338 K during 20 ns) of DON membrane in a mixture containing large sugar loading (12 sucrose and 12 6-kestose molecules).

An attempt to rationalize the results in terms of pore size and surface effects is mandatory, but not easy. These concepts are invoked, as in this study, in order to make a selection of candidates, but the quantitative results can only be found through the MD simulations. These three zeolites (AET, DON, ETR) already showed the largest diffusivity for sucrose with respect to 6-kestose (see Table 5.2). The pore size and largest sphere that can diffuse are largest for ETR ( $10.1 \times 10.1$  Å and 9.3 Å), hinting that ETR would show the largest flux, but this is not the case, perhaps due to an interaction zeolite-sugar less stabilizing when compared with a sucrose molecule tightly fitted in a channel. According to the relatively narrow values ( $7.9 \times 8.7$  Å and 7.6 Å), AET could be predicted as a zeolite with low flux, and this is indeed found. For DON, the best system found, the pore size and largest sphere that can diffuse ( $8.1 \times 8.2$  Å and 8.1 Å) also indicate it should be a good candidate as it is indeed the case. Longer simulations and larger unit cells could give a more accurate picture, but the current membrane models already give an excellent assessment and allow to confirm that the three zeolites (AET, DON, ETR) are good candidates for selective uptake of sucrose in a sucrose/6-kestose mixture. The MD calculations also indicate DON should be the best candidate due to the large and selective sucrose flux observed.

### 5.3.3 Discussion

Diffusion of sucrose and 6-kestose in extra-large pore zeolites is certainly slow, but still trends have been obtained and assessment of suitable structures for selective diffusion of sucrose has been possible. Both sugars considered, sucrose and 6-kestose, are large in size, with many degrees of freedom and a complex conformational space so that entering the zeolite channels becomes probabilistically difficult.

Bulk systems focus on the behaviour of sugar molecules once inside the micropores and were used as an intermediate step to focus on more realistic systems (that we called membranes) in which the role of the external surface is included. In fact, the role of the external surface (Appendix C, Section C5) has been demonstrated to be crucial, since large molecules do have a strong tendency to remain adsorbed on the external surface. This is one of the difficulties for entering the micropore, with the second difficulty being, as described above, the conformational suitability needed between sugar and micropore. The third aspect is that adsorption at the external surface contributes to pore blocking. With 9.4 and 11.4 Å length for sucrose and 6-kestose, respectively, adsorption near the pore entrance (between 6.8 and 10.6 Å) can easily lead to pore blocking.

The sugar loading simulated in the membranes was deliberately chosen as not small. We tried in this way to include the effects of possible pore blocking and sugar-sugar interactions that appear at high sugar concentration. And indeed we were able to observe sugar (sucrose) uptake in the three best candidate membranes considered (AET, DON, ETR). The increase of loading was demonstrated to be a crucial effect. At larger than monolayer loading the sugar-surface interactions become weaker for those molecules outside the monolayer and this is the factor that allows sugar uptake. We have included a simple energetic analysis to illustrate this aspect (Appendix C, Section C7).

Regarding the synthetic feasibility of the four materials selected, AET [46] has been obtained as  $\text{AlPO}_4$  composition and is hydrothermally stable at the temperature (338 K) suggested for the separation. DON is an even more convenient material since it can be synthesized as pure silica [47], with higher hydrothermal stability than AET. ETR [48] is so far not applicable to this separation since its chemical composition is a gallo-alumino-silicate with a considerably high content of Ga,  $\text{Ga}/(\text{Si}+\text{Al}+\text{Ga})=24\%$ . Thin zeolite membranes, in particular with high-aspect-ratio nanosheets and uniform thickness, similar to those described with the simple models in this study, have been recently prepared in the group of Tsapatsis and have demonstrated excellent performance for the selective separation of p-xylene from a xylenes mixture [49].

Water molecules play a particularly important role through solvation of sugar molecules and interaction with external silanols, as described in previous work [50]. Sugar(surface)-water and sugar(micropore)-water radial distribution functions (Appendix C, Section C6) show the different effects of sugar solvation. The uptake of sugars is heavily influenced by the presence of water. Water uptake (intrusion) in small and medium pore pure silica zeolites is very small at lower pressure than water saturation vapor pressure [51, 52] and this is also what we find in the membrane systems studied. Although external silanols can be eliminated from the external surface [53] in order to make it more hydrophobic, presumably leading to a reduced surface barrier and larger uptake, it is so far less than obvious that this can be applied as a general procedure, and so we stick to our model to the typical silanol termination. The important role of water is confirmed by our simulations without water (not shown for the sake of brevity), which lead to lower sugar uptake. A similar result was found by Siong et al. [54] in the Monte Carlo simulation of uptake of an alcohol/water mixture in silicalite at 303 K.

## 5.4 Conclusions

Molecular dynamics simulations have been carried out to study the separation of a disaccharide (sucrose) from a trisaccharide (6-kestose) using zeolites. Taking into account the molecular size,  $\Phi(x,y,z)$ , of sucrose and 6-kestose, and using descriptors of micropore size, a preliminary list of 11 zeolites from the IZA Atlas has been selected. The selection is based on the principles that: i) from the 3 molecular lengths (across  $x,y,z$ ), only the two smallest,  $\Phi(y,z)$ , are important since the longest goes parallel to the diffusing channel; ii) micropore size should be larger than  $\Phi$  along  $y$  and  $z$  in order to allow diffusion; and iii) molecular size along diffusion ( $y$  or  $z$ ) should be larger than micropore size for diffusion to be precluded.

Molecular dynamics simulations have been carried out for 10 ns in bulk models of the initial set of 11 zeolites, with each system containing only 1 molecule of either sucrose or 6-kestose, plus water molecules. These small systems give a qualitative estimation that allows to select 3 candidate zeolites in which a larger mobility is expected for sucrose than 6-kestose.

With the zeolite short list (AET, DON, ETR), more accurate molecular dynamics calculations have been performed in order to assess if a selective separation of sucrose/6-kestose might be possible. The larger accuracy did not consist in a long simulation time, but mainly in: i) including a ‘membrane’ zeolite model containing two reservoirs and two zeolite layers whose external surface is terminated by silanol groups; and ii) including a mixture of equal number of sucrose and 6-kestose molecules, and so the effect of the mixture is studied directly instead of the less accurate extrapolation from single component. Two different loadings were simulated for each case, chosen so that the large loading corresponds to a larger than monolayer adsorption. This facilitates the uptake by a decrease of the surface barrier effect, leading to weaker sugar-surface interactions.

The calculations at large loading show that the three zeolites (AET, DON, ETR) are selective for sucrose uptake in the sucrose/6-kestose mixture. Finally, DON zeolite shows the largest flux, being therefore an excellent candidate for this separation process.

### Credit authorship contribution statement

IBL and PGI made molecular dynamics calculations and contributed to writing. YS contributed to editing the manuscript and molecular dynamics calculations of bulk systems. AM contributed to molecular dynamics calculations of membrane systems, editing the manuscript and writing the supporting information. JP con-

tributed to the investigation outline. GS contributed to writing the manuscript, designed the membrane models, set up the computational methodology and supervised the molecular dynamics calculations.

### Declaration of competing interest

The authors declare that they have no known competing financial interests or personal relationships that could have appeared to influence the work reported in this paper.

### Acknowledgements

We thank MICINN of Spain for funding through projects RTI2018-101784-B-I00, RTI2018-101033-B-I00, SEV-2016-0683 as well as ASIC-UPV and CESGA for computational facilities. IBL and PGI gratefully acknowledge CSIC for a JAE-Intro fellowship. AM thanks Generalitat Valenciana for the predoctoral fellowship GRISOLIAP/2019/084.

### References

- [1] Van Speybroeck, V.; Hemelsoet, K.; Joos, L.; Waroquier, M.; Bell, R. G.; Catlow, C. R. A. Advances in Theory and Their Application Within the Field of Zeolite Chemistry. *Chem. Soc. Rev.* **2015**, *44* (20), 7044–7111. DOI: 10.1039/C5CS00029G.
- [2] Wiśniewska, M.; Fijałkowska, G.; Nosal-Wiercińska, A.; Franus, M.; Panek, R. Adsorption Mechanism of Poly(vinyl alcohol) on the Surfaces of Synthetic Zeolites: Sodalite, Na-P1 and Na-A. *Adsorption* **2019**, *25* (3), 567–574. DOI: 10.1007/s10450-019-00044-2.
- [3] Choudary, N. V.; Newalkar, B. L. Use of Zeolites in Petroleum Refining and Petrochemical Processes: Recent Advances. *J. Porous Mater.* **2011**, *18* (6), 685–692. DOI: 10.1007/s10934-010-9427-8.
- [4] Baerlocher Ch.; McCusker, L. B. Database of Zeolite Structures, <http://www.iza-structure.org/databases/> (accessed 2021-10-15).
- [5] Bushuev, Y. G.; Sastre, G. Atomistic Simulations of Structural Defects and Water Occluded in SSZ-74 Zeolite. *J. Phys. Chem. C* **2009**, *113* (25), 10877–10886. DOI: 10.1021/jp9013306.

- [6] Combariza, A. F.; Gomez, D. A.; Sastre, G. Simulating the Properties of Small Pore Silica Zeolites Using Interatomic Potentials. *Chem. Soc. Rev.* **2012**, *42* (1), 114–127. DOI: 10.1039/C2CS35243E.
- [7] O'Malley, A. J.; Catlow, C. R. A. Molecular Dynamics Simulations of Longer n-Alkanes in Silicalite: a Comparison of Framework and Hydrocarbon Models. *Phys. Chem. Chem. Phys.* **2013**, *15* (43), 19024–19030. DOI: 10.1039/C3CP52653D.
- [8] O'Malley, A. J.; Catlow, C. R. A. Molecular Dynamics Simulations of Longer n-Alkanes in Silicalite: State-of-the-art Models Achieving Close Agreement with Experiment. *Phys. Chem. Chem. Phys.* **2014**, *17* (3), 1943–1948. DOI: 10.1039/C4CP04898A.
- [9] Smit, B.; Maesen, T. L. M. Molecular Simulations of Zeolites: Adsorption, Diffusion, and Shape Selectivity. *Chem. Rev.* **2008**, *108* (10), 4125–4184. DOI: 10.1021/cr8002642.
- [10] Ghysels, A.; Moors, S. L. C.; Hemelsoet, K.; De Wispelaere, K.; Waroquier, M.; Sastre, G.; Van Speybroeck, V. Shape-Selective Diffusion of Olefins in 8-Ring Solid Acid Microporous Zeolites. *J. Phys. Chem. C* **2015**, *119* (41), 23721–23734. DOI: 10.1021/acs.jpcc.5b06010.
- [11] García-Sánchez, A.; Dubbeldam, D.; Calero, S. Modeling Adsorption and Self-Diffusion of Methane in LTA Zeolites: The Influence of Framework Flexibility. *J. Phys. Chem. C* **2010**, *114* (35), 15068–15074. DOI: 10.1021/jp1059215.
- [12] Zimmermann, N. E. R.; Jakobtorweihen, S.; Beerdsen, E.; Smit, B.; Keil, F. J. In-Depth Study of the Influence of Host–Framework Flexibility on the Diffusion of Small Gas Molecules in One-Dimensional Zeolitic Pore Systems. *J. Phys. Chem. C* **2007**, *111* (46), 17370–17381. DOI: 10.1021/jp0746446.
- [13] Fornefett, I.; Rabet, D.; Buttersack, C.; Buchholz, K. Adsorption of Sucrose on Zeolites. *Green Chem.* **2016**, *18* (11), 3378–3388. DOI: 10.1039/C5GC02832A.
- [14] Buttersack, C.; Fornefett, I.; Mahrholz, J.; Buchholz, K. Specific Adsorption from Aqueous Phase on Apolar Zeolites. In *Studies in Surface Science and*

- Catalysis*; Elsevier, 1997; Vol. 105, 1723–1730. DOI: 10.1016/S0167-2991(97)80636-2.
- [15] Berensmeier, S.; Buchholz, K. Separation of Isomaltose from High Sugar Concentrated Enzyme Reaction Mixture by Dealuminated  $\beta$ -zeolite. *Sep. Purif. Technol.* **2004**, *38* (2), 129–138. DOI: 10.1016/j.seppur.2003.10.012.
- [16] Ching, C. B.; Ho, C.; Hidajat, K.; Ruthven, D. M. Experimental Study of a Simulated Counter-current Adsorption System-V. Comparison of Resin and Zeolite Adsorbents for Fructose-glucose Separation at High Concentration. *Chem. Eng. Sci.* **1987**, *42* (11), 2547–2555. DOI: 10.1016/0009-2509(87)87006-9.
- [17] Ho, C.; Ching, C. B.; Ruthven, D. M. A Comparative Study of Zeolite and Resin Adsorbents for the Separation of Fructose-glucose Mixtures. *Ind. Eng. Chem. Res.* **1987**, *26* (7), 1407–1412. DOI: 10.1021/ie00067a023.
- [18] Ching, C. B.; Ruthven, D. M. A Liquid Phase Chromatographic Study of Sorption and Diffusion of Glucose and Fructose in NaX and KX Zeolite Crystals. *Zeolites* **1988**, *8* (1), 68–73. DOI: 10.1016/S0144-2449(88)80032-0.
- [19] Muralidharan, P. K.; Ching, C. B. Determination of Multicomponent Adsorption Equilibria by Liquid Chromatography. *Ind. Eng. Chem. Res.* **1997**, *36* (2), 407–413. DOI: 10.1021/ie9604278.
- [20] Kuhn, R. C.; Filho, F. M. Separation of Fructooligosaccharides Using Zeolite Fixed Bed Columns. *J. Chromatogr. B* **2010**, *878* (22), 2023–2028. DOI: 10.1016/j.jchromb.2010.05.039.
- [21] Wach, W.; Fornefett, I.; Buttersack, C.; Buchholz, K. Chromatographic Separation of Saccharide Mixtures on Zeolites. *Food Bioprod. Process.* **2019**, *114*, 286–297. DOI: 10.1016/j.fbp.2018.10.008.
- [22] Marín-Navarro, J.; Talens-Perales, D.; Polaina, J. One-pot Production of Fructooligosaccharides by a *Saccharomyces Cerevisiae* Strain Expressing an Engineered Invertase. *Appl. Microbiol. Biotechnol.* **2015**, *99* (6), 2549–2555. DOI: 10.1007/s00253-014-6312-4.

- [23] Talens-Perales, D.; Polaina, J.; Marín-Navarro, J. Enzyme Engineering for Oligosaccharide Biosynthesis. In *Frontier Discoveries and Innovations in Interdisciplinary Microbiology*; Springer, 2016, 9–31. DOI: 10.1007/978-81-322-2610-9\_2.
- [24] Woo, K. S.; Kim, H. Y.; Hwang, I. G.; Lee, S. H.; Jeong, H. S. Characteristics of the Thermal Degradation of Glucose and Maltose Solutions. *Prev. Nutr. Food Sci.* **2015**, *20* (2), 102–109. DOI: 10.3746/pnf.2015.20.2.102.
- [25] Rizki, Z.; Janssen, A. E. M.; van der Padt, A.; Boom, R. M. Separation of Fructose and Glucose via Nanofiltration in Presence of Fructooligosaccharides. *Membranes* **2020**, *10* (10), 298. DOI: 10.3390/membranes10100298.
- [26] Frisch, M. J.; Trucks, G. W.; Schlegel, H. B.; Scuseria, G. E.; Robb, M. A.; Cheeseman, J. R.; Scalmani, G.; Barone, V.; Petersson, G. A.; Nakatsuji, H.; Li, X.; Caricato, M.; Marenich, A. V.; Bloino, J.; Janesko, B. G.; Gomperts, R.; Mennucci, B.; Hratchian, H. P.; Ortiz, J. V.; Izmaylov, A. F.; Sonnenberg, J. L.; Williams-Young, D.; Ding, F.; Lipparini, F.; Egidi, F.; Goings, J.; Peng, B.; Petrone, A.; Henderson, T.; Ranasinghe, D.; Zakrzewski, V. G.; Gao, J.; Rega, N.; Zheng, G.; Liang, W.; Hada, M.; Ehara, M.; Toyota, K.; Fukuda, R.; Hasegawa, J.; Ishida, M.; Nakajima, T.; Honda, Y.; Kitao, O.; Nakai, H.; Vreven, T.; Throssell, K.; Montgomery Jr., J. A.; Peralta, J. E.; Ogliaro, F.; Bearpark, M. J.; Heyd, J. J.; Brothers, E. N.; Kudin, K. N.; Staroverov, V. N.; Keith, T. A.; Kobayashi, R.; Normand, J.; Raghavachari, K.; Rendell, A. P.; Burant, J. C.; Iyengar, S. S.; Tomasi, J.; Cossi, M.; Millam, J. M.; Klene, M.; Adamo, C.; Cammi, R.; Ochterski, J. W.; Martin, R. L.; Morokuma, K.; Farkas, O.; Foresman, J. B.; Fox, D. J. Gaussian 16 Revision C.01, Gaussian Inc. Wallingford CT, 2016.
- [27] Becke, A. D. Density-functional Thermochemistry. III. The Role of Exact Exchange. *J. Chem. Phys.* **1993**, *98* (7), 5648–5652. DOI: 10.1063/1.464913.
- [28] McLean, A. D.; Chandler, G. S. Contracted Gaussian Basis Sets for Molecular Calculations. I. Second Row Atoms, Z=11–18. *J. Chem. Phys.* **1980**, *72* (10), 5639–5648. DOI: 10.1063/1.438980.
- [29] Grimme, S.; Antony, J.; Ehrlich, S.; Krieg, H. A Consistent and Accurate *Ab Initio* Parametrization of Density Functional Dispersion Correction (DFT-



- D) for the 94 Elements H-Pu. *J. Chem. Phys.* **2010**, *132* (15), 154104. DOI: 10.1063/1.3382344.
- [30] Grimme, S.; Ehrlich, S.; Goerigk, L. Effect of the Damping Function in Dispersion Corrected Density Functional Theory. *J. Comput. Chem.* **2011**, *32* (7), 1456–1465. DOI: 10.1002/jcc.21759.
- [31] León, S.; Sastre, G. Computational Screening of Structure-Directing Agents for the Synthesis of Pure Silica ITE Zeolite. *J. Phys. Chem. Lett.* **2020**, *11* (15), 6164–6167. DOI: 10.1021/acs.jpcllett.0c01734.
- [32] Metropolis, N.; Rosenbluth, A. W.; Rosenbluth, M. N.; Teller, A. H.; Teller, E. Equation of State Calculations by Fast Computing Machines. *J. Chem. Phys.* **1953**, *21* (6), 1087–1092. DOI: 10.1063/1.1699114.
- [33] Foster, M. D.; Rivin, I.; Treacy, M. M. J.; Delgado Friedrichs, O. A Geometric Solution to the Largest-free-sphere Problem in Zeolite Frameworks. *Microporous Mesoporous Mater.* **2006**, *90* (1), 32–38. DOI: 10.1016/j.micromeso.2005.08.025.
- [34] Smith, W.; Forester, T. R. DL\_POLY\_2.0: A General-purpose Parallel Molecular Dynamics Simulation Package. *J. Mol. Graphics* **1996**, *14* (3), 136–141. DOI: 10.1016/S0263-7855(96)00043-4.
- [35] Berendsen, H. J. C.; Postma, J. P. M.; van Gunsteren, W. F.; Hermans, J. Interaction Models for Water in Relation to Protein Hydration. In *Intermolecular Forces*; Springer, 1981, 331–342. DOI: 10.1007/978-94-015-7658-1\_21.
- [36] Oie, T.; Maggiora, G. M.; Christoffersen, R. E.; Duchamp, D. J. Development of a Flexible Intra- and Intermolecular Empirical Potential Function for Large Molecular Systems. *Int. J. Quantum Chem.* **1981**, *20* (S8), 1–47. DOI: 10.1002/qua.560200703.
- [37] Gasteiger, J.; Marsili, M. A New Model for Calculating Atomic Charges in Molecules. *Tetrahedron Lett.* **1978**, *19* (34), 3181–3184. DOI: 10.1016/S0040-4039(01)94977-9.

- [38] O'Boyle, N. M.; Banck, M.; James, C. A.; Morley, C.; Vandermeersch, T.; Hutchison, G. R. Open Babel: An Open Chemical Toolbox. *J. Cheminf.* **2011**, *3* (1), 1–14. DOI: 10.1186/1758-2946-3-33.
- [39] Rappe, A. K.; Casewit, C. J.; Colwell, K. S.; Goddard, W. A.; Skiff, W. M. UFF, a Full Periodic Table Force Field for Molecular Mechanics and Molecular Dynamics Simulations. *J. Am. Chem. Soc.* **1992**, *114* (25), 10024–10035. DOI: 10.1021/ja00051a040.
- [40] Kiselev, A. V.; Lopatkin, A. A.; Shulga, A. A. Molecular Statistical Calculation of Gas Adsorption by Silicalite. *Zeolites* **1985**, *5* (4), 261–267. DOI: 10.1016/0144-2449(85)90098-3.
- [41] Catlow, C. R. A.; Freeman, C. M.; Vessal, B.; Tomlinson, S. M.; Leslie, M. Molecular Dynamics Studies of Hydrocarbon Diffusion in Zeolites. *J. Chem. Soc. Faraday Trans.* **1991**, *87* (13), 1947–1950. DOI: 10.1039/FT9918701947.
- [42] Lue, L.; Jepps, O. G.; Delhommelle, J.; Evans, D. J. Configurational Thermostats for Molecular Systems. *Mol. Phys.* **2002**, *100* (14), 2387–2395. DOI: 10.1080/00268970210122145.
- [43] Martínez, L.; Andrade, R.; Birgin, E. G.; Martínez, J. M. PACKMOL: A Package for Building Initial Configurations for Molecular Dynamics Simulations. *J. Comput. Chem.* **2009**, *30* (13), 2157–2164. DOI: 10.1002/jcc.21224.
- [44] Sastre, G.; Kärger, J.; Ruthven, D. M. Molecular Dynamics Study of Diffusion and Surface Permeation of Benzene in Silicalite. *J. Phys. Chem. C* **2018**, *122* (13), 7217–7225. DOI: 10.1021/acs.jpcc.8b00520.
- [45] Yalkowsky, S.; Dannenfelser, R. *Aquasol Database of Aqueous Solubility, Version 5*. Tuscon, Arizona: University of Arizona, College of Pharmacy, 1992.
- [46] Dessau, R. M.; Schlenker, J. L.; Higgins, J. B. Framework Topology of AlPO<sub>4</sub>-8: the First 14-ring Molecular Sieve. *Zeolites* **1990**, *10* (6), 522–524. DOI: 10.1016/S0144-2449(05)80306-9.

- [47] Lobo, R. F.; Tsapatsis, M.; Freyhardt, C. C.; Khodabandeh, S.; Wagner, P.; Chen, C.-Y.; Balkus, K. J.; Zones, S. I.; Davis, M. E. Characterization of the Extra-Large-Pore Zeolite UTD-1. *J. Am. Chem. Soc.* **1997**, *119* (36), 8474–8484. DOI: 10.1021/ja9708528.
- [48] Strohmaier, K. G.; Vaughan, D. E. W. Structure of the First Silicate Molecular Sieve with 18-Ring Pore Openings, ECR-34. *J. Am. Chem. Soc.* **2003**, *125* (51), 16035–16039. DOI: 10.1021/ja0371653.
- [49] Jeon, M. Y.; Kim, D.; Kumar, P.; Lee, P. S.; Rangnekar, N.; Bai, P.; Shete, M.; Elyassi, B.; Lee, H. S.; Narasimharao, K.; Basahel, S. N.; Al-Thabaiti, S.; Xu, W.; Cho, H. J.; Fetisov, E. O.; Thyagarajan, R.; DeJaco, R. F.; Fan, W.; Mkhoyan, K. A.; Siepmann, J. I.; Tsapatsis, M. Ultra-selective High-flux Membranes from Directly Synthesized Zeolite Nanosheets. *Nature* **2017**, *543*, 690–694. DOI: 10.1038/nature21421.
- [50] Cailliez, F.; Trzpit, M.; Soulard, M.; Demachy, I.; Boutin, A.; Patarin, J.; Fuchs, A. H. Thermodynamics of Water Intrusion in Nanoporous Hydrophobic Solids. *Phys. Chem. Chem. Phys.* **2008**, *10* (32), 4817–4826. DOI: 10.1039/B807471B.
- [51] Özgür Yazaydn, A.; Thompson, R. W. Molecular Simulation of Water Adsorption in Silicalite: Effect of Silanol Groups and Different Cations. *Microporous Mesoporous Mater.* **2009**, *123* (1), 169–176. DOI: 10.1016/j.micromeso.2009.03.045.
- [52] Tzani, L.; Trzpit, M.; Soulard, M.; Patarin, J. High Pressure Water Intrusion Investigation of Pure Silica 1D Channel AFI, MTW and TON-type Zeolites. *Microporous Mesoporous Mater.* **2011**, *146* (1), 119–126. DOI: 10.1016/j.micromeso.2011.03.043.
- [53] Norton, A. M.; Kim, D.; Zheng, W.; Akter, N.; Xu, Y.; Tenney, S. A.; Vlachos, D. G.; Tsapatsis, M.; Boscoboinik, J. A. Reversible Formation of Silanol Groups in Two-Dimensional Siliceous Nanomaterials under Mild Hydrothermal Conditions. *J. Phys. Chem. C* **2020**, *124* (33), 18045–18053. DOI: 10.1021/acs.jpcc.0c03875.
- [54] Xiong, R.; Sandler, S. I.; Vlachos, D. G. Alcohol Adsorption onto Silicalite from Aqueous Solution. *J. Phys. Chem. C* **2011**, *115* (38), 18659–18669. DOI: 10.1021/jp205312k.



## Chapter 6

# General Discussion of the Results

### 6.1 Simulation of Biobutanol Recovery Process by LTA and CHA Columns (Chapter 3)

An experimental process designed to recover pure 1-butanol from a fermented mixture was simulated and further understood in the Chapter 3 and Appendix A. The quality of the simulated results lies on the modeling employed. Specially in the case of a classical description, the force fields are usually parameterized considering a set of target structures, and aiming to reproduce specific properties. Consequently, an aspect of great concern is models' accuracy and agreement with the experimental findings. The understanding of the force field limitations, as well as its validation with experimental data, is imperative when the proposed study seeks to mimic experimental processes computationally. Besides, when necessary, improved models need to be generated in order to better describe the series of steps and particularities of an experimental process, such as the proposed by Denayer et al. [1] for biobutanol separation and purification.

Thus, the study of such process required a modification in the force field, to properly describe the external surface T-OH groups (T = Si, Al or P) of the nanosheets simulated by the MD method. Here, the new force field description became even more general, as can describe pure silica, aluminosilicate and silicoaluminophosphate materials, with Brønsted acid sites, and allowing both bulk models or nanosheets with external surface. The analysis of the new set of parameters showed that the model was extended without sacrificing its accuracy on the reproduction of the crystallographic structures, for example. As shown in Table 3.5, such aspect was slightly improved.

Water, despite its apparently simple formulation, is a complex fluid whose behavior is difficult to simulate. There are a significant amount of water models available, trying to reproduce its properties. Still, there is not a universal model that can describe every feature of the water, and its description under confinement (e.g., zeolites micropores) is also a hard task. Although 5 different models (Figure A3) have been tested for the calculation of the water adsorption isotherm, even for the best model (TIP4P/2005), the simulation predicts more pressure than the experiment for the zeolite to start adsorbing. A possible way of improving the models also implies increasing the computational cost, by using core-shell models to properly describe polarization effects, and increasing the amount of interaction sites in the water model (like TIP5P-Ew, with 5 different interaction sites, see Figure A3). Besides, more complex functional forms are not always implemented in the software programs currently used.

Translating the experimental process to a simulation box can be a non-trivial task. For instance, considering the effect of the stripping gas was an important feature to simulate the experimental process of water and ethanol desorption occurring in the LTA column (process B, see Figure 3.1). Without its consideration, few water molecules migrated from the bulk to establish a surface adsorption during the simulation, and a fast equilibrium condition was reached. The stripping gas helps to redirect the vapor mixture from one column to another, and by doing that, remove the molecules superficially adsorbed, shifting the equilibrium in favor of the desorption phenomenon. Even though the stripping gas molecules were not explicitly considered during the MD simulation, its role during the LTA water/ethanol desorption process could be captured by setting the wall that delimited the two reservoirs with an attractive potential towards guest molecules. Such potential could only be felt by the adsorbate molecules once they were detached from the zeolite surface, and located in the center of the reservoirs. This approach was considered to avoid interfering directly in the desorption process, only ‘removing’ guest molecules from the system (by trapping them to the wall) once they completely broke contacts with the nanosheet.

Other important consideration to achieve a good agreement with the experimental results from the literature, was accounting the guest···guest interaction as part of the adsorption energy. On the one hand, such term is not important at low loading, when comparing with the isosteric heat of adsorption, for example.<sup>†</sup> On the other hand, by increasing adsorbates’ uptake, guest···guest interaction becomes important, specially when strong interactions among guest particles are

---

<sup>†</sup>When comparing the adsorption energy with the heat of adsorption, the values will differ by a factor of  $-RT$ , which corresponds to  $-2.6$  kJ/mol at 313 K. The adsorption energy corresponds to  $\Delta U$  (Equation 1.3), while  $\Delta H_{ads}$  is obtained by Equation 1.2.

present, as is the case of water. Only by considering such contribution to the adsorption energy that its value could match quantitatively with the experimental data for the bulk adsorption of the water in SAPO-34 material (Appendix A5).

## 6.2 Linear and Branched Hydrocarbon Separation by Pure Silica STW Zeolite (Chapter 4)

During the study compiled in Chapter 4 (and Appendix B), a crucial point was the search of a model that could offer a good agreement between experimental and simulated adsorption data for all adsorbate molecules, simultaneously. Various force fields available in the literature have been tested for both the adsorption isotherms and heat of adsorption calculations. Concerning the first, the experimental uptake of pentane isomers in pure silica MFI (Si-MFI) could be correctly reproduced (Figure 4.2), as the MFI framework was considered in the original parameterization procedure [2]. The selected force field [3] mainly differ from the original work of Smit et al. [2] by the alkane description. The equilibrium bond angles, functional form for the torsions and  $\sigma_{ij}$  values involving alkane groups (Table 6.1) are different. Such changes improved guests' description and guest...guest interaction, allowing the correct reproduction of 2-methylbutane (2MB) uptake in Si-MFI (Figure B3). While pentane (nC5) and 2MB presented a good agreement with the experimental adsorption data, 2,2-dimethylpropane (2DMP) maximum loading was underestimated in approximately 0.3 mmol/g (Figure B3b). Also, the simulation of alkane adsorption in Si-MFI was highly dependent on the crystallographic structure employed, as shown in Table B3.

**Table 6.1:** Main differences in Lennard-Jones parameters for alkane molecules in force fields reported by Smit et al. [2] and Calero et al. [3].

pair	$\frac{\varepsilon_{ij}}{k_B}$ (K)	$\sigma_{ij}$ (Å)	
		from [2]	from [3]
<b>CH<sub>3</sub> – CH</b>	42.85	4.19	4.22
<b>CH<sub>3</sub> – C</b>	9.30	4.90	5.07
<b>CH<sub>2</sub> – CH</b>	30.85	4.30	4.32
<b>CH<sub>2</sub> – C</b>	6.69	5.03	5.17
<b>CH – C</b>	3.69	5.46	5.53

When employed for pure silica STW (Si-STW) adsorption of alkanes, the validated model offered a poor agreement with the experiments, specially for the adsorption of dibranched isomers. A possible explanation is the difficulty to find

the right packing among such bulky molecules, as the adsorption of them in Si-STW is experimentally feasible (blue curves of Figure 4.1). During the simulations, zeolite framework was kept rigid. This is a usual approach, that reduces the computational cost, allowing more MC cycles to be simulated [4], and presenting low impact on the results when the studied framework presents little flexibility (as is the case of pure silica zeolites, in general) [4, 5]. To understand if Si-STW presented a flexibility that favored the diffusion and adsorption of the dibranched hydrocarbons, Si-STW experimental [6, 7] and IZA [8] geometries (cell parameters in Table B2) were relaxed containing the studied alkanes molecules inside the micropores (considering an uptake closer to the maximum reached experimentally). Then, the ‘empty’ optimized framework was employed in the MC simulations. While the optimization led to a higher cell volume for the experimental frameworks (expanding 42–206 Å<sup>3</sup>, depending on the guest), the opposite was observed for the IZA structure (change in cell volume from -162 to +10 Å<sup>3</sup>, depending on the guest). Even though, no significant improvement in the calculated uptake of the studied alkanes could be observed in the new adsorption isotherms using the Si-STW optimized geometries.

The calculation of the average heat of adsorption considered configurations from the MD simulations, but can also be obtained by the MC method, considering Equation 1.2. The average ensemble values for Equation 1.3 are obtained during a MC simulation, and  $\langle U_h \rangle$  is zero, as the framework is rigid. However, the model selected for the adsorption isotherms simulation specially fails to reproduce the dibranched isomers adsorption, consequently, it is expected that the heat of adsorption calculated using such force field will also diverge from the experimental values. This is confirmed by Figure 6.1, where the smaller deviations were

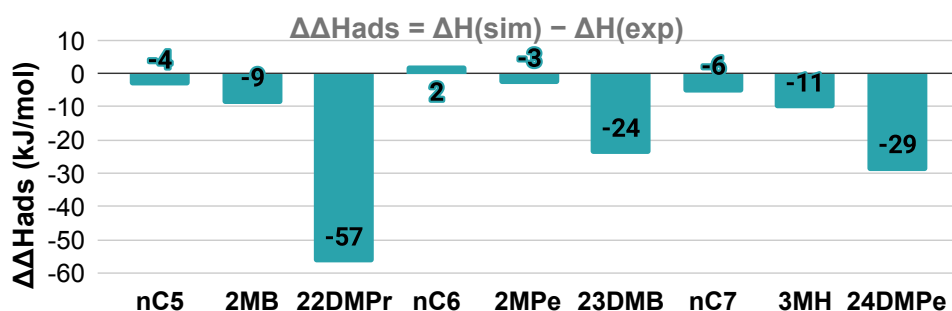


**Figure 6.1:** Difference between simulated and experimental heat of adsorption ( $\Delta\Delta H_{ads}$ ) calculated by the MC method, in RASPA package [9] ( $10^4$  initiation cycles and  $10^6$  production cycles), at 300 K, for a  $3\times 3\times 1$  Si-STW IZA structure [8].



observed for linear and monobranched isomers in Si-STW framework (absolute values from 2 to 11 kJ/mol), while the dibranched guests were poorly described by the model (deviations up to -57 kJ/mol).

Better results for the heat of adsorption were obtained with the MD approach, although the significant difference for the experimental heat of adsorption among isomers in Si-STW framework could not be reproduced quantitatively (slope of lines over the experimental (solid line) and calculated (dashed line) heat of adsorption data, in Figure 4.5). The employed model used an all atom approach for the hydrocarbons, described by Oie et al. force field [10], and the zeolite description given by Sastre et al. [11]. The interaction between zeolite and alkanes was selected among 5 force fields (**ff1** [12, 13], **ff2** [14], **ff3** [15], **ff4** [16] and **ff5** [17]), considering the 3 STW geometries available (Table B2). The difference between simulated and experimental heat of adsorption ( $\Delta\Delta H_{\text{ads}}$ ) for pentane, hexane and heptane isomers in Si-STW geometry from IZA is collected in (Figure 6.2). The smaller  $\Delta\Delta H_{\text{ads}}$  for linear and monobranched alkane isomers was obtained with **ff1** description, while the best agreement with the experimental data for dibranched isomers was observed for **ff4** model.

Thus, none of the tested models could describe accurately all alkane isomers in Si-STW. Seeking to improve such description, an attempt of adjusting both C $\cdots$ O and O $\cdots$ H Lennard-Jones parameters was performed.<sup>†</sup> nC5 ( $q_{st} = -61.5$  kJ/mol) and 22DMPPr ( $q_{st} = -33.1$  kJ/mol) were considered as reference, as presented the greatest difference in the heat of adsorption between linear and dibranched isomers. The two host-guest geometries came from the previous benchmark study (Figure 6.3), selecting among the 10 configurations generated for each alkane. The selected configurations presented the best agreement with the experimental heat of adsorption, which corresponded to nC5 optimized with **ff1** (Figure 6.3a), and 22DMPPr optimized with **ff4** (Figure 6.3b). Besides, both initial configurations considered the Si-STW experimental structure published in 2012.

Single point energy calculations were performed with Figure 6.3 structures, systematically changing  $A_{ij}$  and  $B_{ij}$  Lennard-Jones parameters for both H $\cdots$ O and C $\cdots$ O interacting pairs, and evaluating its effect in the  $\Delta H_{\text{ads}}$  obtained, in order to find a set of Lennard-Jones parameters that could simultaneously reproduce the experimental heat of adsorption value of nC5 and 22DMPPr. By analyzing the  $A_{ij}$  and  $B_{ij}$  values defined for the 5 models previously evaluated during the benchmark, a wider range of values was selected and tested (Table 6.2).

<sup>†</sup>Such parameterization was performed after the publication of the manuscript presented in Chapter 4.

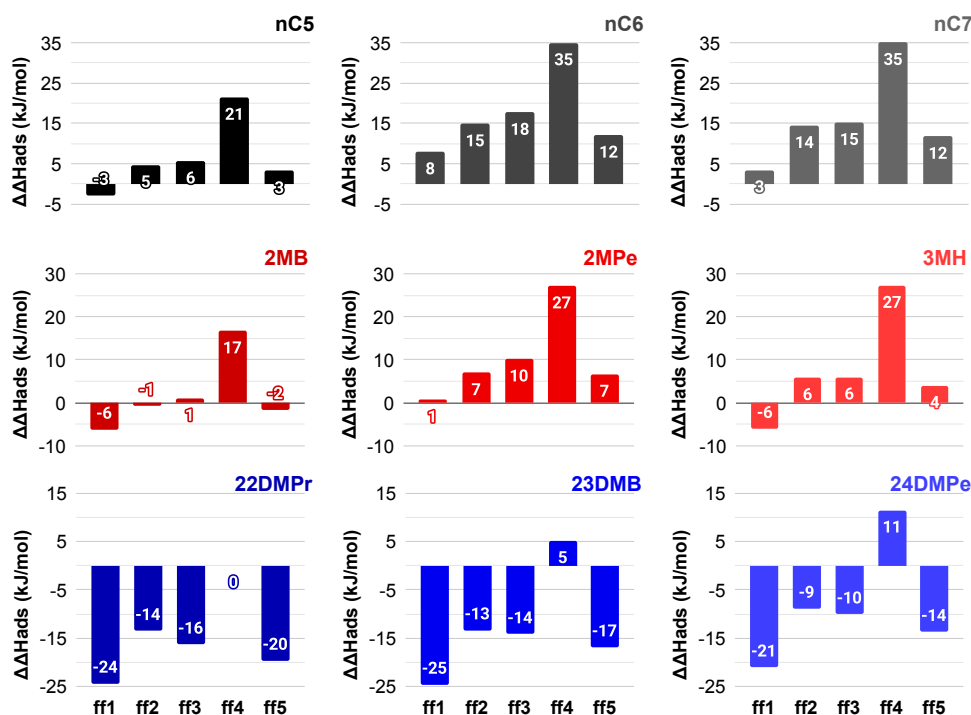


**Figure 6.2:** Difference between simulated and experimental heat of adsorption ( $\Delta\Delta H_{\text{ads}}$ ) of alkane isomers in Si-STW IZA geometries, considering 5 different models (**ff1**–**ff5**) for the zeolite...guest interaction.

Thus, 206448 AB combinations were tested for each alkane isomer, and the results for the 9 best parameter sets (**s1**–**s9**) are reported in Table 6.3. For these sets, the heat of adsorption stabilization was underestimated by  $\approx 11.6$  kJ/mol for the linear alkane, with the opposite behavior for the dibranched hydrocarbon (overestimated by  $\approx 11.9$  kJ/mol).

Therefore, the significant changes in the heat of adsorption of tested isomers in STW still could not be accurately described. The difference between nC5 and 22DMPr adsorption was predicted to be  $\approx 5$  kJ/mol, being more than five times higher in the experiments (28.4 kJ/mol). Furthermore, the benchmark procedure highlighted that the best model to describe the linear and monobranched isomers was **ff1**, and **ff4** when considering dibranched adsorption. By evaluating the Lennard-jones profiles considering the 9 best sets of parameters, the description

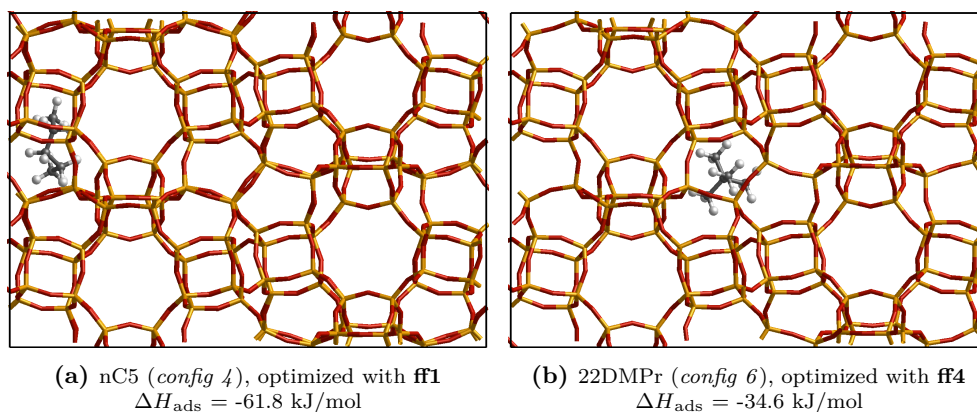


**Figure 6.3:** Optimized configurations from heat of adsorption benchmark, with  $\Delta H_{\text{ads}}$  closer to the experimental value for pentane (a) and 2,2-dimethylpropane (b). The Si-STW experimental structure published in 2012 was considered in both configurations.

**Table 6.2:** Lennard-Jones parameters for  $\text{H}\cdots\text{O}$  and  $\text{C}\cdots\text{O}$  interacting pairs, defined by 5 different models (**ff1** [12, 13], **ff2** [14], **ff3** [15], **ff4** [16] and **ff5** [17]). Range selected for the screening of new Lennard-Jones parameters for  $\text{H}\cdots\text{O}$  and  $\text{C}\cdots\text{O}$  interactions.

model	$\text{H}\cdots\text{O}$ pair		model	$\text{C}\cdots\text{O}$ pair	
	A (eV $\text{\AA}^{12}$ )	B (eV $\text{\AA}^6$ )		A (eV $\text{\AA}^{12}$ )	B (eV $\text{\AA}^6$ )
<b>ff1</b>	1556.40	5.57	<b>ff1</b>	11000.00	17.65
<b>ff3</b>	1704.52	4.58	<b>ff3</b>	13006.98	19.73
<b>ff4</b>	2366.57	4.59	<b>ff4</b>	20637.17	16.85
<b>ff5</b>	1909.92	5.55	<b>ff5</b>	30310.70	22.26
<b>range tested</b>	1300–2800	4.00–6.00	<b>range tested</b>	9000–30800	16.20–22.80

given to the  $\text{C}\cdots\text{O}$  pair resembled **ff4** curve (Figure 6.4, left), while  $\text{H}\cdots\text{O}$  shape was closer to the description given by **ff1** force field (Figure 6.4, right).

As discussed above, despite all efforts to provide an accurate description for the dibranched alkanes in contact with Si-STW structures, such fine-tuning was not possible. Significantly simple models were employed, which can indicate that the nature of this problem needs a more complex description (changing the functional form of the intermolecular interactions, increasing the amount of atom types involved, among others).

**Table 6.3:** Best sets (**s1–s9**) of AB Lennard-Jones parameters for H $\cdots$ O and H $\cdots$ O interacting pairs, and respective  $\Delta H_{ads}$  calculated for pentane (nC5) and 2,2-dimethylpropane (22DMPPr).

set	H $\cdots$ O pair		C $\cdots$ O pair		$\Delta H_{ads}$	
	A	B	A	B	nC5	22DMPPr
<b>s1</b>	2100	6.0	30800	22.8	-50.1	-45.0
<b>s2</b>	2200	6.0	28620	22.8	-50.0	-45.0
<b>s3</b>	2100	6.0	29492	22.5	-50.0	-45.0
<b>s4</b>	2000	6.0	30364	22.2	-50.0	-44.9
<b>s5</b>	1900	5.8	30364	22.5	-49.9	-45.0
<b>s6</b>	1900	6.0	29056	21.3	-49.9	-45.0
<b>s7</b>	1800	6.0	29928	21.0	-49.9	-44.9
<b>s8</b>	1700	6.0	30800	20.7	-49.9	-44.8
<b>s9</b>	2100	6.0	30364	22.8	-49.8	-45.0

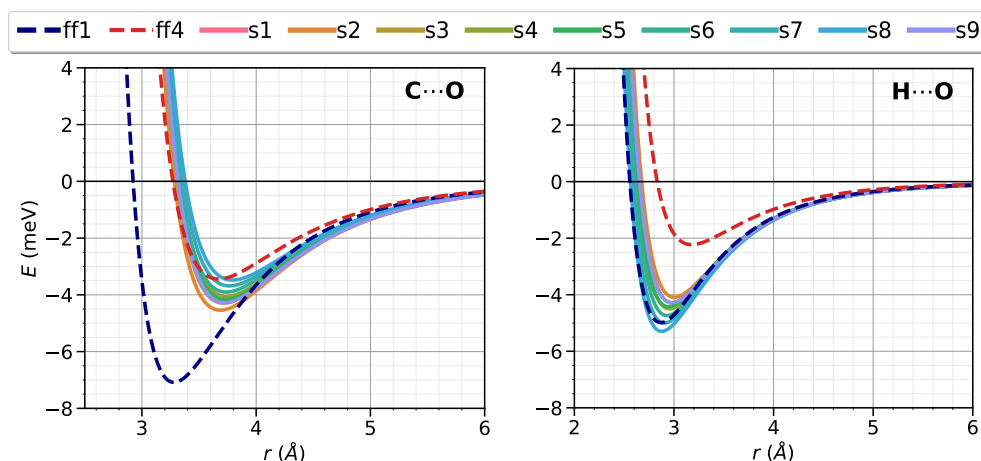


**Figure 6.4:** Lennard-Jones potential profiles for C $\cdots$ O (left) and H $\cdots$ O (right) interaction defined by **ff1**, **ff4** and the nine best sets of AB parameters obtained (**s1–s9**) to reproduce the heat of adsorption of pentane and 2,2-dimethylpropane, simultaneously.

The development of accurate models that can match experimental data is not a trivial task. General force fields or models that can be applied for a wide variety of molecules depend upon a huge effort, where sometimes, the accuracy of the results needs to be sacrificed in order to use a general or simpler description. Besides, the experimental data can be highly dependent on a variety of factors, such as the

presence of defects in the framework, distribution of Al centers, extraframework cations and/or acid sites, as well as crystals' morphology. Consequently, a correct simulation of materials' adsorptive properties will depend not only on the force field accuracy, but in the reproduction of the key features for the host...guest interaction.

### 6.3 Separation of Sucrose/6-Kestose Aqueous Mixture by Zeolites (Chapter 5)

The search for suitable zeolite frameworks with high selectivity towards sucrose molecules is compiled in Chapter 5 and Appendix C. By selecting a representative conformation of the target molecules (sucrose and 6-kestose), the estimation of their molecular size by the 'shoebox' algorithm proved to be a good approach for the first selection of candidates.

The further evaluation of the initial set of candidates considered both sugars mobility inside the micropores, simulating a bulk model (periodic unit cell without external surface) and already considering the presence of solvent molecules (water). Thus, if sucrose molecules can (in principle) be adsorbed, whereas 6-kestose is excluded by size (first selection criteria), how mobile the target molecules are inside zeolites channel system was a second criterion established. It is interesting to note that AEI and ETR frameworks were selected due to a high mobility of sucrose when compared with 6-kestose, while in DON zeolite, sucrose molecules presented a low mobility, but being also selected due to the extremely small diffusion of 6-kestose molecules (Figures 5.3 and 5.4). At the end, DON framework presented the best results for the membrane systems, whose high uptake and selectivity against sucrose may be also related to such diffusional behavior.

Finally, the third selection criterion considered models mimicking the future experimental process of sucrose/6-kestose separation, describing a zeolite membrane system, and increasing the complexity level by adding the external surface. The silanol groups can play an important role, as such polar surface in a hydrophobic silica material possess high affinity for the target aqueous mixture. Its effect was clearly illustrated by the different sugar uptakes obtained in simulations with low and high concentration of sugars, as exemplified for DON framework in Figures C8 and C13. A significant interaction can be present among sugar molecules and the external silanols, both due to the electrostatic interaction and hydrogen bonds. Therefore, at a low sugar concentration, there is a low probability of going from the surface into the silica micropore. By increasing the sugar content, guest molecules can cover completely the external surface in a monolayer. Hence, the

remaining sugar molecules will have a higher probability to diffuse through the micropores, as they present weaker interactions with the zeolite silanols, favoring their bulk adsorption. Such behavior have already been reported in the literature [18], being referred as the *surface barrier effect*. For our membrane simulations, this effect could also be quantified by the interaction energy calculations compiled in Appendix C7.

The gradual increase in the complexity level of the analysis employed during the study allowed to select two promising candidates (AET and DON), in which the latter presented the best uptake of sucrose with 6-kestose exclusion, and that is feasible as a pure silica material (as considered in the simulations). Although the experimental analysis is important to the validation of our screening, our models sought to resemble the future application, by considering the solvent and flexible frameworks, in a temperature that allow higher diffusion and solubility of the sugars without promoting their denaturalization, and analyzing solutions at low and high concentration of sugars.

## References

- [1] Van der Perre, S.; Gelin, P.; Claessens, B.; Martin-Calvo, A.; Remi, J. C. S.; Duerinck, T.; Baron, G. V.; Palomino, M.; Sánchez, L. Y.; Valencia, S.; Shang, J.; Singh, R.; Webley, P. A.; Rey, F.; Denayer, J. F. M. Intensified Biobutanol Recovery by Using Zeolites with Complementary Selectivity. *ChemSusChem* **2017**, *10* (14), 2968–2977. DOI: 10.1002/cssc.201700667.
- [2] Dubbeldam, D.; Calero, S.; Vlugt, T. J. H.; Krishna, R.; Maesen, T. L. M.; Smit, B. United Atom Force Field for Alkanes in Nanoporous Materials. *J. Phys. Chem. B* **2004**, *108* (33), 12301–12313. DOI: 10.1021/jp0376727.
- [3] Sławek, A.; Vicent-Luna, J. M.; Marszałek, B.; Makowski, W.; Calero, S. Quasi-Equilibrated Thermodesorption Combined with Molecular Simulation for Adsorption and Separation of Hexane Isomers in Zeolites MFI and MEL. *J. Phys. Chem. C* **2017**, *121* (35), 19226–19238. DOI: 10.1021/acs.jpcc.7b05347.
- [4] Dubbeldam, D.; Walton, K. S.; Vlugt, T. J. H.; Calero, S. Design, Parameterization, and Implementation of Atomic Force Fields for Adsorption in Nanoporous Materials. *Adv. Theory Simul.* **2019**, *2* (11), 1900135. DOI: 10.1002/adts.201900135.

- [5] Vlugt, T. J. H.; Schenk, M. Influence of Framework Flexibility on the Adsorption Properties of Hydrocarbons in the Zeolite Silicalite. *J. Phys. Chem. B* **2002**, *106* (49), 12757–12763. DOI: 10.1021/jp0263931.
- [6] Rojas, A.; Cambor, M. A. A Pure Silica Chiral Polymorph with Helical Pores. *Angew. Chem. Int. Ed.* **2012**, *51* (16), 3854–3856. DOI: 10.1002/anie.201108753.
- [7] Rojas, A.; Arteaga, O.; Kahr, B.; Cambor, M. A. Synthesis, Structure, and Optical Activity of HPM-1, a Pure Silica Chiral Zeolite. *J. Am. Chem. Soc.* **2013**, *135* (32), 11975–11984. DOI: 10.1021/ja405088c.
- [8] Baerlocher Ch.; McCusker, L. B. Database of Zeolite Structures, <http://www.iza-structure.org/databases/> (accessed 2021-10-15).
- [9] Dubbeldam, D.; Calero, S.; Ellis, D. E.; Snurr, R. Q. RASPA: Molecular Simulation Software for Adsorption and Diffusion in Flexible Nanoporous Materials. *Mol. Simul.* **2016**, *42* (2), 81–101. DOI: 10.1080/08927022.2015.1010082.
- [10] Oie, T.; Maggiora, G. M.; Christoffersen, R. E.; Duchamp, D. J. Development of a Flexible Intra- and Intermolecular Empirical Potential Function for Large Molecular Systems. *Int. J. Quantum Chem.* **1981**, *20* (S8), 1–47. DOI: 10.1002/qua.560200703.
- [11] Ghysels, A.; Moors, S. L. C.; Hemelsoet, K.; De Wispelaere, K.; Waroquier, M.; Sastre, G.; Van Speybroeck, V. Shape-Selective Diffusion of Olefins in 8-Ring Solid Acid Microporous Zeolites. *J. Phys. Chem. C* **2015**, *119* (41), 23721–23734. DOI: 10.1021/acs.jpcc.5b06010.
- [12] Kiselev, A. V.; Lopatkin, A. A.; Shulga, A. A. Molecular Statistical Calculation of Gas Adsorption by Silicalite. *Zeolites* **1985**, *5* (4), 261–267. DOI: 10.1016/0144-2449(85)90098-3.
- [13] Catlow, C. R. A.; Freeman, C. M.; Vessal, B.; Tomlinson, S. M.; Leslie, M. Molecular Dynamics Studies of Hydrocarbon Diffusion in Zeolites. *J. Chem. Soc. Faraday Trans.* **1991**, *87* (13), 1947–1950. DOI: 10.1039/FT9918701947.

- [14] Maurin, G.; Bourrelly, S.; Llewellyn, P. L.; Bell, R. G. Simulation of the Adsorption Properties of CH<sub>4</sub> in Faujasites up to High Pressure: Comparison with Microcalorimetry. *Microporous and Mesoporous Mater.* **2006**, *89* (1–3), 96–102. DOI: 10.1016/j.micromeso.2005.09.024.
- [15] Ghorai, P. K.; Sluiter, M.; Yashonath, S.; Kawazoe, Y. Intermolecular Potential for Methane in Zeolite A and Y: Adsorption Isotherm and Related Properties. *Solid State Sci.* **2006**, *8* (3), 248–258. DOI: 10.1016/j.solidstatesciences.2006.02.016.
- [16] Rappe, A. K.; Casewit, C. J.; Colwell, K. S.; Goddard, W. A.; Skiff, W. M. UFF, a Full Periodic Table Force Field for Molecular Mechanics and Molecular Dynamics Simulations. *J. Am. Chem. Soc.* **1992**, *114* (25), 10024–10035. DOI: 10.1021/ja00051a040.
- [17] Lim, K. H.; Jousse, F.; Auerbach, S. M.; Grey, C. P. Double Resonance NMR and Molecular Simulations of Hydrofluorocarbon Binding on Faujasite Zeolites NaX and NaY: the Importance of Hydrogen Bonding in Controlling Adsorption Geometries. *J. Phys. Chem. B* **2001**, *105* (41), 9918–9929. DOI: 10.1021/jp0045989.
- [18] Sastre, G.; Kärger, J.; Ruthven, D. M. Molecular Dynamics Study of Diffusion and Surface Permeation of Benzene in Silicalite. *J. Phys. Chem. C* **2018**, *122* (13), 7217–7225. DOI: 10.1021/acs.jpcc.8b00520.



## Chapter 7

# Conclusion

During the studies here compiled, the capabilities of the computational methods have been illustrated, addressing processes with zeolite materials that explored the different separation mechanisms available. Valuable insights could be obtained on a molecular level, helping to understand and/or predict the diffusion and adsorptive behavior of a water, sugars, alcohols, and hydrocarbons in numerous microporous frameworks. Complex systems were simulated, where various experimental features were successfully accounted for. For instance, the effect of the concentration of guest molecules in the target mixture, temperature, framework chemical composition and its affinity for guest molecules, as well as nanosheets and membranes performances for the separation of aqueous mixtures have been investigated.

Since a complete experimental study was performed for the biobutanol recovery process developed by Denayer and co-workers, an in-depth theoretical investigation could be done for the individual steps composing such process. A proper usage of the models, by validating the obtained results, understanding their limitations and improving them whenever possible, was an important aspect treated before performing the simulations. Thus, with the systems and the nature of the problem well-defined and described, the target process could be simulated, enabling future investigations focusing on different separation processes by the same approach.

Guests adsorption could be evaluated inside the channel system (bulk), as well as in the surface, when nanosheets/membrane systems were modeled. In the latter, depending on the concentration of the target molecule in the mixture, the ‘surface barrier’ effect impacted their adsorption, which was overcome when concentration is sufficiently high to form a layer of adsorbate molecules on the external surface,

favoring the entry of the remaining molecules into the materials' cavities and channels.

The nature and magnitude of the adsorption energy was also evaluated for the studied systems. The results highlighted the predominance of van der Waals interactions when apolar chains are inside pure silica zeolites, while polar molecules presented significant stabilization coming from the electrostatic interactions with external surfaces and hydrophilic frameworks. Hydrogen bonds also played an important role, as can be present in the external surfaces and in the acidic sites inside the micropores. The estimation of Hydrogen bonds strength based in well established geometrical criteria have been considered during the studies. Such data can be extracted from the simulated trajectories, and provide meaningful insights into host-guest and guest-guest contacts. Hydrogen bond interactions are also known by their cooperativity (increasing the stabilization of former interactions by the establishment of new ones in the surroundings), and directionality (interaction strength increases as the interaction tends to be linear, e.g., Donor-H...Acceptor angle ranging from 165 to 180°), which are interesting features that can be tracked down by future computational studies.

Zeolites offer a wide variety of promising candidates for new applications in the separation field, and the hypothetical structures magnify even more the options. In this sense, the computational chemistry methods are perfectly suited to explore and analyze the candidates. Well tuned models are useful tools for the predictions, that when allied with Machine Learning techniques, for example, have been proved to be a powerful approach. Therefore, zeolites are a rich field to be explored by the theoretical chemistry, in which complex processes can be simulated with accurate classical force fields, considering large systems and still enabling long simulations with reasonable amount of computational resources. Besides, significant part of the research can be done by *in silico* studies, whose systematic evaluation can guide the experimental work, generating less chemical waste and pointing to a sustainable present and future.

## List of Publications During the PhD

1. Oliveira, A. D. S.; Rivero-Buceta, E. M.; Vidaurre-Agut, C.; **Misturini, A.**; Moreno, V.; Jordá, J. L.; Sastre, G.; Pergher, S. B. C. and Botella, P. Sequential Pore Wall Functionalization in Covalent Organic Frameworks and Application to Stable Camptothecin Delivery Systems. *Mater. Sci. Eng. C*, **2020**, *117*, 111263.  
DOI: 10.1016/j.msec.2020.111263
2. Pérez-Botella, E.; **Misturini, A.**; Sala, A.; Palomino, M.; Corma, A.; Sastre, G.; Valencia, S. and Rey, F. Insights into Adsorption of Linear, Mono-branched, and Dibranchd Alkanes on Pure Silica STW Zeolite as a Promising Material for Their Separation. *J. Phys. Chem. C*, **2020**, *124* (49), 26821–26829.  
DOI: 10.1021/acs.jpcc.0c08517
3. Bolaño Losada, I.; Grobas-Illobre, P.; **Misturini, A.**; Polaina, J.; Seminowski, Y. and Sastre, G. Separation of an Aqueous Mixture of 6-kestose/sucrose with Zeolites: A Molecular Dynamics Simulation. *Microporous Mesoporous Mater.*, **2021**, *319*, 111031.  
DOI: 10.1016/j.micromeso.2021.111031
4. **Misturini, A.**; Heinzelmann, G.; Parreira, R. L. T.; Molina, E. F. and Caramori, G. F. Probing the Potential of Ureasil-poly(ethylene oxide) as a Glyphosate Scavenger in Aqueous Milieu: Force-field Parameterization and MD simulations. *New J. Chem.*, **2021**, *45* (42), 19831–19841.  
DOI: 10.1039/D1NJ01145F  
(results obtained during the Master degree)
5. **Misturini, A.**; Rey, F. and Sastre, G. Molecular Simulation of Biobutanol Recovery Using LTA and CHA Zeolite Nanosheets with an External Surface. *J. Phys. Chem. C*, **2022**, *126* (41), 17680–17691.  
DOI: 10.1021/acs.jpcc.2c04331

6. Argente, E.; Valero, S.; **Misturini, A.**; Treacy, M. M. J.; Baumes, L. and Sastre, G. Computer Generation of Hypothetical Zeolites (Chapter 6). In: *Artificial Intelligence-Guided Design and Property Prediction for Zeolites and Nanoporous Materials*; Satre, G., Daeyaert, F., Eds.; John Wiley and Sons Ltd, 2023. ISBN: 9781119819752.  
(book in press)

## Acknowledgments

I can say, with no doubt, that I finish one more chapter of my life filled with gratitude. Looking back, I can only think how lucky I am, being surrounded and guided by amazing people. First of all, I need to thank my parents for always encouraging their curious child, so eager to learn and discover new things. I hope that my father, wherever he is, can see the challenges that I have already overcome, and the many more that will. Because I will keep working, and giving my best, as he always told me to do. They were and are examples of persistence, hard work, organization and motivation, crucial qualities for the researcher that I already am, and the one I want to be.

Learning chemistry was love at first sight. I remember the first time I saw a molecular model kit in high school, and how amazed I was. I always had wonderful teachers and professors, to whom I will always be thankful. The computational chemistry also came early on, since the Quantum Chemistry course given by Prof. Giovanni Finoto Caramori in 2014, during the bachelor degree. I went quickly to his research group, and my bright eyes studying the molecular interactions testify that I did the right choice.

That is why I know I am lucky, all my supervisors were examples of researches and also of human beings, that helped me through the way that brought me here. I am hugely grateful to Germán, who believed in me and was patient enough to overcome the brutal bureaucracy for bringing me from Brazil. Thank you for the opportunity, for the amazing guidance, and all conversations we had. I have learned so much with you on an academic and personal level. Besides being an excellent researcher, Germán is always so nice and polite with everybody, qualities I really admire. I hope I can keep learning from you.

Likewise, thank you very much, prof. Giovanni, for all those years I could learn from you in the UFSC. Giovanni is a role model as a researcher and such a nice person. I also need to give a special thanks to other researchers from the ITQ, such as prof. Fernando Rey, Mercedes Boronat, María Galvez, and my colleagues

Beatriz, Raul, Santiago, Pau, Mario, and Nacho for the help during this journey, as well as the nice conversations and shared moments. Thanks to Inma Cubas, for her patience and help with the paperwork and bureaucracy that immigrants have to deal with. A huge thanks to Mayan, my sweet friend from Brazil, that always listened to me, helped get through the difficult moments, but also shared with me the beautiful ones. You can always count on me.

Besides, I need to thank Dr. Maciej Haranczyk, for his time and conversations, and for helping me to start developing Machine Learning models, during my stay in his group at the IMDEA Materials (Madrid). Also, thanks to the incredibly nice colleagues that I met during those three months: Giulia, Elaheh, Isabel, Davide, Alba, and Isacco. I could enjoy with them the first moments of the ‘new normality’ around Madrid.

It was specially difficult to develop the PhD during so uncertain times for us as society. The pandemics were a source of fear, as we stayed in constant contact with the fragility of life, being even harder when we are so far from our loved ones. Thus, I need to offer a special thanks to Reisel, that survived the pandemics with me. We get out of it as sane and healthy as possible. Thanks for helping, encouraging and sharing with me the last years, I hope that we have many more ahead.

For those I cited and many others, I would like to thank you with all my heart. Now, the only thing left is to enjoy the end of this journey. And this I can learn from the Spanish people, because they really know how to celebrate!

## Appendix A

# Supplementary material for Chapter 3

### A1 Force Field Selection for Monte Carlo Simulations with ITQ-29

#### A1.1 Alcohol adsorption modeling

In Figure A2 were compiled the alcohol adsorption isotherms with various models, using ITQ-29 (structure reported in 2004 [1]) and respective pocket blocking file from RASPA package. Adsorption isotherms considered the van der Waals interaction of adsorbates (ethanol, butanol and water) only with zeolite oxygen atoms, through the Lennard-Jones potential (LJ, Equation A4). Three alcohol models evaluated, labeled as TRAPPE/q1 [2], TRAPPE/q2 [3] and OPLS [4]. Bonded terms for the studied alcohols are collected in Tables A1 and A2, and non-bonded terms at Figure A1.

$$U_{\text{bends}}^{\text{harm}} = \sum_{\text{bends}} \frac{k_{\theta}}{2} (\theta_{ijk} - \theta_{eq})^2 \quad (\text{A1})$$

$$U_{\text{torsion}}^{\text{TRAPPE}} = p_0 + p_1[1 + \cos(\phi_{ijkl})] + p_2[1 - \cos(2\phi_{ijkl})] + p_3[1 + \cos(3\phi_{ijkl})] \quad (\text{A2})$$

$$U_{\text{torsion}}^{\text{OPLS}} = \frac{1}{2}p_0 + \frac{1}{2}p_1[1 + \cos(\phi_{ijkl})] + \frac{1}{2}p_2[1 - \cos(2\phi_{ijkl})] + \frac{1}{2}p_3[1 + \cos(3\phi_{ijkl})] \quad (\text{A3})$$

**Table A1:** Bonded terms for alcohols described by TRAPPE force field. Values for the rigid bond lengths ( $\mathbf{r}$ ), spring constant ( $\mathbf{k}_\theta$ ) divided by Boltzmann constant ( $k_B$ ) and equilibrium value for angles ( $\theta_{eq}$ ). Coefficients for the expression describing the torsional terms ( $\mathbf{p}_0$ ,  $\mathbf{p}_1$ ,  $\mathbf{p}_2$  and  $\mathbf{p}_3$ ) divided by  $k_B$ . C label refers to any type of C-containing bead (CH2, CH2\_q and CH3).

Bond	$\mathbf{r}$ (Å)	functional form			
C-C	1.54	rigid			
C-O	1.43				
O-H	0.945				
Angle	$\mathbf{k}_\theta/k_B$ (K/rad <sup>2</sup> )	$\theta_{eq}$ (°)	functional form		
C-C-C	62500	114.00	Equation A1		
C-C-O	50400	109.47			
C-O-H	55400	108.50			
Torsion	$\mathbf{p}_0/k_B$ (K)	$\mathbf{p}_1/k_B$ (K)	$\mathbf{p}_2/k_B$ (K)	$\mathbf{p}_3/k_B$ (K)	functional form
C-C-C-C	0.00	355.03	-68.19	791.32	Equation A2
C-C-C-O	0.00	176.62	-53.34	769.93	
C-C-O-H	0.00	209.82	-29.17	187.93	

$$U^{LJ}(r_{ij}) = 4\varepsilon \left[ \left( \frac{\sigma}{r_{ij}} \right)^{12} - \left( \frac{\sigma}{r_{ij}} \right)^6 \right] \quad (\text{A4})$$

**Table A2:** Bonded terms for alcohols described by OPLS force field. Values for the rigid bond lengths ( $\mathbf{r}$ ) and angle bends ( $\theta$ ). Coefficients for the expression describing the torsional terms ( $\mathbf{p}_0$ ,  $\mathbf{p}_1$ ,  $\mathbf{p}_2$  and  $\mathbf{p}_3$ ) divided by Boltzmann constant ( $k_B$ ). C label refers to any type of C-containing bead (CH2, CH2\_q and CH3).

Bond	$\mathbf{r}$ (Å)	functional form			
C-C	1.53	rigid			
C-O	1.43				
O-H	0.945				
Angle	$\theta$ (°)	functional form			
C-C-C	112.0	rigid			
C-C-O	108.0				
C-O-H	108.5				
Torsion	$\mathbf{p}_0/k_B$ (K)	$\mathbf{p}_1/k_B$ (K)	$\mathbf{p}_2/k_B$ (K)	$\mathbf{p}_3/k_B$ (K)	functional form
C-C-C-C	0.000	710.043	-136.373	1582.626	Equation A3
C-C-C-O	0.000	353.260	-106.683	1539.852	
C-C-O-H	0.000	419.685	-58.373	375.905	

All ethanol models resulted in adsorption isotherms close to the experimental one, although the best agreement was obtained by the TRAPPE/q1 model (blue curve



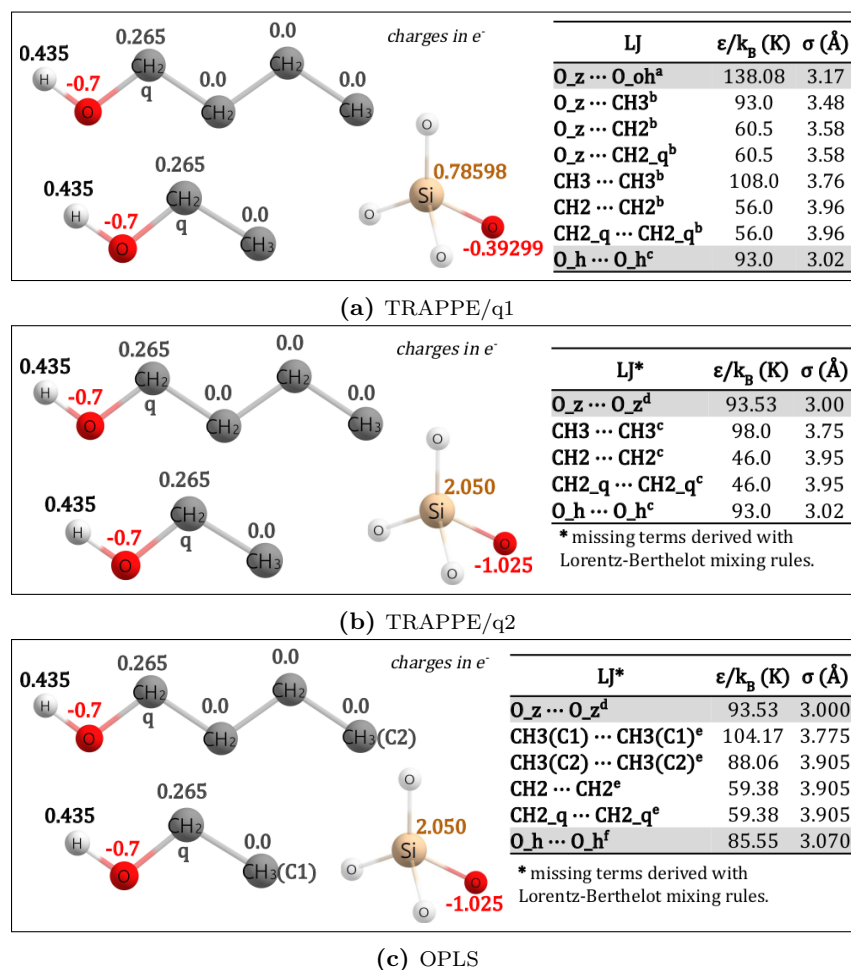


**Figure A1:** Non-bonded terms for the alcohol models. Letters in superscript citing the respective articles (a [2], b [5], c [6], d [3], e [7] and f [4]). Lennard-Jones (LJ, Equation A4) parameters describing the carbon and oxygen atoms of each model, and charges of interacting sites (in black for H, gray for C, red for the O, and dark-yellow for Si).

of Figure A2a). While the OPLS model provides a moderately accurate description of ethanol adsorption isotherm profile, when applied to the simulations with butanol, the adsorbate loading at higher pressures is significantly overestimated (green lines of plots Figure A2a and b, respectively). As the selected model need to consistently describe both alcohols, the TRAPPE/q1 parameter set was se-

lected for the following simulations due to its agreement with the experimental data.

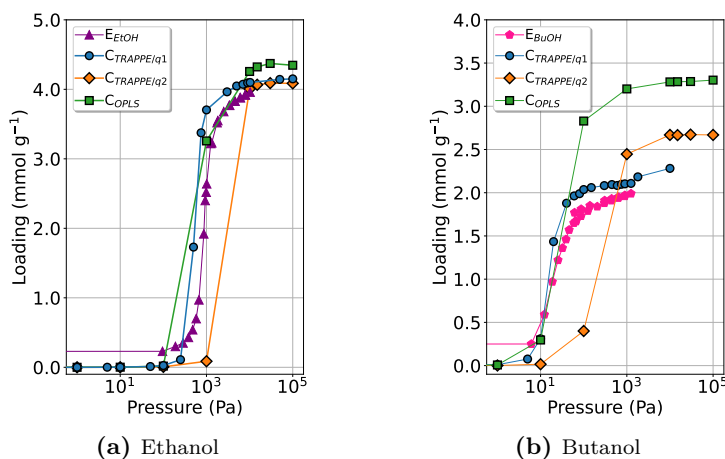


**Figure A2:** Experimental (E) and calculated (C) adsorption isotherms of ethanol (a) and butanol (b) in ITQ-29 structure. Simulated data considering various force fields at 313 K.

### A1.2 Water adsorption modeling

Five different water models were considered: SPC/E [8], TIP3P [9], TIP4P-Ew [10], TIP4P/2005 [11] and TIP5P-Ew [12]. Water molecules were modeled rigid, and the non-bonded terms for each model are summarized in the Figure A3. The LJ interaction  $O(\text{zeolite}) \cdots O(\text{water})$  for the calculation of the water adsorption isotherms were obtained by the Lorentz-Berthelot mixing rules, considering  $O(\text{zeolite}) \cdots O(\text{zeolite})$  from TRAPPE/q2 model (Figure A1b).

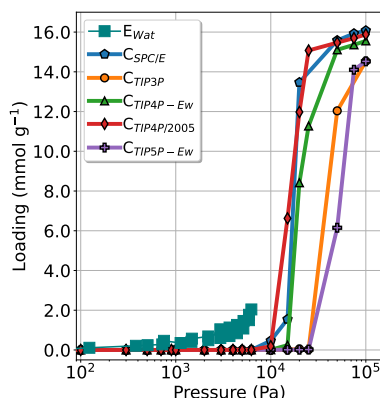
LJ O	SPC/E	TIP3P	TIP4P-Ew	TIP4P/2005	TIP5P-Ew
$\epsilon/k_B$ (K)	78.1530	76.5397	81.8990	93.2	89.5731
$\sigma$ (Å)	3.1656	3.150574	3.16435	3.1589	3.097

Charges (in $e^-$ )	SPC/E	TIP3P	TIP4P-Ew	TIP4P/2005	TIP5P-Ew
O	-0.8476	-0.834	0.0	0.0	0.0
H	0.4238	0.417	-1.04844	-1.1128	0.0
L			0.52422	0.5564	-0.241

**Figure A3:** Water models tested for the adsorption isotherms in ITQ-29, containing three (SPC/E, TIP3P), four (TIP4P-Ew, TIP4P/2005), and five (TIP5P-Ew) interacting sites. Lennard-Jones (LJ, Equation A4) parameters describing the oxygen atom of each model, and charges of interacting sites (in black for H, pink for lone pairs (L), and red for O).

The reproduction of water adsorption isotherms was the most challenging, considering the tested models (Figure A4). Best results were obtained with TIP4P/2005 and SPC/E, although the experimental uptake at higher pressures could not be compared to experiments due to absence of data. The increase in the adsorption for the simulated data is observed at pressures higher than  $10^4$  Pa. Nonetheless, the shape and maximum loading of the simulated adsorption isotherms cannot be confirmed due to the lack of experimental data at this high-pressure region. The selected water model was TIP4P/2005, as it presented the best results when combined with the force field selected to perform the following simulations (with Molecular Dynamics, MD). Such validation will be presented in the next section.



**Figure A4:** Experimental (E) and calculated (C) adsorption isotherms of water in ITQ-29 structure. Simulated data considering various force fields at 313 K.

### A1.3 Long range cutoff treatment

In the MC simulations, a cutoff of  $12.0 \text{ \AA}$  was considered, just being shifted, without tail corrections, as described by the work of Martin-Calvo and co-workers (model selected for alcohols description during adsorption isotherms calculation) [2]. The TIP4P/2005 model has also been successfully employed in zeolite simulations with a cutoff of  $12.0$  [13] and  $11.0$  [14]  $\text{\AA}$ . However, the original TRAPPE-UA description for alcohol molecules considers a spherical cutoff  $14.0 \text{ \AA}$  with analytic tail corrections [6]. The effect of cutoff selection and treatment on water and alcohols adsorption in ITQ-29 was evaluated, and summarized in Figure A5.

The use of a larger cutoff ( $14.0 \text{ \AA}$  and tail corrections) increased the adsorption of the alcohol molecules at low pressure (Figure A5a), converging to the saturation uptake in pressures lower than the experimental or simulated data in the cutoff of  $12.0 \text{ \AA}$ . The same behavior was observed for the butanol uptake in the

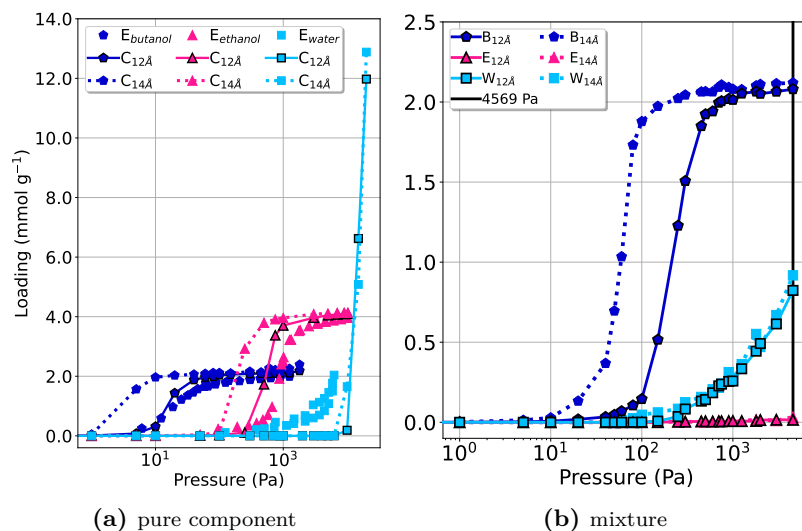


**Figure A5:** (a) Experimental (E) and calculated (C) pure component (butanol, ethanol, water) adsorption isotherms in ITQ-29 at 313 K. (b) Calculated adsorption isotherms of ‘fermented vapor mixture’ in ITQ-29 at 313 K, with the experimental pressure highlighted as a vertical black bar. The calculated curves considered two different treatments for the long-range interactions: truncating the potential and shifting to 12.0 Å ( $C_{12\text{\AA}}$ ), or cutting at 14.0 Å ( $C_{14\text{\AA}}$ ) and considering tail corrections, as implemented in RASPA software.

mixture adsorption isotherm (Figure A5b), and a small impact on ethanol uptake due to its low concentration in the simulated mixture. The water adsorption was less affected on both isotherms, leading to loading slightly larger in the pure component simulations with 14.0 Å of cutoff. The best agreement with the experimental adsorption isotherms was observed for the simulations that truncated the long range interactions and shifted at a cutoff radius of 12.0 Å, and such approach was adopted for the MC simulations reported in the main manuscript.

## A2 Validation of MD Force Field with MC Simulations

The model selected in the previous section is parameterized for an accurate reproduction of adsorption isotherms with Monte Carlo simulations (MC). A second model, specially for zeolite ··· adsorbate interaction description, and the structural features of the simulated materials (including its flexibility) needs to be selected for the MD calculations, and evaluated by its compatibility with the MC model. To do so, two models were employed and compared with the experimental adsorp-

tion data and the models selected in the previous section (Figures A6 and A7). For the MD simulations, the force field needs to describe both silica zeolites and SAPO materials, which significantly reduces the available options. Thus, parameters from Ghysels et al. [15] and Fasano et al. [14] were tested. The latter is based in the first model, with modifications in the partial charges, seeking to improve the reproduction of water adsorption and transport in the SAPO-34 material.

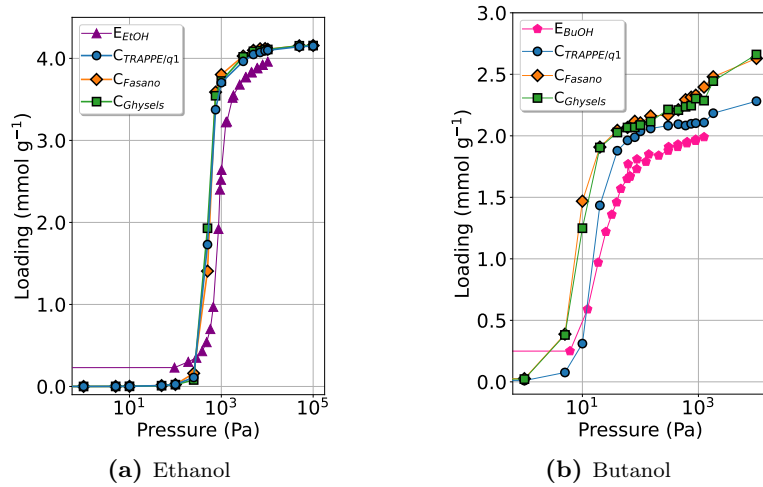


**Figure A6:** Experimental (E) and calculated (C) adsorption isotherms of ethanol (a) and butanol (b) in ITQ-29 structure. Simulated data considering ‘TRAPPE/q1’ (T), ‘Fasano’ (F) and ‘Ghysels’ models at 313 K.

Again, the MC simulations consider a rigid framework, and an effective interaction among adsorbates and the material only through its oxygen atoms. Thus, the main parameters from the MD force field applied to the MC simulations are the charge of framework atoms and the LJ between zeolite O atoms ( $O_z$ ). Remaining interactions were derived with the Lorentz-Berthelot mixing rules, considering the potentials of the adsorbates. Thus, for the model referred as ‘Ghysels’ in Figures A6 and A7, the charges were:  $Si = 2.10 e^-$  and  $O_z = -1.05 e^-$ ; and for ‘Fasano’ model:  $Si = 2.226 e^-$  and  $O_z = -1.113 e^-$ . Furthermore,  $O_z \cdots O_z$  LJ parameters were  $\varepsilon/k_B = 96.05$  K and  $\sigma = 3.11$  Å for both models [15]. It is important to note that these parameters are the same in our improved version of the force field (see section 2.5 of the main manuscript), as our proposed modifications mainly involve the bonded terms of the potential and a description of external surfaces. Here, alcohols were described by TRAPPE-UA force field, and SPC/E and TIP4P/2005 water models were compared, as presented the best results in the previous section.

Ethanol description with both MD models was in excellent agreement with the experimental data and the MC model previously selected (Figure A6a). For butanol adsorption (Figure A6b), MC and MD models presented similar results, with a small overestimation of the experimental value. On the other hand, MD models with water outperformed the MC models (Figure A7). The experimental maximum uptake of water in ITQ-29 (at 6245 Pa, dashed vertical line in Figure A7, left) is accurately described by the ‘Ghysels’ model in conjunction with TIP4P/2005 waters (small overestimation of 0.23 mmol/g, Figure A7, right). Although the ‘Fasano’ has improved charges for water interaction with SAPO materials, the water adsorption isotherm in a pure silica zeolite (ITQ-29) was better reproduced by its original force field definition (of Ghysels and co-workers).

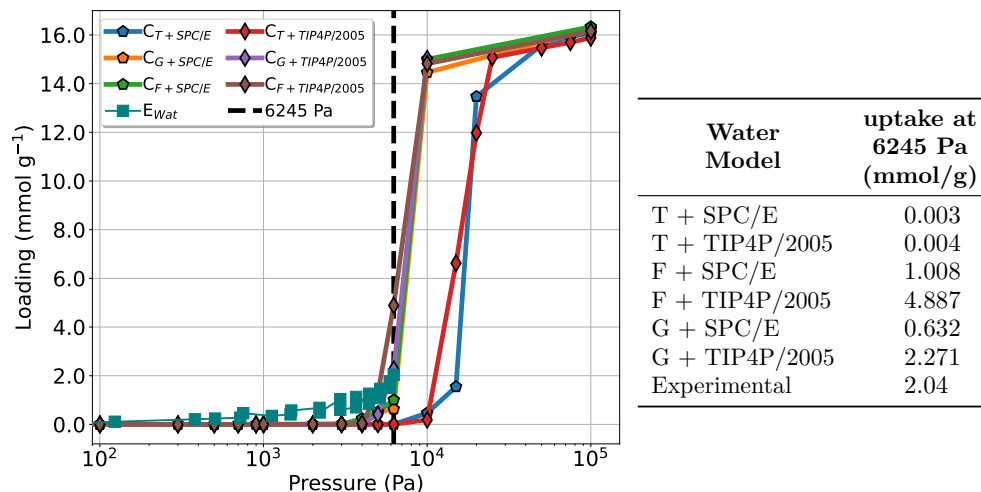


**Figure A7:** Experimental (E) and calculated (C) water adsorption isotherms in ITQ-29 structure. Simulated data considering ‘TRAPPE/q1’ (T), ‘Fasano’ (F) and ‘Ghysels’ (G) models at 313 K.

### A3 Mixture Adsorption Isotherms

With the models selected in the section S1, the adsorption isotherm of 0.07 butanol : 0.01 ethanol : 0.92 water mixture was computed. These molar fractions corresponds to the concentration of the adsorbates in the vapor phase of the fermenter. Considering the experimental pressure of such mixture (4569 Pa), adsorbed molecules are illustrated by Figure A8, the configuration at the end of the MC simulation.

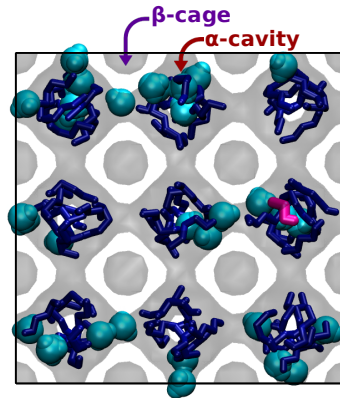


**Figure A8:** Final configuration of mixture (butanol, ethanol, water) adsorption at 4569 Pa and 313 K in ITQ-29  $3\times 3\times 3$  cell. Total of 81 butanol (blue), 1 ethanol (pink), and 32 water (cyan) molecules adsorbed. Zeolite channel system highlighted in gray, composed by  $\alpha$ -cavities and sodalite ( $\beta$ -cages, unaccessible).

## A4 Molecular Dynamics Simulations

Further details about the size and composition of the simulation boxes considered for the Molecular Dynamics simulations are reported in Table A3.

**Table A3:** Size and composition of the Molecular Dynamics (MD) simulation boxes. Beads can correspond to the united atom approach adopted for alcohols description, or each atom of zeolites, water and walls. Water molecules also contained a dummy atom, as defined by TIP4P/2005 [11] force field.

simulation box	MD1 (Figure 4)		MD2 (Figure 5a-c)		MD3 (Figure 5d-f)		
	composition	molecules	beads	molecules	beads	molecules	beads
butanol		81	6	162	6	162	6
ethanol		1	4	2	4	2	4
water		32	4	64	4	64	4
zeolite		1	2700	1	792	1	808
wall		1	448	1	242	1	242
<b>total</b>		<b>116</b>	<b>3766</b>	<b>230</b>	<b>2270</b>	<b>230</b>	<b>2286</b>

## A5 Adsorption Energy

The adsorption energy in the surface and bulk of ITQ-29, SSZ-13 and SAPO-34 materials was also estimated. The optimized geometries of adsorbates ··· framework complexes, considered for the adsorption energy calculations are summarized in Figure A9.

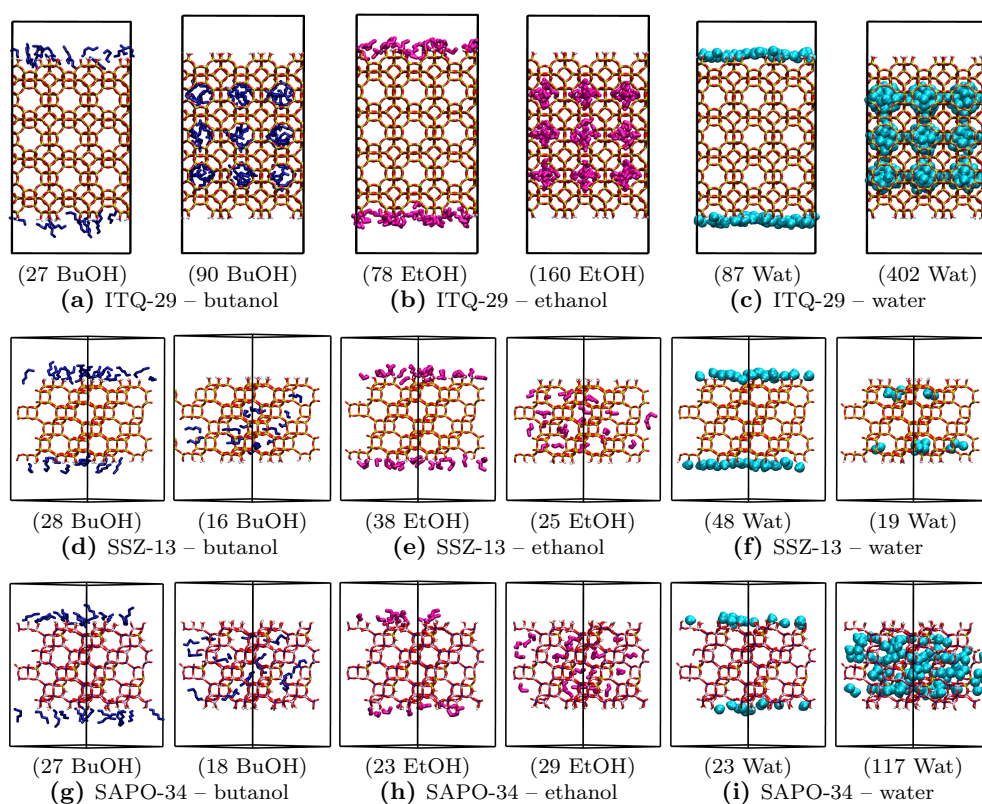


**Figure A9:** Optimized structures employed for the adsorption energy calculation. Butanol (BuOH, blue), ethanol (EtOH, pink), and water (Wat, cyan) adsorption in ITQ-29, SSZ-13 or SAPO-34 bulk or external surface.

Due to the force field description employed, the adsorption energy ( $\overline{\Delta E^{ads}}$ ) can be split into electrostatic ( $E^{Coul}$ ) and van der Waals ( $E^{vdW}$ ) contributions, providing insights about the nature and magnitude of the adsorption energy. Besides, the adsorption energy considered both zeolite ··· guests and guest ··· guest



intermolecular interactions, and the magnitude of the latter was also computed ( $E_{\text{guest}\cdots\text{guest}}$ ). All values are collected in Table A4.

**Table A4:** Adsorption energy ( $\overline{\Delta E^{ads}}$ ) of adsorbates in the bulk or external surface of ITQ-29, SSZ-13 or SAPO-34. Electrostatic ( $E^{Coul}$ ) and van der Waals ( $E^{vdW}$ ) components included, as well as zeo $\cdots$ guest and guest $\cdots$ guest contributions to the adsorption energy ( $E_{\text{zeo}\cdots\text{guest}}$  and  $E_{\text{guest}\cdots\text{guest}}$ , respectively). Energy values in kJ/mol. Loading of each configuration in Figure A9.

complex	bulk					surface					
	$\overline{\Delta E^{ads}}$	$E^{Coul}$	$E^{vdW}$	$E_{\text{zeo}\cdots\text{guest}}$	$E_{\text{guest}\cdots\text{guest}}$	$\overline{\Delta E^{ads}}$	$E^{Coul}$	$E^{vdW}$	$E_{\text{zeo}\cdots\text{guest}}$	$E_{\text{guest}\cdots\text{guest}}$	
ITQ-29	butanol	-84.3	-38.9	-45.4	-51.2	-33.1	-72.0	-63.9	-8.2	-59.1	-12.9
	ethanol	-71.1	-47.6	-23.5	-27.7	-43.4	-66.7	-65.4	-1.2	-48.7	-18.0
	water	-64.6	-66.1	1.6	-12.1	-52.5	-42.7	-47.1	4.4	-24.3	-18.4
SSZ-13	butanol	-83.7	-31.5	-52.2	-68.0	-15.7	-77.7	-65.9	-11.8	-60.1	-17.6
	ethanol	-57.6	-28.5	-29.0	-48.7	-8.9	-66.8	-65.0	-1.7	-53.1	-13.7
	water	-45.4	-43.0	-2.3	-20.9	-24.5	-57.0	-64.9	7.9	-36.3	-20.7
SAPO-34	butanol	-79.2	-34.0	-45.2	-71.2	-8.0	-74.7	-67.8	-6.9	-55.5	-19.2
	ethanol	-68.1	-41.6	-26.4	-57.9	-10.2	-72.2	-71.4	-0.7	-57.3	-14.9
	water	-62.6	-63.1	0.5	-27.4	-35.2	-66.2	-76.4	10.2	-54.0	-12.2

For all frameworks, the nature of the interaction of adsorbates in the bulk has an electrostatic dominance ( $E^{Coul} < E^{vdW}$ ) when the involved molecules are polar (water and ethanol). This is related to the significant guest $\cdots$ guest interactions established among water and ethanol molecules ( $E_{\text{guest}\cdots\text{guest}}$  from -9 to -52 kJ/mol). Especially for the water adsorption in the bulk, the electrostatic character is so pronounced that closer contacts are formed, leading to slightly repulsive contributions of  $E^{vdW}$  in some cases (+0.5 and +1.6 kJ/mol for SAPO-34 and ITQ-29, respectively). Besides, considering  $E_{\text{guest}\cdots\text{guest}}$  stabilization to the adsorption energy was crucial for the accurate reproduction of the heat of adsorption of water in SAPO-34, as discussed in the manuscript.

As the alcohol apolar chain increases (butanol), greater dispersive character ( $E^{vdW} < E^{Coul}$ ) is observed for the bulk adsorption in all zeolites. Inside the micropore, the van der Waals interactions with both polar and apolar moieties of the butanol molecule can be formed with the surrounding zeolite atoms, maximizing the  $E^{vdW}$  contribution to the adsorption energy.

On the other hand, surface adsorption in ITQ-29, SSZ-13 and SAPO-34 is dominated by the electrostatic term, as the main interaction established between zeolite external OH groups and the guests are hydrogen bonds. Furthermore,

smaller  $E_{\text{guest}\cdots\text{guest}}$  contributions are observed for surface adsorption, related to the concentration of guest molecules considered.

## A6 SAPO-34 Structure

The crystallographic CIF employed for SAPO-34 simulations is reported below, and was obtained from previous works [15, 16].

```
#SAPO-34 structure
_cell_length_a      27.4095
_cell_length_b      27.5039
_cell_length_c      29.5008
_cell_angle_alpha   89.9749
_cell_angle_beta    90.0198
_cell_angle_gamma   119.8945

_symmetry_Int_Tables_number 1
_symmetry_space_group_name_H-M P1

loop_
_symmetry_equiv_pos_as_xyz
'x,y,z'

loop_
_atom_site_label
_atom_site_type_symbol
_atom_site_fract_x
_atom_site_fract_y
_atom_site_fract_z
Si      Si      0.164530  0.221560  0.387480
Si      Si      0.336590  0.061460  0.225690
Si      Si      0.054230  0.219860  0.278770
Si      Si      0.664530  0.721560  0.887480
Si      Si      0.836590  0.561460  0.725690
Si      Si      0.554240  0.719860  0.778770
Si      Si      0.164530  0.721560  0.887480
Si      Si      0.336590  0.561460  0.725690
Si      Si      0.054230  0.719860  0.778770
Si      Si      0.664530  0.221560  0.887480
Si      Si      0.836590  0.061460  0.725690
Si      Si      0.554240  0.219860  0.778770
Si      Si      0.164530  0.221560  0.887480
Si      Si      0.336590  0.061460  0.725690
Si      Si      0.054240  0.219860  0.778770
Si      Si      0.664530  0.721560  0.387480
Si      Si      0.836590  0.561460  0.225690
Si      Si      0.554240  0.719860  0.278770
Si      Si      0.164530  0.721560  0.387480
Si      Si      0.336590  0.561460  0.225690
Si      Si      0.054230  0.719860  0.278770
Si      Si      0.664530  0.221560  0.387480
Si      Si      0.836590  0.061460  0.225690
Si      Si      0.554240  0.219860  0.278770
Al      Al      0.112230  0.007870  0.051700
Al      Al      0.494320  0.116720  0.050900
Al      Al      0.220400  0.058190  0.216030
Al      Al      0.449020  0.176420  0.215880
Al      Al      0.385790  0.389320  0.050320
Al      Al      0.442970  0.286580  0.114820
Al      Al      0.333970  0.058580  0.111670
Al      Al      0.216960  0.167990  0.115180
Al      Al      0.329410  0.285420  0.216680
Al      Al      0.110510  0.119790  0.450800
Al      Al      0.051780  0.224230  0.384060
Al      Al      0.003140  0.393860  0.449590
Al      Al      0.161800  0.451220  0.385330
Al      Al      0.172590  0.226920  0.282480
Al      Al      0.049830  0.341020  0.283250
Al      Al      0.276540  0.452910  0.283970
Al      Al      0.284950  0.345860  0.383580
Al      Al      0.384350  0.003090  0.447790
Al      Al      0.612230  0.507870  0.551700
Al      Al      0.994320  0.616720  0.550900
```

A1	A1	0.720400	0.558190	0.716030
A1	A1	0.949020	0.676430	0.715880
A1	A1	0.885790	0.889320	0.550320
A1	A1	0.942970	0.786580	0.614820
A1	A1	0.833970	0.558580	0.611670
A1	A1	0.716960	0.667990	0.615180
A1	A1	0.829400	0.785420	0.716690
A1	A1	0.610510	0.619790	0.950800
A1	A1	0.551780	0.724230	0.884060
A1	A1	0.503130	0.893860	0.949590
A1	A1	0.661800	0.951220	0.885330
A1	A1	0.672600	0.726910	0.782480
A1	A1	0.549830	0.841020	0.783240
A1	A1	0.776540	0.952910	0.783970
A1	A1	0.784950	0.845860	0.883580
A1	A1	0.884350	0.503090	0.947790
A1	A1	0.112240	0.507870	0.551700
A1	A1	0.494320	0.616720	0.550900
A1	A1	0.220400	0.558190	0.716030
A1	A1	0.449020	0.676430	0.715880
A1	A1	0.385790	0.889320	0.550320
A1	A1	0.442970	0.786580	0.614820
A1	A1	0.333970	0.558580	0.611670
A1	A1	0.216960	0.667990	0.615180
A1	A1	0.329410	0.785420	0.716690
A1	A1	0.110510	0.619790	0.950800
A1	A1	0.051780	0.724230	0.884060
A1	A1	0.003130	0.893860	0.949590
A1	A1	0.161800	0.951220	0.885330
A1	A1	0.172590	0.726910	0.782480
A1	A1	0.049830	0.841020	0.783240
A1	A1	0.276540	0.952910	0.783970
A1	A1	0.284950	0.845860	0.883580
A1	A1	0.384350	0.503090	0.947790
A1	A1	0.612230	0.007870	0.551700
A1	A1	0.994320	0.116720	0.550900
A1	A1	0.720400	0.058190	0.716030
A1	A1	0.949020	0.176420	0.715880
A1	A1	0.885790	0.389320	0.550320
A1	A1	0.942970	0.286580	0.614820
A1	A1	0.833970	0.058580	0.611670
A1	A1	0.716960	0.167990	0.615180
A1	A1	0.829400	0.285420	0.716690
A1	A1	0.610510	0.119790	0.950800
A1	A1	0.551780	0.224230	0.884060
A1	A1	0.503130	0.393860	0.949590
A1	A1	0.161800	0.451220	0.885330
A1	A1	0.172590	0.226920	0.782480
A1	A1	0.049820	0.341020	0.783240
A1	A1	0.276540	0.452910	0.783970
A1	A1	0.284950	0.345860	0.883580
A1	A1	0.384350	0.003090	0.947790
A1	A1	0.612230	0.507870	0.051700
A1	A1	0.994320	0.616720	0.050900
A1	A1	0.720400	0.558190	0.216030
A1	A1	0.949020	0.676430	0.215880
A1	A1	0.885790	0.889320	0.050320
A1	A1	0.942970	0.786580	0.114820
A1	A1	0.833970	0.558580	0.111670
A1	A1	0.716960	0.667990	0.115180
A1	A1	0.829400	0.785420	0.216680
A1	A1	0.610510	0.619790	0.450800
A1	A1	0.551780	0.724230	0.384060
A1	A1	0.503130	0.893860	0.449590
A1	A1	0.661800	0.951220	0.385330
A1	A1	0.672600	0.726910	0.282480

Appendix A. Supplementary material for Chapter 3

---

A1	A1	0.549830	0.841020	0.283250
A1	A1	0.776540	0.952910	0.283970
A1	A1	0.784950	0.845860	0.383580
A1	A1	0.884350	0.503090	0.447790
A1	A1	0.112240	0.507870	0.051700
A1	A1	0.494320	0.616720	0.050900
A1	A1	0.220400	0.558190	0.216030
A1	A1	0.449020	0.676430	0.215880
A1	A1	0.385790	0.889320	0.050320
A1	A1	0.442970	0.786580	0.114820
A1	A1	0.333970	0.558580	0.111670
A1	A1	0.216960	0.667990	0.115180
A1	A1	0.329410	0.785420	0.216680
A1	A1	0.110510	0.619790	0.450800
A1	A1	0.051780	0.724230	0.384060
A1	A1	0.003140	0.893860	0.449590
A1	A1	0.161800	0.951220	0.385330
A1	A1	0.172590	0.726910	0.282480
A1	A1	0.049830	0.841020	0.283250
A1	A1	0.276540	0.952910	0.283970
A1	A1	0.284950	0.845860	0.383580
A1	A1	0.384350	0.503090	0.447790
A1	A1	0.612230	0.007870	0.051700
A1	A1	0.994320	0.116720	0.050900
A1	A1	0.720400	0.058190	0.216030
A1	A1	0.949020	0.176420	0.215880
A1	A1	0.885790	0.389320	0.050320
A1	A1	0.942970	0.286580	0.114820
A1	A1	0.833970	0.058580	0.111670
A1	A1	0.716960	0.167990	0.115180
A1	A1	0.829400	0.285420	0.216680
A1	A1	0.610510	0.119790	0.450800
A1	A1	0.551780	0.224230	0.384060
A1	A1	0.503130	0.393860	0.449590
A1	A1	0.661800	0.451220	0.385330
A1	A1	0.672600	0.226920	0.282480
A1	A1	0.549830	0.341020	0.283250
A1	A1	0.776540	0.452910	0.283970
A1	A1	0.784950	0.345860	0.383580
A1	A1	0.884350	0.003090	0.447790
P	P	0.388740	0.392000	0.444080
P	P	0.383480	0.001030	0.054220
P	P	0.108700	0.119200	0.057400
P	P	0.217480	0.055450	0.111450
P	P	0.445450	0.175670	0.109400
P	P	0.218600	0.169210	0.221840
P	P	0.327110	0.283910	0.110590
P	P	0.001770	0.392800	0.055630
P	P	0.443990	0.286750	0.220790
P	P	0.495550	0.117430	0.444170
P	P	0.049150	0.334980	0.389420
P	P	0.114040	0.008800	0.445390
P	P	0.163250	0.453490	0.279540
P	P	0.281190	0.342100	0.276510
P	P	0.276540	0.453940	0.390340
P	P	0.888740	0.892000	0.944080
P	P	0.883480	0.501030	0.554220
P	P	0.608690	0.619200	0.557400
P	P	0.717470	0.555450	0.611450
P	P	0.945450	0.675680	0.609400
P	P	0.718600	0.669210	0.721840
P	P	0.827120	0.783910	0.610590
P	P	0.501770	0.892800	0.555630
P	P	0.943990	0.786750	0.720790
P	P	0.995550	0.617430	0.944170
P	P	0.549150	0.834980	0.889420
P	P	0.614040	0.508800	0.945390
P	P	0.663250	0.953490	0.779540
P	P	0.781190	0.842100	0.776510
P	P	0.776540	0.953950	0.890340
P	P	0.388740	0.892000	0.944080
P	P	0.383480	0.501030	0.554220
P	P	0.108700	0.619200	0.557400
P	P	0.217480	0.555450	0.611450
P	P	0.445450	0.675680	0.609400
P	P	0.218600	0.669210	0.721840
P	P	0.327110	0.783910	0.610590
P	P	0.001770	0.892800	0.555630
P	P	0.443990	0.786750	0.720790
P	P	0.495560	0.617430	0.944170
P	P	0.049150	0.834980	0.889420
P	P	0.114040	0.508800	0.945390
P	P	0.163250	0.953490	0.779540
P	P	0.281190	0.842100	0.776510

P	P	0.276540	0.953950	0.890340
P	P	0.888740	0.392000	0.944080
P	P	0.883480	0.001030	0.554220
P	P	0.608690	0.119200	0.557400
P	P	0.717470	0.055450	0.611450
P	P	0.945450	0.175670	0.609400
P	P	0.718600	0.169210	0.721840
P	P	0.827120	0.283910	0.610590
P	P	0.501770	0.392800	0.555630
P	P	0.943990	0.286750	0.720790
P	P	0.995550	0.117430	0.944170
P	P	0.549150	0.334980	0.889420
P	P	0.614040	0.008800	0.945390
P	P	0.663250	0.453490	0.779540
P	P	0.781190	0.342100	0.776510
P	P	0.776540	0.453940	0.890340
P	P	0.388740	0.392000	0.944080
P	P	0.383480	0.001030	0.554220
P	P	0.108700	0.119200	0.557400
P	P	0.217480	0.055450	0.611450
P	P	0.445450	0.175670	0.609400
P	P	0.218600	0.169210	0.721840
P	P	0.327110	0.283910	0.610590
P	P	0.001770	0.392800	0.555630
P	P	0.443990	0.286750	0.720790
P	P	0.495550	0.117430	0.944170
P	P	0.049160	0.334980	0.889420
P	P	0.114040	0.008800	0.945390
P	P	0.163250	0.453490	0.779540
P	P	0.281190	0.342100	0.776510
P	P	0.276540	0.453940	0.890340
P	P	0.888740	0.892000	0.444080
P	P	0.883480	0.501030	0.054220
P	P	0.608690	0.619200	0.057400
P	P	0.717470	0.555450	0.111450
P	P	0.945450	0.675680	0.109400
P	P	0.718600	0.669210	0.221840
P	P	0.827120	0.783910	0.110590
P	P	0.501770	0.892800	0.055630
P	P	0.943990	0.786750	0.220790
P	P	0.995550	0.617430	0.444170
P	P	0.549150	0.834980	0.389420
P	P	0.614040	0.508800	0.445390
P	P	0.663250	0.953490	0.279540
P	P	0.781190	0.842100	0.276510
P	P	0.776540	0.953950	0.390340
P	P	0.388740	0.892000	0.444080
P	P	0.383480	0.501030	0.054220
P	P	0.108700	0.619200	0.057400
P	P	0.217480	0.555450	0.111450
P	P	0.445450	0.675680	0.109400
P	P	0.218600	0.669210	0.221840
P	P	0.327110	0.783910	0.110590
P	P	0.001770	0.892800	0.055630
P	P	0.443990	0.786750	0.220790
P	P	0.495560	0.617430	0.444170
P	P	0.049150	0.834980	0.389420
P	P	0.114040	0.508800	0.445390
P	P	0.163250	0.953490	0.279540
P	P	0.281190	0.842100	0.276510
P	P	0.276540	0.953950	0.390340
P	P	0.888740	0.392000	0.444080
P	P	0.883480	0.001030	0.054220
P	P	0.608690	0.119200	0.057400
P	P	0.717470	0.055450	0.111450
P	P	0.945450	0.175670	0.109400
P	P	0.718600	0.169210	0.221840
P	P	0.827120	0.283910	0.110590
P	P	0.501770	0.392800	0.055630
P	P	0.943990	0.286750	0.220790
P	P	0.995550	0.117430	0.444170
P	P	0.549150	0.334980	0.389420
P	P	0.614040	0.008800	0.445390
P	P	0.663250	0.453490	0.279540
P	P	0.781190	0.342100	0.276510
P	P	0.776540	0.453940	0.390340
01	0	0.338050	0.037300	0.169610
01	0	0.228310	0.280130	0.406340
01	0	0.075180	0.292680	0.270000
01	0	0.838050	0.537310	0.669610
01	0	0.728310	0.780120	0.906340
01	0	0.575180	0.792680	0.770010
01	0	0.338050	0.537310	0.669610
01	0	0.228310	0.780120	0.906340

Appendix A. Supplementary material for Chapter 3

---

01	0	0.075180	0.792680	0.770010
01	0	0.838050	0.037300	0.669610
01	0	0.728310	0.280130	0.906340
01	0	0.575180	0.292680	0.770010
01	0	0.338050	0.037300	0.669610
01	0	0.228310	0.280130	0.906340
01	0	0.075180	0.292680	0.770010
01	0	0.838050	0.537310	0.169610
01	0	0.728310	0.780120	0.406340
01	0	0.575180	0.792680	0.270000
01	0	0.338050	0.537310	0.169610
01	0	0.228310	0.780120	0.406340
01	0	0.075180	0.792680	0.270000
01	0	0.838050	0.037300	0.169610
01	0	0.728310	0.280130	0.406340
01	0	0.575180	0.292680	0.270000
H1	H	0.112250	0.311570	0.254030
H1	H	0.341270	0.002720	0.170420
H1	H	0.237800	0.272650	0.437350
H1	H	0.612250	0.811570	0.754020
H1	H	0.841270	0.502720	0.670420
H1	H	0.737790	0.772650	0.937350
H1	H	0.112250	0.811570	0.754020
H1	H	0.341270	0.502720	0.670420
H1	H	0.237800	0.772650	0.937350
H1	H	0.612250	0.311570	0.754020
H1	H	0.841270	0.002720	0.670420
H1	H	0.737790	0.272650	0.937350
H1	H	0.112250	0.311570	0.754020
H1	H	0.341270	0.002720	0.670420
H1	H	0.237790	0.272650	0.937350
H1	H	0.612250	0.811570	0.254030
H1	H	0.841270	0.502720	0.170420
H1	H	0.737790	0.772650	0.437350
H1	H	0.112250	0.811570	0.254030
H1	H	0.341270	0.502720	0.170420
H1	H	0.237800	0.772650	0.437350
H1	H	0.612250	0.311570	0.254030
H1	H	0.841270	0.002720	0.170420
H1	H	0.737790	0.272650	0.437350
O2	O	0.033150	0.333410	0.339260
O2	O	0.290870	0.467790	0.340750
O2	O	0.181320	0.216580	0.337920
O2	O	0.293330	0.340180	0.327360
O2	O	0.032570	0.211210	0.328810
O2	O	0.163810	0.469270	0.329100
O2	O	0.204320	0.168000	0.171640
O2	O	0.460410	0.301430	0.171050
O2	O	0.462680	0.179060	0.158040
O2	O	0.198230	0.040800	0.160160
O2	O	0.326220	0.299830	0.159900
O2	O	0.369620	0.000940	0.004500
O2	O	0.123540	0.133670	0.007830
O2	O	0.003530	0.378550	0.005980
O2	O	0.127610	0.008150	0.495440
O2	O	0.370950	0.376180	0.493340
O2	O	0.110900	0.222030	0.269130
O2	O	0.105770	0.404080	0.267530
O2	O	0.284210	0.397190	0.266160
O2	O	0.045990	0.281460	0.403550
O2	O	0.224190	0.455590	0.403050
O2	O	0.268760	0.049300	0.102360
O2	O	0.272870	0.231920	0.097740
O2	O	0.446060	0.228780	0.095110
O2	O	0.395850	0.113210	0.231060
O2	O	0.215540	0.114840	0.234920
O2	O	0.393890	0.293510	0.231690
O2	O	0.440280	0.388430	0.433270
O2	O	0.440270	0.066030	0.431080
O2	O	0.116600	0.062880	0.433230
O2	O	0.055910	0.444500	0.068840
O2	O	0.379760	0.446370	0.067790
O2	O	0.493390	0.327690	0.250110
O2	O	0.324030	0.008840	0.254380
O2	O	0.177400	0.176740	0.249750
O2	O	0.008730	0.189930	0.241910
O2	O	0.174110	0.001880	0.249570
O2	O	0.324440	0.336180	0.248800
O2	O	0.157990	0.159450	0.086280
O2	O	0.493070	0.343930	0.084540
O2	O	0.340790	0.008650	0.081730
O2	O	0.325390	0.494860	0.419180
O2	O	0.159590	0.175990	0.421850
O2	O	0.008670	0.344300	0.417800

02	0	0.340960	0.351090	0.413890
02	0	0.003650	0.166620	0.416570
02	0	0.155510	0.000690	0.417180
02	0	0.170690	0.015540	0.080610
02	0	0.335270	0.331980	0.080300
02	0	0.207020	0.435270	0.272520
02	0	0.223110	0.294630	0.265390
02	0	0.266430	0.394380	0.398790
02	0	0.119460	0.240360	0.392590
02	0	0.109170	0.383900	0.395700
02	0	0.232750	0.115980	0.101450
02	0	0.375680	0.272550	0.103530
02	0	0.384740	0.126170	0.103570
02	0	0.430860	0.227530	0.229900
02	0	0.287970	0.074850	0.219770
02	0	0.278490	0.218110	0.229810
02	0	0.399940	0.451160	0.434660
02	0	0.042870	0.104450	0.436500
02	0	0.054500	0.460580	0.436190
02	0	0.096060	0.059050	0.065710
02	0	0.453140	0.404430	0.062580
02	0	0.493910	0.129930	0.494460
02	0	0.057250	0.123250	0.069590
02	0	0.484430	0.166140	0.079230
02	0	0.442270	0.049190	0.064540
02	0	0.533150	0.833410	0.839260
02	0	0.790870	0.967790	0.840750
02	0	0.681310	0.716590	0.837920
02	0	0.793330	0.840180	0.827360
02	0	0.532580	0.711200	0.828810
02	0	0.663800	0.969270	0.829100
02	0	0.704320	0.668000	0.671630
02	0	0.960400	0.801430	0.671050
02	0	0.962680	0.679060	0.658040
02	0	0.698220	0.540800	0.660160
02	0	0.826220	0.799830	0.659900
02	0	0.869620	0.500940	0.504500
02	0	0.623550	0.633670	0.507830
02	0	0.503530	0.878550	0.505980
02	0	0.627610	0.508150	0.995440
02	0	0.870950	0.876180	0.993340
02	0	0.610900	0.722030	0.769130
02	0	0.605770	0.904080	0.767530
02	0	0.784210	0.897190	0.766160
02	0	0.545990	0.781460	0.903550
02	0	0.724190	0.955590	0.903050
02	0	0.768760	0.549300	0.602370
02	0	0.772870	0.731920	0.597740
02	0	0.946060	0.728790	0.595110
02	0	0.895850	0.613210	0.731060
02	0	0.715540	0.614840	0.734920
02	0	0.893890	0.793510	0.731690
02	0	0.940270	0.888430	0.933270
02	0	0.940270	0.566030	0.931080
02	0	0.616600	0.562880	0.933240
02	0	0.555900	0.944500	0.568840
02	0	0.879760	0.946370	0.567790
02	0	0.993380	0.827690	0.750110
02	0	0.824030	0.508840	0.754380
02	0	0.677400	0.676740	0.749750
02	0	0.508740	0.689930	0.741910
02	0	0.674110	0.501880	0.749570
02	0	0.824440	0.836180	0.748800
02	0	0.657990	0.659450	0.586280
02	0	0.993070	0.843930	0.584540
02	0	0.840790	0.508650	0.581730
02	0	0.825390	0.994860	0.919180
02	0	0.659590	0.675990	0.921850
02	0	0.508670	0.844300	0.917800
02	0	0.840960	0.851090	0.913890
02	0	0.503650	0.666610	0.916570
02	0	0.655510	0.500690	0.917180
02	0	0.670690	0.515540	0.580610
02	0	0.835270	0.831980	0.580300
02	0	0.707030	0.935270	0.772520
02	0	0.723110	0.794630	0.765390
02	0	0.766430	0.894380	0.898790
02	0	0.619460	0.740360	0.892590
02	0	0.609170	0.883900	0.895700
02	0	0.732740	0.615980	0.601450
02	0	0.875680	0.772550	0.603520
02	0	0.884740	0.626170	0.603570
02	0	0.930860	0.727530	0.729900
02	0	0.787970	0.574850	0.719770

Appendix A. Supplementary material for Chapter 3

---

02	0	0.778490	0.718110	0.729810
02	0	0.899940	0.951170	0.934660
02	0	0.542870	0.604450	0.936500
02	0	0.554490	0.960570	0.936190
02	0	0.596060	0.559050	0.565710
02	0	0.953140	0.904430	0.562580
02	0	0.993910	0.629930	0.994460
02	0	0.557250	0.623250	0.569590
02	0	0.984430	0.666140	0.579230
02	0	0.942270	0.549190	0.564540
02	0	0.033150	0.833410	0.839260
02	0	0.290870	0.967790	0.840750
02	0	0.181320	0.716590	0.837920
02	0	0.293330	0.840180	0.827360
02	0	0.032570	0.711200	0.828810
02	0	0.163810	0.969270	0.829100
02	0	0.204320	0.668000	0.671630
02	0	0.460410	0.801430	0.671050
02	0	0.462680	0.679060	0.658040
02	0	0.198230	0.540800	0.660160
02	0	0.326220	0.799830	0.659900
02	0	0.369620	0.500940	0.504500
02	0	0.123550	0.633670	0.507830
02	0	0.003530	0.878550	0.505980
02	0	0.127610	0.508150	0.995440
02	0	0.370950	0.876180	0.993340
02	0	0.110900	0.722030	0.769130
02	0	0.105770	0.904080	0.767530
02	0	0.284210	0.897190	0.766160
02	0	0.045990	0.781460	0.903550
02	0	0.224190	0.955590	0.903050
02	0	0.268760	0.549300	0.602370
02	0	0.272870	0.731920	0.597740
02	0	0.446060	0.728790	0.595110
02	0	0.395850	0.613210	0.731060
02	0	0.215540	0.614840	0.734920
02	0	0.393890	0.793510	0.731690
02	0	0.440280	0.888430	0.933270
02	0	0.440280	0.566030	0.931080
02	0	0.116600	0.562880	0.933240
02	0	0.055910	0.944500	0.568840
02	0	0.379760	0.946370	0.567790
02	0	0.493390	0.827690	0.750110
02	0	0.324030	0.508840	0.754380
02	0	0.177400	0.676740	0.749750
02	0	0.008740	0.689930	0.741910
02	0	0.174110	0.501880	0.749570
02	0	0.324440	0.836180	0.748800
02	0	0.157990	0.659450	0.586280
02	0	0.493070	0.843930	0.584540
02	0	0.340790	0.508650	0.581730
02	0	0.325390	0.994860	0.919180
02	0	0.159590	0.675990	0.921850
02	0	0.008670	0.844300	0.917800
02	0	0.340960	0.851090	0.913890
02	0	0.003650	0.666610	0.916570
02	0	0.155510	0.500690	0.917180
02	0	0.170690	0.515540	0.580610
02	0	0.335270	0.831980	0.580300
02	0	0.207020	0.935270	0.772520
02	0	0.223110	0.794630	0.765390
02	0	0.266430	0.894380	0.898790
02	0	0.119460	0.740360	0.892590
02	0	0.109170	0.883900	0.895700
02	0	0.232750	0.615980	0.601450
02	0	0.375680	0.772550	0.603520
02	0	0.384740	0.626170	0.603570
02	0	0.430860	0.727530	0.729900
02	0	0.287970	0.574850	0.719770
02	0	0.278490	0.718110	0.729810
02	0	0.399940	0.951170	0.934660
02	0	0.042880	0.604450	0.936500
02	0	0.054490	0.960570	0.936190
02	0	0.096060	0.559050	0.565710
02	0	0.453140	0.904430	0.562580
02	0	0.493910	0.629930	0.994460
02	0	0.057250	0.623250	0.569590
02	0	0.484430	0.666140	0.579230
02	0	0.442270	0.549190	0.564540
02	0	0.533150	0.333410	0.839260
02	0	0.790870	0.467790	0.840750
02	0	0.681320	0.216580	0.837920
02	0	0.793330	0.340180	0.827360
02	0	0.532580	0.211210	0.828810



02	0	0.663800	0.469270	0.829100
02	0	0.704320	0.168000	0.671630
02	0	0.960400	0.301430	0.671050
02	0	0.962680	0.179060	0.658040
02	0	0.698220	0.040800	0.660160
02	0	0.826220	0.299830	0.659900
02	0	0.869620	0.000940	0.504500
02	0	0.623550	0.133670	0.507830
02	0	0.503530	0.378550	0.505980
02	0	0.627610	0.008150	0.995440
02	0	0.870950	0.376180	0.993340
02	0	0.610900	0.222030	0.769130
02	0	0.605770	0.404080	0.767530
02	0	0.784210	0.397190	0.766160
02	0	0.545990	0.281460	0.903550
02	0	0.724190	0.455590	0.903050
02	0	0.768760	0.049300	0.602370
02	0	0.772870	0.231920	0.597740
02	0	0.946060	0.228780	0.595110
02	0	0.895850	0.113210	0.731060
02	0	0.715540	0.114840	0.734920
02	0	0.893890	0.293510	0.731690
02	0	0.940270	0.388430	0.933270
02	0	0.940270	0.066030	0.931080
02	0	0.616600	0.062880	0.933240
02	0	0.555900	0.444500	0.568840
02	0	0.879760	0.446370	0.567790
02	0	0.993380	0.327690	0.750110
02	0	0.824030	0.008840	0.754380
02	0	0.677400	0.176740	0.749750
02	0	0.508740	0.189930	0.741910
02	0	0.674110	0.001880	0.749570
02	0	0.824440	0.336180	0.748800
02	0	0.657990	0.159450	0.586280
02	0	0.993070	0.343930	0.584540
02	0	0.840790	0.008650	0.581730
02	0	0.825390	0.494860	0.919180
02	0	0.659590	0.175990	0.921850
02	0	0.508670	0.344300	0.917800
02	0	0.840960	0.351090	0.913890
02	0	0.503650	0.166620	0.916570
02	0	0.655510	0.000690	0.917180
02	0	0.670690	0.015540	0.580610
02	0	0.835270	0.331980	0.580300
02	0	0.707030	0.435270	0.772520
02	0	0.723110	0.294630	0.765390
02	0	0.766430	0.394380	0.898790
02	0	0.619460	0.240360	0.892590
02	0	0.609170	0.383900	0.895700
02	0	0.732740	0.115980	0.601450
02	0	0.875680	0.272550	0.603520
02	0	0.884740	0.126170	0.603570
02	0	0.930860	0.227530	0.729900
02	0	0.787970	0.074850	0.719770
02	0	0.778490	0.218110	0.729810
02	0	0.899940	0.451160	0.934660
02	0	0.542870	0.104450	0.936500
02	0	0.554490	0.460580	0.936190
02	0	0.596060	0.059050	0.565710
02	0	0.953140	0.404430	0.562580
02	0	0.993910	0.129930	0.994460
02	0	0.557250	0.123250	0.569590
02	0	0.984430	0.166140	0.579230
02	0	0.942270	0.049190	0.564540
02	0	0.033150	0.333410	0.839260
02	0	0.290870	0.467790	0.840750
02	0	0.181320	0.216580	0.837920
02	0	0.293330	0.340180	0.827360
02	0	0.032580	0.211210	0.828810
02	0	0.163810	0.469270	0.829100
02	0	0.204320	0.168000	0.671630
02	0	0.460410	0.301430	0.671050
02	0	0.462680	0.179060	0.658040
02	0	0.198230	0.040800	0.660160
02	0	0.326220	0.299830	0.659900
02	0	0.369620	0.000940	0.504500
02	0	0.123550	0.133670	0.507830
02	0	0.003530	0.378550	0.505980
02	0	0.127610	0.008150	0.995440
02	0	0.370950	0.376180	0.993340
02	0	0.110900	0.222030	0.769130
02	0	0.105770	0.404080	0.767530
02	0	0.284210	0.397190	0.766160
02	0	0.045990	0.281460	0.903550

Appendix A. Supplementary material for Chapter 3

---

02	0	0.224190	0.455590	0.903050
02	0	0.268760	0.049300	0.602370
02	0	0.272870	0.231920	0.597740
02	0	0.446060	0.228780	0.595110
02	0	0.395850	0.113210	0.731060
02	0	0.215540	0.114840	0.734920
02	0	0.393890	0.293510	0.731690
02	0	0.440280	0.388430	0.933270
02	0	0.440270	0.066030	0.931080
02	0	0.116600	0.062880	0.933240
02	0	0.055910	0.444500	0.568840
02	0	0.379760	0.446370	0.567790
02	0	0.493390	0.327690	0.750110
02	0	0.324030	0.008840	0.754380
02	0	0.177400	0.176740	0.749750
02	0	0.008740	0.189930	0.741910
02	0	0.174110	0.001880	0.749570
02	0	0.324440	0.336180	0.748800
02	0	0.157990	0.159450	0.586280
02	0	0.493070	0.343930	0.584540
02	0	0.340790	0.008650	0.581730
02	0	0.325390	0.494860	0.919180
02	0	0.159590	0.175990	0.921850
02	0	0.008670	0.344300	0.917800
02	0	0.340960	0.351090	0.913890
02	0	0.003650	0.166620	0.916570
02	0	0.155510	0.000690	0.917180
02	0	0.170690	0.015540	0.580610
02	0	0.335270	0.331980	0.580300
02	0	0.207020	0.435270	0.772520
02	0	0.223110	0.294630	0.765390
02	0	0.266430	0.394380	0.898790
02	0	0.119470	0.240360	0.892590
02	0	0.109170	0.383900	0.895700
02	0	0.232750	0.115980	0.601450
02	0	0.375680	0.272550	0.603520
02	0	0.384740	0.126170	0.603570
02	0	0.430860	0.227530	0.729900
02	0	0.287970	0.074850	0.719770
02	0	0.278490	0.218110	0.729810
02	0	0.399940	0.451160	0.934660
02	0	0.042870	0.104450	0.936500
02	0	0.054500	0.460580	0.936190
02	0	0.096060	0.059050	0.565710
02	0	0.453140	0.404430	0.562580
02	0	0.493910	0.129930	0.994460
02	0	0.057250	0.123250	0.569590
02	0	0.484430	0.166140	0.579230
02	0	0.442270	0.049190	0.564540
02	0	0.533150	0.833410	0.339260
02	0	0.790870	0.967790	0.340750
02	0	0.681310	0.716590	0.337920
02	0	0.793330	0.840180	0.327360
02	0	0.532580	0.711200	0.328810
02	0	0.663800	0.969270	0.329100
02	0	0.704320	0.668000	0.171640
02	0	0.960400	0.801430	0.171050
02	0	0.962680	0.679060	0.158040
02	0	0.698220	0.540800	0.160160
02	0	0.826220	0.799830	0.159900
02	0	0.869620	0.500940	0.004500
02	0	0.623550	0.633670	0.007830
02	0	0.503530	0.878550	0.005980
02	0	0.627610	0.508150	0.495440
02	0	0.870950	0.876180	0.493340
02	0	0.610900	0.722030	0.269130
02	0	0.605770	0.904080	0.267530
02	0	0.784210	0.897190	0.266160
02	0	0.545990	0.781460	0.403550
02	0	0.724190	0.955590	0.403050
02	0	0.768760	0.549300	0.102360
02	0	0.772870	0.731920	0.097740
02	0	0.946060	0.728790	0.095110
02	0	0.895850	0.613210	0.231060
02	0	0.715540	0.614840	0.234920
02	0	0.893890	0.793510	0.231690
02	0	0.940270	0.888430	0.433270
02	0	0.940270	0.566030	0.431080
02	0	0.616600	0.562880	0.433230
02	0	0.555900	0.944500	0.068840
02	0	0.879760	0.946370	0.067790
02	0	0.993380	0.827690	0.250110
02	0	0.824030	0.508840	0.254380
02	0	0.677400	0.676740	0.249750

02	0	0.508740	0.689930	0.241910
02	0	0.674110	0.501880	0.249570
02	0	0.824440	0.836180	0.248800
02	0	0.657990	0.659450	0.086280
02	0	0.993070	0.843930	0.084540
02	0	0.840790	0.508650	0.081730
02	0	0.825390	0.994860	0.419180
02	0	0.659590	0.675990	0.421850
02	0	0.508670	0.844300	0.417800
02	0	0.840960	0.851090	0.413890
02	0	0.503650	0.666610	0.416570
02	0	0.655510	0.500690	0.417180
02	0	0.670690	0.515540	0.080610
02	0	0.835270	0.831980	0.080300
02	0	0.707030	0.935270	0.272520
02	0	0.723110	0.794630	0.265390
02	0	0.766420	0.894380	0.398790
02	0	0.619460	0.740360	0.392590
02	0	0.609170	0.883900	0.395700
02	0	0.732740	0.615980	0.101450
02	0	0.875680	0.772550	0.103530
02	0	0.884740	0.626170	0.103570
02	0	0.930860	0.727530	0.229900
02	0	0.787970	0.574850	0.219770
02	0	0.778490	0.718110	0.229810
02	0	0.899940	0.951170	0.434660
02	0	0.542870	0.604450	0.436500
02	0	0.554490	0.960570	0.436190
02	0	0.596060	0.559050	0.065710
02	0	0.953140	0.904430	0.062580
02	0	0.993910	0.629930	0.494460
02	0	0.557250	0.623250	0.069590
02	0	0.984430	0.666140	0.079230
02	0	0.942270	0.549190	0.064540
02	0	0.033150	0.833410	0.339260
02	0	0.290870	0.967790	0.340750
02	0	0.181320	0.716590	0.337920
02	0	0.293330	0.840180	0.327360
02	0	0.032570	0.711200	0.328810
02	0	0.163810	0.969270	0.329100
02	0	0.204320	0.668000	0.171640
02	0	0.460410	0.801430	0.171050
02	0	0.462680	0.679060	0.158040
02	0	0.198230	0.540800	0.160160
02	0	0.326220	0.799830	0.159900
02	0	0.369620	0.500940	0.004500
02	0	0.123550	0.633670	0.007830
02	0	0.003530	0.878550	0.005980
02	0	0.127610	0.508150	0.495440
02	0	0.370950	0.876180	0.493340
02	0	0.110900	0.722030	0.269130
02	0	0.105770	0.904080	0.267530
02	0	0.284210	0.897190	0.266160
02	0	0.045990	0.781460	0.403550
02	0	0.224190	0.955590	0.403050
02	0	0.268760	0.549300	0.102360
02	0	0.272870	0.731920	0.097740
02	0	0.446060	0.728790	0.095110
02	0	0.395850	0.613210	0.231060
02	0	0.215540	0.614840	0.234920
02	0	0.393890	0.793510	0.231690
02	0	0.440280	0.888430	0.433270
02	0	0.440280	0.566030	0.431080
02	0	0.116600	0.562880	0.433230
02	0	0.055900	0.944500	0.068840
02	0	0.379760	0.946370	0.067790
02	0	0.493390	0.827690	0.250110
02	0	0.324030	0.508840	0.254380
02	0	0.177400	0.676740	0.249750
02	0	0.008730	0.689930	0.241910
02	0	0.174110	0.501880	0.249570
02	0	0.324440	0.836180	0.248800
02	0	0.157990	0.659450	0.086280
02	0	0.493070	0.843930	0.084540
02	0	0.340790	0.508650	0.081730
02	0	0.325390	0.994860	0.419180
02	0	0.159590	0.675990	0.421850
02	0	0.008670	0.844300	0.417800
02	0	0.340960	0.851090	0.413890
02	0	0.003650	0.666610	0.416570
02	0	0.155510	0.500690	0.417180
02	0	0.170690	0.515540	0.080610
02	0	0.335270	0.831980	0.080300
02	0	0.207020	0.935270	0.272520

Appendix A. Supplementary material for Chapter 3

---

02	0	0.223110	0.794630	0.265390
02	0	0.266430	0.894380	0.398790
02	0	0.119460	0.740360	0.392590
02	0	0.109170	0.883900	0.395700
02	0	0.232750	0.615980	0.101450
02	0	0.375680	0.772550	0.103530
02	0	0.384740	0.626170	0.103570
02	0	0.430860	0.727530	0.229900
02	0	0.287970	0.574850	0.219770
02	0	0.278490	0.718110	0.229810
02	0	0.399940	0.951170	0.434660
02	0	0.042880	0.604450	0.436500
02	0	0.054500	0.960570	0.436190
02	0	0.096060	0.559050	0.065710
02	0	0.453140	0.904430	0.062580
02	0	0.493910	0.629930	0.494460
02	0	0.057250	0.623250	0.069590
02	0	0.484430	0.666140	0.079230
02	0	0.442270	0.549190	0.064540
02	0	0.533150	0.333410	0.339260
02	0	0.790870	0.467790	0.340750
02	0	0.681320	0.216580	0.337920
02	0	0.793330	0.340180	0.327360
02	0	0.532580	0.211210	0.328810
02	0	0.663800	0.469270	0.329100
02	0	0.704320	0.168000	0.171640
02	0	0.960400	0.301430	0.171050
02	0	0.962680	0.179060	0.158040
02	0	0.698220	0.040800	0.160160
02	0	0.826220	0.299830	0.159900
02	0	0.869620	0.000940	0.004500
02	0	0.623550	0.133670	0.007830
02	0	0.503530	0.378550	0.005980
02	0	0.627610	0.008150	0.495440
02	0	0.870950	0.376180	0.493340
02	0	0.610900	0.222030	0.269130
02	0	0.605770	0.404080	0.267530
02	0	0.784210	0.397190	0.266160
02	0	0.545990	0.281460	0.403550
02	0	0.724190	0.455590	0.403050
02	0	0.768760	0.049300	0.102360
02	0	0.772870	0.231920	0.097740
02	0	0.946060	0.228780	0.095110
02	0	0.895850	0.113210	0.231060
02	0	0.715540	0.114840	0.234920
02	0	0.893890	0.293510	0.231690
02	0	0.940270	0.388430	0.433270
02	0	0.940270	0.066030	0.431080
02	0	0.616600	0.062880	0.433230
02	0	0.555900	0.444500	0.068840
02	0	0.879760	0.446370	0.067790
02	0	0.993380	0.327690	0.250110
02	0	0.824030	0.008840	0.254380
02	0	0.677400	0.176740	0.249750
02	0	0.508740	0.189930	0.241910
02	0	0.674110	0.001880	0.249570
02	0	0.824440	0.336180	0.248800
02	0	0.657990	0.159450	0.086280
02	0	0.993070	0.343930	0.084540
02	0	0.840790	0.008650	0.081730
02	0	0.825390	0.494860	0.419180
02	0	0.659590	0.175990	0.421850
02	0	0.508670	0.344300	0.417800
02	0	0.840960	0.351090	0.413890
02	0	0.503650	0.166620	0.416570
02	0	0.655510	0.000690	0.417180
02	0	0.670690	0.015540	0.080610
02	0	0.835270	0.331980	0.080300
02	0	0.707030	0.435270	0.272520
02	0	0.723110	0.294630	0.265390
02	0	0.766430	0.394380	0.398790
02	0	0.619460	0.240360	0.392590
02	0	0.609170	0.383900	0.395700
02	0	0.732740	0.115980	0.101450
02	0	0.875680	0.272550	0.103530
02	0	0.884740	0.126170	0.103570
02	0	0.930860	0.227530	0.229900
02	0	0.787970	0.074850	0.219770
02	0	0.778490	0.218110	0.229810
02	0	0.899940	0.451160	0.434660
02	0	0.542870	0.104450	0.436500
02	0	0.554490	0.460580	0.436190
02	0	0.596060	0.059050	0.065710
02	0	0.953140	0.404430	0.062580

02	0	0.993910	0.129930	0.494460
02	0	0.557250	0.123250	0.069590
02	0	0.984430	0.166140	0.079230
02	0	0.942270	0.049190	0.064540

## References

- [1] Corma, A.; Rey, F.; Rius, J.; Sabater, M. J.; Valencia, S. Supramolecular Self-assembled Molecules as Organic Directing Agent for Synthesis of Zeolites. *Nature* **2004**, *431*, 287–290. DOI: 10.1038/nature02909.
- [2] Martin-Calvo, A.; Van der Perre, S.; Claessens, B.; Calero, S.; Denayer, J. F. M. Unravelling the Influence of Carbon Dioxide on the Adsorptive Recovery of Butanol from Fermentation Broth Using ITQ-29 and ZIF-8. *Phys. Chem. Chem. Phys.* **2018**, *20* (15), 9957–9964. DOI: 10.1039/C8CP01034J.
- [3] Kuhn, J.; Castillo-Sanchez, J. M.; Gascon, J.; Calero, S.; Dubbeldam, D.; Vlugt, T. J. H.; Kapteijn, F.; Gross, J. Adsorption and Diffusion of Water, Methanol, and Ethanol in All-Silica DD3R: Experiments and Simulation. *J. Phys. Chem. C* **2009**, *113* (32), 14290–14301. DOI: 10.1021/jp901869d.
- [4] Jorgensen, W. L. Optimized Intermolecular Potential Functions for Liquid Alcohols. *J. Phys. Chem.* **1986**, *90* (7), 1276–1284. DOI: 10.1021/j100398a015.
- [5] Dubbeldam, D.; Calero, S.; Vlugt, T. J. H.; Krishna, R.; Maesen, T. L. M.; Smit, B. United Atom Force Field for Alkanes in Nanoporous Materials. *J. Phys. Chem. B* **2004**, *108* (33), 12301–12313. DOI: 10.1021/jp0376727.
- [6] Chen, B.; Potoff, J. J.; Siepmann, J. I. Monte Carlo Calculations for Alcohols and Their Mixtures with Alkanes. Transferable Potentials for Phase Equilibria. 5. United-Atom Description of Primary, Secondary, and Tertiary Alcohols. *J. Phys. Chem. B* **2001**, *105* (15), 3093–3104. DOI: 10.1021/jp003882x.
- [7] Jorgensen, W. L.; Madura, J. D.; Swenson, C. J. Optimized Intermolecular Potential Functions for Liquid Hydrocarbons. *J. Am. Chem. Soc.* **1984**, *106* (22), 6638–6646. DOI: 10.1021/ja00334a030.

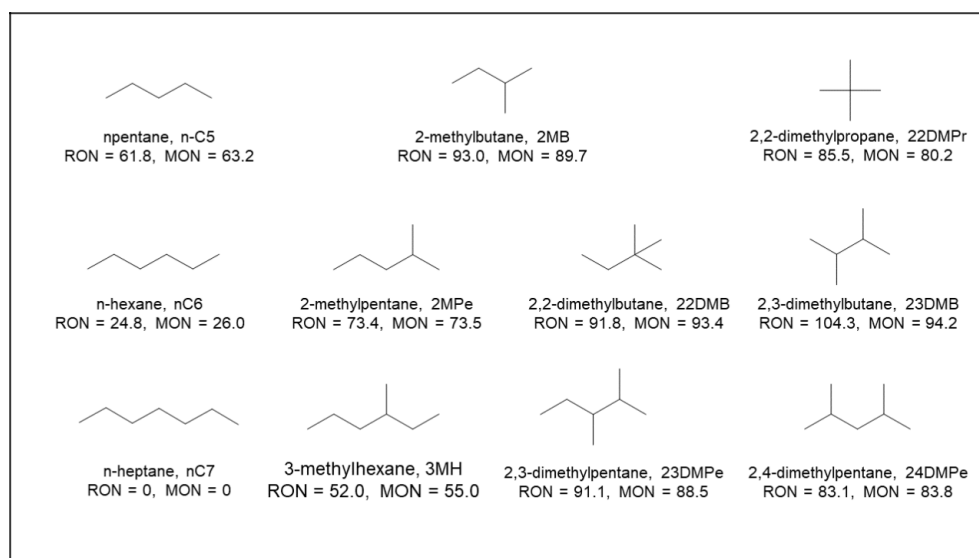
- [8] Berendsen, H. J. C.; Grigera, J. R.; Straatsma, T. P. The Missing Term in Effective Pair Potentials. *J. Phys. Chem.* **1987**, *91* (24), 6269–6271. DOI: 10.1021/j100308a038.
- [9] Jorgensen, W. L.; Chandrasekhar, J.; Madura, J. D.; Impey, R. W.; Klein, M. L. Comparison of Simple Potential Functions for Simulating Liquid Water. *J. Chem. Phys.* **1983**, *79* (2), 926–935. DOI: 10.1063/1.445869.
- [10] Horn, H. W.; Swope, W. C.; Pitner, J. W.; Madura, J. D.; Dick, T. J.; Hura, G. L.; Head-Gordon, T. Development of an Improved Four-site Water Model for Biomolecular Simulations: TIP4P-Ew. *J. Chem. Phys.* **2004**, *120* (20), 9665–9678. DOI: 10.1063/1.1683075.
- [11] Abascal, J. L. F.; Vega, C. A General Purpose Model for the Condensed Phases of Water: TIP4P/2005. *J. Chem. Phys.* **2005**, *123* (23), 234505. DOI: 10.1063/1.2121687.
- [12] Rick, S. W. A Reoptimization of the Five-site Water Potential (TIP5P) for Use with Ewald Sums. *J. Chem. Phys.* **2004**, *120* (13), 6085–6093. DOI: 10.1063/1.1652434.
- [13] Gómez-Álvarez, P.; Noya, E. G.; Lomba, E.; Valencia, S.; Pires, J. Study of Short-Chain Alcohol and Alcohol–Water Adsorption in MEL and MFI Zeolites. *Langmuir* **2018**, *34* (43), 12739–12750. DOI: 10.1021/acs.langmuir.8b02326.
- [14] Fasano, M.; Falciani, G.; Brancato, V.; Palomba, V.; Asinari, P.; Chiavazzo, E.; Frazzica, A. Atomistic Modelling of Water Transport and Adsorption Mechanisms in Silicoaluminophosphate for Thermal Energy Storage. *Appl. Therm. Eng.* **2019**, *160*, 114075. DOI: 10.1016/j.applthermaleng.2019.114075.
- [15] Ghysels, A.; Moors, S. L. C.; Hemelsoet, K.; De Wispelaere, K.; Waroquier, M.; Sastre, G.; Van Speybroeck, V. Shape-Selective Diffusion of Olefins in 8-Ring Solid Acid Microporous Zeolites. *J. Phys. Chem. C* **2015**, *119* (41), 23721–23734. DOI: 10.1021/acs.jpcc.5b06010.
- [16] Sastre, G.; Lewis, D. W.; Catlow, C. R. A. Modeling of Silicon Substitution in SAPO-5 and SAPO-34 Molecular Sieves. *J. Phys. Chem. B* **1997**, *101* (27), 5249–5262. DOI: 10.1021/jp963736k.

## Appendix B

# Supplementary material for Chapter 4

### B1 Experimental Adsorption Data

The studied adsorbates can be found in Scheme B1.



**Scheme B1:** Hydrocarbon molecules used for this study, together with the abbreviation used for this work and their research and motor octane numbers (RON and MON, respectively) [1]

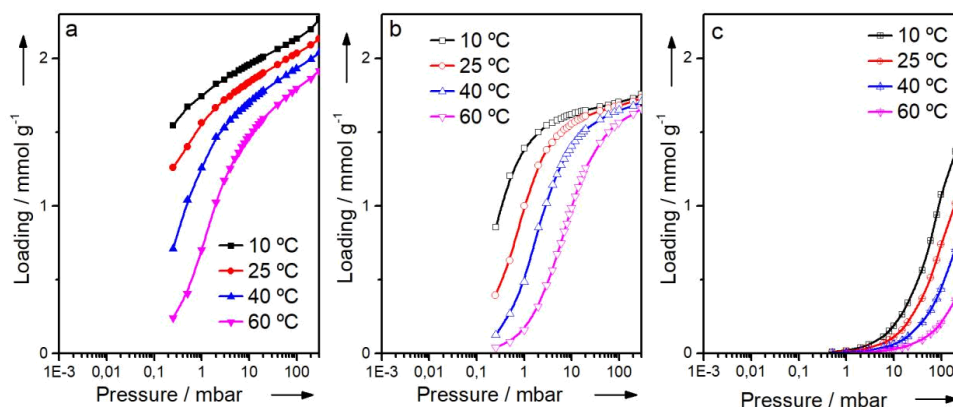


**Figure B1:** Adsorption isotherms of a) n-pentane, b) 2-methylbutane and c) 2,2-dimethylpropane on Si-STW at different temperatures.

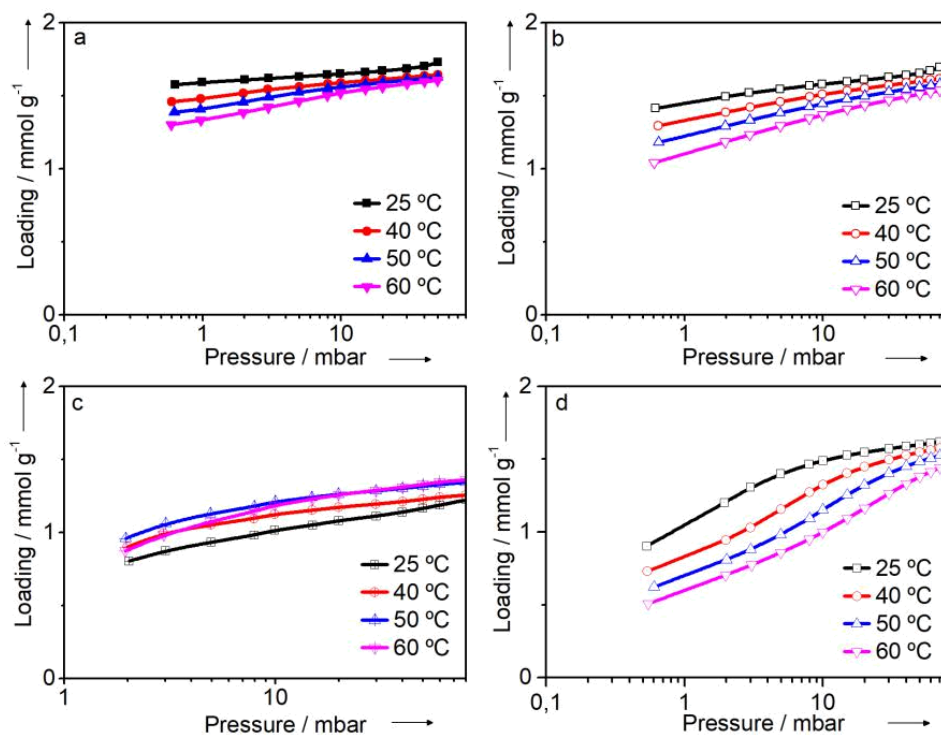


**Figure B2:** Adsorption isotherms of a) n-heptane, b) 3-methylhexane, c) 2,3-dimethylpentane and d) 2,4-dimethylpentane on Si-STW at different temperatures.



**Table B1:** Summary of experimentally determined adsorption properties: isosteric heats of adsorption, diffusional time constants at 1 and 50 (C7-fraction), 150 (C6-fraction) or 300 mbar (C5-fraction), respectively and maximum loadings at either 50, 150 or 300 mbar of heptane, hexane or pentane isomers, respectively, on Si-STW, Si-MFI\_large and Si-MFI\_small.

Compound	$q_{st}$ (kJ/mol)*	$D_1/r^2$ (s <sup>-1</sup> )**	$D_{high}/r^2$ (s <sup>-1</sup> )**	$Q_{high}$ (mmol/g)**
<b>Si-STW</b>				
nC5	61.5 (1.5)	$1.3 \cdot 10^{-3}$	$3.0 \cdot 10^{-3}$	2.17
2MB	55.3 (0.9)	$9.1 \cdot 10^{-4}$	$1.9 \cdot 10^{-3}$	1.70
22DMPr	33.3	$3.4 \cdot 10^{-5}$	$2.2 \cdot 10^{-5}$	1.22
nC6	81.0 (1.6)	$1.9 \cdot 10^{-3}$	$1.7 \cdot 10^{-3}$	1.77
2MP	72.2 (1.4)	$1.2 \cdot 10^{-3}$	$2.2 \cdot 10^{-3}$	1.66
22DMB	–	$3.5 \cdot 10^{-6}$	$2.9 \cdot 10^{-6}$	1.00
23DMB	46.0 (1.4)	$3.0 \cdot 10^{-4}$	$9.5 \cdot 10^{-4}$	1.64
nC7	85.8 (1.6)	$1.2 \cdot 10^{-3}$	$1.7 \cdot 10^{-3}$	1.70
3MH	76.3 (1.4)	$1.0 \cdot 10^{-3}$	$1.8 \cdot 10^{-3}$	1.64
23DMPe	–	$< 5 \cdot 10^{-6}$	$< 5 \cdot 10^{-6}$	> 1
24DMPe	58.9 (0.9)	$0.9 \cdot 10^{-3}$	$1.8 \cdot 10^{-3}$	1.60
<b>Si-MFI_large</b>				
nC5	56.1 (0.23)	$1.44 \cdot 10^{-3}$	$2.39 \cdot 10^{-3}$	1.4
2MB	57.3 (0.13)	$7.37 \cdot 10^{-4}$	$1.11 \cdot 10^{-3}$	1.25
22DMPr	–	$2.34 \cdot 10^{-5}$	$3.05 \cdot 10^{-5}$	0.97
<b>Si-MFI_small</b>				
nC5	57.9 (0.29)	$1.58 \cdot 10^{-3}$	$1.40 \cdot 10^{-3}$	1.56
2MB	53.2 (0.14)	$1.36 \cdot 10^{-3}$	$1.34 \cdot 10^{-3}$	1.22
22DMPr	–	$5.5 \cdot 10^{-6}$	$3.25 \cdot 10^{-5}$	0.88

\*The isosteric heat of adsorption could not be calculated at low coverage for some cases. The values at the lowest loading possible (in parentheses) are shown for these. In other cases, due to equilibration issues, the heat of adsorption could not be calculated at all.

\*\*All values at 25 °C.

## B2 Computational Details and Results

### B2.1 Monte Carlo simulations

Calculated adsorption isotherms were determined through Configurational Bias Monte Carlo simulations (CBMC) as implemented in the RASPA [2] software package (version 2.0.25), using the Grand Canonical ensemble, with constant volume, temperature (300 K) and chemical potential. The latter is converted by the software into pressures using the Peng-Robinson equation of state. Hydrocarbon pressures ranged from 0.001 to 1000.0 mbar.

The force field description of Calero et al. [3], successfully applied for hexane isomer separations in MFI and MEL zeolite types, was employed. Simulated systems were modeled considering zeolite framework fixed, and flexible hydrocarbon molecules with a united atom force field, taking into account CH<sub>x</sub> (x = 0,1,2,3) groups as unique beads of neutral charge. Bonds and bends between adsorbate pseudo atoms were described by harmonic potentials and torsions by TraPPE cosine series. Lennard-Jones potentials modeled zeolite-hydrocarbon and adsorbate intramolecular interactions (for beads more than 3 bonds distant), being cut and shifted with the cutoff distance of 12 Å. Host-guest Lennard-Jones interactions are considered only through zeolite O atoms, computed as an effective interaction in which the smaller effect of Si (which is a cation of small size) was included in the O parameters. Zeolite frameworks were obtained from crystallographic data available for all silica MFI (ZSM-5) [4] and STW (HPM-1) [5], and were simulated with unity cells 2×2×2 (a = 40.0 Å, b = 39.8 Å, c = 26.8 Å, α = β = γ = 90.0°) and 3×3×1 (a = b = 35.7 Å, c = 29.9 Å, α = β = 90.0°, γ = 120.0°), respectively.

Simulations were performed during 10<sup>4</sup> initiation cycles (sufficient for the equilibration of our systems' energy) and 10<sup>6</sup> production cycles. Even for the adsorption isotherms performed only with pure components, the use of Rosenbluth factor was crucial for the direct comparison with experiments. It represents the reference state of the ideal gas, and it is used by RASPA package for correcting the gas pressure. Such factor was previously calculated as the Helium void fraction.

Monte Carlo moves employed during simulations were composed by 15% probability of a random displacement in any direction (TranslationProbability keyword); 15% probability of a random rotation around the starting bead (RotationProbability); 15% probability to attempt a partial reinsertion move, where part of the molecule is kept fixed, and the rest is regrown with the configurational bias procedure (CBMCPProbability); 55% probability of a random insertion or deletion move, both equally probable (SwapProbability). The starting bead was maintained as default (atom 0). Bead order and config moves were specified for each compound (needed for Rotation and CBMC attempts) as defined for the same molecule with TraPPE force field (resource files found on RASPA/share/raspa/molecules/ directory). Different combinations of Monte Carlo moves were tested, attempting to improve the insertion of di-branched molecules at framework cavities, unsuccessfully. We also considered a possible effect of framework flexibility (not taken into account in CBMC simulations). The attempts of relaxing framework structure and simulating the isotherm with optimized structures does not lead to a significant increase on the maximum uptake, a similar behavior than that reported by Bueno-Perez et al. [6] for STW framework at near-saturation regimes.

The choice of appropriate unit cell parameters of a zeolite framework, can be crucial for the correct obtention of the loadings computed by the CBMC simulations. On the literature there are 4 crystallographic structures reported for MFI (experiments published in 1987 [4], 1989 [7], 1990 [8] and from IZA database [5]) and 3 for STW (experiments from 2012 [9], 2013 [10] and from IZA database [5]). Unit cell parameters and volumes are collected in Table B2. Preliminary calculations were performed to define which zeolite structure would be employed in CBMC simulations, as exemplified by Table B3 for nC6. We selected MFI 1987 and STW IZA frameworks, as these provided the loading values closest to experimental ones. Furthermore, the results from Table B3 were modeled with a force field developed by Smit and collaborators [11], and calculations underestimated adsorption in some cases (as exemplified in Figure B3a). Some isotherms could be improved by a few force field modifications suggested by Calero and collaborators [3], specifically referring to the mono-branched hydrocarbons (Figure B3b).

**Table B2:** Unit cell parameters and cell volumes of the pure silica MFI and STW frameworks available in the literature.

Framework	a (Å)	b (Å)	c (Å)	$\alpha$ (°)	$\beta$ (°)	$\gamma$ (°)	volume (Å <sup>3</sup> )
MFI 1987	20.022	19.899	13.383	90.00	90.00	90.00	5332.03
MFI 1989	20.121	19.820	13.438	90.00	90.00	90.00	5359.05
MFI 1990	19.879	20.107	13.369	90.00	90.67	90.00	5343.32
MFI IZA	20.090	19.738	13.142	90.00	90.00	90.00	5211.28
STW 2012	11.936	11.936	29.750	90.00	90.00	120.00	3670.33
STW 2013	11.887	11.887	29.915	90.00	90.00	120.00	3642.62
STW IZA	11.902	11.902	29.692	90.00	90.00	120.00	3660.70

Concerning the problems on reproducing experimental uptake of dibranched alkanes in STW, the role of framework flexibility was further explored by calculating the isotherms of adsorption also with force field-optimized frameworks. The three structures available in the literature were optimized (full optimization of atomic coordinates and cell parameters) with dibranched molecules inside, expecting that the alkane loading might expand the zeolite framework. These three expanded zeolite structures (starting from IZA and the two experimentally reported) were then used for the Monte Carlo uptake simulations. All the corresponding MC uptake calculations using these six zeolite structures could not achieve the experimental uptake observed in the case of dibranched alkanes, and were not reported for the sake of brevity.

**Table B3:** n-Hexane loading on MFI and STW frameworks available. CBMC simulations at 300K and 150 mbar, using Smit et al. force field [11] performed for  $10^4$  and  $5 \times 10^4$  initiation cycles,  $10^5$  and  $5 \times 10^4$  production cycles for MFI and STW, respectively.

MFI $2 \times 2 \times 2$	Helium Void Fraction	Loading (mol/uc)	STW $3 \times 3 \times 1$	Helium Void Fraction	Loading (mol/uc)
1987	0.292	7.38	2013	0.304	1.264
1989	0.277	5.88	IZA	0.329	1.565
1990	0.286	7.13			
IZA	0.238	4.75			
experimental [12,13]		7.79 – 8.27 *	experimental **		1.770

\* maximum loadings from different pressures.  
 \*\* of the present article.

Main modifications on the previous force field are in the functional form of bends (harmonic) and torsions (TraPPE cosine series), thus reducing computational cost. Equilibrium bond angles for mono and di-branched hydrocarbons, and sigma values for CH<sub>x</sub> (x = 0, 1, 2, 3) of their Lennard-Jones potential vary, as well. This force field description was chosen for the CBMC simulations, and its functional form and parameters are summarized in Tables B3 and B4.

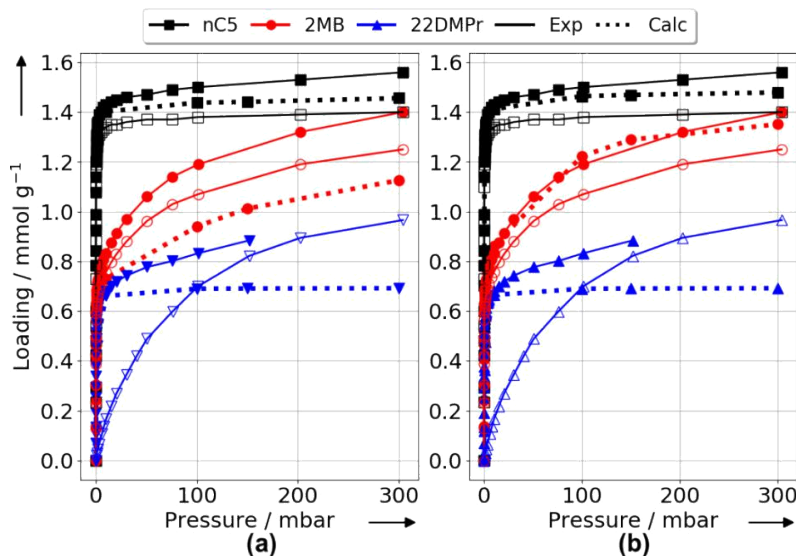


**Figure B3:** Experimental adsorption isotherms for n-pentane isomers on Si-MFI (large crystal size as open and small crystal size as filled symbols) and calculated with force field: (a) Smit et al. [11] and (b) Calero et al. [3]

**Table B4:** Bonded terms employed in CBMC simulations for alkane molecules [3].

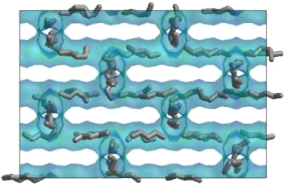
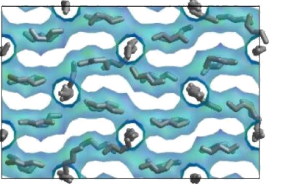
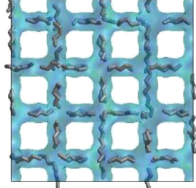
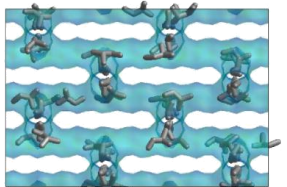
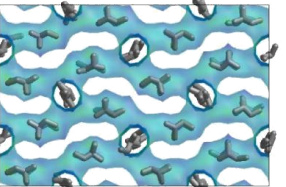
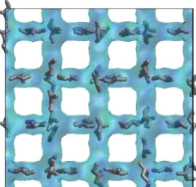
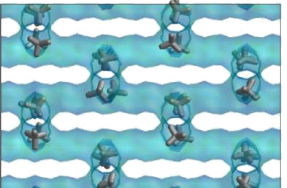
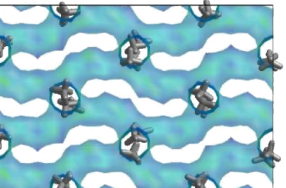
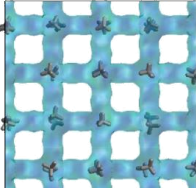
Functional expression	Bonded Term	Parameters	
$U^{\text{bond}} = \frac{1}{2}k_{ij}(r_{ij} - r_{ij}^0)^2$	$\text{CH}_x\text{-CH}_x^*$	$\frac{k_{ij}}{k_B} = 96500 \text{ K}/\text{\AA}^2$	$r_{ij}^0 = 1.54 \text{ \AA}$
$U^{\text{bend}} = \frac{1}{2}k_{ijk}(\theta_{ijk} - \theta_{ijk}^0)^2$	$\text{CH}_x\text{-CH}_2\text{-CH}_x^*$	$\frac{k_{ijk}}{k_B} = 62500 \text{ K}/\text{rad}^2$	$\theta_{ijk}^0 = 114^\circ$
	$\text{CH}_x\text{-CH-CH}_x^{**}$	$\frac{k_{ijk}}{k_B} = 62500 \text{ K}/\text{rad}^2$	$\theta_{ijk}^0 = 112^\circ$
	$\text{CH}_x\text{-C-CH}_x^{**}$	$\frac{k_{ijk}}{k_B} = 62500 \text{ K}/\text{rad}^2$	$\theta_{ijk}^0 = 119.47^\circ$
$U^{\text{torsion}} = p_0$ $+p_1[1 + \cos(\phi_{ijkl})]$ $+p_2[1 - \cos(2\phi_{ijkl})]$ $+p_3[1 + \cos(3\phi_{ijkl})]$	$\text{CH}_x\text{-CH}_2\text{-CH}_2\text{-CH}_x^{**}$	$\frac{p_0}{k_B} = 0.0 \text{ K}$ $\frac{p_2}{k_B} = -68.19 \text{ K}$	$\frac{p_1}{k_B} = 335.03 \text{ K}$ $\frac{p_3}{k_B} = 791.32 \text{ K}$
	$\text{CH}_x\text{-CH}_2\text{-CH-CH}_x^{**}$	$\frac{p_0}{k_B} = -251.06 \text{ K}$	$\frac{p_1}{k_B} = 428.73 \text{ K}$
	$\text{CH}_x\text{-CH-CH-CH}_x^{***}$	$\frac{p_2}{k_B} = -111.85 \text{ K}$	$\frac{p_3}{k_B} = 441.47 \text{ K}$
	$\text{CH}_x\text{-CH}_2\text{-C-CH}_x^{***}$	$\frac{p_0}{k_B} = 0.0 \text{ K}$ $\frac{p_2}{k_B} = 0.0 \text{ K}$	$\frac{p_1}{k_B} = 0.0 \text{ K}$ $\frac{p_3}{k_B} = 461.29 \text{ K}$

\* for x = 0, 1, 2 or 3.    \*\* for x = 1, 2 or 3.    \*\*\* for x = 2 or 3.

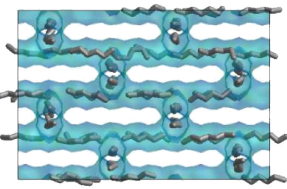
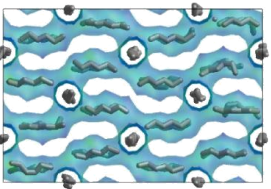
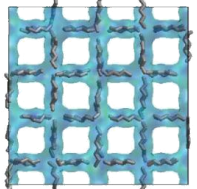
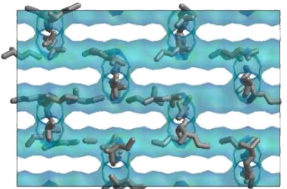
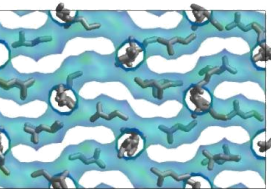
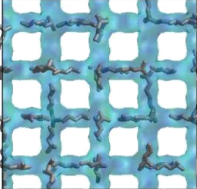
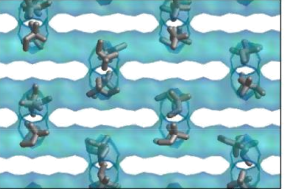
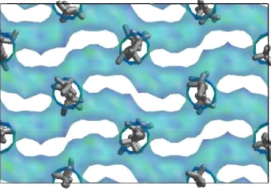
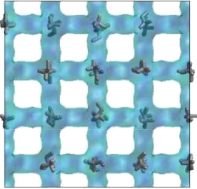
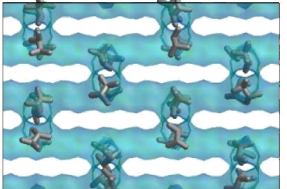
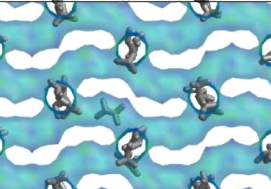
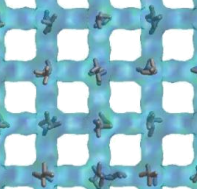
**Table B5:** Lennard-jones parameters employed in CBMC simulations for alkane molecules [3].

Pair	$\frac{\epsilon}{k_B}$ (K)	$\sigma$ (Å)	Pair	$\frac{\epsilon}{k_B}$ (K)	$\sigma$ (Å)
$\text{CH}_3 \cdots \text{O}$	93.00	3.48	$\text{CH}_3 \cdots \text{C}$	9.30	5.07
$\text{CH}_2 \cdots \text{O}$	60.50	3.58	$\text{CH}_2 \cdots \text{CH}_2$	56.00	3.96
$\text{CH} \cdots \text{O}$	40.00	3.92	$\text{CH}_2 \cdots \text{CH}$	30.85	4.32
$\text{C} \cdots \text{O}$	10.00	4.56	$\text{CH}_2 \cdots \text{C}$	6.69	5.17
$\text{CH}_3 \cdots \text{CH}_3$	108.00	3.76	$\text{CH} \cdots \text{CH}$	17.00	4.67
$\text{CH}_3 \cdots \text{CH}_2$	77.77	3.86	$\text{CH} \cdots \text{C}$	3.69	5.53
$\text{CH}_3 \cdots \text{CH}$	42.85	4.22	$\text{C} \cdots \text{C}$	0.80	6.38

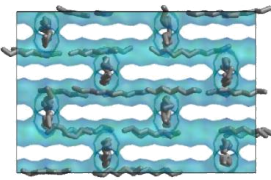
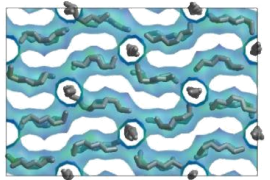
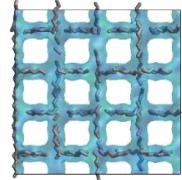
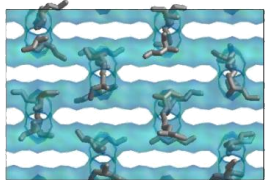
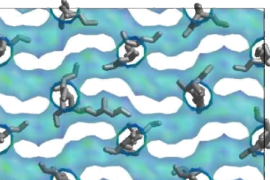
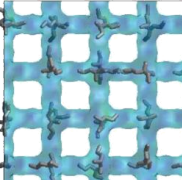
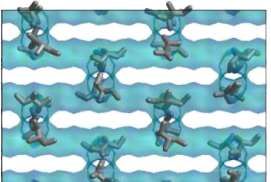
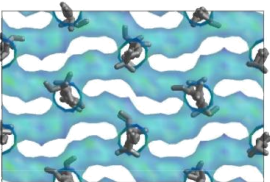
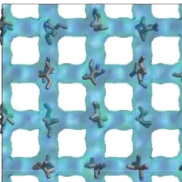
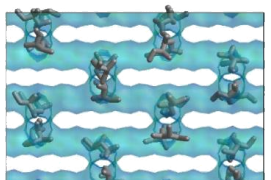
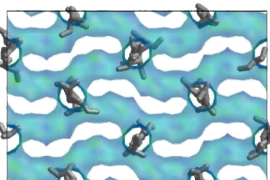
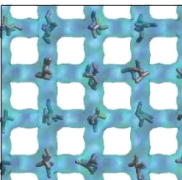
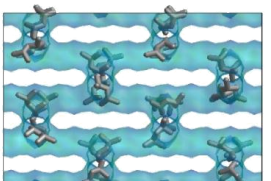
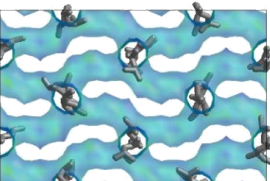
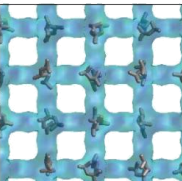
Final configurations from CBMC simulations (at 1000.0 mbar, i.e. above saturation) are summarized in Figures B3 to B8 for MFI  $2 \times 2 \times 2$  and STW  $3 \times 3 \times 3$  with pentane, hexane and heptane isomers. Such unit cells were applied to reach simulation box dimensions larger than twice the nonbonded interactions cutoff of 12.0 Å. All calculated isotherms are plotted in Figure B9.

plane	bc	ac	ab
68 <i>molec</i> <b>nC5</b>			
66 <i>molec</i> <b>2MB</b>			
32 <i>molec</i> <b>22MPr</b>			

**Figure B4:** Final configurations from CBMC simulations of MFI  $2 \times 2 \times 2$  with pentane isomers, at 1000.0 mbar. Channel system view from each plane and number of molecules adsorbed.

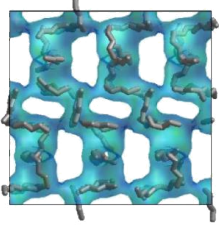
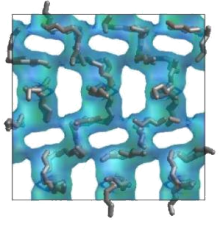
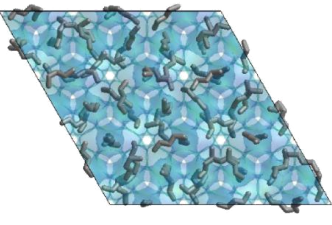
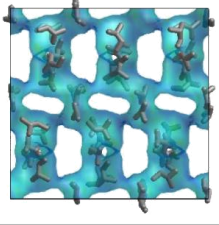
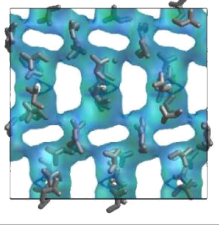
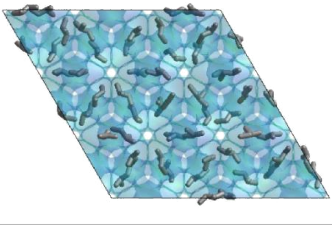
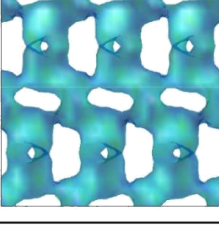
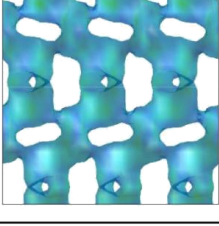
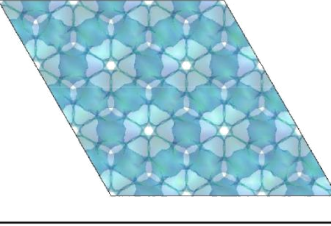
plane	bc	ac	ab
64 <i>molec</i> nC6			
49 <i>molec</i> 2MPe			
32 <i>molec</i> 22DMB			
33 <i>molec</i> 23DMB			

**Figure B5:** Final configurations from CBMC simulations of MFI  $2 \times 2 \times 2$  with hexane isomers, at 1000.0 mbar. Channel system view from each plane and number of molecules adsorbed.

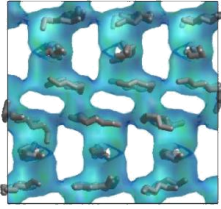
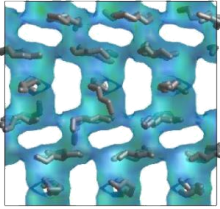
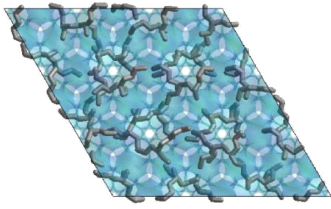
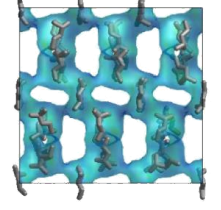
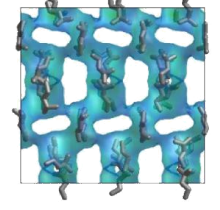
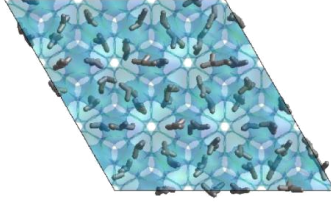
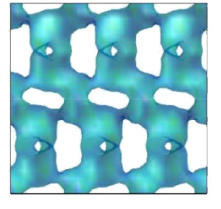
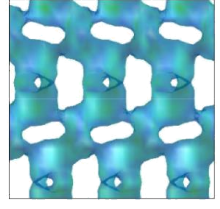
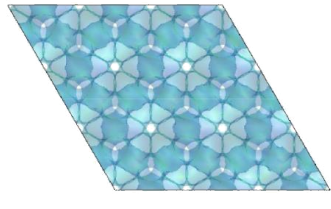
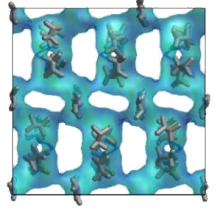
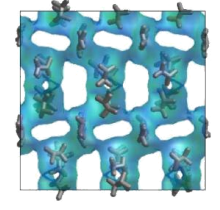
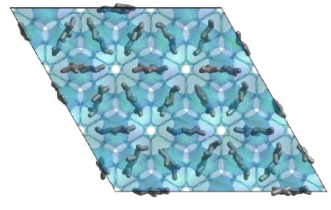
plane	bc	ac	ab
56 molec <b>nC7</b>			
33 molec <b>3MH</b>			
32 molec <b>(R)23DMPe</b>			
32 molec <b>(S)23DMPe</b>			
32 molec <b>24DMPe</b>			

**Figure B6:** Final configurations from CBMC simulations of MFI  $2 \times 2 \times 2$  with heptane isomers, at 1000.0 mbar. Channel system view from each plane and number of molecules adsorbed.

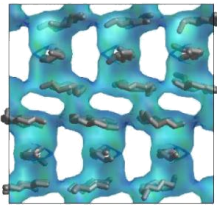
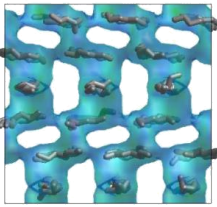
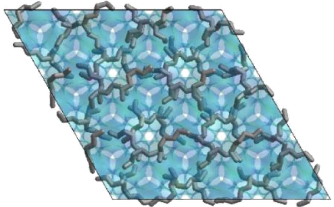
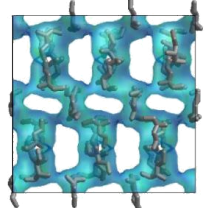
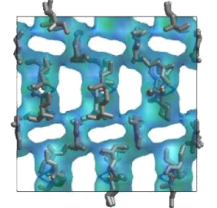
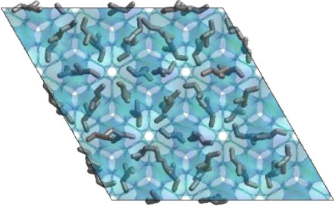
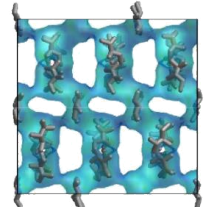
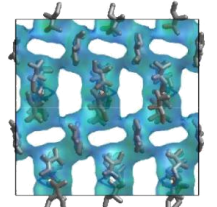
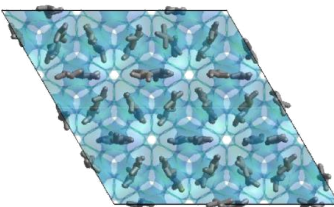
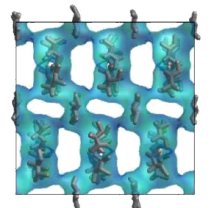
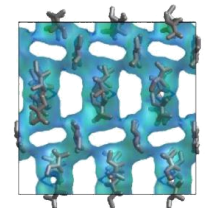
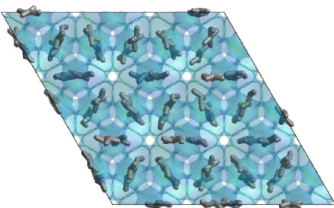
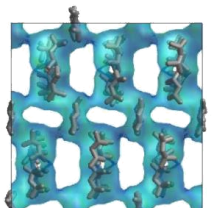
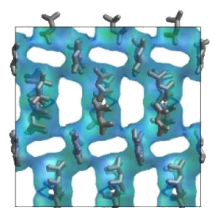
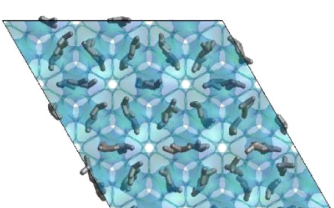


plane	bc	ac	ab
73 molec nC5			
54 molec 2MB			
0 molec 22MPr			

**Figure B7:** Final configurations from CBMC simulations of STW  $3 \times 3 \times 1$  with pentane isomers, at 1000.0 mbar. Channel system view from each plane and number of molecules adsorbed.

plane	bc	ac	ab
54 molec nC6			
54 molec 2MPe			
0 molec 22DMB			
54 molec 23DMB			

**Figure B8:** Final configurations from CBMC simulations of STW  $3\times 3\times 1$  with hexane isomers, at 1000.0 mbar. Channel system view from each plane and number of molecules adsorbed.

plane	bc	ac	ab
54 molec <b>nC7</b>			
54 molec <b>3MH</b>			
54 molec <b>(R)23DMPe</b>			
54 molec <b>(S)23DMPe</b>			
54 molec <b>24DMPe</b>			

**Figure B9:** Final configurations from CBMC simulations of STW  $3 \times 3 \times 1$  with heptane isomers, at 1000.0 mbar. Channel system view from each plane and number of molecules adsorbed.

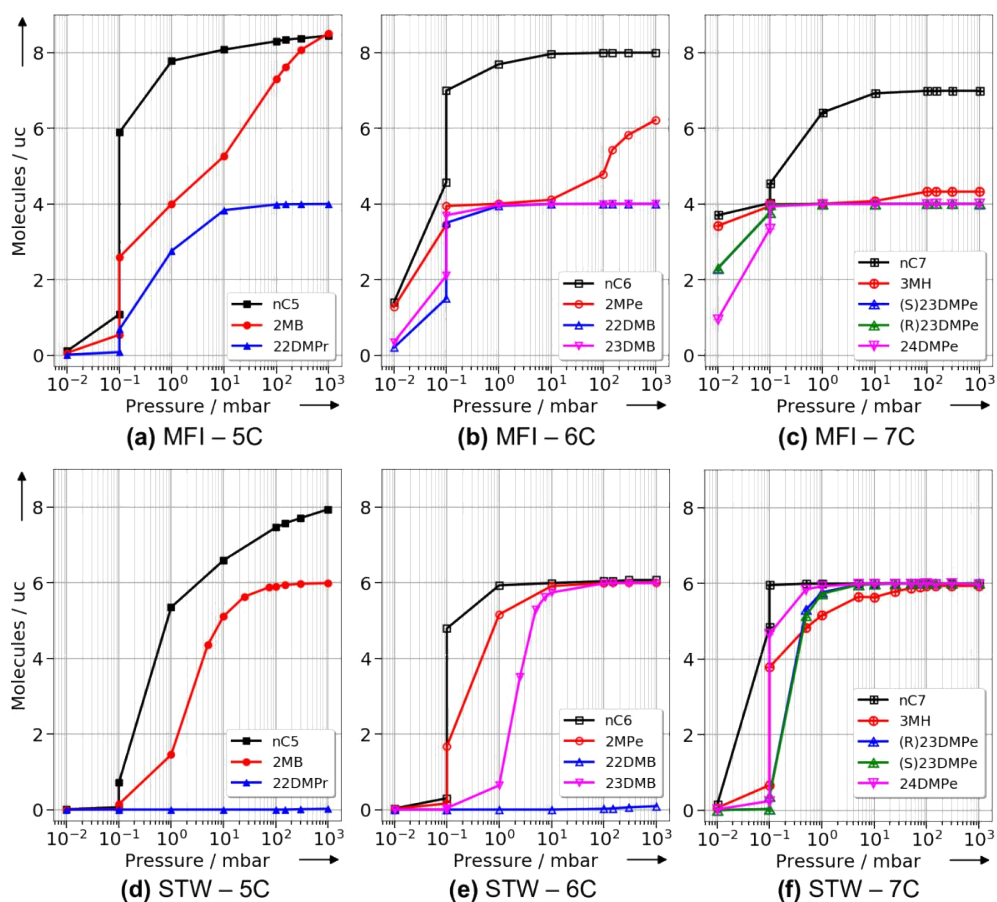


**Figure B10:** Adsorption isotherms calculated from CBMC simulations of pentane (a, d), hexane (b, e) and heptane (c, f) isomers on MFI  $2 \times 2 \times 2$  and STW  $3 \times 3 \times 1$  frameworks, respectively.

The model employed predicts no adsorption of 22DMP<sub>r</sub> and 23DMB on Si-STW. However, this is observed experimentally, albeit in small amounts. In this way, the same force field used in the Molecular Dynamics simulations (All-atom, see more details in the next subsection) was applied in order to prove a possible adsorption of di-branched hydrocarbons. These CBMC simulations overestimated experimental loadings, but no reliable results could be obtained due to an energy drift error that could not be fixed.

Even so, the change of the model allowed to predict the adsorption, although in a qualitative way, highlighting that di-branched adsorbates can fit in STW channel system (as illustrated in Figure B11).

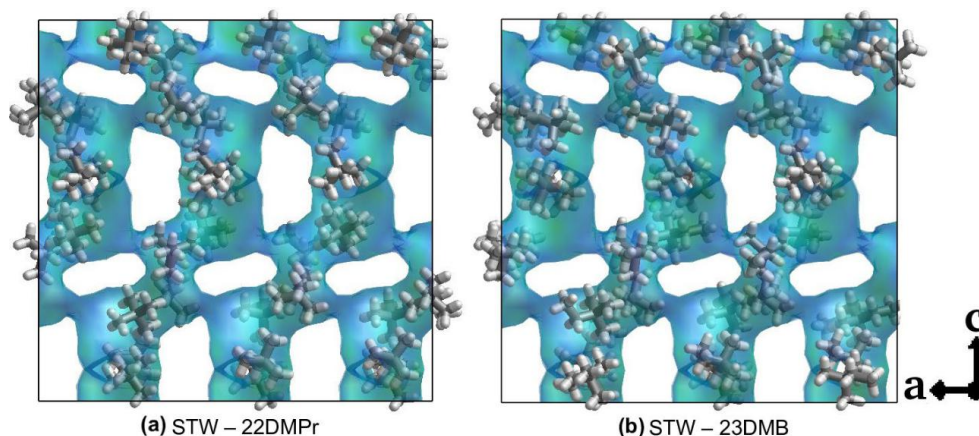


**Figure B11:** Final configurations from CBMC simulations with All atom model for 22DMPPr (a) and 23DMB (b) in STW, at 300.0 and 150.0 mbar, respectively.

### *B2.2 Molecular Dynamics simulations*

In order to facilitate a visual understanding of the diffusivity of pentane, hexane and heptane isomers in the zeolites studied, the trajectories from Molecular Dynamics (MD) simulations, performed with DL\_POLY (version 2.20) [14], were analysed. Simulation boxes contained 6 alkane molecules inside each zeolite (low loading), defining a fully flexible system. The unit cells considered for each zeolite are: MFI  $2 \times 1 \times 2$  ( $a = 40.2 \text{ \AA}$ ,  $b = 19.7 \text{ \AA}$ ,  $c = 26.3 \text{ \AA}$ ,  $\alpha = \beta = \gamma = 90.0^\circ$ ) and STW  $2 \times 2 \times 2$  ( $a = b = 23.8 \text{ \AA}$ ,  $c = 59.8 \text{ \AA}$ ,  $\alpha = \beta = 90.0^\circ$ ,  $\gamma = 120.0^\circ$ ), with both crystallographic data taken from IZA database [5]. After equilibration, time evolution of the system was computed on the NVT ensemble for 10 ns, using the Leapfrog integrator and with a 1.0 fs time step. Temperature was maintained at 298.0 K with Evans thermostat, periodic boundary conditions were considered and a cutoff of 9.0  $\text{\AA}$  was selected for the nonbonding forces.

For zeolite modeling, the force field of Sastre et al. was employed [15]. The Coulombic interaction is accounted for, and point charges of 2.1 and -1.05  $e^-$  are assigned for silicon and oxygen atoms, respectively. Three body potentials for

O–Si–O and Si–O–Si interactions are treated by a screened harmonic function and van der Waals terms by Lennard-Jones potentials.

Alkane topologies are ensured by means of bonds and bends defined as harmonic potentials, and truncated Fourier series describing rotational barriers of dihedral angles, as developed by Oie et al. [16]. Adsorbate molecules were modeled using an all-atom force field, in which the atomic charges were calculated using HF/6-31G\* level of theory with Gaussian 09 (Revision A.02) [17] and subsequently adjusted to ensure CHx as neutral groups. Host-guest interactions are described by Lennard-Jones terms using parameters reported by Catlow and coworkers [18].

Although the ideal option was to have a good force field for both MD and MC methods, we could not find a proper choice. Thus, we tried to employ the most appropriate model for each case, i.e., the united atom model being highly accurate to reproduce the adsorption isotherms, and the MD model selected from a benchmark among 5 different all atom models (such preliminary results not reported for the sake of brevity).

Force Field parameters employed on MD simulations are summarized on Tables B6 to B8.

**Table B6:** Lennard-jones parameters employed in MD simulations.

Pair	$A_{ij}$ (eV/Å <sup>12</sup> )	$B_{ij}$ (eV/Å <sup>6</sup> )	Pair	$A_{ij}$ (eV/Å <sup>12</sup> )	$B_{ij}$ (eV/Å <sup>6</sup> )
Si ... Si*	0.5601	0.0004	C ... O**	11000.00	17.654
O ... Si*	172.6992	0.1086	H ... O**	1556.40	5.5717
O ... O**	26877.9664	29.8306	C ... C**	1.96920e+4	18.0933
C ... Si	0.00	0.00	C ... H**	2.80000e+3	5.8415
H ... Si	0.00	0.00	H ... H**	3.84840e+2	1.9867

\* from Sastre et al. [15].

\*\* from Catlow et al. [18].

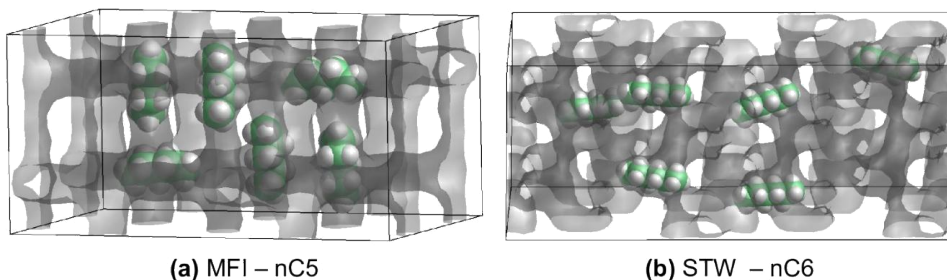


**Figure B12:** Initial configuration of MD simulation boxes in MFI 2×1×2 (a) and STW 2×2×2 (b) zeolite.

**Table B7:** Bonded terms employed in MD simulations for alkane molecules 20 and zeolite framework [15].  $C_{(x)}$  groups for any kind of  $sp^3$  carbon,  $C_{(2)}$  secondary,  $C_{(3)}$  tertiary and  $C_{(4)}$  quaternary carbon atoms.

Functional expression	Bonded Term	Parameters		
$U^{\text{bond}} = \frac{1}{2}k_{ij}(r_{ij} - r_{ij}^0)^2$	H-C <sub>(x)</sub>	$k_{ij} = 28.71 \frac{\text{eV}}{\text{\AA}^2}$	$r_{ij}^0 = 1.095 \text{\AA}$	
	C <sub>(x)</sub> -C <sub>(x)</sub>	$k_{ij} = 27.46 \frac{\text{eV}}{\text{\AA}^2}$	$r_{ij}^0 = 1.520 \text{\AA}$	
$U^{\text{bend}} = \frac{1}{2}k_{ijk}(\theta_{ijk} - \theta_{ijk}^0)^2$	H-C <sub>(x)</sub> -H	$k_{ijk} = 2.06 \frac{\text{eV}}{\text{rad}^2}$	$\theta_{ijk}^0 = 109.5^\circ$	
	H-C <sub>(x)</sub> -C <sub>(x)</sub>	$k_{ijk} = 2.50 \frac{\text{eV}}{\text{rad}^2}$	$\theta_{ijk}^0 = 109.2^\circ$	
	C <sub>(x)</sub> -C <sub>(4)</sub> -C <sub>(x)</sub>	$k_{ijk} = 3.56 \frac{\text{eV}}{\text{rad}^2}$	$\theta_{ijk}^0 = 109.5^\circ$	
	C <sub>(x)</sub> -C <sub>(3)</sub> -C <sub>(x)</sub>	$k_{ijk} = 3.56 \frac{\text{eV}}{\text{rad}^2}$	$\theta_{ijk}^0 = 110.1^\circ$	
	C <sub>(x)</sub> -C <sub>(2)</sub> -C <sub>(x)</sub>	$k_{ijk} = 3.56 \frac{\text{eV}}{\text{rad}^2}$	$\theta_{ijk}^0 = 110.4^\circ$	
	$U^{\text{torsion}} = A[1 + \cos(m\phi_{ijkl} - \delta)]$	H-C <sub>(x)</sub> -C <sub>(x)</sub> -H	A = 0.0050 eV	m = 3
H-C <sub>(x)</sub> -C <sub>(x)</sub> -C <sub>(x)</sub>				
C <sub>(x)</sub> -C <sub>(x)</sub> -C <sub>(x)</sub> -C <sub>(x)</sub>		A = 0.0032 eV	m = 3	$\delta = 0.0^\circ$
$U^{\text{tbp}} = \frac{1}{2}k_{ijk}(\theta_{ijk} - \theta_{ijk}^0)^2 \exp\left[-\left(\frac{r_{ij}}{\rho_1} + \frac{r_{ik}}{\rho_2}\right)\right]$	O-Si-O	$k_{ijk} = 1.4944 \frac{\text{eV}}{\text{rad}^2}$	$\theta_{ijk}^0 = 109.47^\circ$	$\rho_1 = \rho_2 = 99.9999 \text{\AA}$
	Si-O-Si	$k_{ijk} = 1.5509 \frac{\text{eV}}{\text{rad}^2}$	$\theta_{ijk}^0 = 142.71^\circ$	$\rho_1 = \rho_2 = 99.9999 \text{\AA}$

**Table B8:** Atomic charges calculated with HF/6-31G\* and used in the simulations, in a.u.

C group	HF/6-31G*	simulated	H group	HF/6-31G*	simulated
H3C-R	-0,476	-0,468	R-CH3	0,158	0,156
H2C-R2	-0,299	-0,312	R2-CH2	0,153	0,156
HC-R3	-0,148	-0,156	R3-CH	0,152	0,156
R4-C	-0,029	0,000	-	-	-

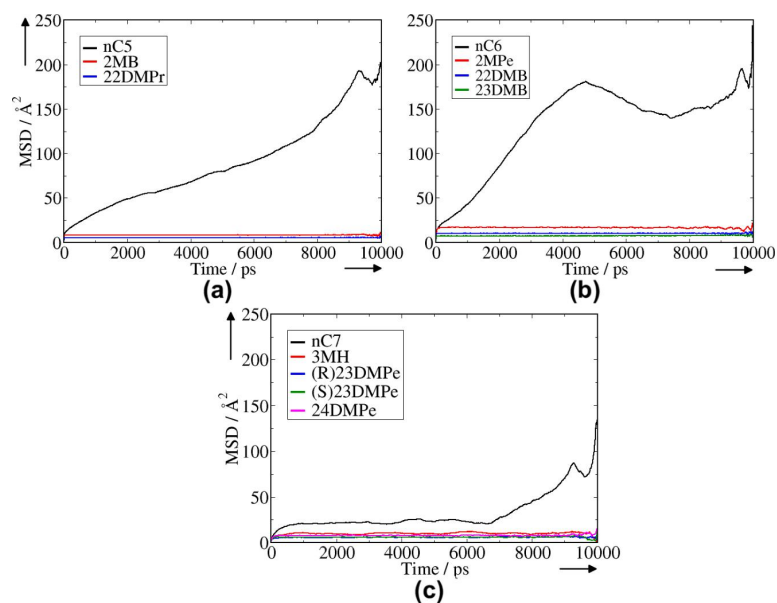


**Figure B13:** Mean Square Displacements (MSD, in  $\text{\AA}^2$ ) of pentane (a), hexane (b) and heptane (c) isomers on MFI  $2 \times 1 \times 2$  zeolite during MD simulation time, in ps.

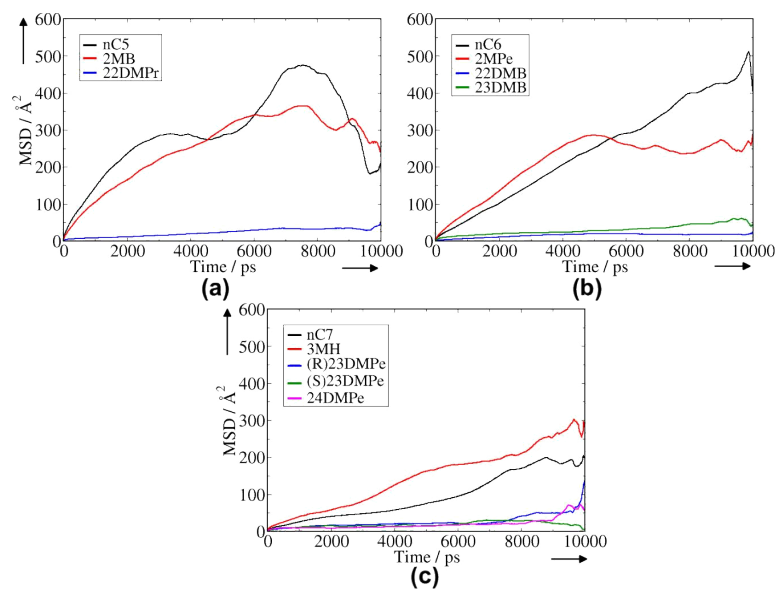


**Figure B14:** Mean Square Displacements (MSD, in  $\text{\AA}^2$ ) of pentane (a), hexane (b) and heptane (c) isomers on STW  $2 \times 2 \times 2$  zeolite during MD simulation time, in ps.



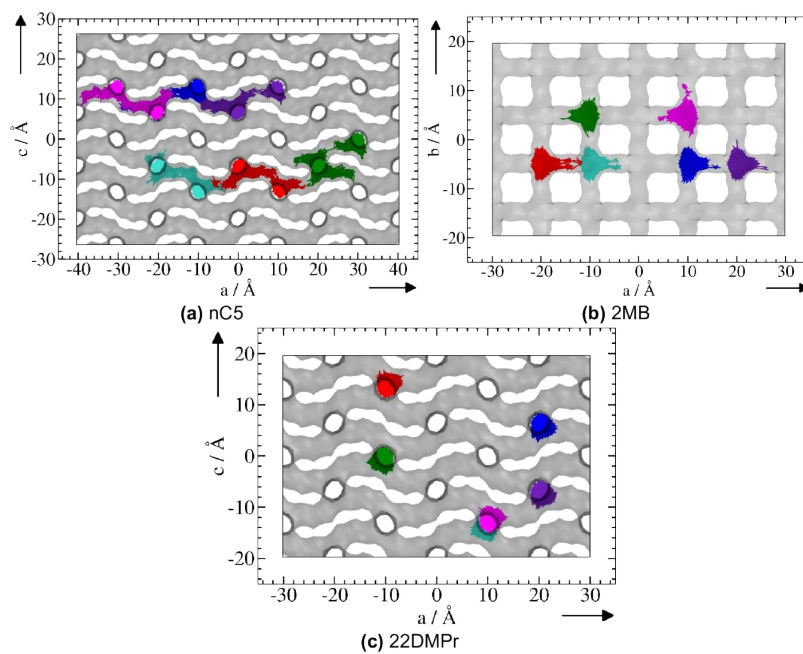


**Figure B15:** Trajectories of pentane isomers on MFI  $2 \times 1 \times 2$  zeolite during MD simulation.

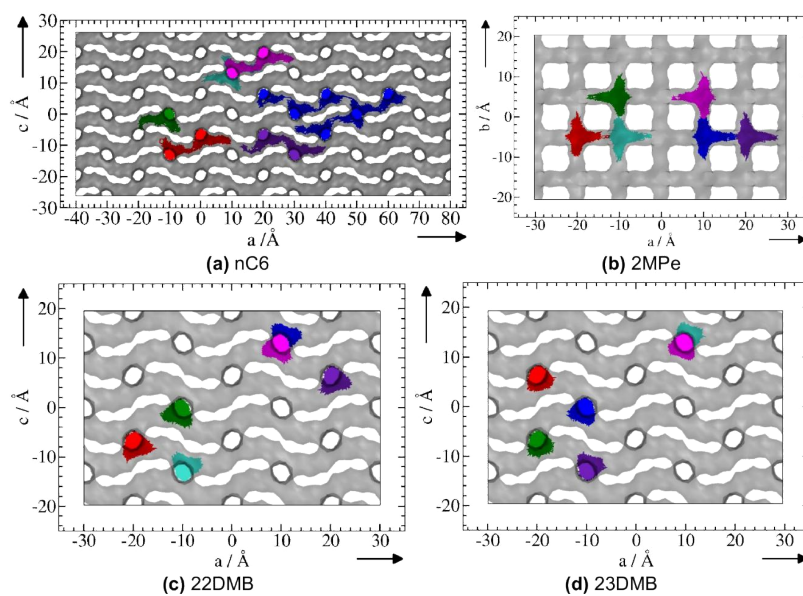


**Figure B16:** Trajectories of hexane isomers on MFI  $2 \times 1 \times 2$  zeolite during MD simulation.

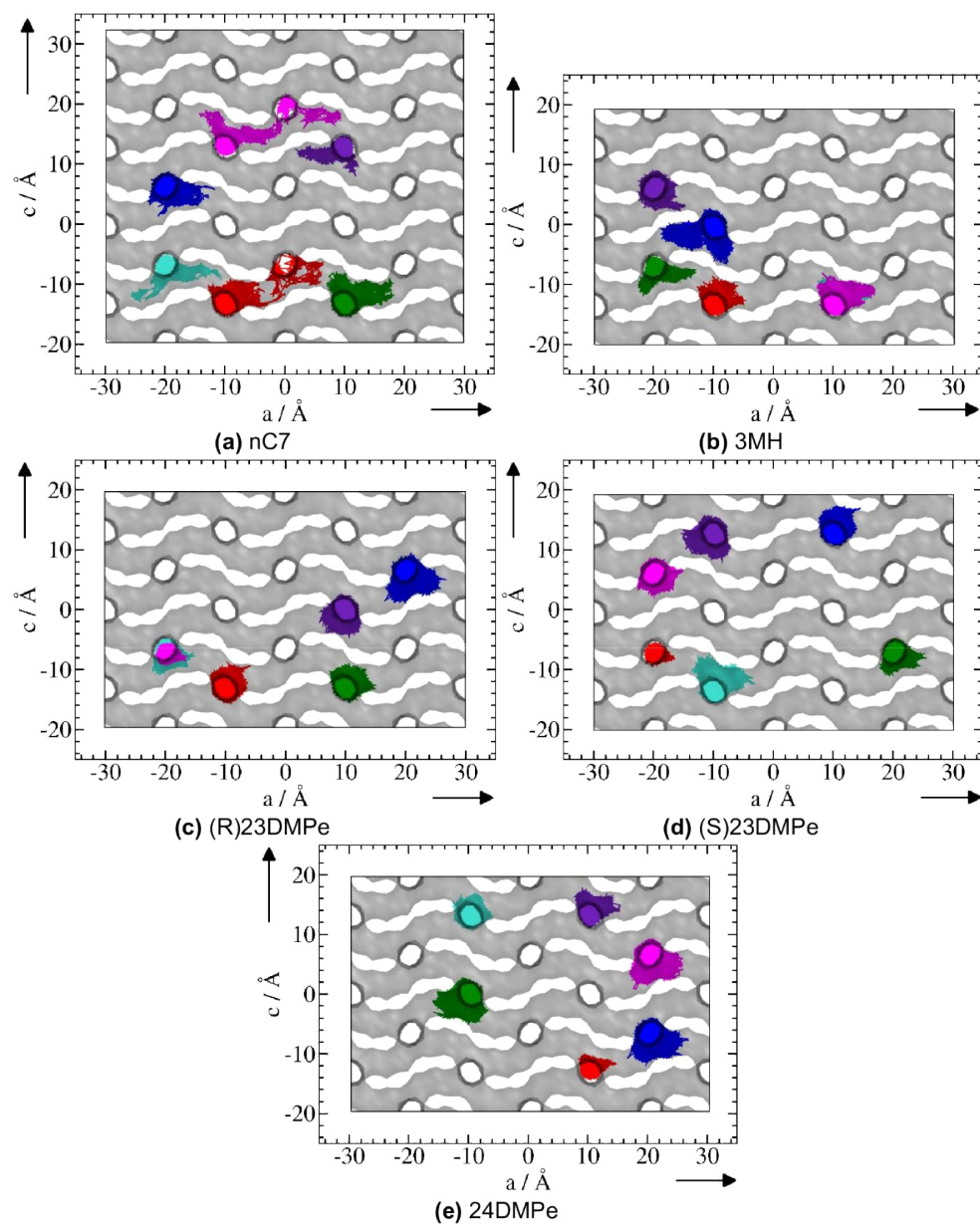


**Figure B17:** Trajectories of heptane isomers on MFI 2x1x2 zeolite during MD simulation.

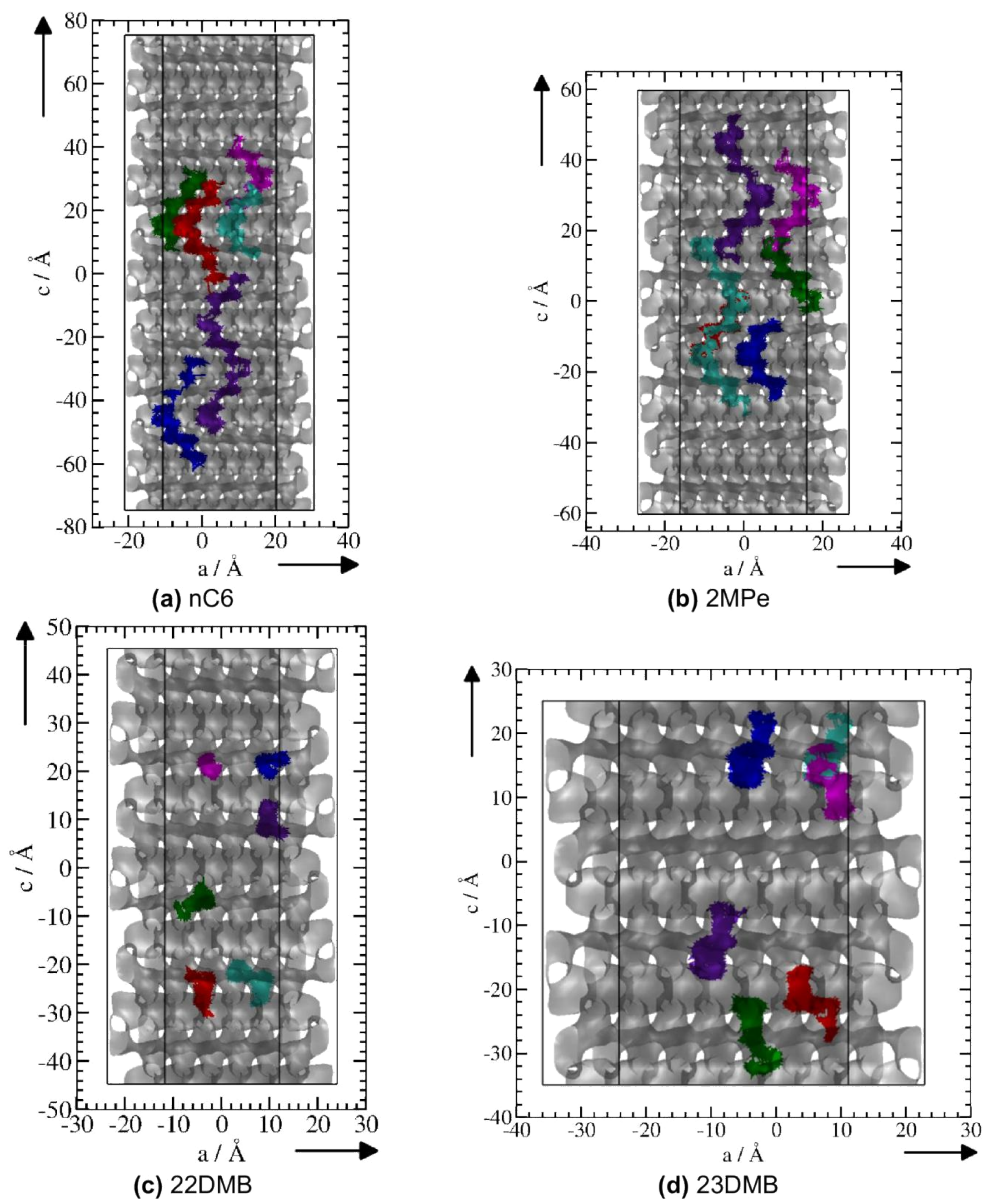


**Figure B18:** Trajectories of hexane isomers on STW  $2 \times 2 \times 2$  zeolite during MD simulation.

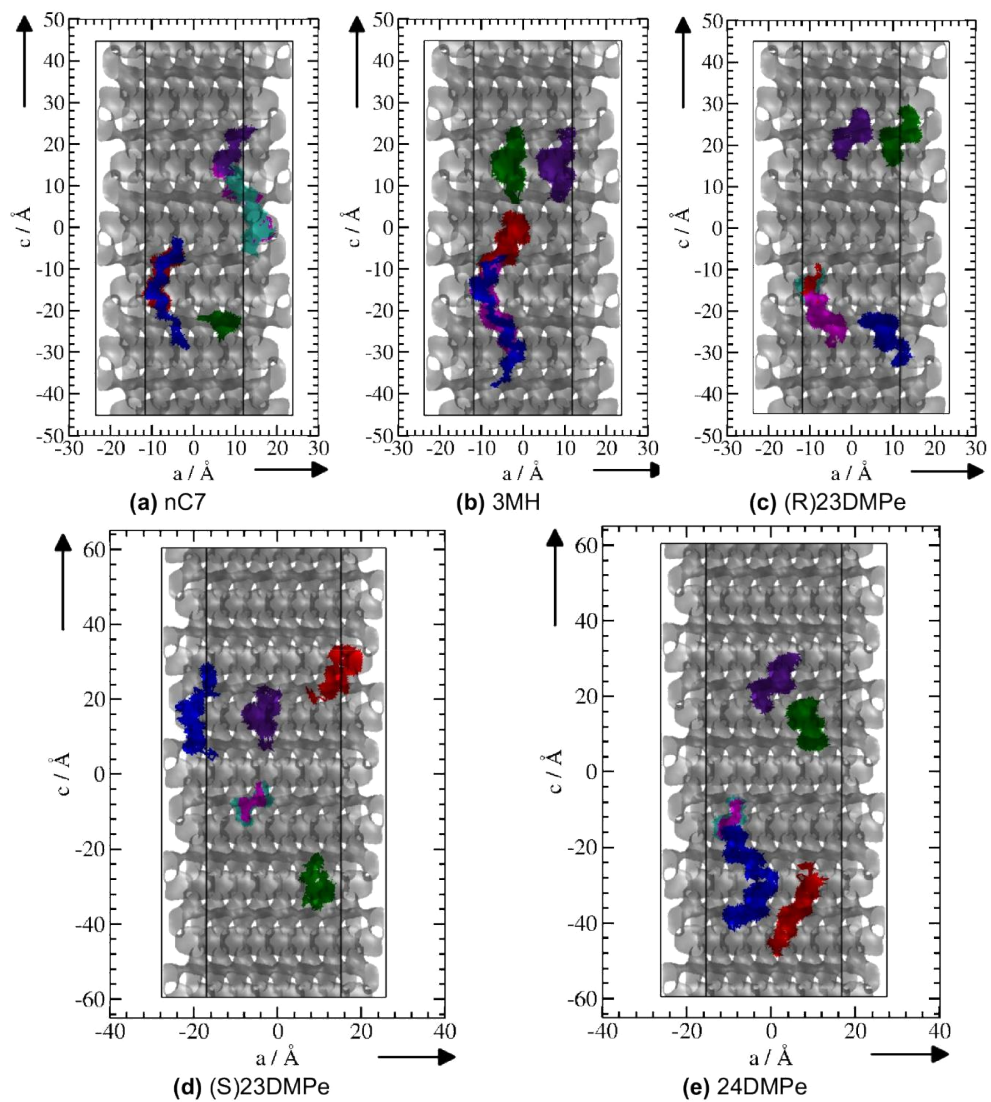


**Figure B19:** Trajectories of heptane isomers on STW  $2 \times 2 \times 2$  zeolite during MD simulation.

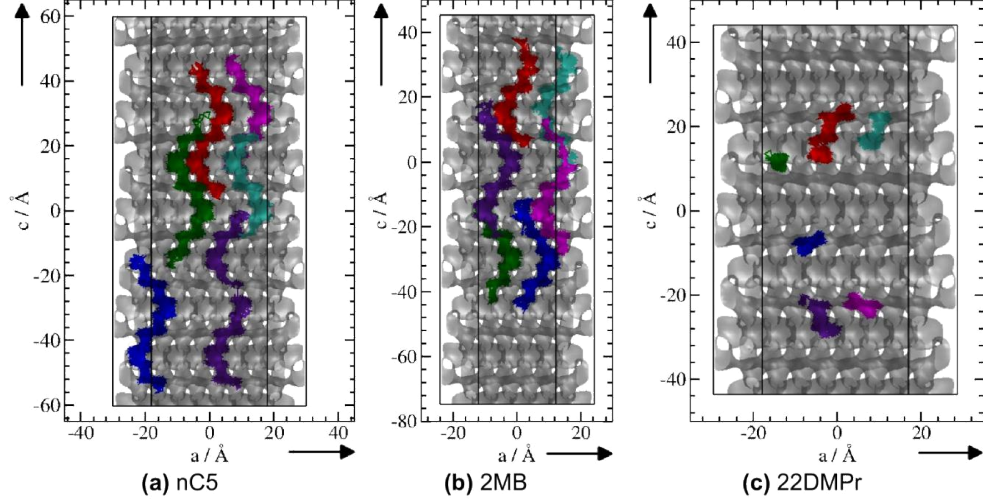


**Figure B20:** Trajectories of pentane isomers on STW  $2 \times 2 \times 2$  zeolite during MD simulation (this is the same as Figure 4.6 in the main text).

### B2.3 Heat of adsorption

From the MD simulations, the heats of adsorption ( $\overline{\Delta H_{ads}^{theo}}$ ) could be calculated through Eq. B1. Here  $E_{zeo-HC}$  is the total energy of the system zeolite-hydrocarbon (HC) with the hydrocarbon adsorbed in the zeolite.  $E_{zeo}$  is the total energy of the zeolite, and  $E_{HC}^{intra}$  is the intramolecular HC energy. Therefore,  $\overline{\Delta H_{ads}^{theo}}$  takes into account both intermolecular interactions between Zeolite-HC and HC-HC. The latter contribution increases with hydrocarbon concentration, affecting the final uptake.

$$\overline{\Delta H_{ads}^{theo}} = E_{zeo-HC} - (E_{zeo} + E_{HC}^{intra}) \quad (B1)$$

The nature of  $\overline{\Delta H_{ads}^{theo}}$  was analyzed by its dispersive and electrostatic contributions (Eq. B2). Dispersion term is obtained through Eq. B3, by the sum of Lennard-Jones (LJ) energy values between zeolite and HC ( $E_{zeo-HC}^{LJ}$ ), and HC intermolecular ( $E_{HC-HC}^{LJ}$ ). The electrostatic contribution to  $\overline{\Delta H_{ads}^{theo}}$  is given by Eq. B4.

$$\overline{\Delta H_{ads}^{theo}} = E_{vdw} + E_{elec} \quad (B2)$$

$$E_{vdw} = E_{zeo-HC}^{LJ} + E_{HC-HC}^{LJ} \quad (\text{B3})$$

$$E_{elec} = \overline{\Delta H_{ads}^{theo}} - E_{vdw} \quad (\text{B4})$$

In order to have a statistical average, 10 configurations were sampled from the MD simulation, and each one was subjected to a geometry optimization using GULP package (version 4.3.2) [19]. The same force field description provided during the simulation was considered in such calculations, realized at constant pressure. All energy terms described above were derived from the optimized structures. In this way, energy values are an average, which is a consistent way of considering all adsorption sites. All energy values obtained are collected in Tables B9 and B10 below, and the heats of adsorption plotted in Figures B21 and B22.

**Table B9:** Heat of adsorption for pentane, hexane and heptane isomers in MFI. Experimental data from this work, from literature ( $q_{st}$ ) and simulated at 300K by Dubbeldam et al. [11] ( $\overline{\Delta H_{ads}^{sim}}$ ). Average values of theoretical heat of adsorption from this work ( $\overline{\Delta H_{ads}^{theo}}$ ), its van der Waals ( $\overline{E_{vdw}}$ ) and electrostatic ( $\overline{E_{elec}}$ ) contributions, with respective standard deviations. All energy values in kJ/mol. Loading of  $\overline{\Delta H_{ads}^{theo}}$ : 0.208 mmol/g (1.5 molecules/u.c.), and experimental loading in parentheses and mmol/g.

MFI	$q_{st}$	$\overline{\Delta H_{ads}^{sim}}$	$\overline{\Delta H_{ads}^{theo}}$	$\overline{E_{vdw}}$	$\overline{E_{elec}}$
nC5	-56.1 (0.23)*, -57.9 (0.29)**, -57.7 <sup>a</sup>	-57.93	-59.5 ± 2.9	-58.3 ± 3.0 (98.1%)	-1.1 ± 0.4 (1.9%)
2MB	-57.3 (0.13)*, -53.2 (0.14)**, -56.1 <sup>a</sup>	-55.77	-56.7 ± 0.9	-55.5 ± 0.9 (97.8%)	-1.2 ± 0.3 (2.2%)
22DMP <sub>r</sub>	–	–	-54.1 ± 0.7	-53.0 ± 0.7 (97.9%)	-1.1 ± 0.3 (2.1%)
nC6	-68.8 <sup>a</sup> , -71.0 <sup>b</sup>	-68.06	-70.1 ± 2.6	-68.6 ± 2.9 (97.9%)	-1.5 ± 0.6 (2.1%)
2MPe	-66.8 <sup>a</sup> , -70.7 <sup>b</sup>	-67.88	-66.2 ± 1.3	-65.1 ± 1.1 (98.3%)	-1.1 ± 0.4 (1.7%)
22DMB	-63.9 <sup>a</sup> , -68.0 <sup>b</sup>	-62.20	-65.2 ± 1.0	-64.1 ± 0.7 (98.3%)	-1.1 ± 0.4 (1.7%)
23DMB	-63.4 <sup>a</sup> , -68.2 <sup>b</sup>	-65.70	-65.1 ± 1.2	-64.0 ± 1.0 (98.3%)	-1.1 ± 0.6 (1.7%)
nC7	-79.6 <sup>a</sup>	-78.32	-82.8 ± 1.5	-81.5 ± 1.9 (98.5%)	-1.3 ± 0.5 (1.5%)
3MH	-78.0 <sup>a</sup>	-77.00	-80.5 ± 1.2	-78.9 ± 1.1 (98.0%)	-1.6 ± 0.4 (1.9%)
(R)23DMPe	-74.1 <sup>a</sup>	-76.18	-76.8 ± 1.1	-75.8 ± 1.2 (98.6%)	-1.1 ± 0.4 (1.4%)
(S)23DMPe			-76.4 ± 0.8	-75.7 ± 0.9 (99.1%)	-0.7 ± 0.3 (0.9%)
24DMPe	–	–	-77.3 ± 2.7	-76.0 ± 1.4 (98.2%)	-1.4 ± 3.1 (1.8%)

\* MFI Large sample. \*\* MFI Small sample. <sup>a</sup> Denayer et al. [20] <sup>b</sup> Ferreira et al. [21]

**Table B10:** Heat of adsorption for pentane, hexane and heptane isomers in STW. Experimental data from this work ( $q_{st}$ ), average values of theoretical heat of adsorption ( $\overline{\Delta H_{ads}^{theo}}$ ), its van der Waals ( $\overline{E_{vdw}}$ ) and electrostatic ( $\overline{E_{elec}}$ ) contributions, with respective standard deviations. All energy values in kJ/mol. Loading of  $\overline{\Delta H_{ads}^{theo}}$ : 0.260 mmol/g (0.75 molecules/u.c.), and experimental loading in parentheses and mmol/g.

STW	$q_{st}$	$\overline{\Delta H_{ads}^{theo}}$	$\overline{E_{vdw}}$	$\overline{E_{elec}}$
<b>nC5</b>	-61.5 (1.5)	$-63.9 \pm 1.4$	$-61.9 \pm 1.2$ (96.9%)	$-2.0 \pm 0.5$ (3.1%)
<b>2MB</b>	-55.3 (0.9)	$-62.7 \pm 2.0$	$-61.6 \pm 2.0$ (98.4%)	$-1.0 \pm 0.3$ (1.6%)
<b>22DMPPr</b>	-33.1 (0.011)	$-58.8 \pm 0.8$	$-58.4 \pm 0.8$ (99.3%)	$-0.4 \pm 0.7$ (0.7%)
<b>nC6</b>	-81.0 (1.6)	$-77.0 \pm 1.5$	$-75.2 \pm 1.5$ (97.6%)	$-1.8 \pm 0.3$ (2.4%)
<b>2MPe</b>	-72.2 (1.4)	$-73.1 \pm 1.5$	$-72.0 \pm 1.5$ (98.5%)	$-1.1 \pm 0.4$ (1.5%)
<b>22DMB</b>		$-70.7 \pm 1.1$	$-70.4 \pm 0.7$ (99.7%)	$-0.2 \pm 0.5$ (0.3%)
<b>23DMB</b>	-46.0 (1.4)	$-72.9 \pm 1.6$	$-72.4 \pm 1.4$ (99.3%)	$-0.5 \pm 0.6$ (0.7%)
<b>nC7</b>	-85.8 (1.6)	$-85.3 \pm 2.3$	$-83.4 \pm 2.1$ (97.8%)	$-1.9 \pm 0.4$ (2.2%)
<b>3MH</b>	-76.3 (1.4)	$-85.4 \pm 2.1$	$-84.0 \pm 1.7$ (98.3%)	$-1.4 \pm 0.7$ (1.6%)
<b>(R)23DMPe</b>		$-82.3 \pm 1.7$	$-81.9 \pm 1.4$ (99.4%)	$-0.5 \pm 0.6$ (0.6%)
<b>(S)23DMPe</b>		$-85.0 \pm 1.3$	$-85.2 \pm 1.4$ (100.0%)	$0.2 \pm 0.3$ (0.0%)
<b>24DMPe</b>	-58.9 (0.9)	$-81.9 \pm 1.6$	$-81.1 \pm 1.2$ (99.0%)	$-0.8 \pm 0.5$ (1.0%)

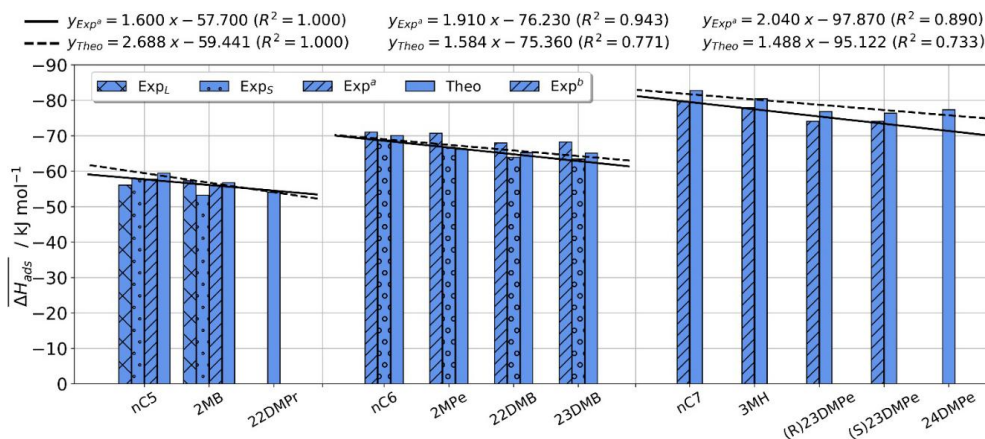


**Figure B21:** Theoretical (solid color) and Experimental (bar with patterns) heats of adsorption of C5, C6 and C7 alkanes in MFI. Experimental values for MFI Small (Exp<sub>S</sub>) and Large (Exp<sub>L</sub>) samples, from Denayer et al. (Exp<sup>a</sup>) [22] and Ferreira et al. (Exp<sup>b</sup>) [21].

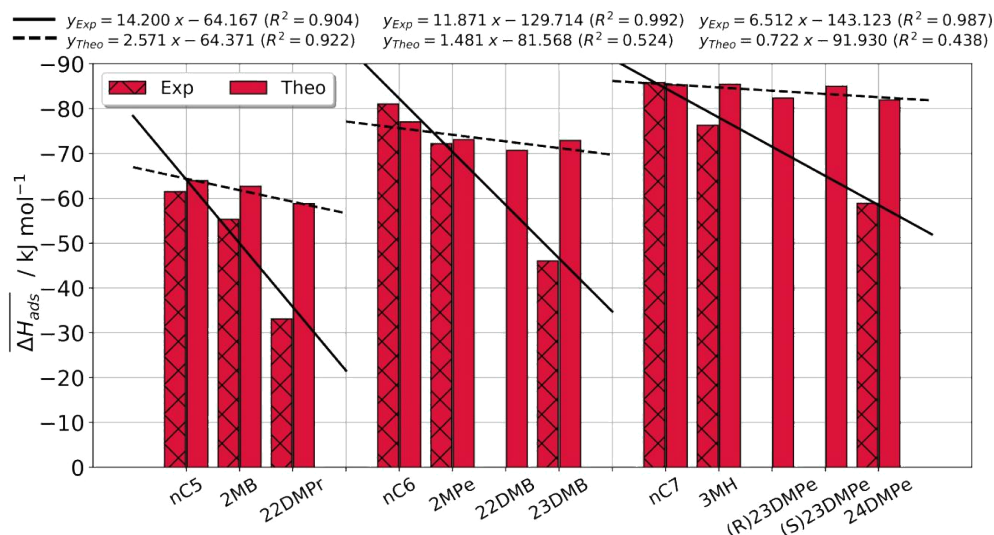


**Figure B22:** Theoretical (solid color) and Experimental (bar with patterns) heats of adsorption of C5, C6 and C7 alkanes in STW.

A direct comparison with the experimental values on Si-STW needs to be done carefully, since the loading values at which the experimental heat of adsorption has been calculated are considerably larger (0.9-1.6 mmol/g) than the simulated ones (ca. 0.2 mmol/g).

Calculations were not able to reproduce quantitatively the trends from linear to mono-branched and dibranched alkanes observed experimentally for Si-STW, but qualitatively the trend is reproduced (Figure B22). For all zeolites and alkanes, the main contribution to heat of adsorption comes from the dispersive term (above 90%).

## References

- [1] Demirbas, A.; Balubaid, M. A.; Basahel, A. M.; Ahmad, W.; Sheikh, M. H. Octane Rating of Gasoline and Octane Booster Additives. *Pet. Sci. Technol.* **2015**, *33* (11), 1190–1197, DOI: 10.1080/10916466.2015.1050506.



- 
- [2] Dubbeldam, D.; Calero, S.; Ellis, D. E.; Snurr, R. Q. RASPA: Molecular Simulation Software for Adsorption and Diffusion in Flexible Nanoporous Materials. *Mol. Simul.* **2016**, *42* (2), 81–101, DOI: 10.1080/08927022.2015.1010082.
- [3] Sławek, A.; Vicent-Luna, J. M.; Marszałek, B.; Makowski, W.; Calero, S. Quasi-Equilibrated Thermodesorption Combined with Molecular Simulation for Adsorption and Separation of Hexane Isomers in Zeolites MFI and MEL. *J. Phys. Chem. C* **2017**, *121* (35), 19226–19238, DOI: 10.1021/acs.jpcc.7b05347.
- [4] Van Koningsveld, H.; Van Bekkum, H.; Jansen, J. C. On the Location and Disorder of the Tetrapropylammonium (TPA) Ion in Zeolite ZSM5 with Improved Framework Accuracy. *Acta Crystallogr. Sect. B* **1987**, *43* (2), 127–132, DOI: 10.1107/S0108768187098173.
- [5] Ch. Baerlocher; McCusker, L. B. Database of Zeolite Structures <http://www.iza-structure.org/databases/> (accessed 2021-10-15).
- [6] Bueno-Perez, R.; Balestra, S. R. G. G.; Cambor, M. A.; Min, J. G.; Hong, S. B.; Merklings, P. J.; Calero, S. Influence of Flexibility on the Separation of Chiral Isomers in STW-Type Zeolite. *Chem. Eur. J.* **2018**, *24* (16), 4121–4132, DOI: 10.1002/chem.201705627.
- [7] Van Koningsveld, H.; Tuinstra, F.; Van Bekkum, H.; Jansen, J. C. The Location of Pxylyene in a Single Crystal of Zeolite HZSM5 with a New, Sorbate-induced, Orthorhombic Framework Symmetry. *Acta Crystallogr. Sect. B* **1989**, *45* (4), 423–431, DOI: 10.1107/S0108768189004519.
- [8] van Koningsveld, H.; Jansen, J. C.; van Bekkum, H. The Monoclinic Framework Structure of Zeolite H-ZSM-5. Comparison with the Orthorhombic Framework of as-Synthesized ZSM-5. *Zeolites* **1990**, *10* (4), 235–242, DOI: 10.1016/0144-2449(94)90134-1.
- [9] Rojas, A.; Cambor, M. A. A Pure Silica Chiral Polymorph with Helical Pores. *Angew. Chem. Int. Ed.* **2012**, *51* (16), 3854–3856, DOI: 10.1002/anie.201108753.
- [10] Rojas, A.; Arteaga, O.; Kahr, B.; Cambor, M. A. Synthesis, Structure, and Optical Activity of HPM-1, a Pure Silica Chiral Zeolite. *J. Am. Chem. Soc.* **2013**, *135* (32), 11975–11984, DOI: 10.1021/ja405088c.

- [11] Dubbeldam, D.; Calero, S.; Vlugt, T. J. H.; Krishna, R.; Maesen, T. L. M.; Smit, B. United Atom Force Field for Alkanes in Nanoporous Materials. *J. Phys. Chem. B* **2004**, *108* (33), 12301–12313, DOI: 10.1021/jp0376727.
- [12] Krishna, R.; van Baten, J. M. Diffusion of Hydrocarbon Mixtures in MFI Zeolite: Influence of Intersubsection Blocking. *Chem. Eng. J.* **2008**, *140* (1–3), 614–620, DOI: 10.1016/j.cej.2007.11.026.
- [13] Zhu, W.; Kapteijn, F.; Van der Linden, B.; Moulijn, J. A. Equilibrium Adsorption of Linear and Branched C6 Alkanes on Silicalite-1 Studied by the Tapered Element Oscillating Microbalance. *Phys. Chem. Chem. Phys.* **2001**, *3* (9), 1755–1761, DOI: 10.1039/B100941I.
- [14] Smith, W.; Forester, T. R. DL\_POLY 2.20: A General-Purpose Parallel Molecular Dynamics Simulation Package. *J. Mol. Graph.* **1996**, *14* (3), 136–141, DOI: 10.1016/s0263-7855(96)00043-4.
- [15] Ghysels, A.; Moors, S. L. C.; Hemelsoet, K.; De Wispelaere, K.; Waroquier, M.; Sastre, G.; Van Speybroeck, V. Shape-Selective Diffusion of Olefins in 8-Ring Solid Acid Microporous Zeolites. *J. Phys. Chem. C* **2015**, *119* (41), 23721–23734, DOI: 10.1021/acs.jpcc.5b06010.
- [16] Oie, T.; Maggiora, G. M.; Christoffersen, R. E.; Duchamp, D. J. Development of a Flexible Intra and Intermolecular Empirical Potential Function for Large Molecular Systems. *Int. J. Quantum Chem.* **1981**, *20* (S8), 1–47, DOI: 10.1002/qua.560200703.
- [17] Frisch, M. J.; Trucks, G. W.; Schlegel, H. B.; Scuseria, G. E.; Robb, M. A.; Cheeseman, J. R.; Scalmani, G.; Barone, V.; Mennucci, B.; Petersson, G. A. et al. *Gaussian 09*. Gaussian, Inc., Wallingford CT 2009.
- [18] Catlow, C. R. A.; Freeman, C. M.; Vessal, B.; Tomlinson, S. M.; Leslie, M. Molecular Dynamics Studies of Hydrocarbon Diffusion in Zeolites. *J. Chem. Soc. Faraday Trans.* **1991**, *87* (13), 1947–1950, DOI: 10.1039/FT9918701947.
- [19] Gale, J. D. GULP: A Computer Program for the Symmetry-Adapted Simulation of Solids. *J. Chem. Soc. Faraday Trans.* **1997**, *93* (4), 629–637, DOI: 10.1039/A606455H.

- 
- [20] Denayer, J. F. M.; Baron, G. V.; Martens, J. A.; Jacobs, P. A. Chromatographic Study of Adsorption of n -Alkanes on Zeolites at High Temperatures. *J. Phys. Chem. B* **1998**, *102* (1), 3077–3081, DOI: 10.1016/0950-4214(93)85014-M.
- [21] Ferreira, A. F. P.; Mittelmeijer-Hazeleger, M. C.; Blik, A. Can Alkane Isomers Be Separated? Adsorption Equilibrium and Kinetic Data for Hexane Isomers and Their Binary Mixtures on MFI. *Adsorption* **2007**, *13* (2), 105–114, DOI: 10.1007/s10450-007-9010-z.
- [22] Denayer, J. F.; Souverijns, W.; Jacobs, P. A.; Martens, J. A.; Baron, G. V. High-Temperature Low-Pressure Adsorption of Branched C5-C8 Alkanes on Zeolite Beta, ZSM-5, ZSM-22, Zeolite Y, and Mordenite. *J. Phys. Chem. B* **1998**, *102* (23), 4588–4597, DOI: 10.1021/jp980674k.



## Appendix C

# Supplementary material for Chapter 5

### C1 Conformer Search for Sugar Molecules

The ab-initio calculation using the semi-empirical hybrid functional B3LYP and taking into account the interactions of vdW optimizes the geometry of the molecules, finding accurately low energy configurations. However, they may not correspond to the overall energy minimum of a structure, as the potential energy surface of a given molecule becomes increasingly complex when the number of atoms in the molecule increases, as it is the case in sucrose (45 atoms) and 6-kestose (66 atoms).

In order to find whether the available configurations differ much from the global minimum, i.e. the global ground state, a study of conformers [1] was performed. The scanning method, through systematic searches around particular torsion angles, allows to build an image of the energy barriers to rotation. We have performed a systematic grid scan to find the conformations of each specified torsion angle that is varied over a grid of equally spaced values. In the systematic grid scan the torsion was allowed to be varied around the full  $360^\circ$ , where the torsion angles will be evenly spaced throughout the full circle. 7776 conformations of sucrose and 46656 of 6-kestose molecules were considered feasible by this method, as these are sterically allowed.

From these analyzed structures, 4578 and 12772 were accepted and were nonequivalent. Calculation energies for each of these configurations is shown (Figure C1). A Smart algorithm, that combines Quasi-Newtonian (BFGS) [2–5], adjusted basis set Newton-Raphson [6], and stepped descendant algorithms [7], was used for

geometry optimization in the universal force field [8–10]. The conformational analysis using the torsions and generating each molecule with the particular dihedral angles allows to obtain a new molecular conformation whose corresponding molecular size is subsequently calculated with the shoebox algorithm (Figure C2).

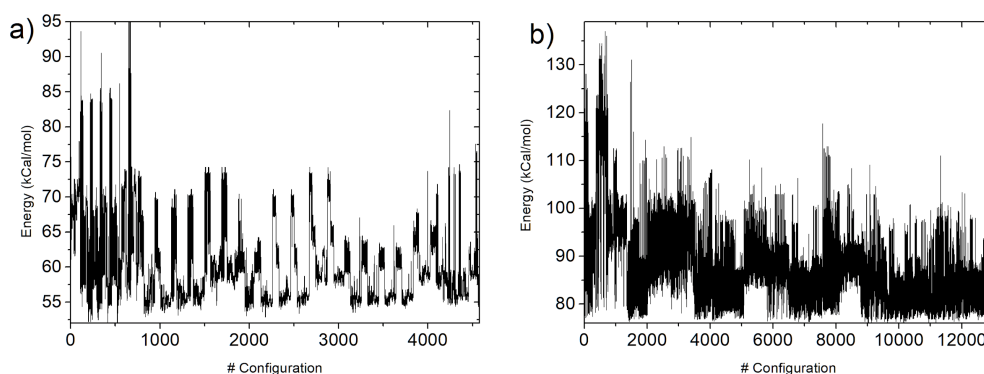


**Figure C1:** Total energies for the conformers of a) sucrose and b) 6-kestose.

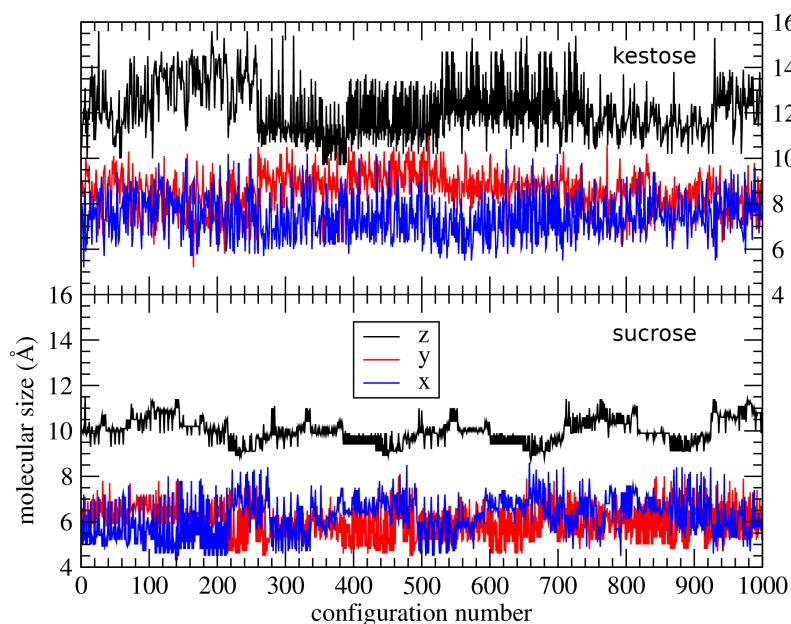


**Figure C2:** Molecular size (using shoebox algorithm) of the different conformations of sucrose and 6-kestose. A representative number of configurations (1000) are shown.

## C2 Force Field Description

Functional forms are presented in Equations A1 to A6.

$$U^{Coulomb}(r_{ij}) = \frac{1}{4\pi\epsilon_0} \frac{q_i q_j}{r_{ij}} \quad (C1)$$

$$U^{LJ}(r_{ij}) = \left( \frac{A}{r_{ij}^{12}} \right) - \left( \frac{B}{r_{ij}^6} \right) \quad (C2)$$

$$U^{morse}(r_{ij}) = E_0 [1 - e^{-k(r_{ij}-r_0)^2}] - E_0 \quad (C3)$$

$$U^{harm}(r_{ij}) = \frac{1}{2} k_b (r_{ij} - r_0)^2 \quad (C4)$$

$$U^{harm}(\theta_{ijk}) = \frac{1}{2} k_\theta (\theta_{ijk} - \theta_0)^2 \quad (C5)$$

$$U^{torsion}(\phi_{ijkl}) = A [1 + \cos(m\phi_{ijkl} - \delta)] \quad (C6)$$

**Table C1:** Atom types description and point charges assigned (C1)

Species	Atom Type	charge (e-)
zeolite silicon	<b>Si</b>	2.100
zeolite oxygen	<b>O2</b>	-1.050
silanol oxygen	<b>O3</b>	-0.950
silanol hydrogen	<b>H3</b>	0.425
water oxygen	<b>O4</b>	-0.820
water hydrogen	<b>H4</b>	0.420
sugar sp3 carbon	<b>C3</b>	
sugar hydrogen	<b>H1</b>	Figure C3
sugar sp3 oxygen	<b>O1</b>	

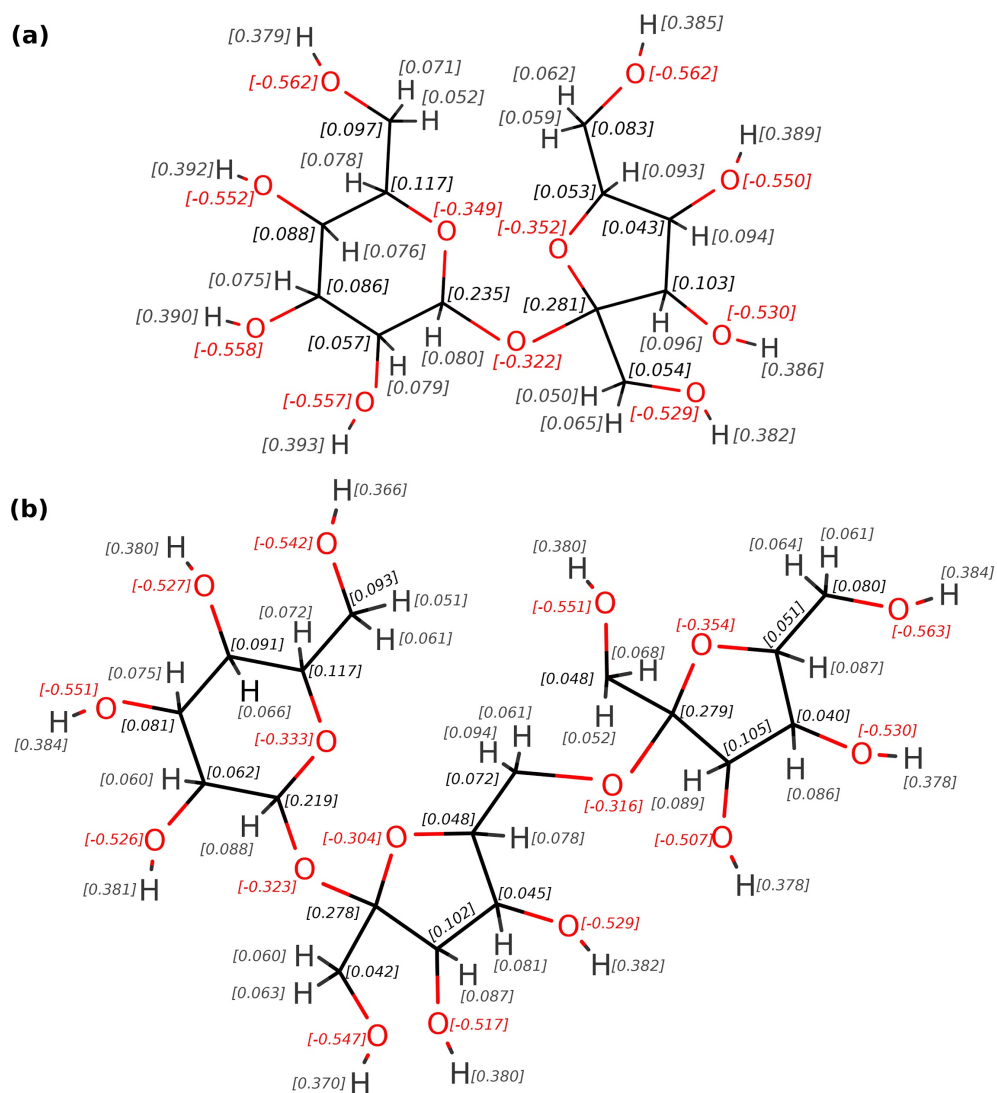


**Figure C3:** Point charges assigned for each atom of sucrose (a) and 6-kestose (b) molecules by Gasteiger-Marsili method [11].



**Table C2:** Lennard-Jones parameters (C2). Oz refers to any zeolite Oxygen (O2 and O3 atom types); <sup>a</sup> from [12]; <sup>b</sup> from [8]; <sup>c</sup> from [13]; <sup>d</sup> from [14, 15]. Other parameters were obtained by applying the Lorentz-Berthelot combination rules (both references separated by comma).

Interaction	Pair	A (eV/Å <sup>12</sup> )	B (eV/ Å <sup>6</sup> )
Zeolite – Zeolite	Si ... Si <sup>a</sup>	0.5601	0.0004
	Oz ... Oz <sup>a</sup>	26877.9664	29.8306
	H3 ... H3 <sup>b</sup>	636.6071	2.2042
	Si ... O2 <sup>a</sup>	172.6992	0.1086
	Si ... O3 <sup>a</sup>	218.1689	0.9583
	Si ... H3	0.0000	0.0000
	Oz ... H3 <sup>d</sup>	1556.4000	5.5717
Sugar – Sugar <sup>b</sup>	C3 ... C3	48465.403	29.710
	O1 ... O1	8787.3614	9.5632
	H1 ... H1	636.60710	2.2042
	C3 ... O1	20636.933	16.856
	C3 ... H1	5554.5856	8.0925
	O1 ... H1	2365.1844	4.5912
Water – Water <sup>c</sup>	O4 ... O4	27289.5057	27.1237
	H4 ... H4	0.0000	0.0000
	H4 ... O4	0.0000	0.0000
Zeolite – Sugar	Si ... C3	0.0000	0.0000
	Si ... O1	0.0000	0.0000
	Si ... H1	0.0000	0.0000
	Oz ... C3 <sup>d</sup>	11000.0000	17.6540
	Oz ... O1 <sup>b,d</sup>	15368.3572	16.8901
	Oz ... H1 <sup>d</sup>	1556.4000	5.5717
	H3 ... C3 <sup>b</sup>	5554.5856	8.0925
	H3 ... O1 <sup>b</sup>	2365.1844	4.5912
Zeolite – Water	H3 ... H1 <sup>b</sup>	636.6071	2.2042
	Si ... O4 <sup>c</sup>	123.6319	0.1042
	Si ... H4 <sup>c</sup>	0.0000	0.0000
	Oz ... O4 <sup>a,c</sup>	27082.9544	28.4449
	Oz ... H4 <sup>a,b</sup>	4136.5087	8.1088
	H3 ... O4 <sup>b,c</sup>	4168.0563	7.7321
Sugar – Water	H3 ... H4 <sup>b</sup>	636.6071	2.2042
	O4 ... C3 <sup>b,c</sup>	36367.5253	28.3874
	O4 ... O1 <sup>b,c</sup>	15485.5658	16.1056
	O4 ... H1 <sup>b,c</sup>	4168.0563	7.7321
	H4 ... C3 <sup>b</sup>	5554.5855	8.0924
	H4 ... O1 <sup>b</sup>	2365.1843	4.5912
	H4 ... H1 <sup>b</sup>	636.6071	2.2042

**Table C3:** Functional forms and parameters for bonds. Constant  $k_b$  is expressed in  $\text{\AA}^{-1}$  when functional form is C3, and in  $\text{eV \AA}^{-2}$  for C4.

Bond	Functional form	$k_b$	$r_0$ ( $\text{\AA}$ )	$E_0$ (eV)
O3 – H3	C3	2.1986	0.9476	7.0525
C3 – C3		27.46	1.520	–
C3 – H1	C4	28.71	1.095	–
C3 – O1		31.22	1.425	–
O1 – H1		43.70	0.958	–
O4 – H4	C4	48.0595	1.0000	–

**Table C4:** Parameters for angles (C5).

Bend	$k_\theta$ (eV/rad <sup>2</sup> )	$\theta_0$ (deg)	Bend	$k_\theta$ (eV/rad <sup>2</sup> )	$\theta_0$ (deg)
O2 – Si – O2	1.4944	109.47	C3 – O1 – C3	3.75	110.0
O2 – Si – O3	1.4944	109.47	C3 – O1 – H1	4.74	108.0
Si – O2 – Si	1.5509	142.71	H1 – C3 – C3	2.50	109.2
H3 – O3 – Si	1.5480	109.47	H1 – C3 – H1	2.06	109.2
C3 – C3 – C3	3.56	110.4	H1 – C3 – O1	3.12	109.5
C3 – C3 – H1	2.50	109.2	O1 – C3 – O1	3.56	109.5
C3 – C3 – O1	6.12	108.5	H4 – O4 – H4	3.9695	109.47

**Table C5:** Parameters for torsions (Equation C6).

Torsion	A (eV)	(degree)	m
C3 – C3 – C3 – C3	0.0032	0.0	3.0
C3 – C3 – C3 – H1	0.0050	0.0	3.0
H1 – C3 – C3 – H1	0.0050	0.0	3.0
C3 – C3 – C3 – O1	0.0048	0.0	3.0
C3 – C3 – O1 – C3	0.0087	0.0	3.0
C3 – C3 – O1 – H1	0.0072	0.0	3.0
C3 – O1 – C3 – H1	0.0087	0.0	3.0
C3 – O1 – C3 – O1	0.0087	0.0	3.0
O1 – C3 – C3 – O1	0.0048	0.0	3.0
H1 – C3 – C3 – O1	0.0072	0.0	3.0
H1 – C3 – O1 – H1	0.0048	0.0	3.0

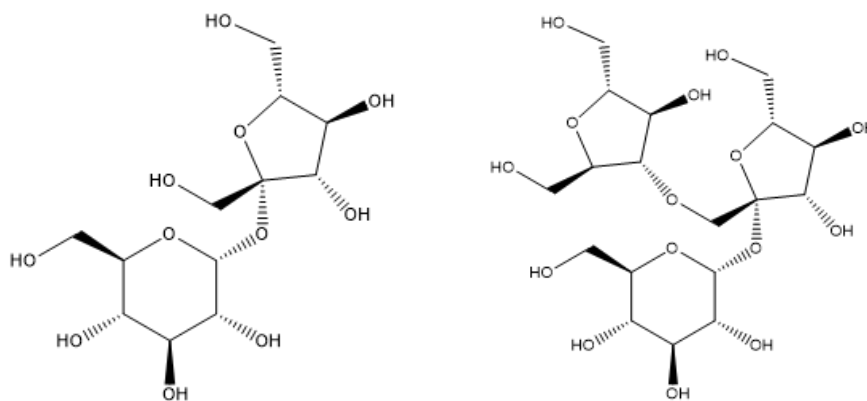


**Figure C4:** Chemical structures of sucrose (left) and 6-kestose (right).

Cartesian coordinates for sucrose and 6-kestose geometries considered in the procedure of molecular size measurement are reported below.

45

Sucrose fitted by shoebox algorithm

H	1.396404782	7.567434932	4.385827189
H	4.612614992	5.077901646	5.746867208
H	5.053032334	0.649544996	5.910806629
H	3.103462492	5.634687397	0.126295484
H	0.245882013	4.984075620	3.072219612
H	3.979728701	2.807104265	0.470473155
H	9.119885383	3.995550825	3.521978370
H	7.748504338	1.168712962	1.913873358
H	2.221111837	5.132951360	4.532049450
H	3.111853092	6.644602606	4.730519916
H	7.203024232	5.831589972	4.984545831
H	5.868489436	5.595828485	3.829282484
H	3.390498233	1.214546554	4.330209855
H	4.483372349	0.176023492	3.389095612
H	3.590763503	6.837234053	2.415430728
H	1.213762075	6.498801488	1.642949265
H	0.769774182	4.199533532	0.693032626
H	2.026351305	2.299270333	1.813351203
H	3.002723635	3.384362643	3.713501658
H	7.096418716	3.495076621	5.664502169
H	7.052980212	3.897645344	2.645155961
H	7.079190730	1.242609030	4.104023733
C	2.411101931	6.107708329	4.088030737

C	6.275635339	5.292478600	4.797172490
C	4.450157454	0.934029778	4.172309019
C	3.016716965	5.953354297	2.674133548
C	2.007853333	5.750492772	1.531355629
C	1.380117515	4.352129402	1.590749463
C	2.485856093	3.281257427	1.616738137
C	3.469655030	3.565315380	2.742815724
C	6.553681558	3.799888695	4.769501623
C	7.297691138	3.286111157	3.520108816
C	6.676478643	1.910545514	3.333255397
C	5.218066260	2.165735286	3.691042348
O	1.123118870	6.745215026	4.078819577
O	5.303283113	5.218838431	5.966880625
O	5.028502079	0.381435964	5.336077711
O	2.593890705	6.315350060	0.349281695
O	0.614249892	4.140193673	2.775624996
O	3.142732348	3.292688993	0.351122514
O	8.697881387	3.149926318	3.678604742
O	6.808772845	1.360169788	2.045588980
O	3.992662179	4.887327115	2.684949532
O	4.572417364	2.716780022	2.548900851
O	5.278533050	3.086737171	4.772846071

66

6-kestose fitted by shoebox algorithm

H	3.849504040	0.711424263	0.320900138
H	10.53303699	2.695948282	5.481806225
H	7.089802625	0.380481650	4.415902221
H	4.301270813	0.427719386	4.313633328
H	0.191178952	1.432826438	2.835186607
H	2.932795692	4.262925183	6.029725501
H	3.719705583	7.612595611	0.359453827
H	8.558696231	2.924907263	0.109894073
H	5.980175238	4.243941129	2.205380129
H	1.922099484	2.580617368	1.156201766
H	3.563944653	2.969321551	0.593215532
H	6.178305546	8.111445895	6.477446521
H	10.16244130	4.434418429	3.951910680
H	11.36462332	3.588153628	2.949666064
H	2.893568771	8.848548500	5.037243735
H	6.505070434	2.177126780	5.791821748
H	5.252015552	2.506622478	4.589579655
H	4.528298091	1.672621386	2.456114114
H	2.262605762	0.459173774	2.892557880
H	1.156409035	1.488505558	4.996697818
H	0.986676349	4.016459315	4.784705791

---

H	3.474581561	5.558212759	1.330342757
H	2.245301430	6.667341116	2.016567684
H	9.908748741	1.580674157	2.915675324
H	2.029362794	4.372899252	2.670407906
H	8.757494988	4.218140267	2.004309691
H	5.506736654	4.371214743	5.261154555
H	6.889812984	5.186582702	6.016651050
H	7.116002149	1.684037471	2.168090884
H	4.548315504	6.609595131	5.965414550
H	4.464359927	8.338144980	3.485340584
H	6.873509188	6.801571561	4.041975084
C	2.955288144	2.241339775	1.138540927
C	10.59811274	3.455464278	3.717946651
C	6.253503549	2.112383719	4.724478111
C	3.531589239	2.135318882	2.554004321
C	2.690597893	1.270146757	3.507005239
C	1.523502194	2.060063259	4.133758418
C	1.911861677	3.453249118	4.613456315
C	3.319869849	6.488801249	1.892365310
C	9.503960421	2.555846284	3.188779223
C	2.690364515	4.174926240	3.514495230
C	8.682570750	3.126833235	2.029515271
C	6.402864002	4.963235439	5.063500124
C	7.245573016	2.742358296	2.400617056
C	7.282735612	2.890928040	3.928833655
C	5.060954163	7.162517359	5.164678255
C	4.016220544	7.564898398	4.127026501
C	5.991274196	6.237327489	4.348879052
C	3.912935656	6.297013110	3.286313035
O	2.941562740	0.974135655	0.490385595
O	11.23611058	2.886073048	4.853443186
O	6.202620103	0.762232941	4.294357483
O	3.417040361	0.720101361	4.592468921
O	0.481537204	2.285425284	3.176459658
O	2.681764076	3.359027417	5.798096585
O	3.971568258	7.578056451	1.279003847
O	9.119335246	2.564405454	0.805296433
O	6.258662461	3.460916117	1.695363759
O	5.676184254	8.327892394	5.683516347
O	2.772274888	7.966643096	4.651717268
O	3.816158568	3.429671235	3.095827429
O	8.538957123	2.326731890	4.270433155
O	7.316227259	4.286570179	4.205892004
O	3.165985713	5.375289713	4.077888528
O	5.265408087	5.892902718	3.148424985

### C3 Mean Square Displacements for 6-Kestose and Sucrose on Zeolites.

Figure C5 shows the mean square displacements (MSD) for 6-kestose and sucrose in all 11 zeolites studied. From the linear (and more accurate) region of the MSD data (5 ns), a linear fit was obtained, from which the self-diffusion coefficient ( $D$ ) for each sugar molecule was calculated using the Einstein equation (Table C6). More details are given in previous work [12, 16].

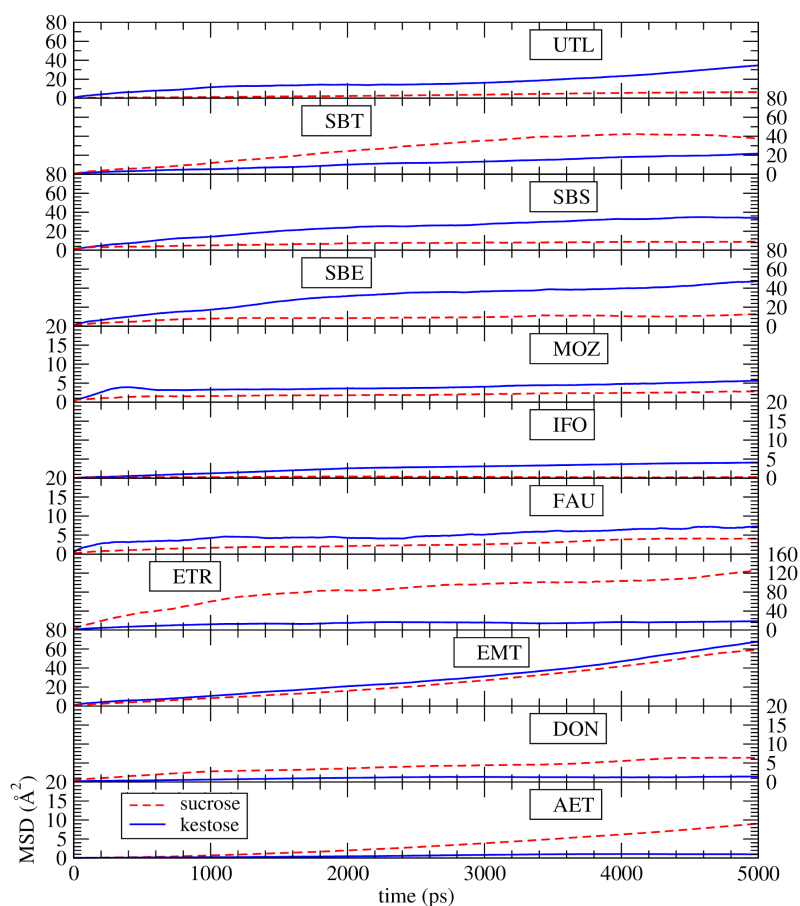


**Figure C5:** Mean square displacements (MSD) for sucrose (dashed line) and 6-kestose (solid line) in 11 zeolites at 338 K. All systems include water, as specified in Table 5.2. The simulations corresponding to this figure were run for 10 ns but the diffusion coefficients were obtained using only the first 5 ns of the mean square displacements plot since the tail of these plots shows always the less accurate data.

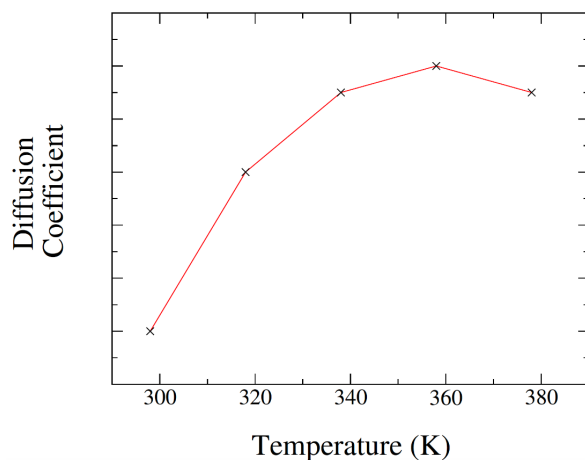
**Table C6:** Diffusion Coefficients (D) for sucrose and 6-kestose on the 11 zeolites at 338 K. All systems include water, as specified in Table 5.2.

Zeolite	Sucrose	Kestose	D ( $10^{-6}$ cm <sup>2</sup> /s)
AET	0	1	0.004087
AET	1	0	0.030471
DON	0	1	0.003677
DON	1	0	0.017740
EMT	0	1	0.208966
EMT	1	0	0.191984
ETR	0	1	0.035890
ETR	1	0	0.303841
FAU	0	1	0.014977
FAU	1	0	0.011851
IFO	0	1	0.013292
IFO	1	0	0.000071
MOZ	0	1	0.009213
MOZ	1	0	0.005391
SBE	0	1	0.129732
SBE	1	0	0.023659
SBS	0	1	0.102576
SBS	1	0	0.019923
SBT	0	1	0.067014
SBT	1	0	0.149114
UTL	0	1	0.084237
UTL	1	0	0.022253

Diffusion coefficients have also been calculated at 378 K from the corresponding mean square displacement plots (Figure C6). The results (Table C7) show an increase with respect to values at 338 K but this is not always the case. Although an increase with temperature is expected, some factors can explain the apparently anomalous results:

- a) molecular dynamics were carried out in bulk systems containing only one sugar molecule. This gives bad statistics. The lack of linearity of the MSD plots seems to confirm this aspect.
- b) diffusion is slow, as it correspond to molecules of similar size to the microporous channels. This is a usual situation when molecular size precludes the diffusion of one or several components in a mixture.
- c) large molecules do not necessarily increase their self-diffusivity as temperature raises. This effect has been recently investigated in collaboration by some of the authors [17].

Regarding the latter, in our particular case, increasing the temperature increases the mobility of both sugars. At a certain temperature threshold, the internal degrees of freedom lead to bulkier sugar conformations whose mobility is hindered due to increasing sugar-zeolite van der Waals repulsions. We would expect a behaviour such as the one in the qualitative plot below:



The ratio between diffusion coefficients for sucrose/6-kestose at 378 K has also been calculated (Table C8) and, although the numerical values are not accurate, according to the argument above, the conclusion obtained is in agreement with that obtained at 338 K, that AET, DON and ETR are the zeolites chosen for a more accurate study. EMT and SBS could also be selected according to the values in the new table, but they are not in agreement with the results at 338 K. At both temperatures, zeolites AET, DON, ETR show consistently relatively large ratios for the diffusion coefficients sucrose/6-kestose.



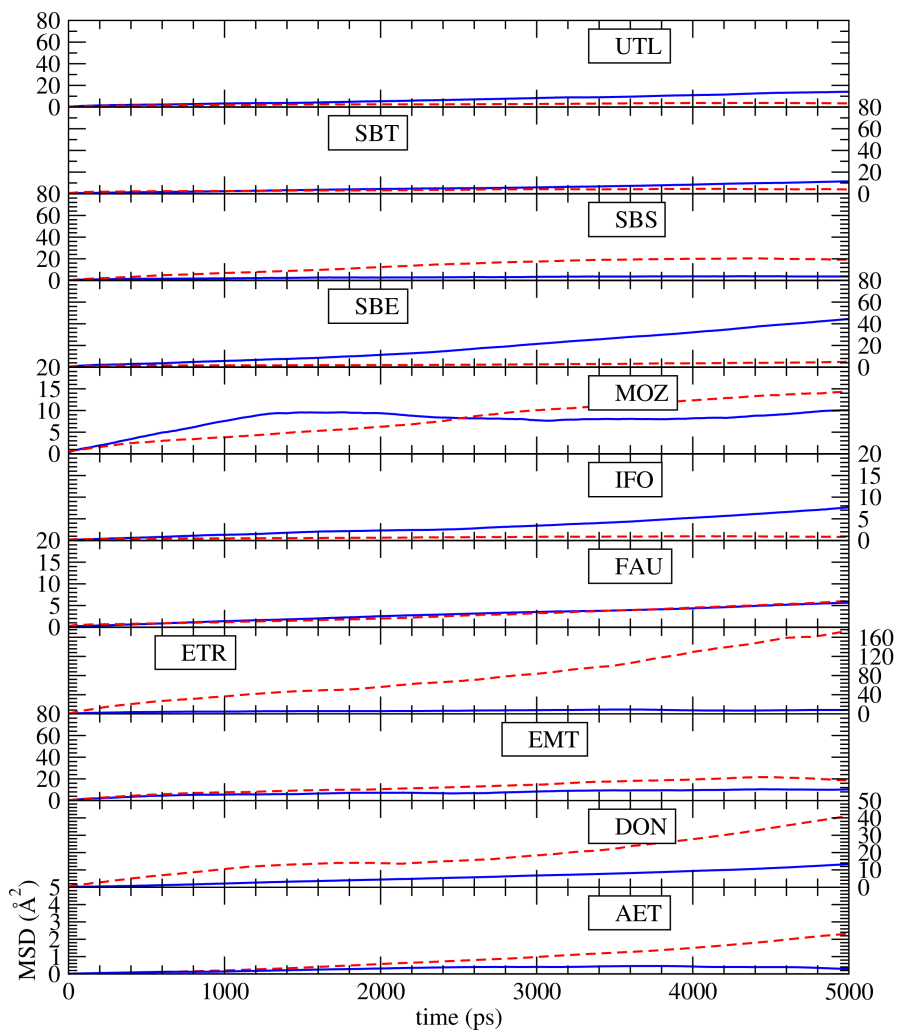


**Figure C6:** Mean square displacements (MSD) for sucrose (dashed line) and 6-kestose (solid line) in 11 zeolites at 378 K. All systems include water, as specified in Table 5.2. The simulations corresponding to this figure were run for 10 ns but the diffusion coefficients were obtained using only the first 5 ns of the mean square displacements plot since the tail of these plots shows always the less accurate data.

**Table C7:** Diffusion Coefficients (D) for sucrose and 6-kestose on the 11 zeolites at 378 K. All systems include water, as specified in Table 5.2.

Zeolite	Sucrose	Kestose	D ( $10^{-6}$ cm <sup>2</sup> /s)
AET	0	1	0.0074
AET	1	0	0.0013
DON	0	1	0.0414
DON	1	0	0.1120
EMT	0	1	0.0262
EMT	1	0	0.0657
ETR	0	1	0.0183
ETR	1	0	0.5281
FAU	0	1	0.0175
FAU	1	0	0.0184
IFO	0	1	0.0229
IFO	1	0	0.0022
MOZ	0	1	0.0175
MOZ	1	0	0.0260
SBE	0	1	0.1474
SBE	1	0	0.0113
SBS	0	1	0.0097
SBS	1	0	0.0692
SBT	0	1	0.0347
SBT	1	0	0.0095
UTL	0	1	0.0442
UTL	1	0	0.0094

**Table C8:** Ratio of diffusion coefficients for sucrose/6-kestose in zeolites at 378 K.

Zeolite	$D_S/D_K$
AET	5.7
DON	2.7
EMT	2.5
ETR	28.9
FAU	1.1
IFO	0.1
MOZ	0.7
SBE	0.1
SBS	7.1
SBT	0.3
UTL	0.2

## C4 Trajectories of Sucrose and 6-Kestose in Membrane Simulations

To assess the diffusion of sugar molecules during the simulations containing the membrane model, Figures C7 to C10, were generated from the computed trajectories (20 ns) with low concentration of sugar. Sugar dynamics were also depicted, in Figures C12 to C14, for simulations with higher concentration of sugar, also computed during 20 ns. The representation of the zeolite channels allows a visualization of the regions and extension of sucrose and 6-kestose uptake. Figure C11 shows the thickness of the zeolite external surface in which sugar molecules adsorb strongly. When increasing sugar loading above the monolayer, incoming sugar molecules are less strongly adsorbed at the external surface and the probability to enter the zeolite micropore increases.

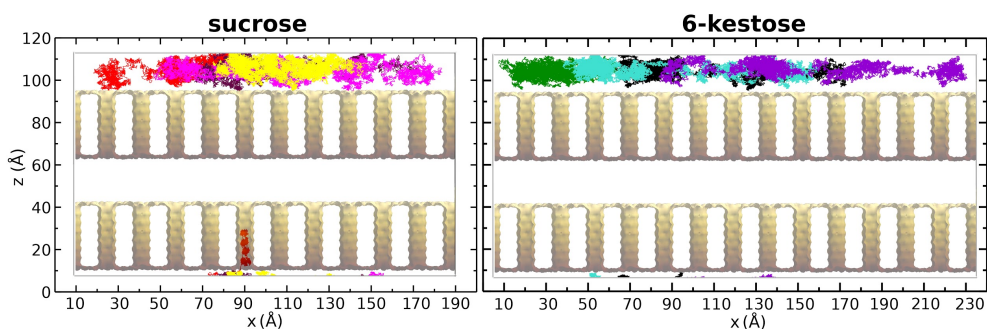


**Figure C7:** Sucrose (left) and 6-kestose (right) trajectories during MD simulation (20 ns) of AET membrane in a mixture containing 4 sucrose and 4 6-kestose molecules, at 338K.

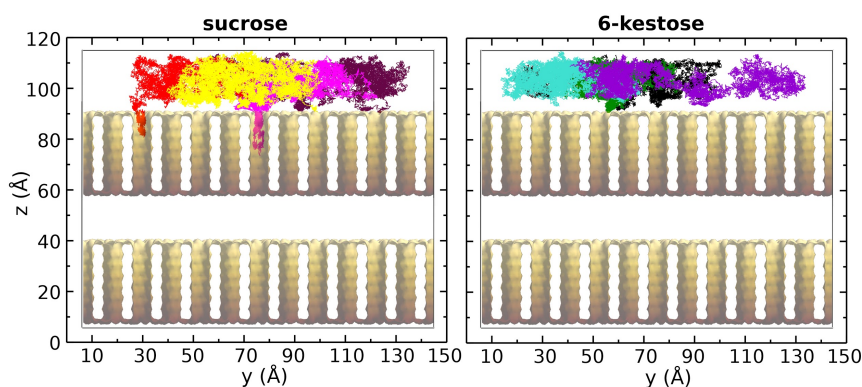


**Figure C8:** Sucrose (left) and 6-kestose (right) trajectories during MD simulation (20 ns) of DON membrane in a mixture containing 4 sucrose and 4 6-kestose molecules, at 338K.

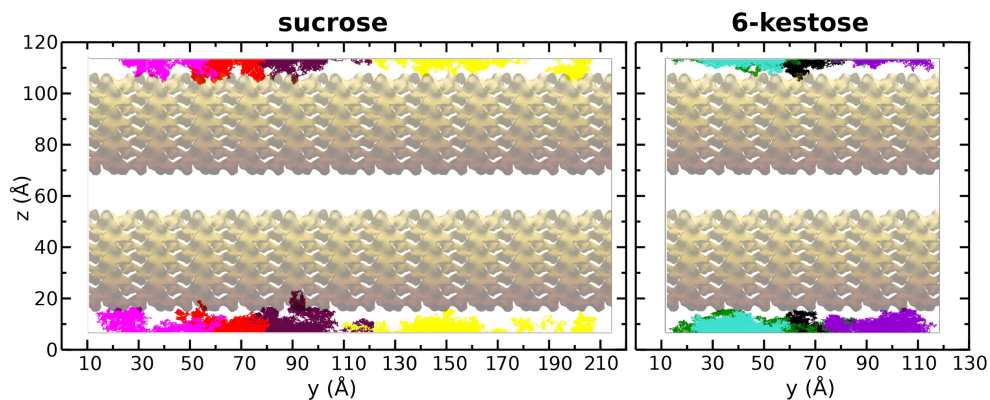


**Figure C9:** Sucrose (left) and 6-kestose (right) trajectories during MD simulation (20 ns) of ETR membrane in a mixture containing 4 sucrose and 4 6-kestose molecules, at 338K.

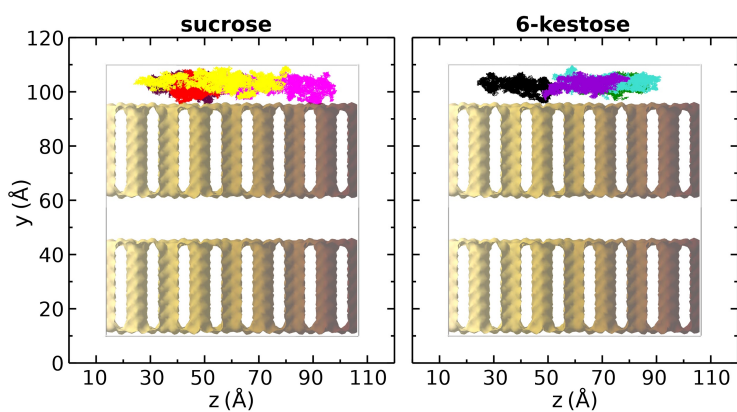


**Figure C10:** Sucrose (left) and 6-kestose (right) trajectories during MD simulation (20 ns) of IFO membrane in a mixture containing 4 sucrose and 4 6-kestose molecules, at 338K.

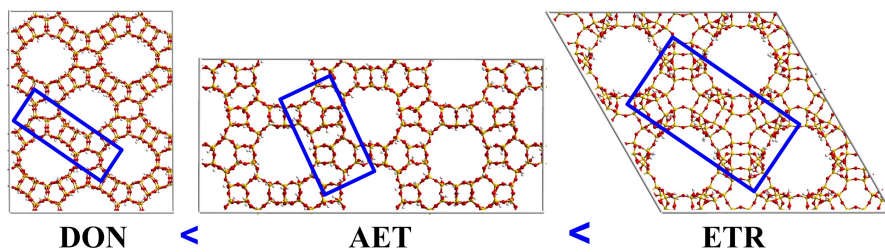


**Figure C11:** Comparison between zeolite wall thickness of AET, DON and ETR membranes.

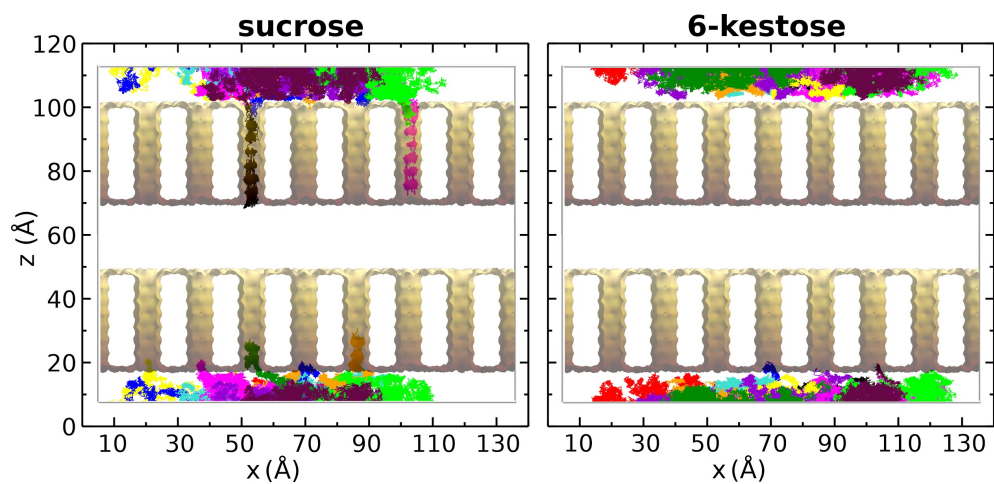


**Figure C12:** Sucrose (left) and 6-kestose (right) trajectories during MD simulation (20 ns) of AET membrane in a mixture containing large sugar loading: 12 sucrose and 12 6-kestose molecules, at 338K.

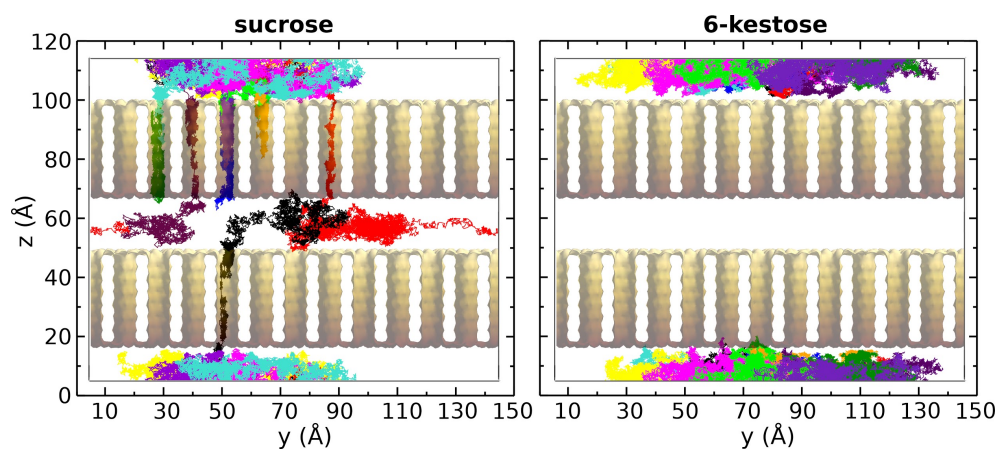


**Figure C13:** Sucrose (left) and 6-kestose (right) trajectories during MD simulation (20 ns) of DON membrane in a mixture containing large sugar loading: 12 sucrose and 12 6-kestose molecules, at 338K.

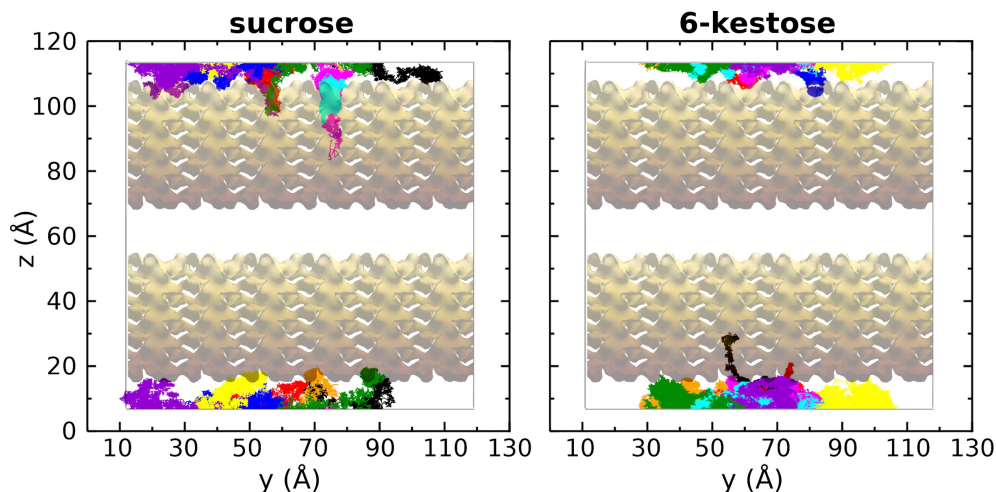


**Figure C14:** Sucrose (left) and 6-kestose (right) trajectories during MD simulation (20 ns) of ETR membrane in a mixture containing large sugar loading: 9 sucrose and 9 6-kestose molecules, at 338K.

## C5 Surface Effects in the Adsorption of Sugar Molecules

Uptake of sugar molecules will not only be influenced by pore size (Figure C15), but also by the adsorption of molecules at the external surface which, in turn, will depend on the ratio of ‘empty space’/‘total external surface’, that we call ‘channel/surface (%)’ (Table C10). ‘Empty space’ will be calculated as the area of the channels, whilst ‘total external surface’ will be calculated as the total amount of external surface available in the corresponding crystallographic plane. We indicate below the individual calculations (Table C9), plus also the sugar concentration per channel (Figure C16), and we plot the results for the different zeolites, along with the pore sizes. A monotonic increase of pore size versus channel/surface is observed (Figure C17), which means the larger the channel, the smaller will be the effect of surface adsorption and this should contribute to increase the uptake. However, a second effect, perhaps more important, is the thickness of the zeolite walls as seen in Figure C11, which shows the order, from lower to higher, DON, AET and ETR. According to this, the thin walls of DON will contribute less to the surface barrier effect and will allow an easier entrance of sugar molecules into the channels. Contrarily, for ETR, the large thickness will maximize surface adsorption and will contribute to less uptake. This is in

agreement with the result obtained, and this explanation is just an attempt to rationalize such results.

**Table C9:** Number of channels/unit cell (u.c.) and the orientation considered for the calculation of channel and unit cell surface area, considering the area equation of an ellipse and parallelogram, respectively. Percentage of the channel with respect to the total surface of the unit cell.

zeolite	channels/ u.c.	channel orientation	channel area ( $\text{\AA}^2$ )	u.c. surface area ( $\text{\AA}^2$ )	channel/ surface (%)
AET	2	c	53.98	472.08	22.9%
DON	2	c	52.17	441.36	23.6%
EMT	1	c	41.85	256.65	16.3%
ETR	1	c	80.12	368.72	21.7%
FAU	4	[110]	43.01	838.17	20.5%
IFO	2	b	77.42	374.53	41.3%
MOZ	3	c	37.38	843.13	13.3%
SBE	2	a $\equiv$ b	41.85	502.90	16.6%
SBS	2	a $\equiv$ b	37.93	469.94	16.1%
SBT	3	a $\equiv$ b	44.72	705.35	19.0%
UTL	2	c	52.98	405.02	26.2%

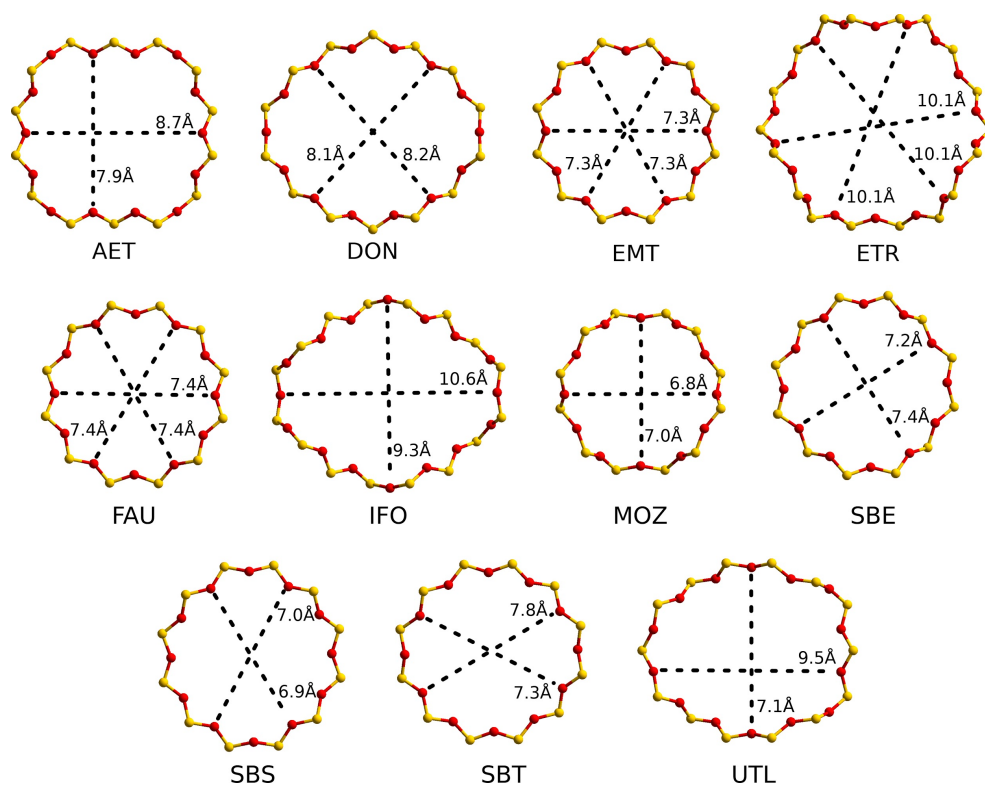


**Figure C15:** IZA dimensions (Å) of the largest channel of zeolites in this study.

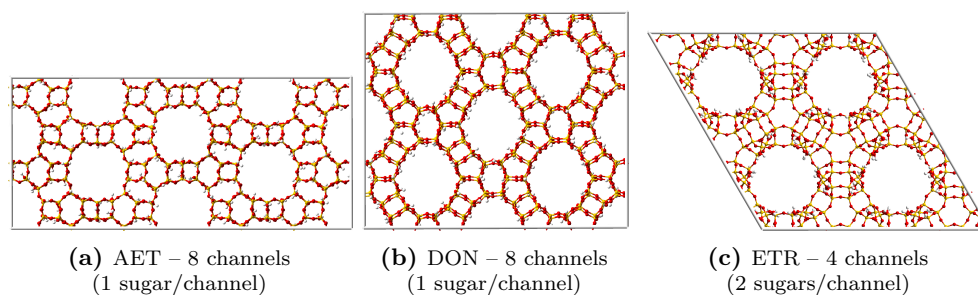


**Figure C16:** View of the membrane models along the channels: AET (a), DON (b) and ETR (c). Concentration of sugar molecules/channel in each membrane for simulations with low sugar concentration (4 sucrose/4 6-kestose mixture).



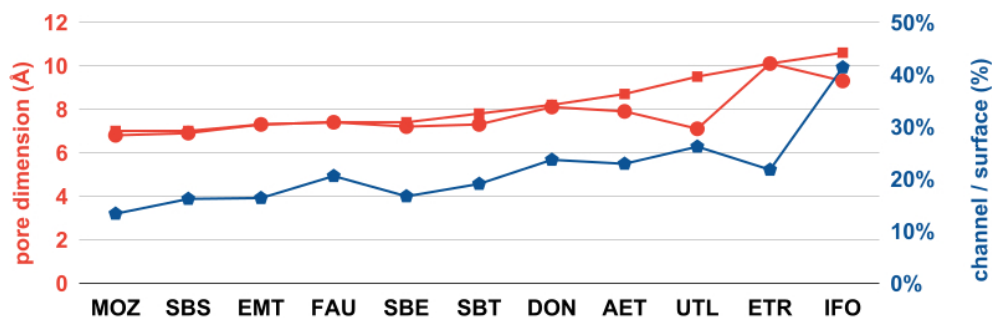


**Figure C17:** Channel size (red lines) and percentage of the channel on the surface of the unit cell (blue line), for all zeolites investigated.

We have also calculated the surface density of silanols as a measure of the hydrophilicity of the surface. The calculation was made dividing the number of silanol groups by the corresponding framework surface area, and the framework surface area was calculated as: total-external-surface = framework-surface + channel-surface, with the calculations of ‘total-external-surface’ and ‘channel-surface’ described above. The degree of hydrophilicity (Table C10) indicates similar values for AET, DON and ETR, and a considerably larger value for IFO. Hydrophobic surfaces, with less sugar-surface interaction, will contribute to increase the probability to enter the sugar molecules in the zeolite channels. The similar values obtained for AET, DON and ETR do not allow to assess any preferential structure for sugar uptake according to this concept.

**Table C10:** Number of silanol groups in each surface, and its concentration per surface area and framework area. Framework area is total surface minus channel surface.

zeolite	-OH in surface	-OH/surface area ( $\text{\AA}^{-2}$ )	-OH/framework area ( $\text{\AA}^{-2}$ )
AET	72	0.153	0.198
DON	64	0.145	0.190
ETR	48	0.130	0.166
IFO	88	0.235	0.401

## C6 Sugar-water Radial Distribution Functions (RDF).

Water molecules play an essential role in the diffusion of the sugar molecules through the pores, acting as a solvent. Care has been taken in the force field definition of the sugar-water interactions (Table C2). With many terminal O-H,

these molecules should interact strongly with water molecules, forming hydrogen bonds. Sucrose contains 8 alcohol and 3 ester groups and 6-kestose contains 11 alcohol and 5 ester groups. For practical reasons below we will call the sugar oxygens in these groups as O1.

Some insights into the solvation of the sugar molecules in the membrane systems can be gained by comparing the solvation of the sugars, according to their location (either at the external zeolite surface or inside the zeolite micropore) as shown in Figure C18.

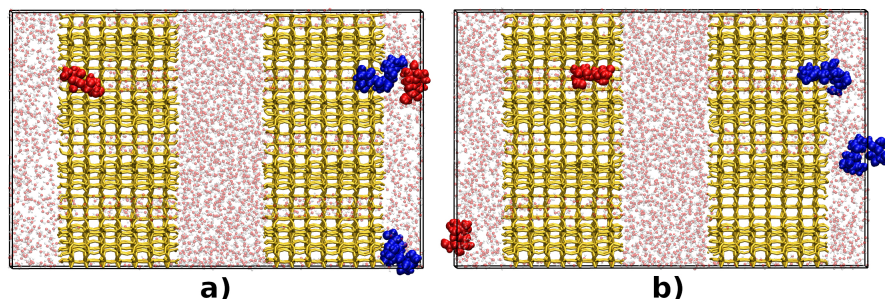


**Figure C18:** Different locations of selected sugar molecules (sucrose, red; 6-kestose, blue) in AET membrane (in yellow). Sucrose and 6-kestose appear at two different locations: external surface, and micropore. Frames on the a) beginning and b) ending of MD simulation (of high concentration), show selected molecules with no exchange ‘micropore’  $\leftrightarrow$  ‘external surface’ along the entire 20 ns run. Water molecules depicted with transparency, and other sugar molecules from the simulation were omitted for the sake of clarity.

Calling H4 to the hydrogen atoms of the water molecules, the O1—H4 radial distribution functions (Figure C19) give us valuable information about the sugar-water interactions and also in particular (at short ranges) the hydrogen bonding between sugar-water.

The RDF plot shows as a main conclusion that sugar molecules at the surface are more solvated than those at the micropore, as observed from the larger RDF values in the short O1—H4 distance interval (2-7 Å). This makes sense by considering that sugar molecules at the external surface are not only more accessible but also from the fact that water uptake will rarely achieve water-bulk density inside the micropore according to the common knowledge of water adsorption in zeolites. Hence, by having density lower than 1 g/cm<sup>3</sup> inside the micropore, water will not be able to solvate sugar molecules so effectively in the micropore as at the external membrane surface.

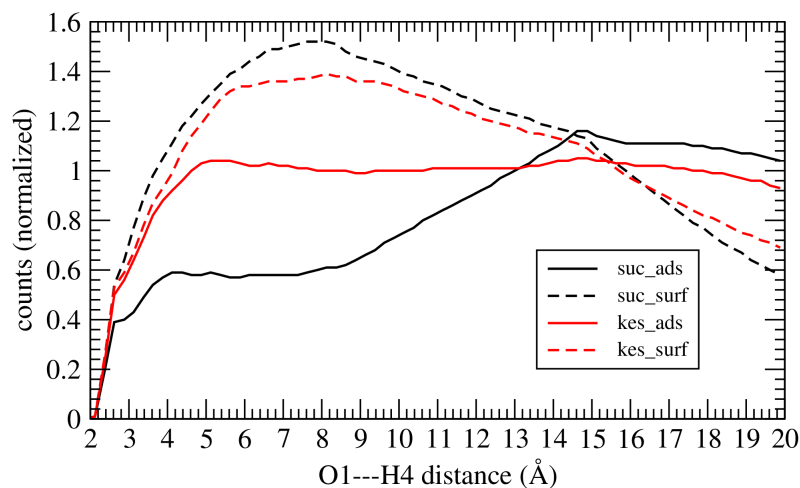


**Figure C19:** O1(sugar)-H4(water) radial distribution functions in AET membrane for the different types of sugar: sucrose (suc) and 6-kestose (kes), at: external surface (surf) and micropore (ads).

It is uncertain how this will contribute to the diffusivity of sugars inside the zeolite micropore since many factors come into play simultaneously. Probably decreasing the solvation of sugar inside the micropore may contribute to diffuse faster than if the solvation was that of the solution. On the other hand, the desolvation of sugar when jumping into the micropore contributes to reduce the energetic stability of the sugar molecule and makes this ('out  $\rightarrow$  in' diffusion) a more endothermic process, hence contributing to the surface barrier that we have mentioned in the main manuscript. So far we just describe the physics of the system in general. It is not clear to what extent the sugar solvation degree can be tuned up, depending on the sugar concentration. These, as well as pressure, would be interesting aspects to optimize in a real separation process, also perhaps designing membranes made of tunable thickness in which the relative weight of external surface and intracrystalline resistances could also be a parameter that will influence selective permeance for each of the sugar molecules.

## C7 Energetic Analysis of Sugar Adsorption on Zeolite Membranes.

In order to evaluate the interaction energy between zeolite membrane, sugar and water molecules, three different models were considered (depicted in Figure C20)

that take into account all types of interactions between the three membrane constituents: zeolite (Z), sugar (S, sucrose or 6-kestose) and water (W). In particular, sugar molecules can be located either as: adsorbed directly at the zeolite surface (S1) or on top of another sugar molecule (S2), as shown in Figure C20c. This is crucial since the main aspect we wish to study here is the different binding of sugar molecules (S1, S2), knowing that the weaker the binding the easier will be to jump inside the zeolite channels.

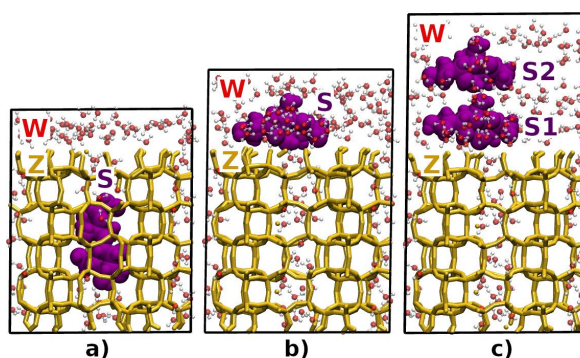


**Figure C20:** Models considered for  $E_{AB}^{sp}$  calculation. Zeolite membrane (Z, in yellow, representing AET, ETR, or DON frameworks), water molecules (W, with transparency) and sugar molecules (S, in purple, representing sucrose and/or 6-kestose molecules) in different positions: a) one sugar adsorbed in the zeolite channel, b) one and c) two sugar molecules in membrane surface. In the latter case, sugar index increases with its distance from the membrane.

The geometries containing every combination of sugars (sucrose and 6-kestose) adsorbed (either at the external surface or in the intracrystalline micropore) at AET, DON and ETR membranes (models in Figure C20) were optimized with GULP package (version 4.3.2) [18], with the same force field previously employed on the MD simulations. Then, single point energy calculations were performed to assess the interaction energy ( $E_{AB}^{int}$ ) for each pair A and B, with A,B being any of: Z,S,W, according to Equation C7:

$$E_{AB}^{int} = E_{AB}^{sp} - (E_A^{sp} + E_B^{sp}) \quad (C7)$$

where  $E_{AB}^{sp}$ ,  $E_A^{sp}$  and  $E_B^{sp}$  are single point calculations (using the optimized geometry) containing AB, A and B. Thus, contains the electrostatic and van der Waals contributions arising from A–B interaction. For water, a mean value was reported ( $E_{WB}^{int}$ ), divided by the total number of water molecules in the system.

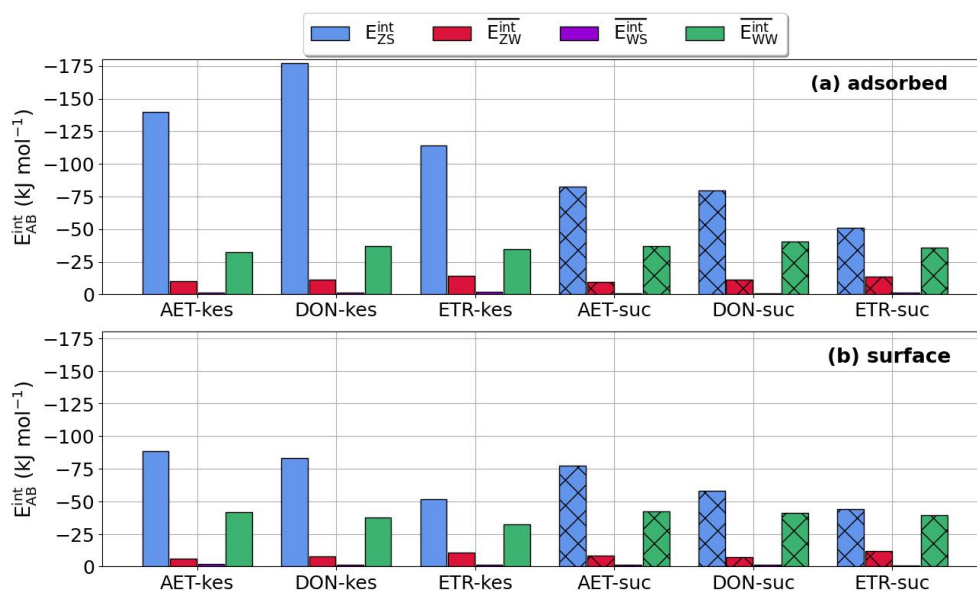


**Figure C21:** Interaction energy for systems containing one sugar molecule (a) adsorbed in the membrane channel or (b) interacting with membrane surface. Energy values between Zeolite–Sugar ( $E_{ZS}^{int}$ , in blue), Zeolite–Water ( $E_{ZW}^{int}$ , in pink), Water–Sugar ( $E_{WS}^{int}$ , in purple) and Water–Water ( $E_{WW}^{int}$ , in green) interacting pairs. Sugar molecules were 6-kestose (kes, in solid colors) or sucrose (suc, crosshatched bars). Energy values involving water were divided by the total number of water molecules.

Analyzing the energy interactions of systems containing a single molecule of sugar (graphs of Figure C21 and Table C11), the greater stabilization comes from Zeolite–Sugar interactions ( $E_{ZS}^{int}$ ), ranging from -44 to -177 kJ/mol. For every framework, such interactions are stronger when the sugar is adsorbed in the zeolite channel (Figure C21a), as the sugar molecule is surrounded by membrane channel atoms, maximizing zeolite-sugar contacts. In contrast, a weaker interaction is established through the silanol groups on the membrane surface (Figure C21b) and the sugar molecule.

**Table C11:** Interaction energy (in kJ/mol) for systems containing one sugar molecule adsorbed in the membrane channel (a) or interacting with membrane surface (s). Energy values between Zeolite–Sugar ( $E_{ZS}^{int}$ ), Zeolite–Water ( $E_{ZW}^{int}$ ), Water–Sugar ( $E_{WS}^{int}$ ) and Water–Water ( $E_{WW}^{int}$ ) interacting pairs. The total number of water molecules in each box is the sum of water in the surface ( $n^\circ\text{W}(s)$ ) and adsorbed into membrane channels ( $n^\circ\text{W}(a)$ ). Sugar molecules were 6-kestose (k) or sucrose (s). Energy values involving water were divided by the total number of water molecules.

system	$E_{ZS}^{int}$	$E_{ZW}^{int}$	$E_{WS}^{int}$	$E_{WW}^{int}$	$n^\circ\text{W}(s)$	$n^\circ\text{W}(a)$
AET-k(a)	-140.10	-9.91	-1.24	-32.23	62	69
AET-k(s)	-88.20	-6.29	-1.86	-41.45	110	78
AET-s(a)	-82.38	-9.72	-0.73	-37.01	63	69
AET-s(s)	-77.38	-8.13	-1.21	-42.42	88	80
DON-k(a)	-177.51	-11.16	-1.22	-37.10	47	48
DON-k(s)	-83.19	-7.93	-1.55	-37.28	71	66
DON-s(a)	-79.61	-11.08	-0.86	-40.32	49	56
DON-s(s)	-58.19	-7.28	-1.29	-41.19	88	61
ETR-k(a)	-114.13	-14.04	-1.67	-34.81	48	101
ETR-k(s)	-51.43	-10.84	-1.38	-32.53	58	119
ETR-s(a)	-51.16	-13.85	-1.11	-35.58	48	107
ETR-s(s)	-43.79	-12.01	-0.89	-39.38	66	119

Regarding the nature of sugar, a greater stabilization of  $E_{ZS}^{int}$  is observed for 6-kestose on models (a) and (b). That is consistent with its greater molecular size (contains an extra ring when compared with sucrose), which increases the number of functional groups and consequently, interaction sites. It is important to note that despite the highest magnitude of  $E_{ZS}^{int}$  in the systems containing 6-kestose adsorbed into the membrane, this does not necessarily imply 6-kestose will uptake easily since the entropic contribution was not taken into account here. Another aspect we highlight is that the calculated models (a to c) were designed to give some insights into the system’s energetics, by considering a single configuration. The system dynamics, not included here, would allow to analyze more molecular configurations and obtain better statistics.

The framework effect on  $E_{ZS}^{int}$  for the adsorbed structures (model (a)) is related with the channel size, where smaller channels maximizes Zeolite–Sugar interaction, increasing the interaction strength. Hence,  $E_{ZS}^{int}$  follows the order:  $\text{DON} \leq \text{AET} < \text{ETR}$  for both sugars, following the same trends of ring size:  $\text{DON} (8.1 \times 8.2 \text{ \AA}) < \text{AET} (7.9 \times 8.7 \text{ \AA}) < \text{ETR} (10.1 \times 10.1 \text{ \AA})$ .

On the other hand, when considering the membrane surface (model (b)), the  $E_{ZS}^{int}$  stabilization can be correlated with the concentration of silanol groups on

the membrane surface. Thus,  $E_{ZS}^{int}$  values follow the same trend that the amount of silanols/framework area: AET (0.198 Å<sup>-2</sup>) > DON (0.190 Å<sup>-2</sup>) > ETR (0.166 Å<sup>-2</sup>).

Concerning water interactions, the most stabilizing ones are water-water (with  $E_{WW}^{int}$  ranging from -32 to -42 kJ/mol), followed by water-zeolite ( $E_{ZW}^{int}$  stabilization is -11.6 kJ/mol, on average), and finally water-sugar molecules ( $E_{WS}^{int}$  is -1.3 kJ/mol, on average). This relates to the increasing capacity to coordinate each water molecule by: sugar, zeolite and other water molecules.

Zeolite-water interactions ( $E_{ZW}^{int}$ ) become stronger when a larger number of silanol groups are available to interact, i.e. when sugar locates in the channels instead of the external surface. Similarly sugar-water interactions ( $E_{WS}^{int}$ ) become stronger when sugars are located at the external surface, being more accessible.

The surface barrier effect mentioned in the main manuscripts can be explained by evaluating the energetics of models (b) and (c) (Table C12). The models with two sugar molecules (S1: monolayer, near the zeolite surface and S2: forming the adsorbate bilayer) give a valuable information.

If the interactions Z-S1 are stronger than S1-S2, then molecules in the bilayer (S2) do have more probability to migrate into the channel by being less attached than those in the monolayer (S1). This demonstrates that sugar uptake is larger at larger loading (Section 5.3.2.2) than at dilute loading (Section 5.3.2.1), according to what we have called ‘surface barrier’ in the Chapter 5.

The analysis of the energies below (Table C12) confirm this explanation. Monolayer interactions ( $E_{ZS}^{int}$  and  $E_{ZS1}^{int}$ ), ranging from -38 to -86 kJ/mol (values strongly depending on the sugar conformation) are the strongest. Sugar bilayer interactions ( $E_{S1S2}^{int}$ ) are less stabilizing, with the range -7 to -27 kJ/mol.

**Table C12:** Interaction energy for systems containing sugar molecules above the membrane surface. Energy values between Zeolite-Sugar molecule ( $E_{ZS}^{int}$  and  $E_{zS1}^{int}$ , for sugar at monolayer) and Sugar-Sugar ( $E_{S1S2}^{int}$ ) interacting pairs. Sugar index increases with membrane distance (1 or 2).

Sucrose (s)	AET	DON	ETR	6-kestose (k)	AET	DON	ETR
$E_{ZS}^{int}$ (s)	-77.4	-58.2	-43.8	$E_{ZS}^{int}$ (k)	-88.2	-83.2	-51.4
$E_{ZS1}^{int}$ (s1s2)	-85.8	-43.5	-37.5	$E_{ZS1}^{int}$ (k1k2)	-70.9	-42.1	-82.9
$E_{S1S2}^{int}$ (s1s2)	-7.3	-6.6	-26.9	$E_{S1S2}^{int}$ (k1k2)	-21.6	-57.7	-59.1

## C8 Simulation Performance Benchmark

In order to evaluate the performance of the membrane simulations, the 4 zeolite systems were simulated for 100000 steps (100 ps) with 1, 2, 4, 8 and 16 cores, and the results were summarized in the graph of Figure C22. CPU performance may vary within the same machine depending on the nodes employed.

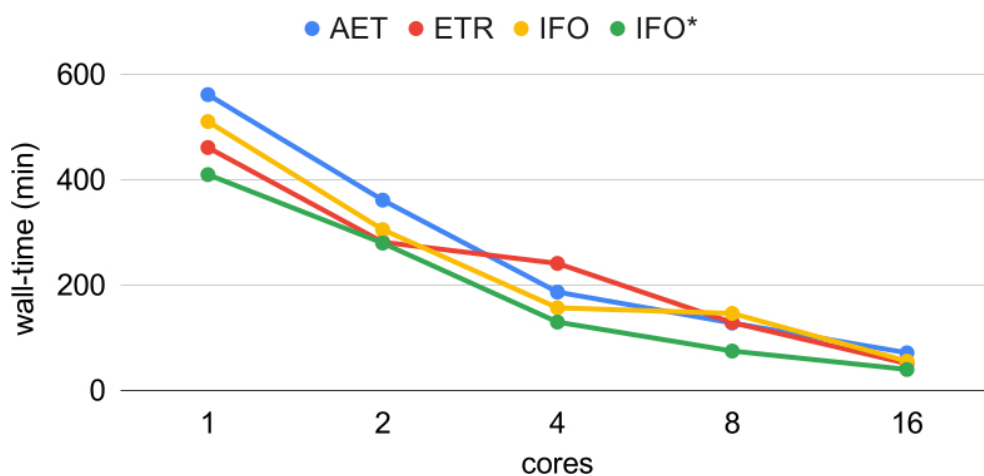


**Figure C22:** Simulation wall-time for membrane simulations in 1 to 16 cores. Simulation box contains 11724 (AET), 9249 (ETR) and 10080 (IFO) atoms. IFO and IFO\* were performed in different machines.

## References

- [1] Metropolis, N.; Rosenbluth, A. W.; Rosenbluth, M. N.; Teller, A. H.; Teller, E. Equation of State Calculations by Fast Computing Machines. *J. Chem. Phys.* **1953**, *21* (6), 1087–1092. DOI: 10.1063/1.1699114.
- [2] Broyden, C. G. The Convergence of a Class of Double-rank Minimization Algorithms 1. General Considerations. *IMA J. Appl. Math.* **1970**, *6* (1), 76–90. DOI: 10.1093/imamat/6.1.76.
- [3] Fletcher, R. A New Approach to Variable Metric Algorithms. *Comput. J.* **1970**, *13* (3), 317–322. DOI: 10.1093/comjnl/13.3.317.



- [4] Goldfarb, D. A Family of Variable-metric Methods Derived by Variational Means. *Math. Comput.* **1970**, *24* (109), 23–26. DOI: 10.1090/S0025-5718-1970-0258249-6.
- [5] Shanno, D. F. Conditioning of Quasi-Newton Methods for Function Minimization. *Math. Comput.* **1970**, *24* (111), 647–656. DOI: 10.1090/S0025-5718-1970-0274029-X.
- [6] Ermer, O. Calculation of Molecular Properties Using Force Fields. Applications in Organic Chemistry. In *Bonding forces*; Springer, 2005, 161–211. DOI: 10.1007/3-540-07671-9\_3.
- [7] Levitt, M.; Lifson, S. Refinement of Protein Conformations Using a Macromolecular Energy Minimization Procedure. *J. Mol. Biol.* **1969**, *46* (2), 269–279. DOI: 10.1016/0022-2836(69)90421-5.
- [8] Rappe, A. K.; Casewit, C. J.; Colwell, K. S.; Goddard, W. A.; Skiff, W. M. UFF, a Full Periodic Table Force Field for Molecular Mechanics and Molecular Dynamics Simulations. *J. Am. Chem. Soc.* **1992**, *114* (25), 10024–10035. DOI: 10.1021/ja00051a040.
- [9] Casewit, C. J.; Colwell, K. S.; Rappe, A. K. Application of a Universal Force Field to Organic Molecules. *J. Am. Chem. Soc.* **1992**, *114* (25), 10035–10046. DOI: 10.1021/ja00051a041.
- [10] Casewit, C. J.; Colwell, K. S.; Rappe, A. K. Application of a Universal Force Field to Main Group Compounds. *J. Am. Chem. Soc.* **1992**, *114* (25), 10046–10053. DOI: 10.1021/ja00051a042.
- [11] Gasteiger, J.; Marsili, M. A New Model for Calculating Atomic Charges in Molecules. *Tetrahedron Lett.* **1978**, *19* (34), 3181–3184. DOI: 10.1016/S0040-4039(01)94977-9.
- [12] Ghysels, A.; Moors, S. L. C.; Hemelsoet, K.; De Wispelaere, K.; Waroquier, M.; Sastre, G.; Van Speybroeck, V. Shape-Selective Diffusion of Olefins in 8-Ring Solid Acid Microporous Zeolites. *J. Phys. Chem. C* **2015**, *119* (41), 23721–23734. DOI: 10.1021/acs.jpcc.5b06010.

- [13] Bushuev, Y. G.; Sastre, G. Atomistic Simulations of Structural Defects and Water Occluded in SSZ-74 Zeolite. *J. Phys. Chem. C* **2009**, *113* (25), 10877–10886. DOI: 10.1021/jp9013306.
- [14] Catlow, C. R. A.; Freeman, C. M.; Vessal, B.; Tomlinson, S. M.; Leslie, M. Molecular Dynamics Studies of Hydrocarbon Diffusion in Zeolites. *J. Chem. Soc. Faraday Trans.* **1991**, *87* (13), 1947–1950. DOI: 10.1039/FT9918701947.
- [15] Kiselev, A. V.; Lopatkin, A. A.; Shulga, A. A. Molecular Statistical Calculation of Gas Adsorption by Silicalite. *Zeolites* **1985**, *5* (4), 261–267. DOI: 10.1016/0144-2449(85)90098-3.
- [16] Botella, P.; Corma, A.; Sastre, G. Al-ITQ-7, a Shape-Selective Zeolite for Acylation of 2-Methoxynaphthalene. *J. Catal.* **2001**, *197* (1), 81–90. DOI: 10.1006/jcat.2000.3057.
- [17] Yuan, J.; Liu, Z.; Wu, Y.; Han, J.; Tang, X.; Li, C.; Chen, W.; Yi, X.; Zhou, J.; Krishna, R.; Sastre, G.; Zheng, A. Thermal Resistance Effect on Anomalous Diffusion of Molecules Under Confinement. *Proc. Natl. Acad. Sci. U.S.A.* **2021**, *118* (21), e2102097118. DOI: 10.1073/pnas.2102097118.
- [18] Gale, J. D.; Rohl, A. L. The General Utility Lattice Program (GULP). *Mol. Simul.* **2003**, *29* (5), 291–341. DOI: 10.1080/0892702031000104887.

